

An entanglement perspective on phase transitions, conventional and topological order

Inaugural-Dissertation

zur

Erlangung des Doktorgrades

der Mathematisch-Naturwissenschaftlichen Fakultät

der Universität zu Köln

vorgelegt von

Johannes Helmes

aus Kamp-Lintfort



Köln 2017

Berichterstatter: Prof. Dr. Simon Trebst

Prof. Dr. David Gross

Tag der mündlichen Prüfung: 02.12.2016

Contents

1. Introduction	11
2. Entanglement measures	15
2.1. Characterization of entanglement	15
2.2. Entanglement entropy	17
2.2.1. Von Neumann entropy	19
2.2.2. Rényi entropies	20
2.2.2.1. Replica trick	21
2.2.2.2. Experimental measurement	23
2.2.3. Boundary law of many-body ground states	25
2.3. Mutual information	29
2.4. General entanglement measures	30
I. Quantum phase transitions	33
3. Singular behavior at critical points	35
3.1. Quantum critical bilayers	36
3.2. Off-critical behavior of the boundary coefficient	37
3.3. Quantum Monte Carlo results	39
II. Critical theories	43
4. Corner entanglement	45
4.1. Logarithmic contribution	45
4.2. General properties	47
4.3. Field theory	48
4.4. Low-lying degrees of freedom	49
5. Free theories	51
5.1. Free boson	51
5.1.1. Correlator-based entropy computation	53
5.2. Free Dirac fermion	54
5.2.1. Lattice field theory	55
5.2.2. Correlator-based entropy computation	56
6. Lattice results in 2+1 dimensions	59
6.1. Numerical extraction of corner entanglement	59
6.1.1. Direct fit	60

6.1.2. Numerical linked-cluster expansion	61
6.1.3. Incremental regions	64
6.2. Interacting theories	65
6.3. Free theories	68
6.3.1. Infra-red scaling	69
6.3.2. Angle dependence	70
6.3.3. Duality	73
7. Summary	77
 III. Topological order	 79
8. Topological entanglement entropy	81
8.1. Long-ranged entanglement	82
8.2. Addition schemes	84
8.3. Classical analogue of entanglement entropy	87
8.3.1. Volume law	88
8.3.2. Classical topological order	88
9. Quantum error-correcting codes	91
9.1. Error correction in quantum computation	91
9.2. Toric code	96
9.2.1. Definition	96
9.2.2. Ground state	99
9.2.3. Excitations	101
9.2.4. Loop tension	103
9.2.5. Classical variant	105
9.3. Three-dimensional ‘toric’ code	106
9.3.1. Classical variants	109
9.4. X-cube code	111
9.5. Cubic code	112
10. Monte Carlo approach	115
10.1. Representation and measurement	115
10.1.1. Specific heat	115
10.1.2. Topological entropy	116
10.1.2.1. Replica trick	116
10.1.2.2. Thermodynamic integration	117
10.1.2.3. Addition schemes	118
10.2. Update algorithms	121
10.2.1. Local updates	122
10.2.2. Global pattern updates	125
10.2.2.1. Winding operator updates	125
10.2.2.2. Cluster-like updates	125
10.2.2.3. Lattice walk updates	126

11. Results for stabilizer codes	135
11.1. Two-dimensional classical toric code	135
11.1.1. Finite temperature crossover	135
11.1.2. Connectivity contribution	136
11.2. Three-dimensional classical codes	144
11.2.1. Specific heat	145
11.2.2. Finite temperature	150
11.2.3. Membrane tension	152
11.2.4. Quantum to classical mapping	154
12. Summary	157
13. Conclusion	161
A. Quantum Monte Carlo updates for bilayer models	167
B. Formulae for the entanglement entropy from groundstate correlations	169
B.1. Free boson	169
B.2. Free Dirac fermion	170
References	173

Abstract

The interplay of the constituents of interacting many-body systems may reveal emergent properties on the macroscopic scale which are not inherent to the individual constituents. These properties are expressed in macroscopic observables describing the state — denoted as the phase of the system. Continuous phase transition between phases are generically manifested in critical behavior, for example, a divergence of a macroscopic observable. The identification of the present phase of a system and the classification of critical phenomena into universality classes are exciting challenges of condensed-matter physics.

In this thesis, we use entanglement entropies as macroscopic quantities for the characterization of phases of quantum matter and critical theories. For ground-states of quantum many-body systems the entanglement entropy is a measure of the amount of entanglement between two subsystems. The generic dependence of the entanglement entropy on the size and shape of the subsystems is contained in the well-known boundary law — stating a scaling of the entanglement entropy with the boundary between the two subsystems. We numerically investigate how the coefficient of this dependence reflects quantum phase transitions in simple spin-half bilayer models.

Subleading terms to the boundary law such as a logarithmic contribution provide universal numbers for the criticality of field theories. We examine free and interacting theories from an entanglement entropy perspective in order to assess the role of the coefficient of the logarithmic correction induced by corners in the subsystems. Beyond its universality, this coefficient also quantifies degrees of freedom of low-lying excitations in the conformal field theory describing a critical point.

A constant contribution to the boundary law indicates the presence of so-called topological order in the ground state of a many-body system. This extremely useful property can also be identified in classical counterparts of entanglement entropy which we study at the example of various toric code models. To this endeavor, we have designed Monte Carlo techniques which allow for an efficient numerical computation of the constant contribution. In particular, we analyze via entanglement entropies under which conditions remnants of topological order are present in the quantum system at finite temperature and at perturbations from a magnetic field. The major motivation behind this effort is to use topological order for the robust storage of a quantum information — a basic need for the construction of quantum computers.

Kurzzusammenfassung

Die Bestandteile eines wechselwirkenden Vielteilchensystems können durch ihr Zusammenspiel emergente Eigenschaften des Gesamtsystems hervorrufen, die den einzelnen Teilchen nicht innewohnen. Diese Eigenschaften werden in makroskopischen Observablen ausgedrückt, die den Zustand — auch als Phase des Systems bezeichnet — beschreiben. Kontinuierliche Übergänge zwischen Phasen gehen üblicherweise mit kritischem Verhalten einher, zum Beispiel mit der Divergenz einer makroskopischen Observable. Die Bestimmung der vorliegenden Phase eines Systems sowie die Einteilung der kritischen Phänomene in Universalitätsklassen sind spannende Herausforderungen der Physik kondensierter Materie.

In dieser Arbeit verwenden wir Verschränkungsentropien als makroskopische Größen für die Charakterisierung von Phasen von Quantensystemen und kritischen Feldtheorien. Für Grundzustände von Quanten-Vielteilchensystemen ist die Verschränkungsentropie ein Maß für den Betrag der Verschränkung zwischen zwei Teilsystemen. Die generische Abhängigkeit der Verschränkungsentropie von der Größe und Geometrie des Teilsystems wird im bekannten Boundary-Law zum Ausdruck gebracht: Die Verschränkungsentropie skaliert mit der Größe des Randes zwischen den Teilsystemen. Wir untersuchen numerisch, inwiefern der Koeffizient dieser Abhängigkeit Quantenphasenübergänge in einfachen Spin- $\frac{1}{2}$ Zweischicht-Modellen wiedergibt.

Terme niedrigerer Ordnung im Boundary-Law wie zum Beispiel ein logarithmischer Beitrag stellen universelle Größen für die Kritikalität von Feldtheorien dar. Wir beleuchten freie und wechselwirkende Feldtheorien aus der Perspektive der Verschränkungsentropien, um die Rolle des Koeffizienten der logarithmischen Korrektur — induziert durch Ecken in den Teilsystemen — zu beurteilen. Über die Universalität hinaus misst dieser Koeffizient auch die Freiheitsgrade von niedrig-energetischen Anregungen in einer konformen Feldtheorie, welche einen kritischen Punkt beschreiben.

Ein konstanter Beitrag zum Boundary-Law weist auf sogenannte topologische Ordnung im Grundzustand des Vielteilchensystems hin. Diese äußerst nützliche Eigenschaft kann auch in klassischen Varianten der Verschränkungsentropien nachgewiesen werden, was wir am Beispiel zahlreicher Toric-Code Modelle durchführen. Zu diesem Zweck haben wir Monte-Carlo-Algorithmen entworfen, die eine effiziente numerische Berechnung des konstanten Beitrags ermöglichen. Mit Hilfe der Verschränkungsentropien analysieren wir insbesondere, unter welchen Bedingungen Überbleibsel von topologischer Ordnung des Grundzustands bei endlicher Temperatur oder bei Störungen durch ein Magnetfeld im Quantenzustand vorhanden sind. Die Hauptmotivation dieses Unterfangens besteht darin, topologische Ordnung auszunutzen, um Quanteninformation robust zu speichern — eine Grundvoraussetzung für die Konstruktion von Quantencomputern.

1. Introduction

The fundamental requirement for any quantitative investigation of a physical phenomenon is a mathematical description of the state of the considered system. This description is conceptually simple if the system has few constituents — a set of numbers denoting the (usually three-dimensional) vector components of the position, velocity, etc. is sufficient and manageable. However, in a typical condensed matter physics problem myriads of particles locally interact and collectively engender so-called emergent phenomena. A (microscopic) description is hence not only inconvenient due to the large number of necessary variables but also inappropriate because it is not set on a macroscopic scale where the phenomenon is perceptible. It is one of the great achievements of the domain of thermodynamics and statistical physics to exhaustively describe such a system at equilibrium by only a few macroscopic quantities such as energy, temperature, volume, pressure, etc.

We qualitatively observe on the macroscopic level that many-body systems can appear in different *phases* of matter. A central aspect of many-body physics is to identify these phases as well as *transitions* between them via appropriate macroscopic observables. For example, a system consisting of magnetic degrees of freedom could exhibit a ferromagnetically *ordered* phase at a sufficiently low temperature. This phase is characterized by a finite total magnetization. Upon increasing temperature, a phase transition to the magnetically disordered phase (paramagnet) takes place which implies a vanishing of the total magnetization. The two variables — magnetization and temperature — of the system enable us to detect and locate the transition. In this approach, the magnetization is the so-called order parameter in the Landau theory of the phase transition [1].

Order-disorder transitions, like the above example, are accompanied by the breakdown of correlations between the constituents. It is hence intuitive that in addition to the magnetization also the (spatial) *correlation length* is expected to provide a signature of the transition. This quantity denotes the typical spatial distance over which the degrees of freedom are correlated and is hence infinite in the ordered phase and decays as a power law to a finite value in the disordered phase. The point in the parameter space where the correlation length becomes infinite is denoted as the *critical point*. In its vicinity a rich spectrum of singular behavior of several macroscopic observables allows for a classification of the continuous phase transitions into universality classes [2].

In this thesis, we consider yet another quantity which provides universal information about the phase of a many-body system and its critical behavior. It represents an enhanced conceptualization of the idea to consider correlations in the state of the system as a footprint of order. Instead of the characteristic length scale of correlations, we focus on the aspect of dependencies which exist between two parts if they are correlated. In other words, the knowledge of the state of one part implies partial

1. Introduction

knowledge about the other. This notion opens up an information theory perspective and therein — in the quest for a quantification — suggests an *entropic* measure of correlations.

So far, we have outlined our relevant aspects of the physics of phase transitions in the realm of *classical* statistical mechanics. All macroscopic observables are hence thermal averages over the configurations in the ensemble. However, we want to examine *quantum* phase transitions which take place in the groundstate of a quantum system — a single many-body state as opposed to a statistical ensemble. The fundamental difference between interacting classical and quantum many-body systems is that in the latter degrees of freedom can be *entangled*, i.e. they exhibit a very counterintuitive form of a correlation which is unique to the quantum world [3]. As we expect correlations — and thereby the amount of entanglement — to undergo a significant change at a quantum phase transition we want to measure precisely this type of correlation in the groundstate with our macroscopic quantity. Combining the two desired features of the measure we want to use in this thesis, we arrive at the mathematical concept of our need, namely *entanglement entropy* [4].

Entanglement is mostly referring to a phenomenon between *two* participants — a notion which is in contradiction to the present *many*-body context. The workaround to this issue is to introduce a *bipartition* of our many-body system and consider entanglement between the resulting two subsystems. Subsequently, the adaptation of the concept of entropy in the information theory sense provides the quantification of entanglement. There are many ways to perform the necessary bipartition. This choice adds a technical degree of freedom to the problem which influences the value of the entanglement entropy although the total physical system is not changed. We hence need to understand the dependency of the entanglement entropy on the (non-physical) choice of the bipartition and — one step further — extract the universal parts which actually have physical significance. This decomposition is done by the *boundary law* of entanglement entropies and its subleading contributions [5]. If we compute the entanglement entropy for varying subsystem sizes of the bipartition, we obtain a leading term which scales linear in the size of the boundary of the subsystem. Subleading logarithmic (in the subsystem size) or constant terms are independent of the size of the bipartition (but not of its geometry) and their coefficients are hence candidates for universal quantities classifying phases or critical behavior.

After a broad introduction to the issue of measuring entanglement and a discussion of the boundary law, the structure of this thesis follows basically the orders of the contributions to the boundary law. With regard to the systems and phenomena considered, each Part focusses on its own physical problems.

In Part one, we provide a brief discussion of the physical content of the *boundary coefficient*. Even though it is non-universal and hence does not enhance our knowledge about a specific system at criticality it can nevertheless qualitatively reflect a phase transition by exhibiting a local maximum at the critical point [6]. We support these findings by quantum Monte Carlo simulations for bilayer spin-half models. An interesting aspect of this signature of the phase transition is that it sheds light on the role of an amplitude mode on the ordered side of the transition.

In Part two, we demonstrate the universality of the subleading *logarithmic con-*

tribution in gapless critical Hamiltonians — induced by corners in the bipartition [7]. The entanglement entropy perspective here constitutes a two-fold complementary description of criticality: For interacting systems corner entanglement adds another universal quantity to those of the order parameter paradigm of Landau. On the other hand, for conformal field theories there is a surprising equivalence between its canonical characteristic quantity, the central charge, and corner entanglement. We consider quantum critical spin-half bilayers as our interacting systems and study them with quantum Monte Carlo simulations. For these models we relate the value of their critical corner entanglement to their (known) $O(N)$ universality classes. The notion that N plays a crucial role leads over to studying degrees of freedom of low-lying excitations of conformal field theories via corner entanglement. We select the free boson and free Dirac fermion theories and carry out our entanglement entropy calculations on appropriate lattice field theories thereof.

A key role is taken by a subleading *constant contribution* in the boundary law of entanglement entropies which we will point out in Part three of this thesis. Specifically, it indicates the existence of *topological order* in gapless Hamiltonians [8]. This concept of order in a many-body system is characterized by the fact that fundamental properties of the system depend on its topology. It does not allow for a description via a local order parameter. In fact, a finite constant contribution of the entanglement entropy — also known as topological entanglement entropy — is often the only known indicator of topological order. Beyond the fundamental interest in topological order as an explanation for phenomena such as the fractional quantum Hall effect [9] we focus in this thesis on a potential application, namely quantum computing. The well-studied two-dimensional toric code model at its groundstate embodies a concept for the storage of quantum information which is robust against local perturbation by exploiting topological order [10]. We investigate this model and three-dimensional variants thereof from the perspective of topological entanglement entropies. Our main interest is the finite-temperature stability of topological order in the considered models which is of great importance for the practical relevance of the concept of such a quantum memory [11]. In addition, we examine the robustness of topological order against local perturbations by a magnetic field. It turns out, that the phenomenon of topological order can be spotted in a purely classical context via so-called classical Rényi entropies. In order to obtain a finite constant contribution, a non-trivial bipartition has to be performed which divides either subsystem A or B into two disconnected parts. We adopt this classical perspective and perform Monte Carlo simulations of our models and show how the topological entropy unambiguously detects transitions between topologically ordered and trivial phases.

2. Entanglement measures

To understand and classify phenomena in quantum many-body systems the usual approach has been for a long time to look at order parameters of the system, its spectrum of excitations or its response to external perturbations. A substantially different method — adapted from quantum information theory — is introduced in this Chapter as it constitutes the approach pursued in this thesis: The study and quantification of entanglement contained in ground states of quantum many-body systems. The underlying idea is that the wavefunction describing the ground state contains all (quantum) correlations governing the phases of matter. Accessible measures of entanglement hence often allow for a complementary characterization of e.g. critical phenomena and sometimes they even entail the only known identification of a quantum phase — as in the realm of topologically ordered phases.

In the wake of the Einstein Podolsky Rosen (EPR) paradox [12], entanglement was regarded mainly as a qualitative phenomenon. This Chapter starts off by a quantum information theory perspective on what entanglement is (Sec. 2.1). From this perspective, entanglement is often considered as a resource which can be exploited in quantum information processing and is believed to be responsible for the speed-up of quantum computation compared to classical computation. In trying to understand this resource, the *quantification* of entanglement underwent a rising interest in the context of quantum information science. Entropies of density matrices, introduced in Sec. 2.2, are basic tools for measuring entanglement. This concept is very successfully transferred to condensed-matter physics where it quantifies the entanglement in a pure quantum state via a bipartition of the many-body system. The entropy of the reduced density matrix of this bipartition is called *entanglement entropy*. Beyond two definitions thereof we discuss a prevalent boundary law of the entanglement entropy that generically occurs in locally interacting quantum systems. We also summarize an experiment that can measure entanglement entropies. Away from pure states the mutual information, introduced in Sec. 2.3, is an insightful quantity for example in thermally excited states. In Sec. 2.4 we discuss general criteria of entanglement measures for mixed states and explicitly present three examples, partly based on the entanglement entropy.

2.1. Characterization of entanglement

We begin with the technical definition of entanglement as our starting point in this discussion. We consider a composite quantum system, e.g. a state of two qubits¹

$$|\psi\rangle = \frac{|00\rangle + |11\rangle}{\sqrt{2}}, \quad (2.1)$$

¹A qubit is two-state quantum system with basis states denoted by $|0\rangle$ and $|1\rangle$.

2. Entanglement measures

also known as one of the Bell states. If — as in this example — it is impossible to write the quantum state as a direct product of two single qubit states, $|\psi\rangle = |a\rangle \otimes |b\rangle$, we define the state to be *entangled*. In the early days of quantum mechanics the consequences of entanglement were perceived as paradoxical [12] because they are contradictory to a notion of *local realism* — assumed to be an axiom of any scientific theory. Later, J. S. Bell derived an inequality between correlations of different measurements on entangled states in his seminal work [13]. This inequality would hold if local realism is to be obeyed. However, the violation of this inequality, indeed found² in a series of experiments [14–16], clearly forced the abandonment of the local reality axiom.

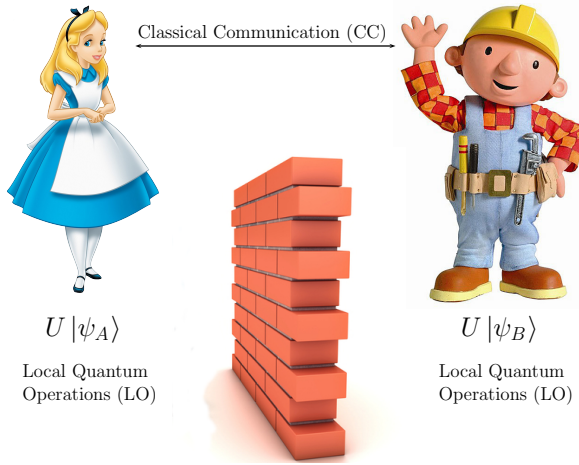


Figure 2.1.: Sketch of the LOCC paradigm. Alice and Bob can communicate classically and perform local quantum operations in their respective laboratory. No quantum particles can be transferred between them. ©BBC, Disney.

Beyond the above definition we further want to give an intuition from a quantum information theory perspective on what entanglement actually is, following the review article in Ref. [4]. This will be very helpful for our understanding of possibilities and limits of the quantification of entanglement. We first paraphrase entanglement by *quantum correlations* of many-body quantum states which takes us to the question what distinguishes them from classical correlations. To this end, we make an excursion to the quantum information technological paradigm of LOCC

— **local quantum operations and classical communication**. The underlying motivation for LOCC operations is the quest for communication between different quantum states in a quantum circuit. Unfortunately, decoherence hampers the lossless direct transmittal of quantum states over long distances. However, performing local quantum operations (LO) on both sides of the communication is much less threatened by decoherence since laboratory conditions close to ideal can be set. By the additional use of classical communication (CC) which is likewise close to perfect the local quantum operations can be applied in a coordinated way on both sides. The quantum computation setup could then consist of an initial distribution of quantum states over (noisy) quantum channels and further processing them by LOCC operations alone. Targeting to narrow down entanglement we now define classical correlations (between the distant partners) as those which can be created by LOCC operations. Further, we may find correlations in the quantum systems that *cannot* be created that way and therefore must have been already present in the initial state. A way to identify these quantum correlations is to use the noisy quantum state and

²Strictly speaking, it was not Bell’s original inequality but variants thereof which were tested in experiments.

LOCC operations to perform a task that cannot be simulated by classical correlations. Entanglement can hence be regarded as a *resource* needed in addition to LOCC operations for such tasks, e.g. the violation of the Bell inequality, and can conversely be defined as the correlations that cannot be created by LOCC.

As a completion of our characterization we now list a few properties of entanglement that will help tackling the problem of entanglement quantification. First, (i) the amount of entanglement in a separable state is zero. This statement follows not only from the mathematical definition but also from the fact that LOCC operations can create separable states from scratch. Further, (ii) LOCC operations do not increase entanglement. We can understand this property from considering two quantum states described by density matrices ρ and σ . If we can transform ρ into σ using LOCC operations, any task we can do with σ can also be done with ρ and LOCC. Hence, σ cannot contain more of the resource entanglement than ρ . A consequence of this property is (iii) that local unitary operations leave the amount of entanglement invariant. It follows from the fact that local unitary operations are invertible and belong to LOCC. Very important for the availability of an appropriate measure of entanglement is (iv) the notion that there exist maximally entangled states. Specifically, it can be shown [4] that for a bipartite quantum system with both subsystems of dimension d the state

$$|\psi_d^+\rangle = \frac{|0,0\rangle + |1,1\rangle + \dots + |d-1,d-1\rangle}{\sqrt{d}} \quad (2.2)$$

must be maximally entangled as a consequence of (ii) because every other pure or mixed state of the system can be obtained by LOCC on $|\psi_d^+\rangle$. It is evident that a requirement for an entanglement measure is that it be maximal for this state.

As a final remark we emphasize that without exception our notions of entanglement involve *two* parts or subsystems between which entanglement can be spotted: The LOCC paradigm assumes two participants in the communication and any correlation considered refers to the two parts — also the Bell inequalities are statements for pairs of particles. In a quantum information context this is quite natural because often communication between one sender and one receiver is considered (albeit cluster states and multi-user communication pose interesting scenarios as well). However, in a many-body system in condensed-matter physics we are interested in the collective behavior and the role of entanglement of *multiple* equally important constituents. No ‘natural’ bipartiteness is present in this context but we desire³ it for the measurement of entanglement, because this approach is best understood and most tractable. This leads to the apriori artificial bipartition of many-body systems that we are going to carry out in the following discussions.

2.2. Entanglement entropy

The objects of our interest are (pure) ground states of quantum many-body systems, whose density matrices are of the form $\rho = |\psi\rangle\langle\psi|$ and obey $\text{Tr}\rho^2 = 1$. In our

³There exist approaches for measuring entanglement in multipartite systems, reviewed in Refs. [3, 4]. However, no unified characterization of multiparty entanglement exists and a definition of an appropriate is not unique even for pure states. We will therefore not consider it in this thesis.

2. Entanglement measures

attempt to quantify (some of) the entanglement contained in ρ we subdivide the total system into two complementary parts A and $B \equiv \bar{A}$ which we assume to be entangled. We are apriori free how we choose this bipartition, but we expect the amount of entanglement to depend on this choice such that we seek to understand its influence.

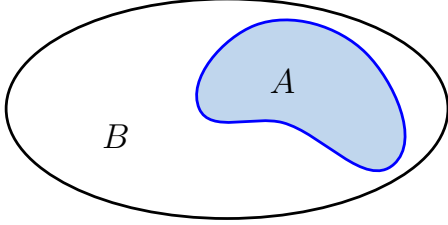


Figure 2.2.: Cartoon picture of a bipartition of a many-body system.

Having performed this bipartition, e.g. like in Fig. 2.2, we have to find separate descriptions of the degrees of freedom in either part. In the most simple case, it is possible to write $|\psi\rangle\langle\psi| = |\psi_A\rangle\langle\psi_A| \otimes |\psi_B\rangle\langle\psi_B|$, i.e. a direct product of two pure states for A and B . It follows from the definition of entanglement that in this case, no entanglement is present between parts A and B and any quantity measuring entanglement would have to be zero.

Moreover, the knowledge of the state of the total system is sufficient to fully know the state of its parts. This is different if such a factorization is not possible: Entanglement between the subsystems entails that the full information of the state of the total system does not allow inference on the state of the subsystems — in the most extreme case (such as the Bell states) the state of the subsystem is completely unknown. Subsystem A will be described by a *reduced* density matrix ρ_A which contains the available information of A . In case there is no entanglement it is pure, otherwise it is mixed because it encodes the probabilistic element in the knowledge of A .

The amount of (classical) mixedness in ρ_A is the key to quantifying the entanglement between A and B as pointed out in Ref. [17]. To access it, we first need to find a decomposition of the total $|\psi\rangle$ into states of the form $|i\rangle_A \otimes |i\rangle_B$, i.e. in respectively orthonormal bases of subsystem A and B . Such a form is obtained by the Schmidt decomposition

$$|\psi\rangle = \sum_i \lambda_i |i\rangle_A |i\rangle_B \quad (2.3)$$

with positive coefficients λ_i satisfying $\sum_i \lambda_i^2 = 1$. These so-called Schmidt coefficients pave the way to a quantification of the mixedness of ρ_A : If we only look at subsystem A , λ_i^2 is the probability to find the subsystem in state $|i\rangle_A$. In terms of density matrices it follows from Eq. (2.3) that for pure states $\rho = |\psi\rangle\langle\psi|$ we have

$$\rho_A \equiv \text{Tr}_B \rho = \sum_i \lambda_i^2 |i\rangle_A \langle i|_A \quad \text{and} \quad \rho_B \equiv \text{Tr}_A \rho = \sum_i \lambda_i^2 |i\rangle_B \langle i|_B, \quad (2.4)$$

where $\text{Tr}_{A/B}$ corresponds to the *partial* trace, i.e. the trace over the degrees of freedom of subsystem A or B only. A very important observation is, that ρ_A and ρ_B have identical eigenvalues, such that any function of the λ_i would be symmetric under a swap of the subsystems $A \leftrightarrow B$.

We expect a measure of entanglement to quantify the lack of information about the state of A given that we know ρ . Therefore it is justified to impose the following conditions on any entanglement measure E [3]:

1. Unitary transformation do not change the value of E , which implies that E is a function of the eigenvalues λ_i^2 of ρ_A only.
2. E is a continuous function of the λ_i^2 .
3. As demanded generically by a measure, E is additive if we have several independent copies of the system: $E(|\psi\rangle \otimes |\psi\rangle) = 2E(|\psi\rangle)$.

If translated to probability distributions, these requirements are identical to those of entropy in information theory — a quantity measuring the lack of information about the outcome of a random event. Hence, it is obvious to use the quantum mechanical analogues of entropies, applied to the density matrix ρ_A or ρ_B to quantify the bipartite entanglement of the pure state ρ . In the following, we present two forms of such entropies — the von Neumann entropy and the generalized Rényi entropies — which differ only in the imposed general additivity.

2.2.1. Von Neumann entropy

The von Neumann entropy [18] is a straightforward adaption of the Shannon entropy [19] for a discrete probability distribution $\{p_1, p_2, \dots, p_n\}$ to density matrices in quantum statistics. Entropy can be regarded as a measure for the amount of information we gain on average about a system by triggering and observing one random event of the distribution. The definition of the Shannon entropy $H(p_1, p_2, \dots, p_n)$ follows uniquely from imposing the conditions

1. H is continuous in the probabilities p_i ,
2. For an equiprobable distribution $p_i = \frac{1}{n}, i \in \{1 \dots n\}$ the entropy is maximal, i.e. $H(p_1, p_2, \dots, p_n) \leq H(\frac{1}{n}, \frac{1}{n}, \dots, \frac{1}{n})$ and strictly increasing with n , $H(\frac{1}{n}, \dots, \frac{1}{n}) < H(\frac{1}{n+1}, \dots, \frac{1}{n+1})$,
3. If we group the underlying random process into subprocesses, the total entropy is the entropy assigned to the belonging to a group plus the weighted sum of the entropies of the random process within the groups, e.g.

$$\begin{aligned} H(q_1, q_2, \dots, q_n = rp_n, q_{n+1} = (1-r)p_n) = \\ H(p_1 = q_1, p_2 = q_2, \dots, p_n) + p_n H(r, 1-r). \end{aligned}$$

The last condition ensures the additivity postulated above as a requirement for an entanglement measure, since the direct product of two copies of a random distribution has the entropy

$$\begin{aligned} & H(p_1 p_1, p_1 p_2, \dots, p_1 p_n, p_2 p_1, \dots, p_n p_n) \\ &= H(p_1, p_2, \dots, p_n) + \sum_{i=1}^n p_i H(p_1, p_2, \dots, p_n) \\ &= 2H(p_1, p_2, \dots, p_n). \end{aligned}$$

2. Entanglement measures

We therefore have $H(p_1, p_2, \dots, p_n) = -\sum_{i=1}^n p(x_i) \log_2 p(x_i)$ for the Shannon entropy, such that the translation to the quantum case, the von Neumann entropy, reads

$$S(\rho) = -\text{Tr} [\rho \ln \rho], \quad (2.5)$$

where we take the natural logarithm instead of \log_2 — the latter being commonly used in information theory in order to quantify information in binary digits. We use this definition to define our *bipartite von Neumann entanglement entropy* for pure states of a many-body system bipartitioned into parts A and B as

$$S_1(A) = -\text{Tr} [\rho_A \ln \rho_A]. \quad (2.6)$$

Note that if ρ_A is pure, we have $S(\rho_A) = 0$ which satisfies that a separable state $\rho = \rho_A \otimes \rho_B$ contains no entanglement. The subscript ‘1’ refers to the fact that Eq. (2.6) is a special case of the more general Rényi entropies defined in the next paragraph.

2.2.2. Rényi entropies

The third condition that led to the definition of the Shannon entropy can be weakened without giving up additivity. We replace it by:

- 3’. For two independent probability distributions \mathcal{P} and \mathcal{Q} the entropy of their direct product is given by $H(\mathcal{P} * \mathcal{Q}) = H(\mathcal{P}) + H(\mathcal{Q})$.

The so-called Rényi entanglement entropies [20] resulting from this modification are defined by

$$S_\alpha(A) = \frac{1}{1-\alpha} \ln [\text{Tr} \rho_A^\alpha]. \quad (2.7)$$

Satisfying (3’) but not (3.) allows more freedom in the definition of the entropy function, which is expressed in an additional parameter $\alpha \neq 1$ also called the *order* of the Rényi entropy. As indicated above, the limit of $\alpha \rightarrow 1$ recovers the von Neumann entropy, which can be proven by the use of l’Hôpital’s rule.

Interestingly, the special case of $\alpha = 2$ reveals a relation to the purity condition of density matrices, $\text{Tr} \rho^2 = 1$. We have seen above that for entangled subsystems A and B , ρ_A is *not* pure ($\text{Tr} \rho_A^2 < 1$) and hence the second Rényi entropy $-\frac{1}{2} \ln \text{Tr} \rho_A^2$ can be used as a measure of the purity of ρ_A after canceling the logarithm. The family of Rényi entropies has also gained interest in the study of the *entanglement spectrum* [21], — the spectrum of the “entanglement Hamiltonian” H_E defined via $\rho_A = \exp(-H_E)$. Low-energy excitations of H_E are believed to carry universal information about the phase of matter. Due to $\rho_A^\alpha = \exp(-\alpha H_E)$ the Rényi entropy for a large α corresponds to the low-temperature regime of H_E with temperature $T = 1/\alpha$. Large- α Rényi entropies hence provide a tool to access the low-energy section of the entanglement spectrum. A major motivation for the use of Rényi entropies instead of the von Neumann entropy is the availability of a numerical procedure to compute $S_\alpha(A)$ for integer α without having to directly compute and diagonalize ρ_A — the *replica trick*. Our physical observations are not qualitatively affected by this preference since the Rényi entropies are expected to

exhibit same entropic behavior as the von Neumann entropy due to their common defining conditions.

However, a few shortcomings of the Rényi entropies have to be mentioned. While the von Neumann entropy obeys subadditivity for a system composed of interdependent subsystems, i.e. $S_1(FG) \leq S_1(F) + S_1(G)$, the Rényi entropies in general do not [22]. For fixed ρ_A the mapping $\alpha \rightarrow S_\alpha(A)$ is a continuous function of α which monotonically decreases upon increasing α , see Fig. 2.3. Hence, compared to Eq. (2.6) it estimates the amount of mixedness of ρ_A to be smaller for $\alpha > 1$. In addition, if we consider the limit $\alpha \rightarrow \infty$ it becomes apparent from the definition in Eq. (2.7) that the largest eigenvalue $\lambda^{(\max)}$ of ρ_A dominates the trace of ρ_A^α , such that $S_\infty(A) = -\ln \lambda^{(\max)}$. In the context of the study of the low-energy part of entanglement spectra this issue has been pointed out by A. Chandran et al. [23] to be problematic as much less eigenvalues of ρ_A contribute to $S_{\alpha \rightarrow \infty}(A)$ than to $S_1(A)$. As a consequence, the physical importance of the largest eigenvalues of ρ_A is possibly overestimated by relying on $S_{\alpha \rightarrow \infty}(A)$. Since statistical averages of physical observables are computed using the *full* spectrum of ρ_A , e.g. $\langle O_A \rangle = \text{Tr}(O_A \rho_A)$, the physical conclusions from $S_{\alpha \rightarrow \infty}(A)$ could be biased and even exhibit artifactual behavior.

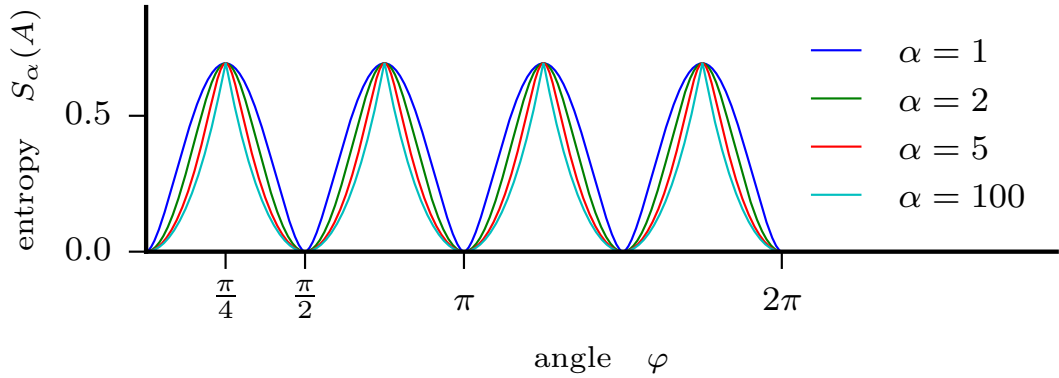


Figure 2.3.: Comparison of entanglement entropies for a simple state $|\psi\rangle = \sin \varphi |0_A 0_B\rangle + \cos \varphi |1_A 1_B\rangle$. As expected, the entropies vanish for $\varphi = n\pi/2$, where either $\sin \varphi = 0$ or $\cos \varphi = 0$. Hence, they reflect that there is no entanglement for product states $|\psi\rangle = \pm |00\rangle$ and $|\psi\rangle = \pm |11\rangle$. On the other hand, we have $\sin \varphi = \pm 1/\sqrt{2}$ and $\cos \varphi = \pm 1/\sqrt{2}$ for $\varphi = \pi/4, 3\pi/4, \dots$. The resulting state is maximally entangled and therefore the entanglement entropies become maximal at these angles.

2.2.2.1. Replica trick

The explicit computation of the reduced density matrix ρ_A in general requires the knowledge and numerical accessibility of the density matrix ρ of the entire system. For ground states, we have $\rho = |\psi\rangle\langle\psi|$ but unless the system is exactly solvable, an explicit form of $|\psi\rangle$ in a single-site composite basis is often unknown. We therefore have to consider the limit $\beta \rightarrow \infty$ from finite-temperature results. According to the Gibbs distribution we have in this case $\rho = Z(\beta)^{-1} \exp(-\beta H)$, where $Z(\beta) = \text{Tr} \exp(-\beta H)$ is the partition function. The exact diagonalization (ED) of the Hamiltonian H provides ρ , but for a large Hilbert space the Hamiltonian of a

2. Entanglement measures

many-body system becomes a huge matrix such that an ED is computationally impossible. However, this problem can be circumvented for Rényi entropies, Eq. (2.7), by the so-called *replica trick* which directly⁴ computes $\text{Tr} \rho_A^\alpha$ numerically for integer values of $\alpha \geq 2$ at finite inverse temperature β .

Originally, the replica trick has been established [24] in field theory, by expressing density matrices as Euclidean path integrals. It has been used to compute the von Neumann entropy as the limit $\alpha \rightarrow 1$ from the Rényi entropies [25, 26] before the interest in the Rényi entropies itself came up, together with an embedding of the replica trick in a quantum Monte Carlo approach [27].

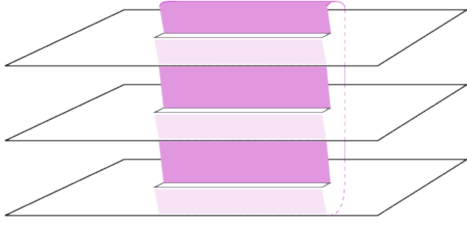


Figure 2.4.: Sketch of the Riemann surface for $\alpha = 3$ on which the path integral has to be computed. Periodic boundary conditions are assumed for one dimension of the white sheets representing the copies of part B . The pink sheets constitute the surface on which the path integral of part A is evaluated. ©P. Calabrese.

In its field theory variant the idea of the replica trick is to translate the necessary tracings and exponentiation in Eq. (2.7) to an appropriate manifold on which the path integral in $d + 1$ dimensions has to be computed. The partition function $Z(\beta)$ is simply expressed as a path integral which is cyclic in imaginary time τ , i.e. by identifying (or “sewing together”) the edges at $\tau = 0$ and $\tau = \beta$. For ρ_A we first have to perform the trace over part B , which corresponds to the same operation but for the degrees of freedom in part B only. Hence, the manifold on which the path integral is carried out is a cylinder of

circumference β where part A is cut out at $\tau = 0$. The remaining trace over part A of ρ_A raised to the power α is realized by taking α copies of these cylinders and cyclically sewing together the cut parts A , as illustrated in Fig. 2.4. The periodicity in imaginary time direction of the parts of the manifold belonging to region A is hence $\alpha \cdot \beta$. We thereby obtain an α -sheeted Riemann surface on which the path integral is computed — resulting in a *modified partition function* $Z[A, \alpha, \beta]$ such that the Rényi entropies are expressed as a function of a ratio between partition functions

$$S_\alpha(A) = \frac{1}{1 - \alpha} \ln \frac{Z[A, \alpha, \beta]}{Z(\beta)^\alpha}. \quad (2.8)$$

For our purpose of computing Rényi entropies for lattice Hamiltonians, which have a discrete Hilbert space, the replica trick can be derived without resorting to quantum field theory. This is done in the following for $\alpha = 2$. We denote the basis of the Schmidt decomposition for the bipartite system, Eq. (2.3), from now on by

⁴without explicitly computing ρ

$\{|a_k\rangle |b_k\rangle\}$. We have

$$\begin{aligned}
 \text{Tr}(\rho_A^2) &= \sum_k \langle a_k | \rho_A^2 | a_k \rangle \\
 &= \sum_{k,l} \langle a_k | \rho_A | a_l \rangle \langle a_l | \rho_A | a_k \rangle \\
 &= \sum_{k,l,m,n} \langle a_k b_m | \rho | a_l b_m \rangle \langle a_l b_n | \rho | a_k b_n \rangle \\
 &= \frac{1}{Z^2} \sum_{k,m,n} \langle a_k b_m | e^{-\beta H} [\mathbb{1}_A \otimes |b_m\rangle \langle b_n|] e^{-\beta H} | a_k b_n \rangle. \quad (2.9)
 \end{aligned}$$

A numerical procedure to approximately compute $\text{Tr}\rho_A^2$ would have to perform the three summations in the last expression of Eq. (2.9). In a quantum Monte Carlo scheme, the propagators $\exp(-\beta H)$ are decomposed into transfer matrices in imaginary time steps $\Delta\tau$ running twice from 0 to β . We see, that basis states of B need to be summed over in each replica (b_m and b_n), respectively satisfying the periodic boundary condition at $\tau = \beta$. Hence, the two copies of part B have to be considered fully independently. On the other hand, the inner summation over all basis states of part A translates to an identity operation $\mathbb{1}_A$ which implies that the configuration of A after the propagation from 0 to β is not constrained to the state at $\tau = 0$. Only the outer summation of basis states of A is performed (a_k), i.e. the propagation has a periodicity of 2β . Fig. 2.5 represents the last expression of Eq. (2.9).

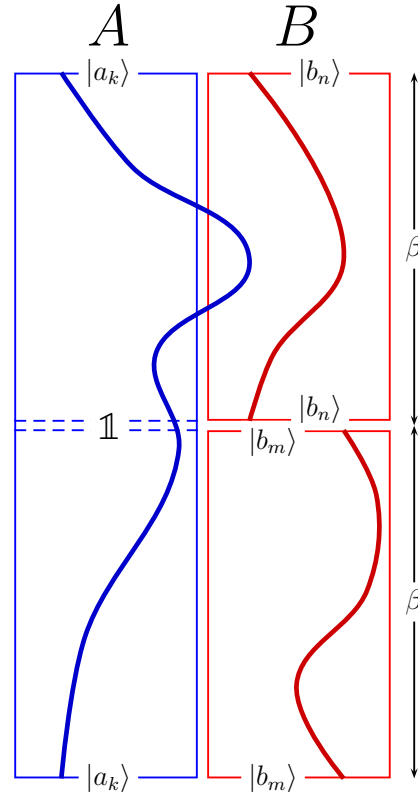


Figure 2.5.: Schematic picture of the replica trick for $\alpha = 2$. Dashed lines indicate that the copies of part A in both replicas are sewed together. Thick lines represent world lines in the path integral picture.

2.2.2.2. Experimental measurement

For a long time the study of entanglement entropies was susceptible to criticism due to its pure conceptual approach as opposed to experimentally observable quantities

2. Entanglement measures

in many-body systems like, for example, structure factors. However, this shortcoming could be strikingly eliminated by the seminal work of Islam et al. [28] in which the entanglement entropy could be experimentally measured by a scheme related to the replica trick. We briefly outline the scheme of this experiment and show the measurement result for the Rényi entropy with $\alpha = 2$.

A very successful experimental set-up to explore quantum physics relies on optical lattices [29], i.e. periodic potentials created by interfering laser beams. In the local minima of such a potential single atoms can be trapped and cooled to nearly zero temperature, thereby representing a many-body state governed by quantum physics. In order to probe the bipartite entanglement entropy, at first an entangled many-body state needs to be prepared. For two or three entangled particles this was successfully accomplished already in the experiments that proved a violation of Bell's inequality, see above.

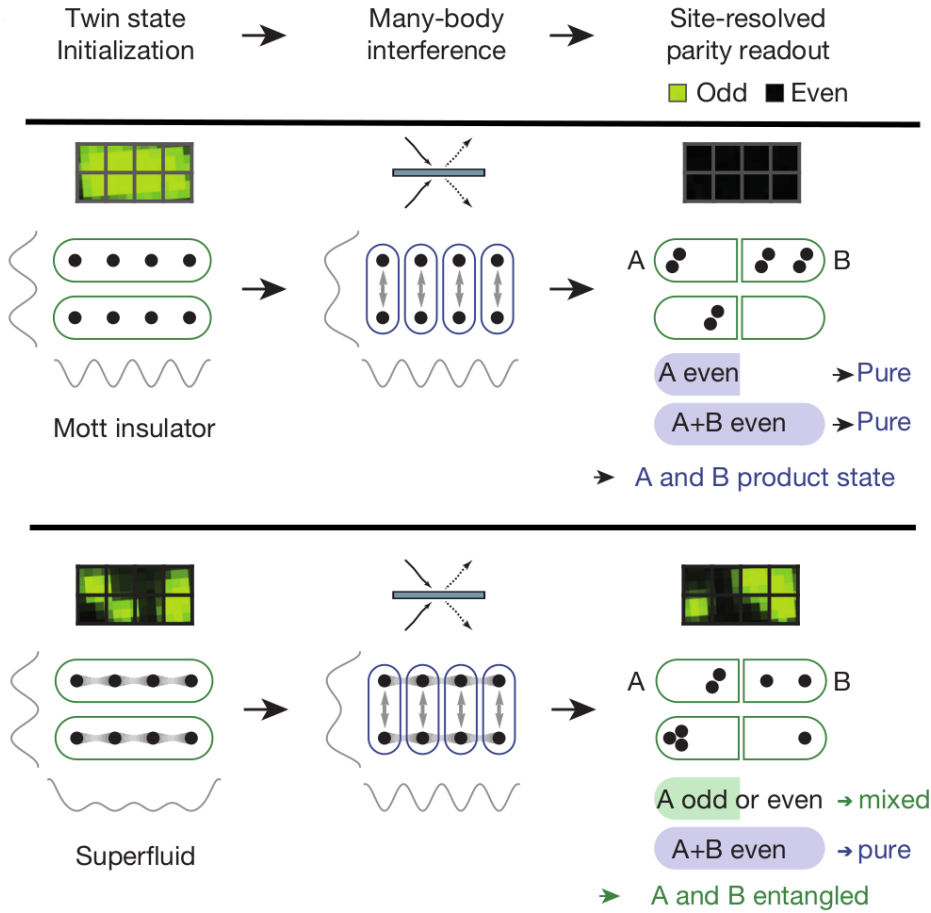


Figure 2.6.: Protocol for the measurement of the Rényi entanglement entropy with $\alpha = 2$ for a system of four atoms. The system is prepared in a product state (top panel) or an entangled state (bottom panel). An interference with a beam splitter produces an output state in which a readout of the parity of the sites in subsystem *A* translates to the presence or absence of entanglement. Figure taken from Ref. [28].

A genuine *many*-body entangled state can be obtained in an optical lattice from applying controlled laser pulses on a Mott insulating state of neutral ^{87}Rb atoms [30]. To measure entanglement, two copies (for $\alpha = 2$) of entangled states are prepared,

like in the replica trick, and the pairs of particle counterparts in each copy are coupled via a beam splitter [31], see also the bottom panel of Fig. 2.6. It was pointed out in Ref. [32] that the parity of the number of atoms on every lattice site in both copies gives access to the entanglement entropy: The average total parity $\langle P \rangle$ of a subsystem is one for pure states, which means that there is an even number of atoms in each copy of the subsystem. On the other hand a mixed state has $\langle P \rangle = 0$, i.e. there can be an even or odd number of atoms in the subsystem. Due to $\text{Tr}\rho^2 = \langle P \rangle$ we have a direct measure of the second Rényi entropy up to the logarithm. Putting these ideas together, the authors of Ref. [28] used two copies of four interacting ^{87}Rb atoms described by a Bose-Hubbard Hamiltonian

$$H = -J \sum_{\langle i,j \rangle} a_i^\dagger a_j + \frac{U}{2} \sum_i a_i^\dagger a_i (a_i^\dagger a_i - 1),$$

with tunneling rate J and onsite repulsion energy U . This system undergoes a phase transition from an entangled superfluid to a separable Mott insulating phase upon increasing U . For true bipartite states no entanglement should be detected in the large- U Mott insulating phase. The other limit of a superfluid phase exhibits entanglement. In the top left corner of Fig. 2.7 the bipartitions of the four-site system are depicted. The measurement result of the second Rényi entropy for this transition using these bipartitions convincingly reflects the expected entanglement.

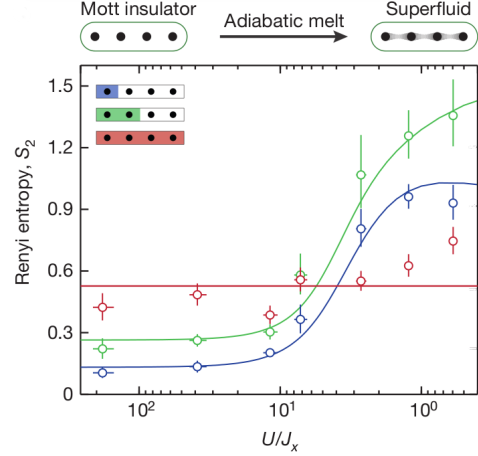


Figure 2.7.: Measurement results of the Rényi entropy for three different bipartitions (marked in blue, green and red). Across the transition from the Mott insulating phase to the superfluid phase the entanglement entropy clearly indicates the creation of entanglement. Note, that the x axis denotes *decreasing* U/J_x from left to right. The red data points are expected to show no entanglement as they correspond to the total system. Figure taken from Ref. [28].

2.2.3. Boundary law of many-body ground states

In the beginning of this Section we have started our analysis of entanglement via entropies by introducing a bipartition. This bipartition is owed to technical reasons and somewhat arbitrary in the first instance. It is therefore essential to understand the influence of the choice of the subsystem in order to extract actual universal properties of the quantum many-body system. The seminal work of Bombelli et al. [33] investigated this dependence in field theories of coupled harmonic oscillators and obtained as a by-product that the leading term of the entropy of the reduced density matrix is in general *linear* in the size of the boundary between the subsystems. This was, however, not a coincidence as the goal of this work was to explain the so-called *area law* of black hole entropy — also known as Bekenstein-Hawking entropy — by a quantum mechanical approach. From semi-classical arguments the black hole entropy has been found [34, 35] to depend on the surface area A of the black hole,

2. Entanglement measures

i.e. $S_{BH} = Ac^3/4G\hbar$ with the speed of light c and the gravity constant G . About two decades later the quantum information theoretic interest [36] in entanglement entropies arose. The term ‘area law’ is actually inappropriate for systems in other than three spatial dimensions and we therefore denote a behavior

$$S_\alpha(A) = \mathcal{A}L_A^{d-1} \quad (2.10)$$

with linear size L_A of the d -dimensional subsystem A by a *boundary law* in this thesis. Here, \mathcal{A} refers to the boundary coefficient. Subleading terms in Eq. (2.10) are called *corrections* to the boundary law and systems in which the leading order exceeds the L_A^{d-1} dependence are said to *violate* the boundary law.

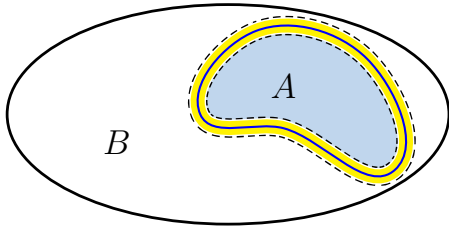


Figure 2.8.: Taking away the degrees of freedom near the boundary of the subsystem leaves a bulk of part A which has no significant entanglement with part B .

After the pioneering work in very specific systems the assumption that ground states of sensible quantum systems (i.e. having a local Hamiltonian) generically satisfy the boundary law of entanglement entropies became increasingly accepted, see for example the review articles Refs. [3, 5, 37]. Heuristically, it can be understood from arguing that entanglement is created via the local interactions of the Hamiltonian. For pairs of particles which have no direct interaction in the Hamiltonian this

implies that entanglement between them can only be established in a sequential way by forming a connecting chain of interacting neighbors. We have seen above that the mechanism of entanglement measurement works via turning entanglement into (classical) mixedness by tracing out one of the entangled partners. As a consequence of the locality, the particles of subsystem A which have an interaction with a particle in part B are mainly affected by the tracing out. Hence, the entanglement entropy should scale with the number of these cut interactions which is precisely the length of the boundary. Taking away the degrees of freedom in the proximity of the boundary we expect the bulk of subsystem A to behave like a pure state as it is part of such one. The bulk of part A does thus not contribute to the entanglement entropy, see Fig. 2.8.

We note in passing that the existence of a boundary law is crucial for the simulatability of the system via several numerical techniques. The density matrix renormalization group (DMRG) approach [38, 39] is based on representing the system by so-called matrix product states (MPS). These states satisfy the boundary law by construction and thereby implicitly assume it to be valid in the physical system in order to be a good representation thereof. In dimensions $d \geq 2$, projected entangled pair states (PEPS) [40, 41] or the multiscale entanglement renormalization ansatz (MERA) [42] provide such boundary-law inherent representations which are used in appropriate tensor network methods to simulate the system.

The term ‘entropy’ evokes the context of statistical physics and thermodynamics where we know that thermal entropy as a function of state is *extensive* in the volume of the considered system. At first sight one might be surprised that entanglement entropies do not obey such a volume law. However, the two kinds of entropy have

little in common such that a quantitative comparison is almost misplaced. First of all, entanglement entropies live in the realm of quantum ground states, i.e. where the statistical entropy is zero⁵ anyway (due to $\text{Tr}\rho^2 = 1$). Also in a classical statistical mechanics ensemble at zero temperature the entropy is zero⁶. From this perspective neither a volume law nor a boundary law is satisfied. But we consider the entropy of the reduced density matrix which exhibits a different structure than a statistical mechanics system. In the latter, the degrees of freedom take *random* values. They follow some known distribution but the number of possible configurations grows exponentially in the system size. Due to the logarithm in its definition it implies an extensivity of the entropy. A quantum system of random states, e.g. maximally entangled qubits, would likewise have a volume law [37]. However, the ground state of a reasonable quantum system defined by a local Hamiltonian is not random. Instead, it is an eigenstate of this Hamiltonian whose constituting basis states are only a small subset of the Hilbert space, specifically those which feature entanglement between locally interacting sites. A mixture on a subsystem is hence drawn from this small subset of the Hilbert space such that the corresponding entropy is subextensive.

We now present a brief survey of available rigorous results for the scope of validity of the boundary law. In one-dimensional systems a boundary law means that the entanglement entropy is constant for all subsystem sizes. Here, the situation is quite clear [5]: A boundary law always holds for local and gapped Hamiltonians. It has first been shown for bosonic systems [43] and XY spin chains [44] which can be mapped to a model of free fermions via a Jordan-Wigner transformation. Hastings [45] provided a general proof of the boundary law for non-critical one-dimensional systems. At criticality quantum many-body system are described by conformal field theories (CFT). Earlier works rooted in the context of black-hole physics found a divergence for the entanglement entropy of conformal field theories [46, 47] scaling with the logarithm of the system size with a coefficient related to the central charge C of the CFT, $S(A) = C/3 \log L_A$. We will come back to this prominent result in Sec. 4.1. This contrast between the boundary law in the non-critical regime and its violation for critical (gapless) system reveals a general one-to-one correspondence of the satisfaction of the boundary law and the (non-) criticality of the system [48].

In higher dimensions rigorous statements about the boundary law are few and far between. For quasifree bosonic models (harmonic lattices) a boundary law holds regardless of the dimension [49]. From a field theory perspective, the same result was found for massive free scalar fields [24] with logarithmic corrections if the theory is critical. The situation is considerably different for critical fermionic models. It has been shown that the boundary law is violated if the system exhibits a finite Fermi surface [50, 51]. In this case, the leading term scales as $L_A^{d-1} \log L_A$ which is still subextensive but exceeding a boundary size scaling.

There is one special two-dimensional class of critical systems which allow for a

⁵For a degenerate ground state we could assume a statistical mixture of the ground states which would result in a constant entropy originating from this mixture.

⁶Consider for example the Ising model at $T = 0$, i.e. a symmetry broken configuration with all spins pointing either up or down with probability 1.

2. Entanglement measures

proof of the boundary law, namely the quantum Lifshitz universality class. Without going into details of its field theoretical description we present this very elegant argument, following Ref. [52]. The particularity of systems belonging to this class (among them the quantum dimer model and the eight-vertex model) is that their dynamical critical exponent is $z = 2$ instead of the usual $z = 1$. As a consequence [53] the ground state wavefunction *itself* is conformally invariant at the critical point, instead of the usual criticality of the action of the field theory. Those critical points are also called *conformal quantum critical points* (CQCP). Their decisive property for the derivation of the boundary law is that the basis of the Hilbert space of the wavefunction is the configuration space of a two-dimensional *classical* model [53].

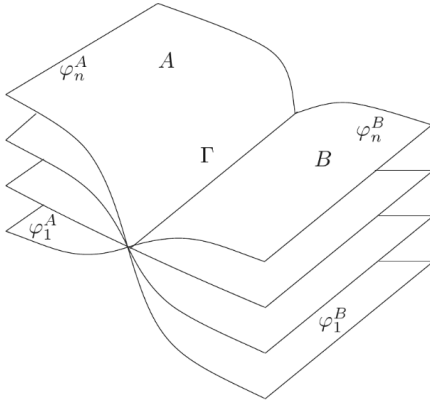


Figure 2.9.: Book-geometry of the manifold on which the modified partition function is defined. Picture taken from Ref [54].

Hence, we can map the system to a classical statistical-mechanics system whose partition function is conformally invariant in a $2 + 0$ dimensional equivalence. Using the replica trick, introduced above, to compute the entanglement entropy we have to determine [54] a modified classical partition function Z_α on $\alpha \in \mathbb{N}$ copies of the system where the degrees of freedom are identified on the common boundary Γ as shown in Fig. 2.9. This partition function is compared to α independent copies of the system such that Eq. (2.8) becomes

$$S_\alpha(A) = \frac{1}{1 - \alpha} \ln \frac{Z_\alpha}{Z^\alpha}.$$

Since Z and Z_α are *classical* partition functions, we can express the entanglement entropies via the free energy $F_\alpha = -\ln Z_\alpha$, i.e.

$$S_\alpha(A) = \frac{F_\alpha - \alpha F_1}{1 - \alpha}. \quad (2.11)$$

It is known [55] that the free energy of a conformally invariant classical system has a leading extensive term and subleading linear and constant corrections and possible a term in $\ln L$, yielding $F = L^2 f + aL + c \ln L + e + \mathcal{O}(L^{-1})$. Since the boundary Γ is of measure zero with respect to a two-dimensional plane it can be regarded as a defect such that its existence does not significantly affect the volume of the modified partition function Z_α . Hence, the volume of Z_α is simply α times the volume of a single copy, such that the extensive terms of the free energies cancel out in Eq. (2.11). The entanglement entropies thus scale at most linear in L which is a boundary law.

We comment on why this argument is not generally applicable, even though the replica trick likewise leads to a classical representation of the quantum system, see Fig. 2.5. For the replica trick, we use a quantum-to-classical mapping by discretizing the imaginary time representing the inverse temperature. Hence, by construction we are at a non-zero temperature which we try to keep as low as possible. In the limit of $T \rightarrow 0$ the classical systems become infinitely large such that Eq. (2.11)

represents a subtraction of infinities and therefore does not allow for a conclusion about $S_\alpha(A)$.

In the above discussion about the validity of a boundary law it was already being indicated that emergent subleading corrections can reveal a deep physical significance. Since they constitute the core elements of this thesis we provide a short overview thereof. Gapless systems can exhibit corrections which are logarithmic in the linear subsystem size L_A . They can appear in the non-critical regime with gapless excitations [56] as well as at critical points [7]. The latter case is the subject of part II of this thesis where we will see that they can be induced by designing subsystem A as to have sharp corners. In contrast to the boundary coefficient (\mathcal{A} in Eq. (2.10)) the coefficient of the logarithmic term is *universal* — rendering it a useful quantity for the characterization of criticality. Another class of systems features a universal constant correction to the boundary law. It appears in systems exhibiting *topological order* [57] — a type of order in a quantum phase which can in general not be characterized by an order parameter. The constant correction is used to construct a quantity called *topological entanglement entropy* from carefully chosen bipartitions of the quantum systems [58, 59]. It provides a witness of the presence of topological order and thereby replaces the unavailable order parameter. Part three of this thesis deals with this topic area using variants of the prototypical toric code model [10] as objects of study.

2.3. Mutual information

For pure ground states the entanglement entropies discussed in Sec. 2.2 exhaustively quantify bipartite entanglement. However, they forfeit a significant part of this capability if applied directly to bipartitions of a mixed state ρ as, for example, thermal states (at temperature $T > 0$) of quantum systems. The reason is an intertwining of the statistical mixedness of ρ with the mixedness due to tracing out subsystem B which cannot be resolved by $S_\alpha(A)$. In this case, it is instructive to consider the total (quantum and classical) correlations between the subsystems A and B , measured by the *mutual information* [60]

$$I_\alpha(A : B) = S_\alpha(A) + S_\alpha(B) - S_\alpha(AB), \quad (2.12)$$

based on the Rényi entanglement entropies. It is motivated by gathering the amount of information of both subsystems, measured by their entropies. Simply adding them would doubly count the information that is common to A and B which is therefore subtracted. The mutual information can hence be interpreted as quantifying the information about B we have if we know A . To illustrate this, we consider the two extreme cases: If A and B are independent, we acquire no information about B if we get to know information about A , which implies $I_\alpha(A : B) = 0$. On the other hand, if A and B are completely correlated, every outcome of A is mapped to an outcome of B and we have $S_\alpha(A) = S_\alpha(B) = S_\alpha(AB)$. The information about A provides the same information about B which is expressed through $I_\alpha(A : B) = S_\alpha(A)$. Since $S_\alpha(AB) = 0$ for pure states it is obvious that $I_\alpha(A : B) = 2S_\alpha(A)$, i.e. it carries the same information as the entanglement entropies in this case.

2.4. General entanglement measures

The mutual information is not a measure of entanglement for mixed states as it does not strip off the classical correlations. Unlike for pure states, where the entanglement entropies represent a unique measure derived from the LOCC paradigm, the situation is more axiomatic and ambiguous for mixed states. Following Ref. [4] we present a list of possible postulates for entanglement measures and subsequently introduce three examples — the relative entropy of entanglement, the entanglement of formation and the entanglement cost.

In Sec. 2.1 we have postulated that entanglement cannot increase under LOCC operations. To illustrate this, we make use the operator-sum representation of quantum operations via *Kraus operators* [60]. Quantum operations — among them LOCC operations — on a state ρ can be expressed with a set of matrices A_k , satisfying $\sum_k A_k^\dagger A_k = 1$, as

$$\rho' = \sum_k A_k \rho A_k^\dagger \equiv \sum_k p_k \rho_k, \quad (2.13)$$

i.e. as a superposition of the states ρ_k of outcome k with corresponding probability $p_k = \text{Tr}(A_k \rho A_k^\dagger)$. The effect of the quantum operation can hence be interpreted by replacing ρ by ρ_k with probability p_k . In the case that we have knowledge about the state after the operation, the new (normalized) density matrix is given by

$$\rho_k = \frac{A_k \rho A_k^\dagger}{\text{Tr}(A_k \rho A_k^\dagger)}. \quad (2.14)$$

The crucial point is now, that for the (von Neumann) entropy we can have $S(\rho_k) > S(\rho)$, see for example Ref. [61]. For a true entanglement measure this case is cured by considering averages over many repetitions of this operation. Possible postulates for an appropriate *bipartite* entanglement measure $E(\rho)$ for mixed states are:

1. $E(\rho)$ is a mapping from density matrices into \mathbb{R}^+ , where ρ is bipartite. Since the notion of maximally entangled states

$$|\Phi_d^+\rangle = \frac{|0,0\rangle + |1,1\rangle + \dots + |d-1,d-1\rangle}{\sqrt{d}} \quad (2.15)$$

is retained, it makes sense to normalize the measure as to have $E(|\Phi_d^+\rangle\langle\Phi_d^+|) = \log d$.

2. For a separable state ρ we have $E(\rho) = 0$.
3. Under LOCC operations, $E(\rho)$ does not increase *on average*. This statement can be written as

$$E(\rho) \geq \sum_k p_k E\left(\frac{A_k \rho A_k^\dagger}{\text{Tr} A_k \rho A_k^\dagger}\right). \quad (2.16)$$

4. In the special of a pure state $\rho = |\psi\rangle\langle\psi|$, the entanglement measure is identical to the entanglement entropy, $E(|\psi\rangle\langle\psi|) = S(\rho_A)$.

The first three conditions constitute the requirements for a so-called entanglement monotone, proposed in Ref. [61]. In (4.) We have intentionally left unspecified the concrete form (von Neumann or Rényi) of the entanglement entropy. This thesis is based on the assumption that Rényi entropies carry the same physical information as the von Neumann entropy [22] but in the context of quantum information, mostly the von Neumann entropy is considered as the unique entanglement entropy. Hence, we note that Eq. (2.16) leads to the von Neumann entropy in (4.) and would have to be adapted if Rényi entropies are desired.

Relative entropy of entanglement

As suggested above, a measure for entanglement in mixed quantum states based on entropies needs to eliminate their inherent part of classical correlations. The introduction of the mutual information (Sec. 2.3) poses a preliminary work for a possible realization of this endeavor. In particular, it can be expressed as a *Kullback-Leibler divergence* — a quantity assigning the notion of a distance to a pair of probability distributions $p(x)$ and $q(x)$ on a configuration space X , more precisely

$$\begin{aligned} D(p||q) &= \sum_{x \in X} p(x) \ln \frac{p(x)}{q(x)} \\ &= \sum_{x \in X} p(x) \ln p(x) - p(x) \ln q(x), \end{aligned} \quad (2.17)$$

also referred to as relative entropy. It can be adapted immediately to density matrices ρ and σ , yielding

$$D(\rho||\sigma) = \text{Tr}(\rho \ln \rho) - \text{Tr}(\rho \ln \sigma). \quad (2.18)$$

Further, for the (von Neumann) mutual information we have

$$\begin{aligned} I_1(A : B) &= \text{Tr}(\rho_{AB} \ln \rho_{AB}) - \text{Tr}(\rho_A \ln \rho_A) - \text{Tr}(\rho_B \ln \rho_B) \\ &= \text{Tr}(\rho_{AB} \ln \rho_{AB}) - \text{Tr}(\rho_{AB} \ln(\rho_A \otimes \rho_B)) \\ &= D(\rho_{AB}||\rho_A \otimes \rho_B). \end{aligned} \quad (2.19)$$

Hence, we see that the mutual information measures the distance between the state of the total system and the non-entangled but possibly classically correlated direct product of ρ_A and ρ_B , i.e. of the density matrices carrying the available information from ρ_{AB} about the subsystems. Apriori it is not clear whether $\rho_A \otimes \rho_B$ contains all classical correlations within ρ . But this insight inspires the definition of the *relative entropy of entanglement* [4] by searching the nearest separable state and taking the divergence as the as a measure of entanglement:

$$E_R^X(\rho) = \inf_{\sigma \in X} D(\rho||\sigma). \quad (2.20)$$

This definition includes a dependence on the space of states X which we generally choose to comprise all two-party product states in the Hilbert space of ρ .

Entanglement of formation

Another approach to quantify entanglement that is also based on the entanglement entropies is the *entanglement of formation* [4]. It considers all possible pure state decompositions of the form $\rho = \sum_k p_k |\psi_k\rangle\langle\psi_k|$ of a mixed state ρ . We can measure the bipartite entanglement for all $|\psi_k\rangle\langle\psi_k|$ of a particular decomposition by means of the von Neumann entanglement entropy and compute an average entropy by weighting every $S(\text{Tr}_B |\psi_k\rangle\langle\psi_k|)$ with p_k . The entanglement of formation is defined as the minimal average entropy of all pure state decompositions, i.e.

$$E_F(\rho) = \inf \left\{ \sum_k p_k S(\text{Tr}_B |\psi_k\rangle\langle\psi_k|) : \rho = \sum_k p_k |\psi_k\rangle\langle\psi_k| \right\}. \quad (2.21)$$

Entanglement cost

A more operational motivation for an entanglement measure leads to the definition of the *entanglement cost* [4]. We want to obtain the state of interest ρ by applying LOCC operations on maximally entangled two-qubit states $|\Phi\rangle = \frac{1}{\sqrt{2}}(|0,0\rangle + |1,1\rangle)$. To this end, we combine many of such two-qubit states, say K , into a state of dimension $D = 2^K$. The (pure) state corresponding to this combination is denoted as $|\Phi_D^+\rangle\langle\Phi_D^+|$. We could now try to find the smallest K such that an appropriate LOCC operation Ψ on $|\Phi_D^+\rangle\langle\Phi_D^+|$ approximately yields ρ . However, we put this quest into the so-called *asymptotic regime*, i.e. we try to obtain n copies of ρ simultaneously for some large integer n . This is a more general setting that avoids the hard problem of deciding whether one particular mixed state can be transformed in another state with certainty via LOCC. Moreover, it opens up the notion of a *rate* r at which many copies of the initial state can be transformed into many copies of the target state. The entanglement cost is precisely such a rate, namely the best possible rate for the transformation described above:

$$E_C(\rho) = \inf \left\{ r : \lim_{n \rightarrow \infty} \left[\inf_{\Psi} \text{Tr} |(\rho^{\otimes n} - \Psi(|\Phi_{2^{rn}}^+\rangle\langle\Phi_{2^{rn}}^+|))| \right] = 0 \right\}. \quad (2.22)$$

The inner infimum aims at minimizing the deviation between the n copies of the target state and the transformed state by looking for the best LOCC operation Ψ . In other words, r blocks of n two-qubit maximally entangled states are needed to approximately obtain n copies of ρ via LOCC operations in the asymptotic limit. This quantity is very hard to compute in general. It is assumed [4], but not proven to be equal to the entanglement of formation, Eq. (2.21).

Part I.

Quantum phase transitions

3. Singular behavior at critical points

In quantum many-body systems with local interactions we generically expect the entanglement entropy to exhibit a boundary law, i.e. its leading term scales linear with the boundary length L_A of subsystem A of the bipartition. As pointed out in Sec. 2.2.3, the underlying mechanism can be understood from the notion that entanglement is established between neighboring particles via their interaction in the Hamiltonian. Inverting this picture we can conclude that the existence of a boundary law in a particular model indicates that the quantum correlations between two subsystems are primarily contained in the correlations between the cut pairs of constituents along the boundary [5]. We therefore have reason to assume that the boundary coefficient a of the entanglement entropy is related to the correlation length ξ of the system. Such a relation evokes a special interest in the entanglement entropy at quantum phase transitions which typically exhibit a *diverging* correlation length.

A heuristic argument which goes back to Matt Hastings [62] predicts the existence of a boundary law even if the correlation length is infinite. This argument, which is explained in the following for a d -dimensional system, is based on the assumption that the contributions of the correlations to the entanglement entropy S are identical at every length scale and of order $\mathcal{O}(1)$, denoted by \mathcal{A} . We now add up these contributions from all length scales by repeatedly rescaling the considered correlation length $\xi^{(i)}$ by a factor λ , i.e. $\xi^{(i+1)} = \lambda \xi^{(i)}$. For $\xi^{(1)} = 1$ we obtain $S^{(1)} = \mathcal{A}L_A$ because there are L_A positions of pairs along the boundary, all contributing one unit \mathcal{A} . After the first iteration, we have $\xi^{(2)} = \lambda$ and there are only L_A/λ^{d-1} positions of groups of λ^d particles whose common correlations with another such group across the boundary contribute at this length scale. This step is repeated until λ reaches the linear size of the total system. Counting all the contributions we obtain

$$S = \sum S^{(i)} = \mathcal{A} \left(L_A + L_A \frac{1}{\lambda^{d-1}} + L_A \frac{1}{\lambda^{2(d-1)}} + \dots \right) = \mathcal{A}L_A \lambda^{d-1} \sim L_A, \quad (3.1)$$

using the geometric series and $\lambda > 1$.

For clarity, this argument is pictured for a particular example in Fig. 3.1. Note, that the rescaling procedure must start at an initial correlation length $\xi = 1$. Hence, we can also learn from this argument that the boundary coefficient a depends on the short-distance cutoff (lattice spacing) which implies that it is *non-universal* — as opposed to its subleading corrections. Therefore, it is often not considered in the context of critical behavior because it cannot be used to *classify* the transition. However, a recent study [6] points out that — under certain conditions — it can

3. Singular behavior at critical points

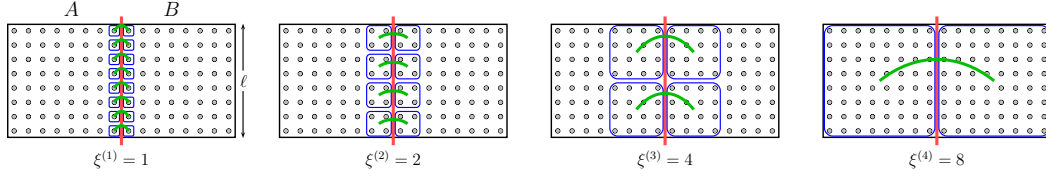


Figure 3.1.: Sketch of the heuristic argument [62] for the existence of a boundary law in the entanglement entropy for infinite correlation length. We set $\lambda = 2$ and rescale the considered correlation length from left to right. The boundary length is $L_A = 8$ such that the contributions from left to right add up to $S = \mathcal{A}(8 + 4 + 2 + 1)$. In the thermodynamic limit $L_A \rightarrow \infty$ the entanglement entropy yields $S = \mathcal{A}L_A(1 + 1/2 + 1/4 + 1/8 + 1/16 + \dots) = 2\mathcal{A}L_A \sim L_A$.

provide a footprint of a quantum phase transition by showing a *cusp* at the critical point.

In this Chapter we expand this investigation by contributing further numerical evidence on antiferromagnetic quantum critical points. We will first introduce in Sec. 3.1 three spin-half bilayer models that have such quantum phase transitions.

Subsequently, in Sec. 3.2, we discuss the low energy physics on both sides of the critical point that enable the existence of a cusp. Finally, we show results for the boundary coefficient of these models obtained from Monte Carlo simulations in a stochastic series expansion of the Hamiltonians in Sec. 3.3.

3.1. Quantum critical bilayers

We consider antiferromagnetic quantum spin bilayer models in $d = 2$ spatial dimensions that undergo a phase transition induced by the spontaneous breaking of a continuous $O(N)$ symmetry. These models have in common that their phase transition is driven by a coupling parameter g such that the system becomes critical at $g = g_c$. For our cases the system is divided into an ordered low- g phase with an infinite correlation length and a magnetically disordered large- g phase where the correlation length decreases to zero upon moving away from the critical point.

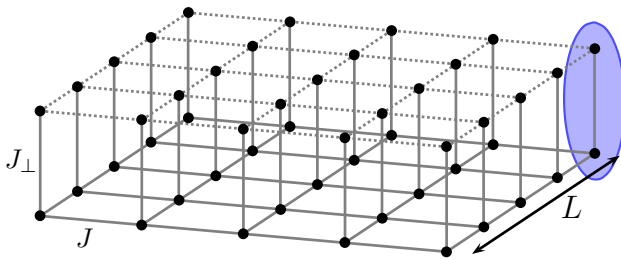


Figure 3.2.: Geometry of the bilayer and necklace spin models and location of the couplings J and J_\perp . Dashed interactions are absent in the necklace model. An example for a typical dimer in the large- g phase is depicted in blue.

Square lattice bilayers of spin-half degrees of freedom are simple models related to bilayer cuprates [63] that can be tuned through a quantum phase transition in the $O(2)$ or $O(3)$ universality class in $d = 2$. They are accessible to quantum Monte Carlo simulations, e.g. via a stochastic series expansion [64] and are therefore excellent candidates for the investigation of the phase transition from an entanglement entropy

perspective. We consider three bilayer models which feature slightly different se-

3.2. Off-critical behavior of the boundary coefficient

tups in the coupling strengths of the intralayer couplings J and interlayer coupling J_\perp . The coupling ratio $g = J_\perp/J$ is our tuning parameter and separates the antiferromagnetically ordered phase ($g \ll g_c$) from the disordered phase in which singlet dimers with one spin in each layer are formed ($g \gg g_c$). We consider periodic boundary conditions in both lattice directions and finite lattice sizes of linear extent L for our simulations. Fig. 3.2 depicts the common geometry of the bilayer models.

The first model is the antiferromagnetic spin-half bilayer Heisenberg model

$$H_1 = J \sum_{\langle i,j \rangle} \sum_{l=1}^2 \mathbf{S}_{i,l} \mathbf{S}_{j,l} + J_\perp \sum_i \mathbf{S}_{i,1} \mathbf{S}_{i,2} , \quad (3.2)$$

where i labels a unit cell consisting of two spins (one in each layer) in the (two dimensional) lattice. The index l denotes the layer (1 or 2). This model is well understood and its phase transition in the $O(3)$ universality class is known to occur at $g_c = 2.5220(1)$, see Ref. [65].

Using the same notation, the Hamiltonian for the second model — the bilayer XY model — reads

$$H_2 = J \sum_{\langle i,j \rangle} \sum_{l=1}^2 (S_{i,l}^x S_{j,l}^x + S_{i,l}^y S_{j,l}^y) + J_\perp \sum_i (S_{i,1}^x S_{i,1}^x + S_{i,2}^y S_{i,2}^y). \quad (3.3)$$

Its phase transition between a transverse antiferromagnetically ordered and a dimerized singlet phase belongs to the $O(2)$ universality class and has been estimated to occur at a value of $g_c = 5.460(1)$ in Ref. [66].

Very similar is the third model, a necklacelike bilayer model with XY interactions. In this model the intralayer couplings have been removed from (3.3) in one of the layers, yielding

$$H_3 = J \sum_{\langle i,j \rangle} (S_{i,1}^x S_{j,1}^x + S_{i,1}^y S_{j,1}^y) + J_\perp \sum_i (S_{i,1}^x S_{i,1}^x + S_{i,2}^y S_{i,2}^y). \quad (3.4)$$

This model can also be regarded as a square lattice spin system with a local impurity attached to each lattice site. We will therefore refer to it as the Kondo necklace model. The critical point (again in the $O(2)$ universality class) of this model is also estimated in Ref. [66] to be at $g_c = 2.7755(5)$.

Due to the spontaneous breaking of a continuous symmetry in the ordered phase all these models exhibit Goldstone modes for $g < g_c$. They give rise to a logarithmic correction to the boundary law of the entanglement entropy [56] which will be addressed briefly in Chapter 4.

3.2. Off-critical behavior of the boundary coefficient

In this Section we review the nature of the transition and its consequences for the boundary coefficient. The large- g limit has been worked out in the work of

3. Singular behavior at critical points

Ref. [26]. In $d = 2$ dimensions near the critical point we generally assume a scaling form [7, 67]

$$S = a \frac{L_A}{\delta} + c \ln \frac{L_A}{\delta} + D + S_0 \left(\frac{L}{\xi} \right) \quad (3.5)$$

where δ is the short distance cutoff and L is the characteristic length scale of the total system. The constant contribution D depends on the aspect ratio of the subsystems [68] and S_0 contains the corrections due to the correlation length ξ . Since we consider two-dimensional models we can choose a bipartition where the logarithmic and the constant contribution vanish ($c = 0, D = 0$), e.g. an infinite cylinder cut into two semi-infinite regions separated by a flat boundary [26]. Hence, we can then focus on the simplified scaling forms of the entanglement entropy

$$S = a \frac{L_A}{\delta} + \gamma, \quad \gamma = S_0 \left(\frac{L}{\xi} \right) \quad (3.6)$$

for the *critical* system with $L/\xi \rightarrow 0$, where S_0 becomes the so-called geometric correction γ , as well as

$$S = a(g) \frac{L_A}{\delta} + r \frac{L}{\xi} \quad (3.7)$$

away from the critical point at $g = g_c$. The second scaling assumes a non-universal, analytic function $a(g)$ for the boundary coefficient perturbed away from the critical point. In addition, the non-analytic scaling with $g - g_c$ is accounted for in the second term of the right hand side of (3.7) with a universal coefficient r . More specifically rL/ξ scales as $(g - g_c)^\nu$, where ν is the correlation length exponent [26]. For $O(N)$ models we have $\nu < 1$ for $d = 2$, which implies that the non-analytic contribution dominates. The coefficient r has been computed analytically¹ in Ref. [26] for the $O(N)$ model to be $r = -N/(144\pi)$ for the von Neumann entropy. Since $\gamma = 0$ to leading order [26] we have an unambiguous and precise prediction of an exponential decay of the boundary coefficient on the disordered large- g side. This argument is not applicable to the unordered phase $g < g_c$ because $\xi = \infty$ in this case. In order to have a cusp singularity in $a(g)$ at g_c we need a reduction of $a(g)$ as g decreases away from the critical point. The key to this is the softening of additional modes close to the phase transition, namely so-called amplitude modes [69]. In the following we will elucidate the low energy excitations of our class of antiferromagnetic models in the symmetry broken phase and establish the connection to the entanglement entropy.

It is well understood from Goldstone's theorem [70] that the spontaneous breaking of a continuous symmetry leads to gapless excitations — also called Goldstone modes. In the case of a spin model these modulations are spin waves with an infinite wavelength. Let us further associate a field $\psi(r, t) = |\psi(r, t)|e^{i\phi(r, t)}$ with the corresponding order parameter that describes the phase transition in the Landau theory. The Goldstone modes then correspond exactly to the fluctuations of the *phase* ϕ of the field $\psi(r, t)$. But more important in this context is the fact, that also the *amplitude* $|\psi(r, t)|$ may exhibit fluctuations that evoke amplitude modes provided

¹To be precise, r depends on the choice of ξ . For this computation the authors in Ref. [26] have selected $\xi = m^{-1}$, where m is the gap to the first excitation.

the system exhibits particle-hole symmetry [69]. Unlike the Goldstone modes they are gapped in general. Amplitude modes were derived theoretically in condensed-matter [71] and particle physics [72, 73] — in the latter context also denoted as Higgs modes. They could be observed experimentally using ultracold atoms [74, 75] but also in superconductors [76]. Ref. [69] provides a comprehensive review of their appearance in quantum many-body systems.

For spin models amplitude modes are fluctuations in the magnitude of the magnetization. An experiment using TiCuCl_3 , modeled in a most simple way by a Heisenberg-like $O(3)$ Hamiltonian ($d = 3$), identified the emergence of gapped amplitude modes in the antiferromagnetically ordered phase [77]. Moreover, it showed that upon approaching the critical point the gap of the amplitude mode closes. A recent numerical study [6] examines whether this closing of the gap is reflected by the boundary coefficient a of the entanglement entropy in the Bose-Hubbard model undergoing an $O(2)$ transition. The increase of a is identified with this closing on the ordered side of the transition. The authors argue that an increase in the number of massless excitations leads to a richer entanglement spectrum in the groundstate.

In the remainder of this Chapter we will add further numerical evidence to the existence of such a cusp in the boundary coefficient a at the critical point of $O(2)$ and $O(3)$ spin models in $d = 2$ dimensions.

3.3. Quantum Monte Carlo results

The three models introduced in the previous section allow for a sign-problem free quantum Monte Carlo (QMC) simulation. Via the replica trick (see Sec. 2.2.2.1) the Rényi entanglement entropy of a chosen bipartition can be obtained either by a thermodynamic integration [27] or by an ensemble switching sampling [78]. We employ the latter technique embedded in a stochastic series expansion (SSE) [64] of the Hamiltonian, an efficient finite temperature QMC approach which is explained in Appendix A. In order to simulate the groundstate physics of the quantum system we choose a sufficiently large inverse temperature, fixed to the linear system size $\beta = L$ in our simulations.

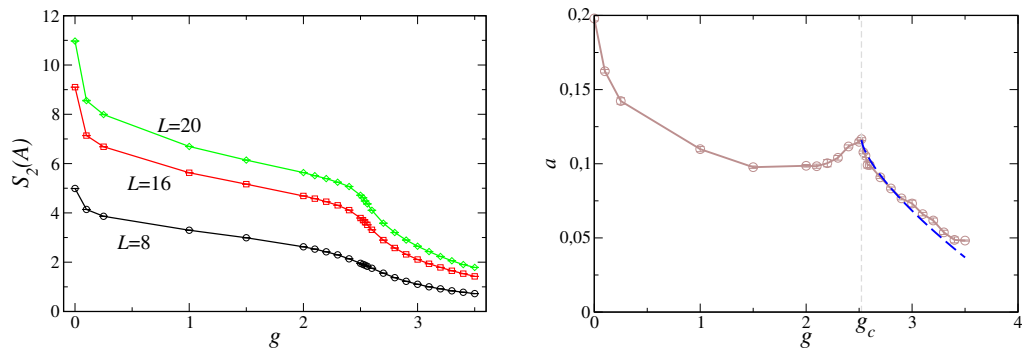


Figure 3.3.: Results for the entanglement entropy S_2 (left panel) and its leading boundary coefficient a for the bilayer Heisenberg model as a function of the coupling ratio g .

For the bilayer Heisenberg model we show our results for the second Rényi entropy ($\alpha = 2$) in Fig. 3.3. In the left panel the full entropy S_2 is plotted for some

3. Singular behavior at critical points

linear system sizes L over a range of coupling ratios g varying from 0 to 3.5, hence covering the critical value $g_c = 2.5220$. From the full S_2 we can beautifully apprehend how the entanglement entropy reflects the macroscopic state of the many-body system. The value of S_2 is maximal at $g = 0$ and undergoes a sharp decrease when g is increased to ~ 0.25 . At $g = 0$ the system decouples into two independent layers and hence has twice the symmetry ($O(3) \times O(3)$) than at finite g . The drop of the entanglement entropy marks the reduction of the symmetry. Upon further increasing g the value of S_2 decreases monotonously and develops a shoulder at g_c — thereby providing a weak signature of the phase transition. In the large- g phase the entanglement entropy vanishes which can be very well understood by the fact that the state of the system is dominated by singlet dimers between neighboring spins of different layers. In other words, no boundary segment of the bipartition cuts through a dimer and S_2 cannot capture the dimer correlations.

The right panel of Fig. 3.3 shows the leading boundary coefficient a of $S_2(A)$. It has been extracted by a least-squares fit to the boundary law (3.1) for the available system sizes $L = 8, \dots, 20$. We observe that a clearly exhibits a cusp near the critical point, suggesting that gapless amplitude modes emerge for $g \lesssim g_c$ in the bilayer Heisenberg model. Moreover, on the disordered site, we test our numerical data against the scaling ansatz in Ref. [26] for $d = 2$, i.e. $a - a(g_c) \propto |g - g_c|^\nu$ for $g \gtrsim g_c$. The correlation length exponent for this model has a value of $\nu = 0.710(2)$, computed in Ref. [79]. Our fit of this ansatz to a in the vicinity of the critical point shows that our data are consistent with this scaling behavior.

It would be desirable to obtain the exponent ν from an unbiased fit to our data. But since these QMC simulation become computationally very expensive upon increasing $L = \beta$, we are restricted in the system size and too few data points are available for the fit. On the other hand, it is indeed remarkable that we can identify the cusp and confirm the scaling within statistical uncertainty using relatively small system sizes only.

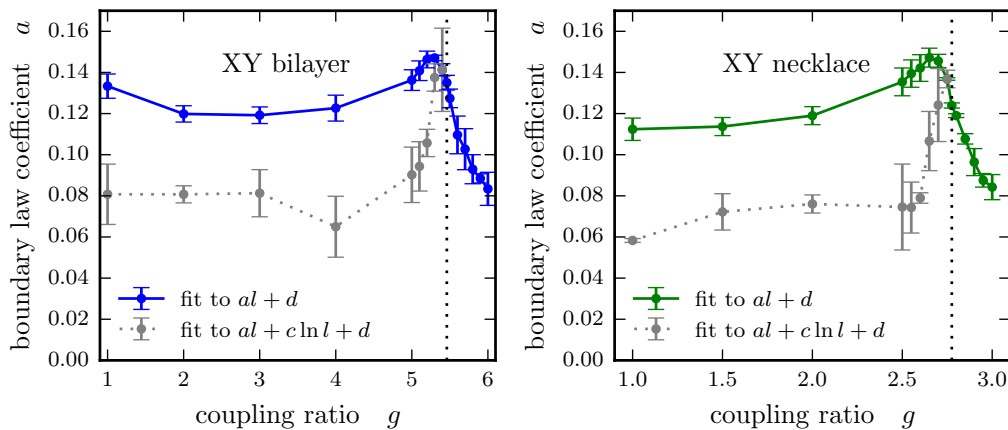


Figure 3.4.: Boundary coefficient a for the bilayer (left panel) and necklace (right panel) XY model. Data have been obtained by linear regression fits to the entanglement entropy of system with linear sizes $L = 8, \dots, 16$.

The entanglement entropy of two the XY models (3.3) and (3.4) with a quan-

tum phase transition in the $O(2)$ universality class has been computed at the critical points using QMC simulations in Ref. [66] with a focus on the logarithmic contribution to the boundary law. Here, we complement this study by an investigation of the boundary coefficient a in the environment of g_c . Unlike in the bilayer Heisenberg model, we have to use a non-deterministic Monte Carlo update which further decreases the computational efficiency of the sampling. We therefore only achieve linear system sizes of $L = 8, \dots, 16$ for these models. For every coupling ratio g we perform a fit of the entanglement entropy $S_2(L_A)$ against the boundary length L_A supposing a linear dependence $S_2(L_A) = aL_A + D$. The results are plotted in Fig. 3.4 and show a cusp at the critical points for the bilayer XY (left panel) as well as for the necklace XY model (right panel). Our data allow for the qualitative conclusion that the conjectures of Ref. [6] are supported by our QMC results concerning the ordered side $g < g_c$ since the boundary coefficient increases as $g \rightarrow g_c$. Also a decay on the disordered side is observed, in accordance with Ref. [26]. However, the maximum of a is slightly below g_c for both models (solid curves). The reason for this offset is that our linear fit neglects the expected logarithmic contribution from Goldstone modes in the ordered phase. We further perform a fit *including* such a term, aware of the fact that it has to be interpreted very carefully as only five datapoints are available. The results are shown as grey dotted lines in Fig. 3.4 and provide evidence for our hypothesis: The maximum clearly moves towards the critical coupling ratio where — at the same time — the logarithmic contribution should vanish such that the gray and the blue/green curves would collapse for $g \geq g_c$.

In summary, we can conclude that the boundary coefficient of the boundary law of entanglement entropy provides a signature of quantum phase transitions with gapless amplitude modes by showing a cusp singularity. Conversely, the role of amplitude modes in phase transitions of many-body system can be further investigated using entanglement entropies. From the numerical point of view the boundary coefficient a is a much better accessible quantity than its subleading corrections. Albeit being non-universal it may still help to identify the breaking of a continuous symmetry and capture its accompanying features.

Part II.

Critical theories

4. Corner entanglement

In order to have a many-body system undergo an entanglement entropy analysis the bipartitioning is inevitable. From the physical point of view the size and shape of the subsystems are somewhat arbitrarily chosen parameters that introduce additional ambiguity in the analysis. The role of the boundary law discussed in the previous chapter is a good example how we can understand and eliminate this ambiguity by focussing on the boundary *coefficient* — carrying the physical information. In critical systems, corners in the subsystem shape can similarly be used as a tool that induces a universal subleading contribution to the entanglement entropy which is logarithmic in the linear system size L . In the discussion of the critical phenomena we frequently use the language of three different perspectives simultaneously and therefore briefly contrast them: From a condensed-matter perspective (i) we hence investigate critical points of scale invariant quantum phase transitions which is equivalent to studying fixed points (e.g. of Wilson-Fisher or Gaussian type) in a renormalization group (RG) point of view (ii). The field theoretic perspective (iii) associates a conformal field theory (CFT) with the critical point and thereby involves the central charge C as a characterizing quantity of the critical system. CFTs corresponding to critical two-dimensional lattice systems are referred to as $2 + 1$ dimensional theories, meaning two spatial and one imaginary time dimension.

This Chapter is organized as follows. We first establish the link between corners and universal logarithmic contributions in Sec. 4.1. Next, in Sec. 4.2, we discuss some general properties of the corner coefficient. We also introduce a field theoretic ansatz for its computation in Sec. 4.3. It will be pointed out that the corner coefficient is related to the central charge of the CFT corresponding to the critical system. In Sec. 4.4 we will motivate the importance of the central charge in quantifying degrees of freedom.

4.1. Logarithmic contribution

The existence of corner induced logarithmic corrections to the entanglement entropy has been derived in Ref. [7]. For a general bipartition with a subsystem A of linear dimension ℓ_A exhibiting a single corner with an opening angle θ , the entanglement entropy hence reads

$$S_\alpha = a_\alpha \frac{\ell_A}{\delta} + c_\alpha(\theta) \ln \left(\frac{\ell_A}{\delta} \right) + \mathcal{O}(1), \quad (4.1)$$

where δ denotes the short-distance cutoff. We will refer to the coefficient $c_\alpha(\theta)$ of this contribution as *corner entanglement*. In a one-dimensional system we would naively not have a notion of a corner and therefore usually consider $d \geq 2$ dimensions for this study. Nevertheless we will now do a brief excursus to critical

4. Corner entanglement

one-dimensional systems which were among the first systems studied from an entanglement entropy perspective [47] and yield for a subsystem of length ℓ_A a relation

$$S = \frac{C}{3} \ln \frac{\ell_A}{\delta} + \mathcal{O}(1). \quad (4.2)$$

The coefficient C is the central charge of the underlying CFT, a universal quantity of the theory that characterizes the low-energy excitations in the gapless spectrum. This famous result is sometimes interpreted as a violation in a boundary law because in one dimension a constant would have to be the leading contribution instead of a logarithmic term. The reason that we mention it here is because we want to reinterpret the logarithm in Eq. (4.2) as the corner entanglement of the 1d chain — considering the point-like boundary of a one-dimensional bipartition as an odd type of a corner. In other words, it is precisely the same mechanism that induces the logarithmic correction in this one dimensional system as corners in the subsystem do in higher dimensions. Below we will see a heuristic derivation of this mechanism. Moreover, the coefficient c_α of the logarithm is likewise universal in critical systems with $d \geq 2$ and similarly characterizes the low-lying degrees of freedom of the CFT.

Before we turn to the subject of this part of the thesis — gapless critical systems in $d = 2$ — we note that there is another situation that gives rise to a subleading logarithmic contribution even in corner-free bipartitions, namely, the existence of Goldstone modes. In the (continuous-) symmetry broken phase the number N_G of Goldstone modes, briefly explained in Sec. 3.2, is related to the coefficient of the logarithmic correction by $c = N_G(d - 1)/2$ for a d -dimensional system [56]. This analytical result was qualitatively supported numerically on a spin-half square lattice Heisenberg model [80] and later confirmed quantitatively in Refs. [81, 82].

We now focus back on the logarithmic contribution at criticality only appearing for bipartitions with corners. Its existence can be understood from another heuristic argument in two-dimensional systems [62]. It is very similar to the argument for the boundary law in Chapter 3. Due to the infinite correlation length we assume that the contribution of the corner to the entanglement entropy is equal on all length scales and of $\mathcal{O}(1)$ so that we denote it by \mathcal{C} . We further add up the corner contributions of all length scales by iteratively rescaling the considered length scale by a factor $\lambda > 1$. As can be seen from Fig. 4.1, the number of corners does not change after rescaling. Necessarily starting with $\xi^{(1)} = 1$ we have $n = \log_\lambda(L)$ rescalings to do for a linear system size L until $\xi^{(n)} \approx L$. Hence, we obtain

$$S_{\text{corner}} = \mathcal{C} \cdot \underbrace{(1 + 1 + 1 + 1 + \dots)}_{\log_\lambda(L)} \sim \mathcal{C} \ln L. \quad (4.3)$$

Fig. 4.1 visualizes this argument for $\lambda = 2$ starting from a 8×8 subsystem with one corner. We can conclude that a corner in a bipartition of a gapless system implies a logarithmic term. It should be emphasized that \mathcal{C} is not identical to c_α in Eq. (4.1) as \mathcal{C} contains information of short-ranged physics in the system (see left example of Fig. 4.1).

One might wonder whether this argument suggests that there should be a dependence of the corner coefficient c_α on the short-distance cutoff δ , similarly as argued

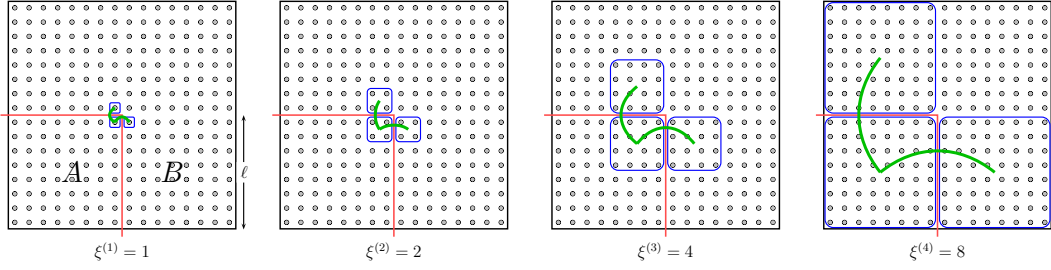


Figure 4.1.: Sketch of the heuristic argument for the existence of a subleading logarithmic contribution to the boundary law in the entanglement entropy induced by a corner of the subsystem provided the correlation length is infinite.

for the boundary coefficient, since we start our rescaling at $\xi^{(1)} = 1$, which is the lattice spacing. Such a dependence would be contradictory to the claim that c_α is universal. The key is the logarithm: In general, we assume $c \ln(L/\delta)$ as our corner induced contribution. But by rewriting it as $c \ln L - c \ln \delta$ we see that the second term is simply a constant and thereby the pure $\ln L$ term is independent of δ .

In Fig. 4.1 we observe that the nature of correlations (green curves in the Figure) entering the counting argument is the same as in Fig. 3.1 for the boundary term. The only difference is that a corner (with $\theta = \pi/2$) has *two* such correlations in two dimensions. Indeed, the effect of corners can be seen as a correction of the overcounting that the boundary term does for the correlations in which corner sites are involved. In other words, the boundary term considers the two correlation pairs between the corner site and its two adjacent sites in the other subsystem as independent. However, since one site is involved in both pairs there must be some common information in these two correlations which reduces the sum of the individual correlations. This argument can be interpreted as a variant of the entanglement monogamy principle [83]. It is exactly this overcounting that induces the corner contribution and also explains why it is negative in $d = 2$. (In fact in $d = 3$ the entanglement entropy has a subleading edge contribution which is negative but then a positive corner contribution because the edges have oversubtracted the corner correlations.)

4.2. General properties

The coefficient of the corner-induced logarithmic contribution to the Rényi entanglement entropy very naturally exhibits a dependence on the opening angle θ of the corner and will hence be denoted by $c_\alpha(\theta)$. In the smooth angle limit $\theta \rightarrow \pi$ the corner disappears and hence $c_\alpha(\theta) \rightarrow 0$. The fact that the entanglement entropy fulfills $S(A) = S(\bar{A})$ for a subsystem A and its complement \bar{A} immediately translates to a reflection symmetry $c_\alpha(2\pi - \theta) = c_\alpha(\theta)$ about π for the corner term. Combining these two observations together with the expectation that $c_\alpha(\theta)$ be analytical near π we conclude that it behaves as [84]

$$c_\alpha(\theta \rightarrow \pi) = \sigma_\alpha \cdot (\pi - \theta)^2 \quad (4.4)$$

4. Corner entanglement

with a constant σ_α independent of the ultraviolet cutoff (system size) and the opening angle. Higher even orders in $(\pi - \theta)$ are expected to dominate as θ is decreased. In the limit of sharp angles the corner entanglement obeys [84]

$$c_\alpha(\theta \rightarrow 0) = \frac{\kappa_\alpha}{\theta} \quad (4.5)$$

with another independent constant κ_α .

Many results in free [84] and interacting [85, 86] theories as well as holographic models [87] suggested that the corner entanglement, specifically the independent coefficient σ_α is a measure of degrees of freedom in the field theory. This notion was made viable by the establishment [88, 89] of a relation between σ_1 of the von Neumann entanglement entropy and the central charge C_T

$$\frac{\sigma_1}{C_T} = \frac{\pi^2}{24} \quad (4.6)$$

valid in any 2+1 dimensional conformal field theory. As we will elucidate in Sec. 4.4, the central charge C_T does provide a measure of degrees of freedom and the universal ratio, Eq. 4.6 translates this property to the corner coefficient. For Rényi entropies with a different index $\alpha \neq 1$ this relation does not hold. On the contrary, σ_α has been computed for different integer α for two theories — the complex boson (cb) and the free Dirac fermion (f) in Ref. [90]. Since $\sigma_\alpha^{(cb)} \neq \sigma_\alpha^{(f)}$ but both theories have $C_T = 3/(16\pi^2)$ their ratio cannot be universal.

However, for the case of these two free theories another surprising relation was found in the same reference: For reciprocal Rényi indices α and $1/\alpha$, a duality

$$\alpha^2 \sigma_\alpha^{(cb)} = \sigma_{1/\alpha}^{(f)} \quad (4.7)$$

between the complex boson and the free Dirac fermion CFT holds in 2+1 dimensions.

The angular dependence (4.4) and this duality (4.7) will be the subject of numerical studies on lattice field theories of the free boson and the free fermion, presented in Sec. 6.3.

4.3. Field theory

We briefly review how the corner entanglement can be calculated using field theory. Based on the reflection symmetry of the corner entanglement about π , specifically $c_\alpha(2\pi - \theta) = c_\alpha(\theta)$, an expansion around π in even powers of the form

$$c_\alpha(\theta) = \sum_{p=1} \sigma_\alpha^{p-1} \cdot (\theta - \pi)^{2p} \quad (4.8)$$

can be made, where the $\sigma_\alpha^{(p)}$ are the smooth limit expansion coefficients. We further use the notation $\sigma_\alpha^{(0)} \equiv \sigma_\alpha$. These coefficients are evaluated partly analytically and otherwise numerically through an integral expression of $c_\alpha(\theta)$ using the replica trick for a sphere with a cut of opening angle θ , see Refs. [7, 84, 91]. Since the

4.4. Low-lying degrees of freedom

approximation of the corner entanglement using this expansion results involuntarily from a cutoff in this series, we refer to it as the truncated series. The smooth limit coefficients are available from the literature up to order $p = 6$ ($p = 7$) for the Dirac fermion (free boson) respectively [92]. A shortcoming of the truncated series approximation is that it fails as $\theta \rightarrow 0$ due to the asymptotic behavior in Eq. 4.5.

Another idea is to make an ansatz for $c_\alpha(\theta)$ that superimposes the behavior at $\theta \rightarrow 0$ and at $\theta \rightarrow \pi$. In Ref. [90] such an ansatz was made involving κ_α and the first smooth limit expansion σ_α , dubbed ‘BMW ansatz’ after the initials of the others. Since it neglects higher smooth limit expansions it is not as accurate as the truncated series for intermediate angles with $\theta \approx \pi/4$. However, a *combined ansatz* refines the idea of such an ansatz by including the truncated series

$$c_\alpha(\theta) = \sum_{p=1}^M \sigma_\alpha^{p-1} \cdot (\theta - \pi)^{2p} + \frac{2\kappa_\alpha}{\pi^{2M+1}} \frac{(\theta - \pi)^{2(M+1)}}{\theta(2\pi - \theta)}. \quad (4.9)$$

It is motivated by performing the infinite sum of the unavailable smooth limit coefficients $\sum_{p=M+1}^{\infty} \sigma_\alpha^{(p-1)} (\theta - \pi)^{2p}$ by a replacement $\sigma^{(p-1)} \rightarrow 2\kappa_\alpha / \pi^{2p+1}$. For further details we refer to Ref. [92].

4.4. Low-lying degrees of freedom

The physics of most critical points features scale invariance and can hence be described by a conformal field theory (CFT) provided the system exhibits Lorentz invariance¹. Extending the characterization by universal critical exponents in a statistical mechanics approach, the CFT perspective opens up another set of properties that are able to classify a critical phenomenon. A fundamental quantity of a certain CFT is the stress tensor central charge, denoted by C_T . In order to define C_T we first need the energy-momentum tensor $T_{\mu\nu}$ of the CFT which is defined by the variation of the action that an infinitesimal coordinate transformation $x^\mu \rightarrow x^\mu + \epsilon^\mu$ induces,

$$\delta S = -\frac{1}{2\pi} \int d^d x T_{\mu\nu} \partial^\mu \epsilon^\nu. \quad (4.10)$$

For a 2+1 dimensional CFT — the relevant case in this thesis — the central charge is then given by the two-point correlation function of $T_{\mu\nu}$

$$\langle T_{\mu\nu}(x) T_{\lambda\rho}(0) \rangle = C_T \frac{\mathcal{I}_{\mu\nu,\lambda\rho}(x)}{|x|^6}, \quad (4.11)$$

with some tensor structure $\mathcal{I}_{\mu\nu,\lambda\rho}$. In the 1+1 dimensional case the exponent in the denominator is four instead of six.

One of the most important properties of the central charge is its additivity for two independent CFTs, i.e. for two theories with actions S_1 and S_2 , their sum $S_1 + S_2$ will have a central charge $C_{T,1} + C_{T,2}$. This statement is true in general in

¹An example of non-Lorentz invariant critical points are so-called Lifshitz points as mentioned in Sec. 2.2.3.

4. Corner entanglement

any dimension and provides a simple reason for why we say that C_T measures the number of degrees of freedom of a CFT.

We emphasize that the scale invariance of the field theory implies a gapless spectrum of excitations and hence we call the field theory massless. The central charge of a massive field theory is always zero, therefore its consideration is only appropriate for massless excitations. This remark helps us understanding the second important reason for the ability of C_T to measure degrees of freedom, namely Zamolodchikov's c -theorem [93]. This theorem states that for any Lorentz invariant renormalizable 1+1 dimensional field theories there exists a function $c(g)$ of the coupling constant g that decreases *monotonically* under the RG flow applied to this theory. The RG flow starts at the ultraviolet (UV) end, where the theory is a CFT exhibiting a $C_{T,UV}$. Flowing to the infrared fixed point the theory becomes another CFT and $c(g_c)$ is the corresponding central charge $C_{T,IR}$. The interpretation of this theorem is that massive degrees of freedom are eliminated under the RG flow because from the ultraviolet end (short-distance cutoff) to the infrared end the length scale λ increases to the limit $\lambda \rightarrow \infty$ and the corresponding mass of the excitation is $m = \lambda^{-1}$. Hence, only the massless part remains in C_T . This elimination is reflected by the c -theorem because $C_{T,UV} > C_{T,IR}$.

Unfortunately, the c -theorem is not valid in general for 2+1 dimensional CFTs, but in many cases [94]². We adopt the general notion that the central charge quantifies degrees of freedom of the CFT and via the direct relation in Eq. (4.6) we have the ability to apply the toolset of entanglement entropy computation for the characterization of CFTs. For free theories we will not consider RG flows but only focus on the central charge at the scale invariant Gaussian fixed point. Upon adding an interaction term ϕ^4 this fixed point can be thought of as the ultraviolet end of an RG flow to a Wilson-Fisher fixed point.

²Analogues to the c -theorem have been proposed for higher dimensions [95], for example the F -theorem for 2+1 dimensions [96] and the a -theorem in 3+1 dimensions [97].

5. Free theories

The two insights that criticality can be described by a conformal field theory and that corner entanglement is universal at critical points opens up the path to study CFTs *themselves* via corner entanglement. To some extent, we leave the realm of condensed matter physics by focussing on a critical theory as we no longer consider phases of matter and their transitions. Among the broad range of CFTs we pick two very simple theories, namely the massless free boson (or free scalar) and the massless free Dirac fermion theory. These theories are well understood and can be treated analytically and numerically using various approaches. For example, their central charges in 2+1 dimensions are known to be $C_T^{\text{boson}} = 3/(32\pi^2)$ and $C_T^{\text{fermion}} = 3/(16\pi^2)$ [98]. Their corner entanglement for a specific corner opening angle θ can be computed using series expansion techniques [90, 91]. This makes these free field theories excellent candidates for a study of the corner entanglement complementary to a CFT treatment. To this end, we use our condensed-matter technique of direct calculations of the entanglement entropy on lattices. We obtain discretized versions of the field theories by introducing a finite short-distance cutoff δ (lattice spacing) in the fields. Once we have a lattice Hamiltonian for our CFT we can compute the entanglement entropy by bipartitioning the system and extract its corner contribution.

The purpose of this Chapter is the introduction of the two free field theories, the free boson (Sec. 5.1) and the free Dirac fermion (Sec. 5.2). In these sections we will discuss the procedure to derive the lattice field theories and present a derivation of exact formulae for the entanglement entropies based on groundstate correlators. This means that we can in principle compute the entanglement entropies without any approximation by a diagonalization of the Hamiltonian.

5.1. Free boson

One of the most simple theories for a real scalar quantum field ϕ is given by an action only involving quadratic terms

$$S[\phi] = \int d^d x dt \left[\frac{1}{2} (\partial_t \phi)^2 - \frac{1}{2} (\nabla \phi)^2 - \frac{1}{2} m^2 \phi^2 \right], \quad (5.1)$$

with a mass m which can be finite and if so, it induces a mass gap in the spectrum. Later, in our entropy calculations we only consider the gapless case $m = 0$ since we are interested in conformal theories but we keep the mass for now.

The equation of motion derived from this action is the Klein-Gordon equation, the relativistic version of the Schrödinger equation. Hence, the corresponding

5. Free theories

single-particle Hamiltonian for this action reads

$$H = \int d^d x \left[\frac{1}{2} \pi^2(x) + \frac{1}{2} (\nabla \phi(x))^2 + \frac{m^2}{2} \phi^2(x) \right], \quad (5.2)$$

where $\pi(x)$ is the canonical momentum of the field $\phi(x)$. Performing a Fourier transformation of the fields we get $\tilde{\phi}_k$ and $\tilde{\pi}_k$ which yields a Hamiltonian

$$H = \frac{1}{2} \sum_k \pi_k \pi_k^\dagger + \omega_k^2 \phi_k \phi_k^\dagger, \quad (5.3)$$

with $\omega_k = \sqrt{m^2 + k^2}$. We see that this is a sum of oscillators involving a coupling only between the $+k$ and $-k$ modes due to $\pi_k^\dagger = \pi_{-k}$ and $\phi_k^\dagger = \phi_{-k}$. The introduction of bosonic creation and annihilation operators $a_k = 1/\sqrt{2\hbar\omega_k}(\omega_k \phi_k + i\pi_k)$ and $a_k^\dagger = 1/\sqrt{2\hbar\omega_k}(\omega_k \phi_k^\dagger - i\pi_k^\dagger)$ decouples these modes, such that we can write the Hamiltonian in terms of normal modes

$$H = \sum_k \hbar \omega_k \left(a_k^\dagger a_k + \frac{1}{2} \right). \quad (5.4)$$

Since the a_k^\dagger, a_k obey bosonic commutation relations $[a_k, a_{k'}^\dagger] = \delta_{k,k'}$ we observe that the excitations of the single-particle quantum system are bosons which giving the theory (5.1) its name. The Hamiltonian (5.2) can alternatively be obtained by considering coupled harmonic oscillators on a lattice and taking the limit of an infinitesimal lattice spacing since their creation and annihilation operators are also bosonic. In fact, such a system of coupled harmonic oscillators was among the first to be subjected to an entanglement entropy analysis [33]. We here now follow the inverse path and discretize (5.2) on a finite two-dimensional lattice of $N = L^2$ sites, simply by taking finite differences for the derivatives and setting the lattice spacing to unity which yields

$$H = \frac{1}{2} \sum_{x,y=1}^L \left[\pi_{x,y}^2 + m^2 \phi_{x,y}^2 + (\phi_{x,y+1} - \phi_{x,y})^2 + (\phi_{x+1,y} - \phi_{x,y})^2 \right], \quad (5.5)$$

where the two discrete coordinates x and y denote a single site. We employ periodic boundary conditions in both lattice dimensions. Rewriting this Hamiltonian by using a matrix M of dimension $N \times N$ we get

$$H = \frac{1}{2} \sum_{i=1}^N \pi_i^2 + \sum_{i,j=1}^N \phi_i M_{ij} \phi_j, \quad (5.6)$$

with indices $i = (x_i, y_i)$ denoting the sites. Only the matrix M — containing the potentials of the harmonic oscillators — is needed for the groundstate correlations and the entropy computation, as explained in the next paragraph.

5.1.1. Correlator-based entropy computation

For the derivation of the formula for the entanglement entropies we follow the review article by Peschel and Eisler, Ref. [99], as well as a more concrete explanation in the appendix of Ref. [100].

The Boltzmann distribution generated by the (Gaussian) Hamiltonian (5.6) is a multivariate normal distribution. Hence, Wick's theorem is satisfied for expectation values $\langle O \rangle = \text{Tr}(\exp(-\beta H)O)$ based on this distribution such that correlation functions of positions (and also momenta) factorize [101] as required like

$$\langle x_m x_n x_k x_l \rangle = \langle x_m x_n \rangle \langle x_k x_l \rangle + \langle x_m x_k \rangle \langle x_n x_l \rangle + \langle x_m x_l \rangle \langle x_n x_k \rangle. \quad (5.7)$$

A computation of correlations inside subsystem A using the reduced density matrix ρ_A must reproduce Wick's theorem. Therefore we make an ansatz

$$\rho_A = \frac{1}{Z} e^{-\sum_q \varepsilon_q b_q^\dagger b_q}, \quad (5.8)$$

with bosonic operators b_q^\dagger, b_q and Z ensuring $\text{Tr}(\rho_A) = 1$. This ansatz indeed incorporates Wick's theorem because it is the exponential of a quadratic “Hamiltonian”¹. The energies ε_q need to be determined such that ρ_A represents the one-particle groundstate correlations of the Hamiltonian (5.6). The latter have been found [102] to be given in terms of the potential matrix M

$$\begin{aligned} X_{ij} &= \langle \phi_i \phi_j \rangle = \frac{1}{2} (M^{-1/2})_{ij} \\ P_{ij} &= \langle \pi_i \pi_j \rangle = \frac{1}{2} (M^{1/2})_{ij} \end{aligned} \quad (5.9)$$

for both the position and momentum degrees of freedom in (5.6). All *mutual* correlations of the form $\langle \phi_i \pi_j \rangle$ vanish. Restricting X and P to subsystem A , i.e. taking only the corresponding rows and columns of these matrices, it is finally derived [102] that the positive eigenvalues ν_q of the matrix $C_A = \sqrt{X_A P_A}$ define the single-particle eigenvalues ε_q as

$$\frac{1}{2} \coth\left(\frac{\varepsilon_q}{2}\right) = \nu_q. \quad (5.10)$$

By combining this relation and the ansatz (5.8) with the definitions of the von Neumann entropy, Eq. (2.6), and Rényi entropy, Eq. (2.7), we obtain

$$S_\alpha(A) = \frac{1}{\alpha - 1} \text{Tr} \ln \left[\left(C_A + \frac{1}{2} \right)^\alpha - \left(C_A - \frac{1}{2} \right)^\alpha \right], \quad (5.11)$$

and

$$S_1(A) = \text{Tr} \left(C_A + \frac{1}{2} \right) \ln \left(C_A + \frac{1}{2} \right) - \left(C_A - \frac{1}{2} \right) \ln \left(C_A - \frac{1}{2} \right) \quad (5.12)$$

for the entropies in terms of C_A . The details of this calculation are carried out in App. B.1. Compared to diagonalizing the full Hamiltonian this formula is a significant computational advantage because only the matrix C_A whose size depends on the size of subsystem A needs to be diagonalized.

¹It should be emphasized that this Hamiltonian is artificial, in particular it is not the Hamiltonian of the total system reduced to the degrees of freedom in subsystem A .

5.2. Free Dirac fermion

A single free fermion with mass m is described by a wavefunction ψ obeying the Dirac equation $i\hbar\frac{\partial\psi}{\partial t} = H_D\psi$ with a Hamiltonian

$$H_D = -i\hbar c\alpha_i\partial_i + \beta mc^2. \quad (5.13)$$

In contrast to the Klein-Gordon equation it is linear in the momenta and in ∂_t and takes into account the spin of the particle. We will set $\hbar = c = 1$ in the following. The objects β and α_i are Hermitian matrices that have to satisfy the algebra $\{\alpha_i, \alpha_j\} = 2\delta_{ij}$, $\{\beta, \alpha_i\} = 0$ and $\beta^2 = 1$. Hence, a wavefunction that solves the equation must have several components $\psi = (\psi_1, \psi_2, \dots, \psi_n)^T$ — called a spinor. In 3+1 space-time dimensions at least four matrices $\beta, \alpha_1, \alpha_2, \alpha_3$ are necessary to solve (5.13) and their dimensionality must be greater or equal to four. An ansatz using so-called γ -matrices which obey $\{\gamma^\mu, \gamma^\nu\} = 2g^{\mu\nu}$ — g being the Minkowski metric — provides the needed matrices β and α_i . However, in the present case we work in 2+1 dimensions which simplifies the quest for the matrices: Simply the Pauli matrices can be used as $\alpha_1 = \sigma_x$, $\alpha_2 = \sigma_y$ and $\beta = \sigma_z$. In momentum space ($-i\partial_j \rightarrow k_j$) the Dirac Hamiltonian then reads

$$H_D = k_x\sigma_x + k_y\sigma_y + m\sigma_z. \quad (5.14)$$

This Hamiltonian describes a fermion with spin 1/2 and momentum $\mathbf{k} = (k_x, k_y)$. It has an energy dispersion

$$\epsilon = \pm\sqrt{\mathbf{k}^2 + m^2}, \quad (5.15)$$

i.e., for $m = 0$ we have a linear spectrum near the Dirac cone at $k = 0$, for both positive and negative energies. The negative energy solutions are interpreted as the antiparticle solutions, e.g. positrons if the original particle is an electron. In the vacuum, all negative energy eigenstates are occupied while the positive eigenstates are empty — a state known as the *Dirac sea*.

Although we are interested in the massless Dirac fermion in its vacuum state, we keep a finite mass m in the Hamiltonian (5.14). This is to deal with a problem arising when we discretize the Hamiltonian on a lattice — the *fermion doubling problem*. It is due to the fact that the linear dispersion relation (5.15) becomes sinusoidal for discrete fields with a finite lattice spacing, i.e. $\epsilon \sim \sin|\mathbf{k}|$. Near $\mathbf{k} = 0$ this discrepancy is negligible but at $k_i = \pi$ additional local Dirac points emerge inside the first Brillouin zone, an effect dubbed fermion doubling². In order to cure this unwanted effect we will manipulate the mass to become \mathbf{k} -dependent in a way that it vanishes at $\mathbf{k} = 0$ but is finite at the additional Dirac points. By this means we induce a gap at all other zeros of the energy dispersion and thereby leave only the point $\mathbf{k} = 0$ critical. Hence, the groundstate physics to be explored unambiguously refers to *one* Dirac cone which is consequently described by one Dirac CFT.

²In a one-dimensional system we double the number of Dirac points whereas in the present two-dimensional case we have four Dirac points, namely at $\mathbf{k} \in \{(0, 0), (0, \pi), (\pi, 0), (\pi, \pi)\}$.

5.2.1. Lattice field theory

In an anticipating manner we modify the Hamiltonian (5.14) by setting $k_i \rightarrow \sin k_i$ such that it reproduces the discrete energy dispersion. At the same time we set the mass m to a dimensionless quantity $m(\mathbf{k}) = 2 - \cos k_x - \cos k_y$ so that the single particle momentum space Dirac Hamiltonian becomes

$$H_D(\mathbf{k}) = \sin(k_x)\sigma_x + \sin(k_y)\sigma_y + (2 - \cos(k_x) - \cos(k_y))\sigma_z. \quad (5.16)$$

In the limit $\mathbf{k} \rightarrow 0$ we recover the Dirac Hamiltonian corresponding to a massless Dirac fermion $H_D = k_x\sigma_x + k_y\sigma_y$. It is not our purpose to seek for a physical interpretation of this Hamiltonian (5.16) in full k -space, e.g. in terms of a material or a toy model. We restrict ourselves to the vicinity of the Dirac point for the application and interpretation of this Hamiltonian.

Now, we derive a lattice Hamiltonian in terms of fermionic creation and annihilation operators acting in position space which collectively represents the massless Dirac fermion. In order to do this, we start from the Hamiltonian in the reciprocal lattice, constructed by creation and annihilation in momentum space $\psi_{\mathbf{k}}^\dagger, \psi_{\mathbf{k}}$ which are fermionic two-spinors. A finite-size lattice will have a finite number of k values such that the discrete lattice Hamiltonian is given by

$$H = \sum_{\mathbf{k}} \psi_{\mathbf{k}}^\dagger H_D(\mathbf{k}) \psi_{\mathbf{k}}. \quad (5.17)$$

A reverse Fourier transformation of the momentum space operators yields our final fermionic operators $c_i^\dagger, c_i, d_i^\dagger, d_i$ which come in two flavours due to the two-spinor property of the $\psi_{\mathbf{k}}$. Therefore, every lattice sites at \mathbf{r}_i labeled by $i = (m, n)$ carries two fermions. For a two-dimensional lattice of size $N = L \times L$ with a spacing set to unity we have

$$\psi_{\mathbf{k}}^\dagger = \frac{1}{V} \sum_i e^{i\mathbf{r}_i \mathbf{k}} \begin{pmatrix} c_i^\dagger \\ d_i^\dagger \end{pmatrix}^T \quad \text{and} \quad \psi_{\mathbf{k}} = \frac{1}{V} \sum_i e^{-i\mathbf{r}_i \mathbf{k}} \begin{pmatrix} c_i \\ d_i \end{pmatrix}, \quad (5.18)$$

which we insert into (5.17) and obtain

$$H = \sum_{\mathbf{k}} \sum_{i,j=1}^L \frac{e^{i\mathbf{r}_i \mathbf{k}}}{V^2} \begin{pmatrix} c_i^\dagger \\ d_i^\dagger \end{pmatrix}^T \begin{pmatrix} 2 - \cos k_x - \cos k_y & \sin k_x - i \sin k_y \\ \sin k_x + i \sin k_y & -2 + \cos k_x + \cos k_y \end{pmatrix} \begin{pmatrix} c_j \\ d_j \end{pmatrix} e^{-i\mathbf{r}_j \mathbf{k}}. \quad (5.19)$$

By using the identities $\sin \varphi = (e^{i\varphi} - e^{-i\varphi})/2i$ and $\cos \varphi = (e^{i\varphi} + e^{-i\varphi})/2$ we see that the sine and cosine translate to hopping terms in the corresponding lattice direction after the sum over \mathbf{k} is expressed as a delta function. The final Hamiltonian can be expressed explicitly as

$$H = \sum_{i,j=1}^L \begin{pmatrix} c_i^\dagger \\ d_i^\dagger \end{pmatrix}^T H_{ij} \begin{pmatrix} c_j \\ d_j \end{pmatrix} \quad (5.20)$$

5. Free theories

with

$$\begin{aligned}
H_{ij} \equiv H_{(m,n),(m',n')} = & -\frac{i}{2}\delta_{m+1,m'}\delta_{n,n'}\sigma_x \\
& -\frac{i}{2}\delta_{m,m'}\delta_{n+1,n'}\sigma_y \\
& + \left[\delta_{m,m'}\delta_{n,n'} - \frac{1}{2}\delta_{m+1,m'}\delta_{n,n'} - \frac{1}{2}\delta_{m,m'}\delta_{n+1,n'} \right] \sigma_z + h.c.
\end{aligned}$$

In principle, it is possible to set open, periodic or antiperiodic boundary conditions on the lattice Hamiltonian (5.20). If we want to use the numerical linked-cluster expansion for the entropy computation, we must employ open boundary conditions.

5.2.2. Correlator-based entropy computation

The approach for the direct computation of the entanglement entropies for fermionic systems is — like in the bosonic case — based on Wick's theorem. It was first derived in Ref. [101] and reviewed also in Refs. [99, 100].

We are interested in the groundstate of the fermionic Hamiltonian (5.20). To obtain the corresponding entanglement entropy, we want to use the one-particle correlations $\langle c_m^\dagger c_n \rangle$ of the groundstate. For these correlations we have factorizations like

$$\langle c_m^\dagger c_n^\dagger c_k c_l \rangle = \langle c_m^\dagger c_l \rangle \langle c_n^\dagger c_k \rangle - \langle c_m^\dagger c_k \rangle \langle c_n^\dagger c_l \rangle, \quad (5.21)$$

because the eigenstates of the Hamiltonian are Slater determinants. Inside a subsystem A of size ℓ the reduced density matrix must reproduce all the correlations including its factorization property. Due to Wick's theorem this can be guaranteed by an ansatz

$$\rho_A = \frac{1}{Z} e^{-H_A} \quad (5.22)$$

with another fermionic Hamiltonian H_A acting on subsystem A — dubbed the entanglement Hamiltonian [100]. We emphasize that H_A is not obtained by reducing the full Hamiltonian to the degrees of freedom belonging to A .

The operation of restricting the full system to subsystem A must be carried out on the correlation matrix

$$C_{ij} = \text{Tr} \left(\rho c_i^\dagger c_j \right), \quad (5.23)$$

where we have, for the sake of readability, omitted correlations of the types $d_i^\dagger c_j$, $c_i^\dagger d_j$ and $d_i^\dagger d_j$. The total correlation matrix C is hence of size $2N \times 2N$. Taking only the corresponding rows and columns of C we obtain the correlation matrix C_A for subsystem A . The crucial point is now, that (i) C_A and H_A are diagonalized by the same unitary transformation U and (ii) the eigenvalues ζ_q of C_A and ϵ_q of H_A are related by

$$\zeta_q = \frac{1}{e^{\epsilon_q} + 1}. \quad (5.24)$$

This can be understood from writing $H_A = \sum_q \epsilon_q f_q^\dagger f_q$ with new fermion operators $c_i = \sum_q U_{qi} f_q$. Since U is unitary, inserting this basis transformation into (5.23)

yields

$$C_{A,ij} = \text{Tr} \left(\rho_A \sum_q U_{iq}^* U_{qj} f_q^\dagger f_q \right). \quad (5.25)$$

Only the elements with $\langle \hat{n}_q \rangle = \langle f_q^\dagger f_q \rangle = 1$ contribute in the sum. The corresponding entry of ρ_A is $e^{-\epsilon_q}$, see (5.22). The condition on the density matrix $\text{Tr} \rho_A = 1$ leads to the normalization $1 + e^{-\epsilon_q}$ on the single-fermion subspaces of the Hamiltonian, yielding $e^{-\epsilon_q} / (1 + e^{-\epsilon_q})$ for the eigenvalue of C_A which proves (5.24).

By diagonalizing C_A we thus obtain the eigenenergies ϵ_q of H_A which only need to be inserted in the definitions of entanglement entropies (2.6) and (2.7) so that we can write down the formulae for the Rényi entropy

$$S_\alpha(A) = \frac{1}{1-\alpha} \sum_{q=1}^{2\ell} \ln(\zeta_q^\alpha + (1-\zeta_q)^\alpha), \quad (5.26)$$

and for the von Neumann entropy

$$S_1(A) = \sum_{q=1}^{2\ell} -\zeta_q \ln \zeta_q - (1-\zeta_q) \ln(1-\zeta_q). \quad (5.27)$$

A detailed derivation of these formulae using Eq. (5.22) is provided in App. B.2.

In the explanation of the steps to arrive at the final formulae we have so far skipped an important part, namely how we obtain the correlation matrix C of the total system, and thereby input the particular state we are computing the entanglement entropy of. To this end we exploit *again* the fact that H and C are diagonalized by the same unitary transformation. Moreover, since we are interested in the vacuum of the fermionic system, the correlation matrix in energy space is very simple. Assuming that the eigenstates are sorted in ascending order according to their eigenenergies we have $\tilde{C} = \text{diag}(1, 1, \dots, 1, 0, 0, \dots, 0)$, since all the negative energy eigenstates are occupied, while the positive ones are empty. The total Hamiltonian is diagonalized by a unitary transformation $V^\dagger H V$ which we apply to $C = V \tilde{C} V^\dagger$. We can then continue with the rest of the procedure by reducing C to C_A . A sketch of the workflow summarizes the discussed method

$$H \xrightarrow{\text{diagonalize}} C \xrightarrow{\text{restrict to } A} C_A \xrightarrow{\text{diagonalize}} H_A \xrightarrow{\text{insert in } \rho_A} S(A).$$

Computationally the diagonalization of the total Hamiltonian H is the most time-consuming operation in the procedure, because the other diagonalization (of C_A) is performed on a usually significantly smaller matrix. It is possible to circumvent [103] the big diagonalization if we impose *periodic* boundary conditions on our system. In this case, all allowed values of \mathbf{k} in Eq. (5.17) can be trivially pre-computed by Bloch moments $k_{x/y} = 2\pi n/L, n \in (0, \dots, N-1)$. Further, we diagonalize the 2×2 Dirac Hamiltonians $H_D(\mathbf{k})$ for all possible \mathbf{k} . On this level we pick only the *eigenvectors*³ corresponding to the negative eigenvalues in order to

³Unitary matrices that diagonalize a matrix A can be constructed from the eigenvectors of A , which is what we are doing here.

5. Free theories

perform the unitary transformation on H_D yielding many 2×2 the correlation matrices. After that we have to (numerically) perform the inverse Fourier transformation to obtain C in terms of the position space fermions $c_i^\dagger, d_i^\dagger, c_i, d_i$. The remainder of the procedure is identical to the one above, but its bottleneck is now merely the diagonalization of C_A instead of H .

6. Lattice results in 2+1 dimensions

We have outlined above how the von Neumann and the Rényi entanglement entropies can be computed exactly for many-body Hamiltonians of free massless theories. In this chapter, we first enhance our numerical toolset in Sec. 6.1 by approximative methods that enable us to extract the subleading corner contribution. The last part of this methodological section is specialized to quantum spin models, described by interacting theories and tractable via quantum Monte Carlo simulations. The major purpose of the present Chapter is to apply these methods to critical theories and obtain results for the corner entanglement $c_\alpha(\theta)$. In Sec. 6.2, lattice models of various $O(N)$ universality classes are studied, mainly at their critical point. We compare the values of the corner entanglement for an opening angle of $\theta = \frac{\pi}{2}$ between complementary numerical methods for identical models. In addition, we motivate a comparison between *different* $O(N)$ models by relating the results to the number of field components N . Finally, in Sec. 6.3 we amply present results for the free boson and the free Dirac fermion lattice theories derived above. Here we compute $c_\alpha(\theta)$ for a range of different opening angles θ . Our findings on the lattice are compared to field theoretic computations of the corner entanglement entropy. Finally, there exists an astonishing duality between the Rényi entanglement entropies of the free boson and the free Dirac fermion which will be introduced in Sec. 6.3.3.

6.1. Numerical extraction of corner entanglement

Having a numerical tool for the computation of the bare entanglement entropy, additional efforts must be taken to access its *subleading* logarithmic contribution. This means, that from the functional form of the entanglement entropy in terms of the linear subsystem size¹ L_A

$$S_\alpha(L_A) = a_\alpha L_A - \mathcal{C}_\alpha \ln L_A + D, \quad (6.1)$$

the coefficient \mathcal{C}_α has to be extracted. It contains the contributions from all corners, so that we have to further separate the individual corner contribution in \mathcal{C}_α , e.g. by a division, if all corners are equal in nature.

In this Section we present three different strategies for this endeavor. First, we discuss a *direct approach* which basically attempts to fit the entanglement entropy

¹We assume a linear dependence of L_A and the boundary length ℓ_A , such that the boundary law can be represented using L_A .

6. Lattice results in 2+1 dimensions

to the behavior in Eq. (6.1). Another possibility is to find a way to remove the boundary contribution $a_\alpha \ell_A$ and perform a linear fit of the remaining part against $\ln \ell_A$. We introduce two methods based on this idea, (i) a numerical linked-cluster expansion and (ii) a quantum Monte Carlo sampling scheme that directly accesses $\mathcal{C}_\alpha \ln L_A$.

6.1.1. Direct fit

A straightforward procedure to obtain the corner coefficient $c_\alpha(\theta)$ from the entanglement entropy (6.1) is to compute $S_\alpha(L_A)$ for a range of linear sizes L_A of the subsystem and perform a least-squares fit to the function (6.1). If we are interested in the contribution of one right-angled corner we choose the subsystem A to be a square, see Fig. 6.1, and obtain $c_\alpha(\theta = \frac{\pi}{2}) = \mathcal{C}_\alpha/4$ due to the four corners of the square. The total system is considered in periodic boundary conditions (PBC) in order to eliminate effects coming from the boundaries.

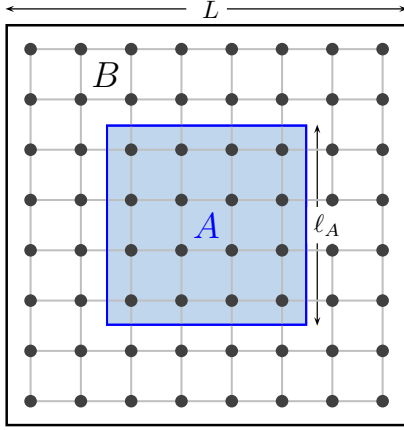


Figure 6.1.: Example for a bipartition which can be used to obtain the corner contribution from corners with an opening angle of $\theta = \frac{\pi}{2}$.

A few aspects have to be considered that are essential for the success of this procedure. First, a sufficiently large subsystem size L_A must be accessible² in the entanglement entropy computation in order to have a wide range of data points to be included in the fitting. This is particularly important as the fitting includes the non-polynomial contribution $\ln L_A$ which becomes harder to distinguish from a constant contribution the larger L_A is. For example, $\ln 32 - \ln 20 < 0.5$. Furthermore, the entanglement entropy in general exhibits a so-called geometric contribution, i.e. a term depending on ratio L_A/L [56, 68, 104]. We therefore keep L_A/L constant when varying the system size which effectively absorbs the geometric contribution in the constant D . Another obstacle for this approach could be that Eq. (6.1) neglects

further contributions, e.g. of $\mathcal{O}(L_A^{-1})$ and $\mathcal{O}(L^{-1})$ although they might be significant in a particular system. Including them would introduce further parameters in the fit which increases the need for a larger data basis.

In addition, corner entanglement arising from corners with opening angles $\theta \neq \frac{\pi}{2}$ can be computed, namely by a *pixelation* of one side of the angle. Angles which obey $\tan \theta = q \in \mathbb{Q}$ pixelate most naturally on the square lattice in a stair-like pattern, depicted in Fig. 6.2. The subsystem needs to be a closed polyhedron, therefore we combine different angles for a particular bipartition and extract the desired contribution from \mathcal{C}_α . More precisely, for angles $\theta > \frac{\pi}{2}$ we exploit the symmetry $c_\alpha(2\pi - \theta) = c_\alpha(\theta)$ of the corner contribution and design bipartitions as bands winding around the periodic lattice (left panel of Fig. 6.3). The contribution from

²Beyond the fact that we want to obtain the corresponding value in a reasonable computing time, we also mean by ‘accessible’ that its statistical error is moderate.

6.1. Numerical extraction of corner entanglement

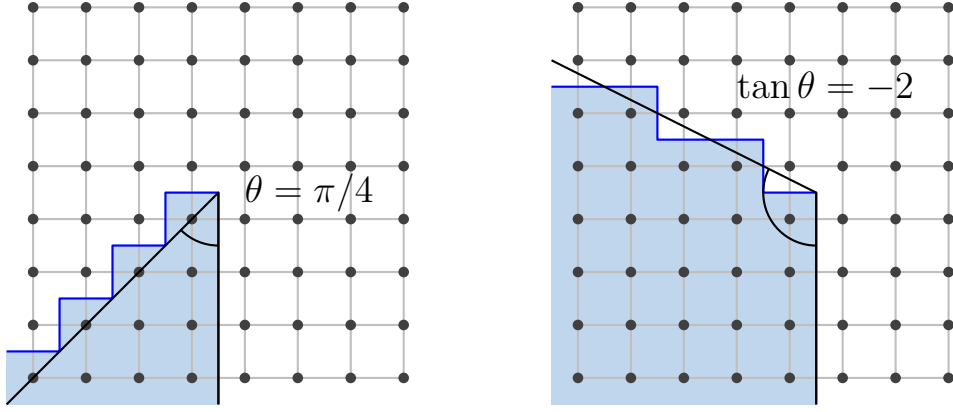


Figure 6.2.: Examples for the pixelation of corners in the entangling boundary, superimposed on an underlying square lattice, with opening angles of $\theta = \pi/4$ (left panel) and $\tan \theta = -2$ (right panel).

a single corner in this case is $c_\alpha(\theta) = \mathcal{C}_\alpha/8$. In the right panel of Fig. 6.3 we show how the knowledge of the contribution of an angle $\theta = \frac{\pi}{2} + \hat{\theta}$ is used to compute its counterpart reflected about $\frac{\pi}{2}$, i.e. $\tilde{\theta} = \frac{\pi}{2} - \hat{\theta}$: We compute the total logarithmic contribution of an appropriate parallelogram and subtract the known corner contributions, $c_\alpha(\tilde{\theta}) = (\mathcal{C}_\alpha - 2c_\alpha(\theta))/2$.

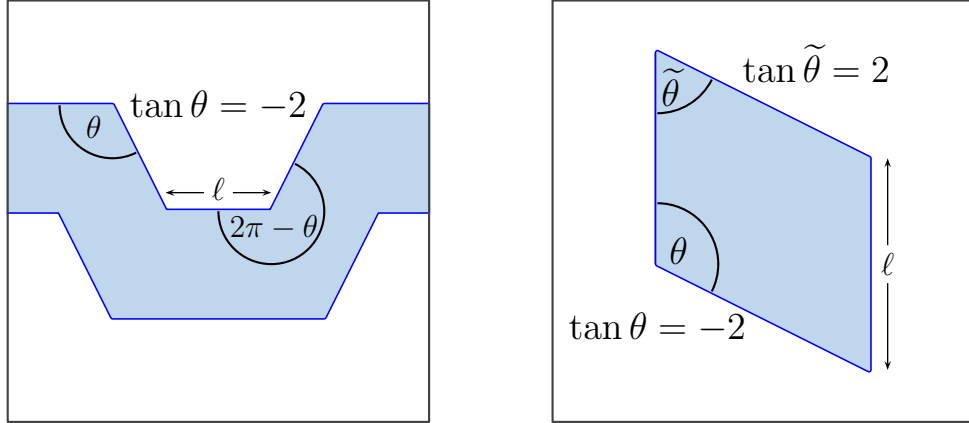


Figure 6.3.: Closed polygons in periodic boundary conditions in order to obtain the corner contribution from fitting the boundary law to the full entanglement entropy. Examples are shown for $\tan \theta = -2$ (left panel) and for $\tan \tilde{\theta} = 2$ (right panel) which requires the subtraction the θ -contribution.

6.1.2. Numerical linked-cluster expansion

The removal of the leading boundary term $a_\alpha L_A$ in Eq. (6.1) can be regarded as the major challenge in extracting the corner entanglement. If we find a way to simply subtract it, we can perform a linear regression fitting of the remaining quantity against $\ln L_A$ which returns the corner coefficient as its slope. The constant part D will translate to another constant $\exp(D)$ returned by this fit and can be discarded. In this paragraph we describe an approach which precisely does this removal of

6. Lattice results in 2+1 dimensions

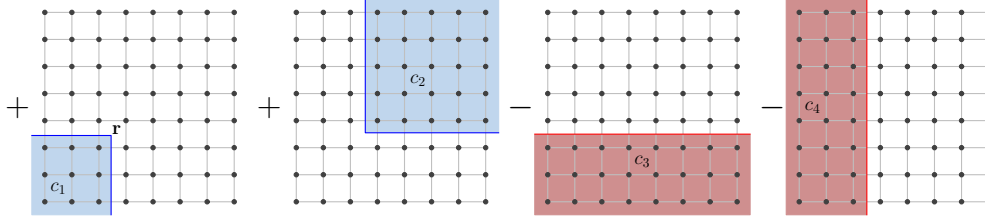


Figure 6.4.: Bipartitions c_1 , c_2 , c_3 and c_4 used to determine the corner entanglement for $\theta = \pi/2$ according to Eq. (6.2).

$a_\alpha L_A$ by the *design* of suitable bipartitions whose entanglement entropies are computed and subsequently added according to the scheme in Fig. 6.4, i.e.

$$P_{\mathbf{r}}(c) = \frac{1}{2} [S_\alpha(c_1) + S_\alpha(c_2) - S_\alpha(c_3) - S_\alpha(c_4)] \quad (6.2)$$

for a location \mathbf{r} of the corner. We see that all boundary contributions are cancelled in the sum of the entropies and the contribution originating from a corner remains doubly — from c_1 and c_2 . It is important to note that open boundary conditions are imposed on the systems here, such that no boundary contributions arise from the outer boundaries of the subsystems c_i . Without any restriction we can adapt the design to corners $\theta \neq \frac{\pi}{2}$, Fig. 6.2 corresponds to bipartition c_1 in this case. This scheme on a lattice is interpreted as a finite-size cluster of order L in which the property P of interest — in our case the corner entanglement — is embedded. A numerical linked-cluster expansion (NLCE) [86, 105], explained below, then allows to obtain estimates of $P(L)$. Subsequently, we have to perform the linear fit of $P(L)$ against $\ln L$ for a range of cluster orders L to get c_α .

The NLCE method works as described in the following. Linked clusters are finite connected sections of the (infinite) system on which the property is computable. In our example, a 2×2 cluster is the smallest that can embed the scheme (6.2) with the corner at its center. A standard cluster expansion approach would consider clusters of arbitrary shape — involving the NP-complete problem of identifying all possible clusters of a given size. Following Ref. [105] we exploit the fact that in our specific models the expansion converges even if only *rectangular* clusters are included. First, we actually compute our property for a particular cluster c by the application of the numerical method of our choice, namely the exact formulae Eqs. (5.11) and (5.26)³. This involves individual computations of $S_\alpha(c_i)$ for the four bipartitions in Fig. 6.4 for every possible location \mathbf{r} of the corner. The value of the property for a cluster c follows as the sum over all corner locations

$$P(c) = \sum_{\mathbf{r}} P_{\mathbf{r}}(c). \quad (6.3)$$

We note, that the number of necessary individual calculations is in general not four times the number of possible corner locations. The two smooth bipartitions c_3 and c_4 are identical for several corner locations but need only be computed once. In

³This computation could be done by a quantum Monte Carlo simulation or a density matrix renormalization group approach as well.

6.1. Numerical extraction of corner entanglement

addition, the value of the property is symmetric under a rotation of the cluster by 180° as $c_1 \leftrightarrow c_2$ — reducing the number of computations by a factor of two. For a model which is isotropic in the spatial dimensions as the free boson, it is sufficient to only consider upright rectangular clusters, i.e. clusters with linear length $L_y \geq L_x$. The other orientation can later be taken care of by an embedding factor

$$e(x) = \begin{cases} 1, & L_x = L_y \\ 2, & L_x > L_y. \end{cases} \quad (6.4)$$

The explicit values of the property are used to recursively define *weights* $W(c)$ for a cluster c according to

$$W(c) = P(c) - \sum_{s \in c} W(s), \quad (6.5)$$

where the sum on the right-hand-side runs over all rectangular subcluster s in c . A particular subcluster s of dimensions $l_x \times l_y$ multiply appears in this sum, since it can be embedded in more than one way in a bigger cluster c of dimensions $L_x \times L_y$. The multiplicity of the embeddings is $m_{s|c} = (L_x - l_x)(L_y - l_y)$. An example of all distinct subclusters s of a 4×4 cluster is shown in Fig. 6.5.

We have to associate an order $\mathcal{O}(c)$, i.e. a typical length scale, to a cluster c . Possible options are the arithmetic mean $(L_x + L_y)/2$ or the geometric mean $\sqrt{L_x L_y}$ but we simply choose the longer side $\mathcal{O}(c) = \max(L_x, L_y)$. This allows us to assign a value of the property *per site* to a given cluster order L . It is given by the sum of all clusters up to the maximal cluster (which is a square of $N = L \times L$) of order L

$$\frac{P(L)}{N} = \sum_c e(c) \times W(c), \quad (6.6)$$

where $e(c)$ is the embedding factor defined above. In the end it is this property per site $P(L)/N$ — evaluated for a range of orders $[2, L_{\max}]$ — that is fitted against $\ln L$ in order to obtain the corner coefficient $c_\alpha(\theta)$. Doing so, we have effectively replaced the length of the subsystem L_A as the linear scale for the boundary law and its subleading logarithmic correction by the cluster order L . However, this is reasonable as the boundary lengths in the bipartitions of the scheme in Fig. 6.4 are precisely L for c_3 and c_4 and on average for c_1 and c_2 .

The computational complexity of the NLCE approach in combination with the exact diagonalization is of order $\mathcal{O}(L^5)$ due to the complexity of the diagonalization itself, $\mathcal{O}(L^3)$, multiplied with the number of possible corner locations $N_r \sim L^2$ in the cluster. We are therefore strongly restricted by the maximal cluster order accessible in this method, but we can estimate the value for $c_\alpha(\theta)$ in the thermodynamic limit by a second extrapolation, see Sec. 6.3.

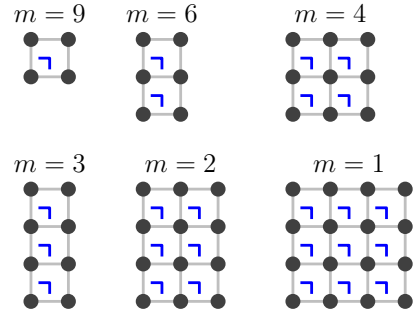


Figure 6.5.: All possible upright rectangular clusters up to a cluster order $L = 4$. Possible corner locations are marked in blue. The multiplicity refers to an embedding of the corresponding cluster in the 4×4 cluster (bottom right).

6.1.3. Incremental regions

Another strategy for the removal of the leading boundary contribution $a_\alpha L_A$ is rooted in a Quantum Monte Carlo (QMC) setup applicable to spin models. The QMC simulations are carried out in a stochastic series expansion (SSE) [64, 106] of the modified partition function $Z[A, 2, \beta]$ that implements the replica trick for the computation of the second Rényi entropy. In order to obtain the Rényi entropy as a statistical observable, we use the ensemble switching approach [78] embedded in the so-called increment trick [107]. The details of the QMC algorithm are briefly explained in App. A. Such a QMC simulation computes the entanglement entropy of a subregion A as the logarithm of the ratio of two partition functions

$$S_2(A) = -\ln \left(\frac{Z[A, 2, \beta]}{Z^2} \right), \quad (6.7)$$

where Z is the partition function of the total system. $Z[A, 2, \beta]$ is the modified partition function at inverse temperature β where the subregion A is connected over the replicas ($\alpha = 2$ in this case). This ratio is sampled by generating a Markov chain of configurations in the *joined* ensemble of both partition functions and allowing to switch between them [78]. Such a switch is performed if all degrees of freedom in subsystem A agree over the replicas. As our measurement, we simply *count* how many times we have been in Z and how many times in $Z[A, 2, \beta]$. A problem arises in the simulation of this ratio if region A is not small: A switch between the ensembles Z^2 and $Z[A, 2, \beta]$ becomes a rare event and hence the QMC results potentially suffers from huge statistical errors.

The increment trick [107] follows from using a series of subregions of $A = A_N \subsetneq A_{N-1} \subsetneq \dots A_2 \subsetneq A_1$ which enables us to rewrite (6.7)

$$\begin{aligned} S_2(A) &= -\ln \left(\frac{Z[A_1, 2, \beta]}{Z^2} \cdot \frac{Z[A_2, 2, \beta]}{Z[A_1, 2, \beta]} \cdot \dots \cdot \frac{Z[A, 2, \beta]}{Z[A_{N-1}, 2, \beta]} \right) \\ &= S_2(A_1) + S_2(A_1 \rightarrow A_2) + \dots + S_2(A_{N-1} \rightarrow A_N), \end{aligned} \quad (6.8)$$

where the intermediate entropies $S(A_i \rightarrow A_{i+1})$ result from individual simulations with a connected region A_i (in the replica trick sense) and a region $A_{i+1} \setminus A_i$ toggling between connected and disconnected in the ensemble switching. By applying the increment trick we obtain $S_2(A)$ from N independent simulations in (6.8) which produce results that have smaller statistical errors than a single simulation for Eq. (6.7) and hence also their sum yields a more accurate estimation of $S_2(A)$.

In order to extract the corner term of our spin-half models, we compute the entanglement entropy for two different bipartitions — a square shaped subregion A^{sq} which has a corner term and a strip shaped subregion A^{st} , i.e. a region with a corner-free boundary winding around the lattice in periodic boundary conditions. Both bipartitions have the *same* boundary length ℓ and we hence expect the *difference* between the two corresponding entanglement entropies $\Delta S = S_2(A^{\text{sq}}) - S_2(A^{\text{st}})$ to have $-c \ln \ell$ as its leading order. The remaining fit of ΔS against $\ln L_A$ can be done as a linear regression and therefore yields significantly more reliable results than a full fit against Eq. (6.1). Combining this bipartitioning with the increment trick, we see that the set of single simulations of incremental regions necessary to

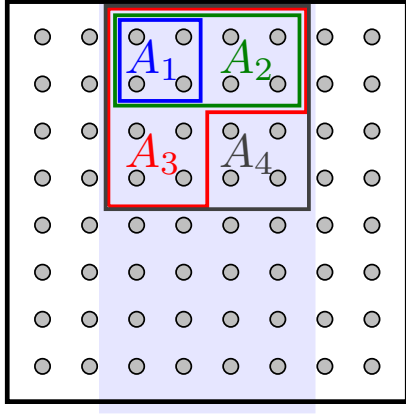


Figure 6.6.: Illustration of the increment trick. The regions A_1, \dots, A_4 constitute a sequence that successively builds up the square subsystem A_4 . This procedure can be continued straightforwardly to the whole strip (shaded region). It is obvious that the square A_4 is “on the way” to the strip.

build up $S_2(A^{\text{st}})$ already includes all incremental regions to compute $S_2(A^{\text{sq}})$, see Fig. 6.6. Even better, the increment trick allows us to *directly* obtain the difference ΔS_2 , i.e. *without* computing $S_2(A^{\text{sq}})$ and $S_2(A^{\text{st}})$ explicitly. To do so, we start the incrementation at $S_2(A^{\text{sq}} \equiv A_{N/2})$:

$$\begin{aligned}
 & S_2(A_{\text{square}} \rightarrow A_{N/2+1}) + S_2(A_{N/2+1} \rightarrow A_{N/2+2}) + \dots + S_2(A_{N-1} \rightarrow A_{\text{strip}}) \\
 &= -\ln \left(\frac{Z[A_{\text{strip}}, 2, \beta]}{Z[A_{\text{square}}, 2, \beta]} \right) \\
 &= -\ln \left(\frac{Z[A_{\text{strip}}, 2, \beta]}{Z^2} \right) + \ln \left(\frac{Z[A_{\text{square}}, 2, \beta]}{Z^2} \right) \\
 &= S_2^{(\text{strip})} - S_2^{(\text{square})}.
 \end{aligned} \tag{6.9}$$

This reduces the computation time by a factor of 2 because the square region does not need to be successively built up by incrementations. We have used this shortcut in order to obtain better estimates for ΔS_2 entering the fit. Nevertheless, we will also show the explicit values for $S_2(A^{\text{st}})$ and $S_2(A^{\text{sq}})$ computed in less accuracy than ΔS_2 .

6.2. Interacting theories

Spin-half lattice models have become excellent candidates for the investigation of corner entanglement after a numerical setup for the computation of the entanglement entropy on lattices [27] was established. At their critical points these models are described by interacting theories. Hence, the corresponding ultraviolet fixed point of a renormalization group flow belongs to the Wilson-Fisher universality class. One of the goals of the numerical studies on the lattice was the comparison of the result for the corner entanglement c from free field theories (Gaussian fixed points) [7] with these $O(N)$ models on the lattice. A priori, there is no reason to assume that they are equal.

Many numerical studies have been carried out in this field [80, 86, 108], in particular, in Ref. [85] a proportionality between the corner entanglement c and the number N characterizing the microscopic degrees of freedom in an $O(N)$ model has been established. This insight raised the question whether corner entanglement

6. Lattice results in 2+1 dimensions

generically quantifies the low-lying energy excitations in a wide range of CFTs. It constitutes actually the point of entry to the discussion in Sec. 4.4 and was subsequently addressed in a series of field theoretic studies [88, 90]. Here, we present results for the second Rényi entropy S_2 for the three bilayer models, introduced in Sec. 3.1 which undergo a phase transition in the two-dimensional $O(2)$ and $O(3)$ universality classes. The strategy to extract their corner entanglement using incremental regions as described above is employed.

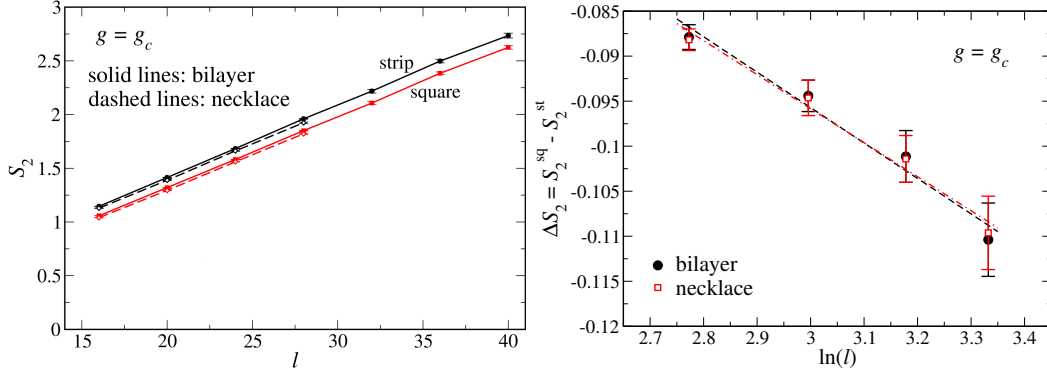


Figure 6.7.: Left panel: Second Rényi entanglement entropy of the XY bilayer and necklace models at their respective critical points. The discrepancy between the strip and the square shaped bipartition indicates the significance of corners in the subsystem. Right panel: Difference between the two entropies plotted against $\ln L_A$. A linear regression is performed in order to extract the logarithmic contribution.

Our results for the two $O(2)$ models, the XY bilayer and XY necklace model, at their critical points are plotted in Fig. 6.7. The left panel shows that the pure entanglement entropy of the square shaped bipartition is shifted by a finite negative amount from the strip shaped value for both models. This observation allows for the conclusion that a negative contribution arises from the four corners appearing in $S_2(A^{sq})$ but not in $S_2(A^{st})$. For the lowest few system sizes $L = 8, 10, 12, 14$ we plot the difference ΔS_2 against $\ln \ell$ in the right panel and perform the proposed linear fit to this data. Larger system sizes were excluded from this analysis due to their larger statistical errors on the corresponding results which are not compatible with the order of magnitude of $c \sim 0.1$. From the fit we obtain a total critical corner entanglement of $\mathcal{C}_2 = -0.0397(7)$ ($\mathcal{C}_2 = -0.037(7)$) for the bilayer (necklace) XY model, respectively. Since the square subregion has four corners, we have a critical contribution per corner with $\theta = \frac{\pi}{2}$ of $c_c = -0.010(2)$ ($c_c = 0.009(2)$) which compare well to each other within statistical uncertainty. For the XY bilayer model c_c has also been computed in Ref. [85] using a numerical linked-cluster expansion (NLCE) of density matrix renormalization group results on finite clusters. A value of $c_c = -0.0111(1)$ was obtained in this work which is in agreement with our QMC result. Since the critical points of both models belong to the same universality class ($O(2)$ in two dimensions) the agreement of their corner entanglement provides evidence for the universal behavior of this quantity — further supported by the agreement between the results of two complementary numerical methods.

The same conclusion can be drawn for the bilayer Heisenberg model — being a representative of the $O(3)$ universality class. Fig. 6.8 shows the data for different values of the coupling ratio g . We obtain a contribution of $c = -0.062(3)$, i.e. a corner entanglement of $c_c = -0.016(1)$ at criticality using the same QMC approach. Also for this model $O(3)$, our QMC result compares well to an estimate for $c_c = -0.0165$ obtained from an NLCE calculation [86].

Furthermore, also a system with a phase transition in the two-dimensional $O(1)$ symmetry class has been studied numerically, namely the transverse field Ising model. The reported result from QMC simulations is $c_c = -0.006(2)$ [108] whereas from an NLCE a value of $c_c = -0.0053$ has been obtained [105]. They agree within statistical uncertainties.

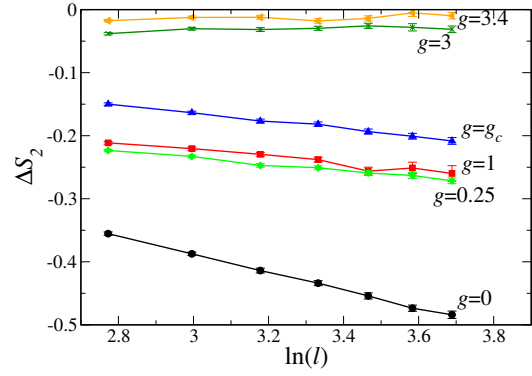


Figure 6.8.: Difference between second Rényi entropies of bipartitions with strip and square shaped subregions A plotted against $\ln L_A$. The slope of the curves is the corner entanglement and is clearly non-zero for $g \geq g_c$, where the system is gapless. Both the slope and the difference itself vanish in the limit $g \ll g_c$.

$O(N)$ model	QMC	NLCE	$N \times$ Gaussian value
TFIM ($N = 1$)	-0.006(2)	-0.0053	-0.0064
Bilayer XY ($N = 2$)	-0.010(2)	-0.0111(1)	-0.0128
Bilayer Heisenberg ($N = 3$)	-0.016(2)	-0.0165	-0.0192

Table 6.1.: Comparison of corner entanglement results of the second Rényi entanglement entropy from a single $\frac{\pi}{2}$ -corner for three $O(N)$ models. The numerical values for these interacting theories from QMC simulations and an NLCE are shown and contrasted to the value for the free theory multiplied by the number of field components.

This collection of available corner entanglement results for a number of Wilson-Fisher fixed points in $O(N)$ model leads to the quest to relate these findings among each other and to the value for a Gaussian fixed point [7] which has been derived from series expansion to be $c_c = -0.0064$. First, we note that such a comparison would have to be done by interpreting an $O(N)$ fixed point as an N -component ϕ^4 theory so that the Gaussian value must be multiplied by N . The comparison to the Gaussian fixed points reveals significant discrepancies within the statistical uncertainties as can be seen from Tab. 6.1. This observation is interpreted in Ref. [86] in the following way. Firstly, the field theories at Wilson-Fisher fixed points are non-free and therefore not the same as the free theory. Secondly, the properties of a Wilson-Fisher fixed point can be obtained by an expansion in $\varepsilon = 3 - d$ around a free theory, where d is the dimensionality. This explains why the values of c_c for

6. Lattice results in 2+1 dimensions

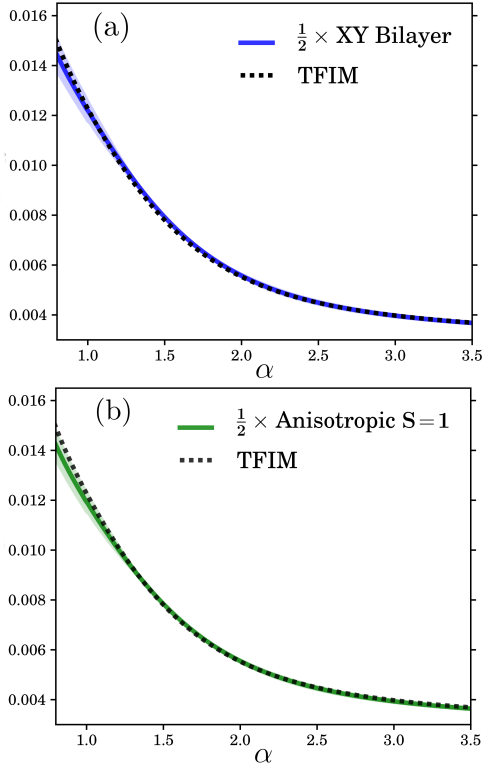


Figure 6.9.: Comparison of the corner entanglement $c_\alpha(\pi/2)$ multiplied by the number of field components N between the transverse field Ising model ($N = 1$) and the XY Bilayer (top panel) as well as a Heisenberg model with a single-ion anisotropy (bottom panel). The curves collapse for a continuous range of Rényi indices α . Figure taken from Ref. [85].

$C_T^{O(N)} \approx N C_T^{O(1)}$ [109] up to 1% suggests to examine if the ratio of critical corner entanglement and the central charge is universal for arbitrary CFTs.

interacting and free theories are close to each other, if the number of field components (N) is factored in. However, both the DMRG and QMC calculations have large finite-size effects such that the actual discrepancy between the Gaussian and the Wilson-Fisher fixed point is not exactly known. More importantly, the authors conclude that if one compares the Wilson-Fisher fixed points *among* each other, it seems that the corner entanglement of $O(N)$ critical points is approximately N times the value for the $O(1)$ critical point. This notion was further scrutinized in Ref. [85] for two $O(2)$ models, namely the spin-half bilayer XY model and a square lattice spin-one Heisenberg model with a single-ion anisotropy for a range of Rényi orders. The results for the corner entanglement are shown in Fig. 6.9 and show a striking evidence that they are twice the corner entanglement of the TFIM, as expected.

We can conclude that the investigations of spin models exhibiting a critical point hint at the connection between microscopic degrees of freedom (N) and corner entanglement. The similar dependency for central charges

6.3. Free theories

We investigate the corner entanglement for both free lattice theories — the massless free boson and the massless free Dirac fermion. Both theories can in principle be treated by the direct approach and by the NLCE, discussed above. However, it turns out that precise results are not guaranteed to be achievable in a reasonable amount of computing time due to the restriction to finite system sizes in lattice computations. We found the free Dirac fermion to be more efficiently tractable by the direct approach whereas the NLCE outperforms the direct approach for the free boson. We will make this statement precise in Sec. 6.3.1 by considering the infra-red scaling of the entanglement entropy in both theories. Following this best practice we compute the angle dependence of the corner entanglement $c_\alpha(\theta)$ in both

theories in Sec. 6.3.2 and interpret our findings in light of the predicted properties introduced in Sec. 4.2. Furthermore, we compare our lattice results to field theoretic series expansions as well as to values for other theories available from the literature. Finally, we consider the emergent duality in Eq. (4.7) between the free boson and the free Dirac fermion which has been derived in the limit of smooth angles $\theta \sim \pi$. We will check whether it holds far below this limit, namely for $\theta = \pi/2$.

6.3.1. Infra-red scaling

This preliminary study is solely intended to identify the infra-red (IR) contribution for both the free boson and the free Dirac fermion theories. On a finite-size lattice, the IR end corresponds to the total linear system size L . We hence aim at finding the largest contribution to the boundary law in Eq. (4.1) which does *not* depend on the subsystem dimension L_A/δ but on L . This is done by keeping the subsystem fixed (and thereby L_A/δ) and calculating the entanglement entropies for a range of *total* system sizes. For simplicity, the region A is chosen to be a single site and we restrict our investigation to the von Neumann entropy S_1 . We compute the entanglement using the correlators Eqs. (5.9) and (5.23) for the free boson and fermion, respectively. If A is a single site, only the correlations $\langle \phi_i \phi_i \rangle$ and $\langle \pi_i \pi_i \rangle$ on this one site need to be evaluated for the free boson. For the free Dirac fermion, where we have two fermionic degrees of freedom per site, we have a 2×2 correlation matrix for the single-site subsystem A . In both cases, we use a direct integral expression in the non-discretized field theory derived in Ref. [91] instead of applying a numerical finite-size scaling method.

For the massless boson the expressions are integrals over momentum space $\langle \phi_i \phi_i \rangle \sim \int d^2 \mathbf{k} \frac{1}{k}$ and $\langle \pi_i \pi_i \rangle \sim \int d^2 \mathbf{k} k$. On the discretized lattice the integrations have to be performed from $2\pi/L$ to $2\pi/\delta$, i.e. from the ultra-violet to the infra-red cut-off in reciprocal space. By substituting the integrand $k \rightarrow 2\pi/x$ we get $d^2 \mathbf{k} \rightarrow (1/x^4) d^2 x$. It follows that the correlators depend on L as $\langle \phi_i \phi_i \rangle \sim \mathcal{O}(1/L)$ and $\langle \pi_i \pi_i \rangle \sim \mathcal{O}(1/L^3)$. Keeping in mind that the correlators still have a leading order $\mathcal{O}(1)$ contribution from the constant L_A/δ , we conclude for the combined correlator $C_{ii} = \sqrt{\langle \phi_i \phi_i \rangle \langle \pi_i \pi_i \rangle} \sim \sqrt{Z + \mathcal{O}(1/L)} \approx Z + \mathcal{O}(1/L)$ with some constant Z . Inserting this into the formula for the von Neumann entanglement entropy, Eq. (5.12), we observe that their IR contribution is of order $\mathcal{O}(1/L)$.

Similar calculations [103] reveal that the entanglement entropy of the massless free Dirac fermion exhibits a leading IR contribution of $\mathcal{O}(1/L^3)$. This implies that finite-size effects are significantly less dominant for the free fermion compared to the free boson.

We numerically test our expectations for the IR correction to the entanglement entropy by computing the integral expressions for the correlators for both massless theories. Plotting the von Neumann entanglement entropy over the predicted IR scaling should yield a linear law as $L \rightarrow \infty$. This is clearly confirmed by our results shown in Fig. 6.10. For the free boson we impose *open* boundary conditions in our computation in agreement with the prerequisite of the NLCE method. Fully anti-periodic boundary conditions or a combination of anti-periodic and periodic boundary conditions in one dimension are expected to exhibit the same behavior.

6. Lattice results in 2+1 dimensions

Only if the boundary conditions are fully periodic, the entanglement entropy diverges due to its logarithm in the definition and the existence of the zero mode $k_x = k_y = 0$ in Eq. (5.16). We have added the von Neumann entanglement entropies for the massive free boson with masses $0 < m \leq 0.5$ which demonstrates how the IR correction of $\mathcal{O}(1/L)$ arises as $m \rightarrow 0$. For a finite mass the entanglement entropy approaches a constant once the system size L exceeds the finite correlation length $\xi \sim m^{-1}$. The inset of Fig. 6.10 shows that the entanglement entropy of the free Dirac fermion on a fully anti-periodic lattice becomes linear in $1/L^3$ as $L \rightarrow \infty$.

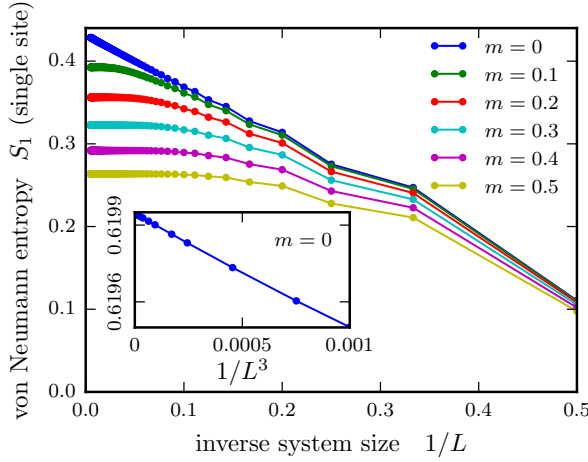


Figure 6.10.: The entropy S_1 for free bosons as a function of $1/L$ for the case where region A is a single site and the lattice has open boundary conditions (the same as the boundary conditions used in the NLCE). Similarly, the inset shows the single-site entropy for the massless fermion and illustrates that the leading IR contribution is $\mathcal{O}(1/L^3)$.

compute the corner entanglement of the free boson. In principle, the NLCE works just as well for the free Dirac fermion but in practice the direct approach is much more efficient for this theory.

We conclude from this examination how we match the two numerical approaches introduced in Sec. 6.1 with the two free theories: The direct approach is hampered for the free boson due to the non-negligible $\mathcal{O}(1/L)$ correction, thus necessitating its inclusion in the fit. An additional parameter in the least-squares fit significantly increases the needed number of data points. Therefore we do not apply the direct approach to the free boson but only to the free Dirac fermion, where the $\mathcal{O}(1/L^3)$ correction is negligible. On the other hand, the NLCE proves to cancel the $\mathcal{O}(1/L)$ correction by its design. We use it to

6.3.2. Angle dependence

In order to elucidate the angle dependence of corner entanglement in the free theories we choose seven angles that pixelate most naturally on a square lattice and compute their contribution. As illustrated in Fig. 6.2 these angles feature a slope of $\pm\frac{1}{2}$, ± 1 , ± 2 or zero of one of their sides. The actual angle is then obtained by taking the arctangent of the slope (except for a slope of zero, where the corresponding angle is $\theta = \pi/2$) and transposing it into the range $[0, \pi]$. We compute the corner entanglement $c_\alpha(\theta)$ for Rényi entropies of order $\alpha = 1, 2, 3, 4$ using the methods described in Sec. 6.1 combined with the formulae for the groundstate correlators given in Chapter 5. Our data from lattice models are compared to the results of the two field theory methods (Sec. 4.3), the *truncated series* and the *combined ansatz*.

As discussed, we employ the direct approach for Dirac fermion and the NLCE for the free boson lattice theory. At first we demonstrate that the raw output of the methods behaves well and is suitable for the fitting and extrapolation that yields $c_\alpha(\theta)$ using the example of the von Neumann entropy ($\alpha = 1$) and a right-angled corner ($\theta = \pi/2$). For the free boson (Fig. 6.11a) we observe that the property P of the NLCE behaves nearly perfectly logarithmic in the cluster order. This provides evidence that the scheme in Fig. 6.4 indeed extracts the corner contribution although the cluster expansion is restricted to rectangular clusters, as discussed above. If we perform a linear fit of P to $\ln L$ the slope is the corner entanglement. Since we are limited to finite cluster sizes, we carry out a *second extrapolation* of our so-obtained estimates of $c_\alpha(\theta)$ in fixed-size fitting intervals $[L_c^{\min}, L_c^{\min} + \Delta L]$. We take L_c^{\min} as the label of the corresponding fitted $c_\alpha(\theta)$ and extrapolate these value pairs to the thermodynamic limit by fitting the $c_\alpha(\theta)$'s linearly to $1/L_c^{\min}$. It is shown in the inset of Fig. 6.11a that this second extrapolation is well-justified as the data points indeed lie on a straight line. For the free fermion theory, our raw data are the full

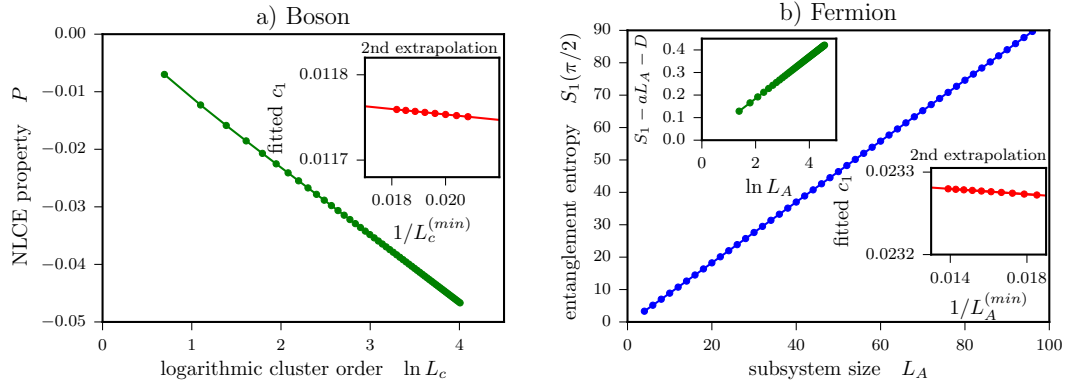


Figure 6.11.: Illustration of the extrapolations from finite-size lattice results. Left Panel: Output of the NLCE for the free boson plotted against $\ln L$. The inset shows the well-behaved second extrapolation. Right Panel: Total Rényi entropy of the free Dirac fermion. The top left inset shows the this data reduced by the fitted boundary term and the constant and plotted against $\ln L_A$ — yielding a straight line. The behavior of the second extrapolation is shown in the bottom right inset.

entanglement entropies, shown in Fig. 6.11b. We first verify that our least-squares fit of the data to Eq. (6.1) yields a significant logarithmic contribution. To do this, we subtract the fitted linear and constant terms from the entanglement entropy and plot the result against $\ln L_A$, see the top left inset of Fig. 6.11b which clearly identifies a logarithmic dependence. Furthermore, we also perform a second extrapolation of fitted corner entanglement estimates for fitting ranges $[L_A^{\min}, L_A^{\min} + \Delta L]$. Analogous to the boson case, we can convince ourselves by considering the bottom right inset of Fig. 6.11b that this step is justified.

Having gauged the numerical methods we now turn to their application on our corner entanglement analysis. We first consider the corner entanglement $c_1(\theta)$ of the von Neumann entropy for our selection of angles, plotted in Fig. 6.12. In Eq. (4.6) we have seen that in the smooth limit $c_1(\theta)$ is proportional to the central charge C_T of the stress-tensor of the CFT. Therefore, we normalize $c_1(\theta)$ by this constant and hence plot the presumed universal ratio. The agreement between the lattice

6. Lattice results in 2+1 dimensions

results and the truncated series is satisfying at large angles $\theta \geq \pi/2$ but a deviation emerges as decreasing θ towards $\arctan 1/2 \approx 0.46$, where it achieves 6% (9%) for the boson (fermion), respectively. In contrast, this deviation amounts to only 1% for both theories between the lattice results and the combined ansatz results at this angle. We also confirm that the universality of $c_1(\theta)/C_T$ holds between the free boson and the Dirac fermion theories even below the smooth limit for $\theta \gtrsim \pi/2$ because the data collapse. The exact numbers can be found in Tables 6.2 and 6.3 for all angles.

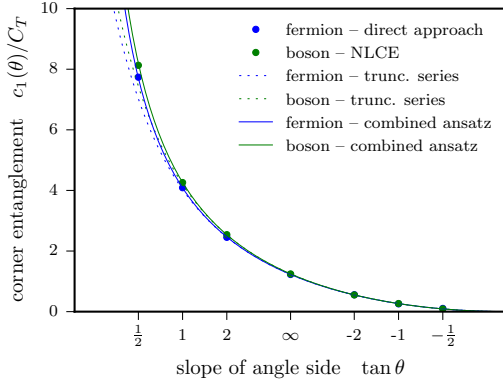


Figure 6.12.: Angle dependence for the von Neumann ($\alpha = 1$) entropy. The numerical lattice data points are represented by the blue and green circles. Series expansion results from the truncated series, Eq. (4.8), are shown by the dashed lines and from the combined ansatz, Eq. (4.9), by the solid lines. In both cases series expansions the highest order in $(\theta - \pi)$ included is 16 for the boson and 14 for the fermion.

Extending our examination to additional Rényi indices $\alpha = 2, 3, 4$ we first compare our findings to available numerical results from the literature. For the free boson, Refs. [7, 104] find $c_1^b(\pi/2) = 0.02366$, $c_2^b(\pi/2) = 0.0128(2)$, $c_3^b(\pi/2) = 0.0100(2)$, in excellent agreement with our results, see Tab. 6.2. Further, Ref. [104] also reports $c_4^b(\pi/2) = 0.0086(2)$, which significantly deviates from both our lattice (0.0092) and combined ansatz (0.00946) results. Due to their consistency we believe that our results are more accurate. One additional comparison can be made for $\alpha = 1/2$, for which Ref. [110] obtains $c_{1/2}^b(\pi/2) = 0.058(2)$, in agreement with our lattice results 0.058. For the Dirac fermion we have only $c_1^f(\pi/2) = 0.02329$ [84] in the literature, which agrees very well with our value (Tab. 6.3). We have summarized our results for $\alpha = 1, 2, 3, 4$ for both theories in Fig. 6.13.

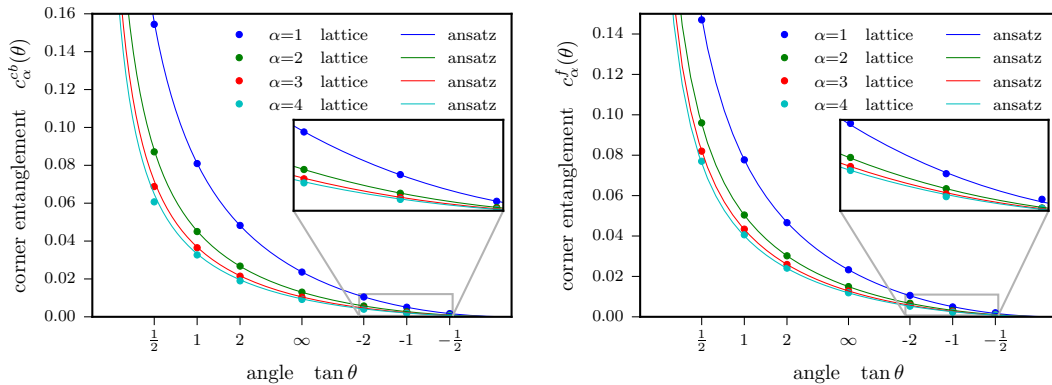


Figure 6.13.: Corner entanglement for Rényi entropies for the free boson (left panel) and the Dirac fermion (right panel). The numerical data is compared to the combined ansatz, Eq. (4.9), at $M = 8$ (7) for the boson (fermion).

Since the first smooth limit coefficients σ_α as well as the sharp limit coefficients

κ_α have been computed for $\alpha = 1, 2, 3, 4$ in Ref. [90] we can try to obtain a unified picture of the functional dependence of $c_\alpha(\theta)$ on the angle θ . In particular, we divide the corner entanglement by σ_α in a first approach and plot the result for different α , see the left panel of Fig. 6.14. Surprisingly, we observe an almost complete collapse of the data for different Rényi entropies in both the lattice numerics and the combined ansatz. It is particularly convincing for angles $\theta \geq \pi/2$ which implies the unexpected insight that the first smooth limit coefficient σ_α alone, i.e. the first-order expansion of $c_\alpha(\theta) = \sigma_\alpha \cdot (\theta - \pi)^2$, essentially determines the corner entanglement far beyond the smooth limit. For $\theta < \pi/2$ a small deviation of the curves becomes apparent. Another normalization, namely a division by κ_α (see Eq. (4.5)), is more appropriate in this limit and yields a striking collapse of the different Rényi entropies, plotted in the right panel of Fig. 6.14.

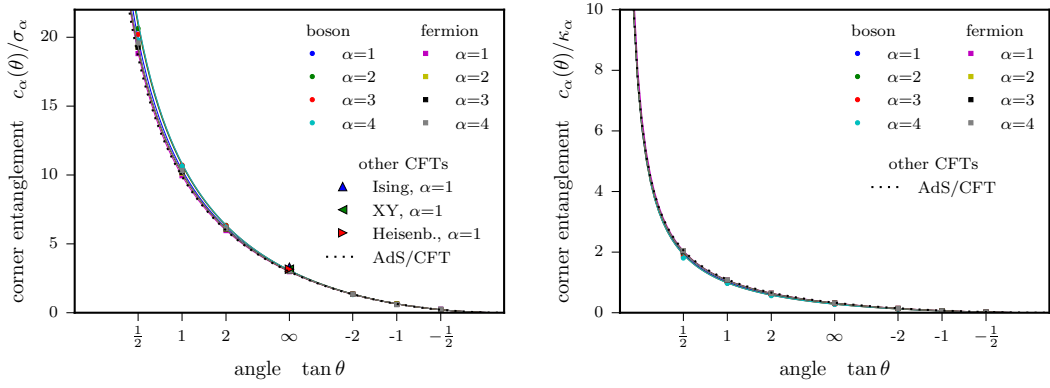


Figure 6.14.: Collapsing the corner entanglement after dividing $c_\alpha(\theta)$ by the smooth limit coefficient σ_α (left panel). The solid lines are obtained using field theory, Eq. (4.9), while the markers are lattice data. We also show the $\pi/2$ data for the $O(N)$ Wilson-Fisher QCPs with Ising, XY and Heisenberg symmetry. The AdS/CFT result corresponds to a strongly-interacting CFT.[87] The solid lines show the combined ansatz. Another way to collapse the data is to divide $c_\alpha(\theta)$ by the sharp limit coefficient κ_α (right panel), which achieves a better agreement for $\theta < \pi/2$.

The *lattice* columns of Tabs. 6.2 and 6.3 contain all the numerical data points plotted in this discussion. It is difficult to rigorously estimate their confidence interval as they are output by fitting procedure that allow for various options. The general limitation of the accuracy is due to the restricted sizes of the lattices for computational reasons. Hence, we expect our data to exhibit systematic uncertainties. We show the digits that we found to be robust against variations in the fitting and extrapolation ranges and estimate that the last digit contains the uncertainty. For smooth angles at $\alpha = 3, 4$ the accuracy is only two digits whereas for $\theta = \pi/2$ we have up to four digits.

6.3.3. Duality

The duality between the free boson⁴ and the Dirac fermion in Eq. (4.7) was derived for the smooth limit of $\theta \rightarrow \pi$. In this section, we study in how far this duality holds

⁴To be precise, we mean the complex boson, corresponding to two real scalar bosons.

$\tan \theta$	$\alpha = 1$			$\alpha = 2$			$\alpha = 3$			$\alpha = 4$		
	series	ansatz	lattice	series	ansatz	lattice	series	ansatz	lattice	series	ansatz	lattice
1/2	0.1453	0.156	0.154	0.08208	0.0881	0.087	0.06686	0.0718	0.069	0.06041	0.0649	0.061
1	0.08037	0.0810	0.0809	0.04494	0.0453	0.0450	0.03652	0.0368	0.0365	0.03296	0.0332	0.033
2	0.04816	0.0482	0.0483	0.02668	0.0267	0.0268	0.02163	0.0217	0.0215	0.01952	0.01953	0.019
∞	0.02367	0.0237	0.0236	0.01297	0.0130	0.0130	0.01049	0.01049	0.0104	0.009459	0.009459	0.0092
-2	0.01051	0.0105	0.0105	0.005718	0.00572	0.00572	0.004617	0.004617	0.00454	0.004160	0.004160	0.0040
-1	0.005040	0.00504	0.00507	0.002733	0.00273	0.00272	0.002205	0.002205	0.00218	0.001986	0.001986	0.0019
-1/2	0.001705	0.00171	0.00170	0.0009226	0.000923	0.000923	0.0007439	0.0007439	0.000747	0.0006700	0.0006700	0.00067

Table 6.2.: **Boson:** Finite angle results for $c_\alpha(\theta)$ for the boson at Rényi index $\alpha = 1, 2, 3, 4$. The series and ansatz (4.9) results are obtained using field theory, whereas the lattice results are obtained numerically using NLCE. The truncated series result includes terms up to $(\theta - \pi)^{16}$, and can be taken as a lower bound for $c_\alpha(\theta)$.

$\tan \theta$	$\alpha = 1$			$\alpha = 2$			$\alpha = 3$			$\alpha = 4$		
	series	ansatz	lattice	series	ansatz	lattice	series	ansatz	lattice	series	ansatz	lattice
1/2	0.1334	0.146	0.147	0.08691	0.0955	0.096	0.07475	0.0821	0.082	0.06921	0.0760	0.077
1	0.07654	0.0776	0.0777	0.04965	0.0503	0.0504	0.04266	0.0433	0.0434	0.03949	0.0400	0.0406
2	0.04672	0.0468	0.0466	0.03017	0.0302	0.0302	0.02589	0.0259	0.0259	0.02396	0.02400	0.0241
∞	0.02329	0.02329	0.02329	0.01496	0.01496	0.01496	0.01282	0.01282	0.01282	0.01185	0.01185	0.01189
-2	0.01043	0.01043	0.0106	0.006669	0.006669	0.00674	0.005710	0.005710	0.00571	0.005278	0.005278	0.00527
-1	0.005022	0.005022	0.0049	0.003204	0.003204	0.0032	0.002742	0.002742	0.0026	0.002534	0.002534	0.0023
-1/2	0.001703	0.001703	0.002	0.001085	0.001085	0.001	0.0009282	0.0009282	0.001	0.0008579	0.0008579	0.001

Table 6.3.: **Fermion:** Finite angle results for $c_\alpha(\theta)$ for the Dirac fermion at Rényi index $\alpha = 1, 2, 3, 4$. The series and ansatz (4.9) results are obtained using field theory, whereas the lattice results are obtained numerically using the direct method. The truncated series includes terms up to $(\theta - \pi)^{14}$, and can be taken as a lower bound for $a_\alpha(\theta)$.

for general angles θ , i.e.

$$\alpha^2 c_\alpha^f(\theta) \stackrel{?}{=} c_{1/\alpha}^b(\theta). \quad (6.10)$$

We first consider the special situation of $\alpha = 1$, i.e. the von Neumann entanglement entropy. If the duality was satisfied for all angles θ , Eq. (6.10) would demand that the corner entanglement of the complex boson and the Dirac fermion are equal for $\alpha = 1$. Fig. 6.12 can be regarded as a plot of this duality and reveals that it holds for angles $\theta \in [\pi/2, \pi]$. This is in accordance with the equality of the smooth limit coefficient $\sigma_1^b = \sigma_1^f = 1/128$ as computed in Ref. [88]. On the other hand, the emergent discrepancy between the complex boson and the fermion curve in this plot indicates a breakdown of the duality in the limit $\theta \rightarrow 0$. Also the sharp limit coefficients $\kappa_1^b = 0.0794$ and $\kappa_1^f = 0.0722$ clearly differ [91] which confirms this observation.

For general Rényi index α we test how far the duality holds at the natural lattice angle $\theta = \pi/2$ — being on the verge of the breakdown for $\alpha = 1$. We plot both sides of Eq. (6.10) for $\alpha \in [\frac{1}{5} \dots 5]$ in the left panel of Fig. 6.15. Since in the region of $\alpha < 1$ this plot is not very informative we make a second plot where $\alpha \rightarrow 1/\alpha$ — showing the same data differently resolved (right panel of Fig. 6.15). We find that the duality does approximately hold even at $\theta = \pi/2$. Also, the data are in agreement with the corner entanglement for $\alpha \rightarrow \infty$ computed in Ref. [90] to be $a_\infty(\pi/2) = 0.0093(0.00715)$ for the fermion (boson), respectively.

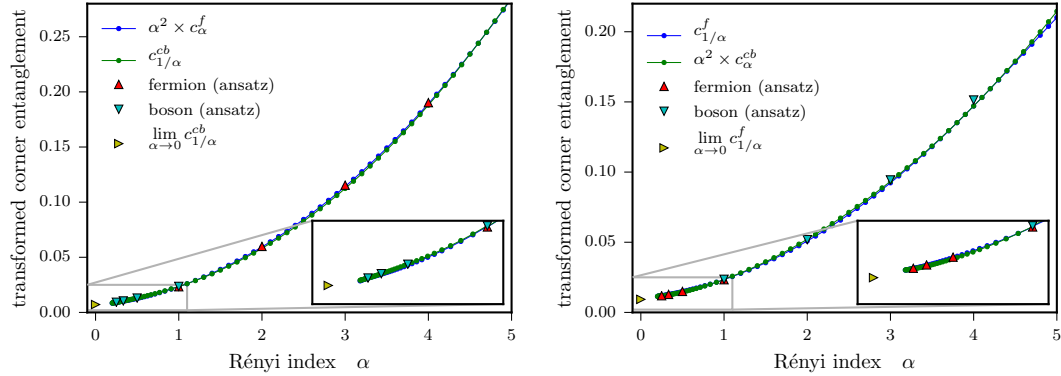


Figure 6.15.: Testing the boson-fermion duality at $\theta = \pi/2$. The data for fermions has been obtained by a fit to the boundary law using an exact diagonalization of the subsystem correlation matrix. For bosons, the NLCE was used. Both plots display the same data with different α prefactors, in order to resolve clearly the duality for both sides of $\alpha = 1$.

The computation of the values of the Rényi entropies involves a sum over many eigenvalues raised to the power of α . This causes a reduction of the accuracy of the result for $\alpha < 1$ due to the limited floating point precision. As an example, let us consider the computation of the $\frac{1}{4}$ -Rényi entropy. In standard floating point numerics, the eigenvalues entering the entropy formulae have a precision of 16 digits. After taking the $\frac{1}{4}$ th power this precision is reduced to four digits. The accuracy of the Rényi entropy is possibly further diminished by the many elements in the sum (5.11). Further, these values of S_α are relied upon in the subsequent procedure of the NLCE or the finite-size fit of the direct approach. As a consequence, it

6. Lattice results in 2+1 dimensions

is difficult to obtain an asymptotic behavior for the corner entanglement from the numerical procedures if $\alpha < 0.5$.

Therefore we apply arbitrary precision numerics for Rényi entropies with $\alpha < 1$. This involves that the algebraic routines needed in the computation, e.g. the diagonalization, are significantly slower than their standard precision counterparts. The finite system sizes or cluster orders achievable within a comparable computing time are hence considerably smaller. Since this problem does not occur for $\alpha \geq 1$ we apply standard floating point operations here, such that the data in Fig. 6.15 originate from two different calculations: high precision but lower order for $\alpha < 1$ and standard precision but higher order else. A slight deviation becoming apparent near $\alpha = 5$ in the right panel of Fig. 6.15 is probably due to this issue. Generally, we cannot rigorously quantify the discrepancy of the duality because our data are afflicted with potential systematic errors from the finite size systems, the finite precision, and the various options in the fitting procedure. Nevertheless, we can conclude that the duality is robust beyond the smooth limit, in particular for $\theta = \pi/2$.

7. Summary

The essence of this Part of the thesis is that logarithmic contributions to the bipartite entanglement entropy constitute universal signatures of criticality in a quantum many-body system. This perspective is compatible and intertwined with the classification of critical phenomena via universal critical exponents in statistical physics. Moreover, since a complementary description of critical points is generically provided by conformal field theories, a connection between the logarithmic contribution and the corresponding CFT is suggestive.

We first established the technical operation to induce logarithmic contributions in the entanglement entropies, namely choosing the subsystem A of the bipartition to have corners. Consequently, we denoted the coefficient of the logarithmic contribution as corner entanglement. After heuristically motivating the reason for this effect of corners we discussed properties of corner entanglement, in particular its dependence on the opening angle of the corner. Series expansions of the corner entanglement in the opening angle open up field theoretic approaches to approximate the corner entanglement. We elucidated the analogy between the corner coefficient of a critical many-body Hamiltonian and the central charge C_T of its underlying CFT. To clarify the role of the central charge we outlined why it counts degrees of freedom of low-lying excitations — seemingly a feature of the corner entanglement as well.

The main focus of the investigations carried out in this Part has been put on the computation of corner entanglement directly in free field theories. We first introduced the free boson and the free Dirac fermion theories in $2 + 1$ dimensions. Since our numerical technique is based on discrete Hamiltonians we carefully explained how these theories are transferred from the continuum to the lattice. The free boson is basically a theory of a grid of harmonic oscillators; its lattice variant is obtained by introducing a finite lattice spacing. In contrast, a more elaborate route has to be followed for the lattice discretization of the free Dirac fermion.

The von Neumann and Rényi entanglement entropies can subsequently be computed exactly in an elegant way from groundstate correlators of the lattice Hamiltonians. We derived these formulae explicitly and related the computational effort to the size of subsystem A of the bipartition.

Before we could obtain results for the free field theories but also for interacting spin models we had to apply a strategy for the extraction of the logarithmic coefficient from the total entanglement entropies. We presented three such computation schemes — a direct fit approach, the numerical linked-cluster expansion and the increment trick of quantum Monte Carlo simulations. All of them are naturally based on finite-size scalings of entanglement entropy results for a range of system sizes. These strategies are adaptable to corners with opening angles θ other than $\pi/2$. We showed how pixelation of one side of the angle enables the computation

7. Summary

of corner entanglement for angles θ that naturally pixelate on the square lattice, that is, $\tan \theta \in \mathbb{Q}$.

We presented our results for interacting theories, specifically, for the Heisenberg bilayer, the XY bilayer and the XY necklace model at their respective critical point. Quantum Monte Carlo simulations were applied in order to compute the corner entanglement for the right-angled corner. Comparing and combining our results with the findings of other works using complementary methods we can conclude that corner entanglement at Wilson-Fisher fixed points in $O(N)$ universality classes scale with N . As expected, they do not agree with the corner entanglement of Gaussian fixed points for theories with the same number N of field components. These findings provide evidence for the notion that corner entanglement measures degrees of freedom (N) just like the central charge C_T of CFTs.

Since the central charge is known exactly for the free boson and free Dirac fermion in $2 + 1$ dimensions it is appropriate to compute the corner entanglement for these free theories on the lattice and relate them to the central charge. We first established our numerical setup by examining the infrared scaling of the entanglement entropy which determined our matching of method and theory, in particular, we used the direct approach for the free Dirac fermion and the NLCE for the free boson. Further, we computed the von Neumann entropy for both theories for a selection of opening angles and verified the universal ratio between corner entanglement $c_1(\theta)$ and the central charge up to an opening angle of $\theta = \pi/2$. This is surprising as the analytical prediction of the universality of this ratio holds only up to the leading order $(\theta - \pi)^2$ of $c_1(\theta)$. Subsequently, we computed the corner entanglement for Rényi entropies $\alpha = 2, 3, 4$ and compared them to field theoretic series expansions — yielding very good agreement. These data for both theories and different Rényi orders could be collapsed on to nearly a single curve by dividing them by the smooth (sharp) limit coefficient σ_α (κ_α) which remarkably underlines the quality of our data and the equivalence of the angle dependence for all considered $c_\alpha(\theta)$.

Finally, we shed light on a duality between the free boson and the free Dirac fermion for reciprocal Rényi indices by testing this relation for $\theta = \pi/2$. It indeed holds within numerical uncertainty up to this angle — far away from the smooth limit $\theta \rightarrow \pi$ — for which the duality has been derived.

As a general conclusion, we can state the robustness of corner entanglement for various critical theories, Rényi indices and corner opening angles with regard to its ability to universally characterize criticality and quantify degrees of freedom of low-lying excitations.

Part III.

Topological order

8. Topological entanglement entropy

The macroscopic observation that matter can appear in qualitatively different states or phases called for a theory that explains and categorizes phases and transitions between them. For a long time, the Landau theory [1] of symmetry breaking in the quantum state was assumed to describe all possible quantum phase transitions. In this Landau paradigm a *local order parameter* is the essential concept which characterizes the transition by acquiring a non-zero value only in the symmetry-broken phase. However, new phases of matter were discovered, for example the fractional quantum Hall effect (FQH) [9, 111], in which different phases can have *identical* symmetry. Hence, these phases cannot be distinguished by symmetry breaking — making it impossible to find a suitable local order parameter. A new kind of order beyond the Landau paradigm was proposed [8] where, instead of an order parameter, new quantum numbers such as the ground state degeneracy characterize the phase of matter. This concept is named *topological order* [112] — inspired by its astonishing consequence that the topology of the space on which the quantum system resides determines the degeneracy of the ground state. Also the states of the FQH effect can be identified by their differing topological order [113].

In this Chapter we elucidate the relation of topological order and entanglement entropy. We first point out in Sec. 8.1 that long-ranged entanglement is the feature that induces topological order in a quantum many-body system. Moreover, we will see that entanglement entropies are able to detect one aspect of topological order via a constant correction in their boundary law. In Sec. 8.2, we present sets of bipartitions that allow for the computation of this topological part in the entanglement entropy and thereby motivate the definition of a *topological entanglement entropy*. At the beginning of this thesis we have amply discussed that the detection of entanglement via entropies is made possible by mapping entanglement to classical mixedness. This insight reveals that for a particular class of systems the combinatorial constraints leading to the constant correction in the entanglement entropy can be reproduced in a purely classical statistical-mechanics context. In Sec. 8.3, we take this perspective by introducing a classical analogue of the entanglement entropy. Despite the fact that the boundary law becomes a volume law for a classical system, it has a very similar constant topological part which will be the object of study in the subsequent Chapters.

8.1. Long-ranged entanglement

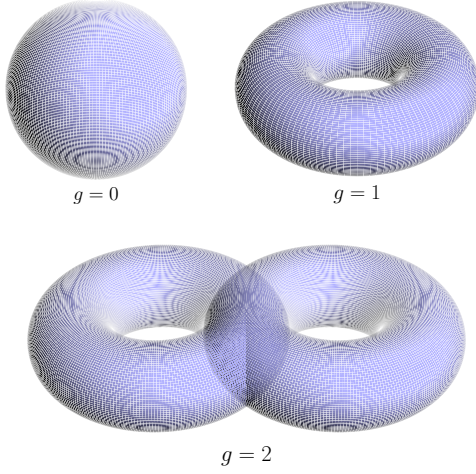


Figure 8.1.: Examples for spaces of different topology, characterized by the genus g . The ground state degeneracy of topologically ordered systems depends on g , e.g. it is 4^g for the toric code model (Chapter 9).

This discussion of (intrinsic) topological order is inspired by the review articles in Refs. [57, 114]. Topological order is a property of the ground state and the nature of excitations of a quantum phase. It is manifested in a dependency of the ground state degeneracy on the topology, more specifically, on the genus g of the surface on which the associated Hamiltonian is defined, see Fig. 8.1 for some examples. This degeneracy cannot be lifted by local perturbations. The presence of ground state degeneracy is a macroscopic description¹ but not the origin of topological order [115]. The low-energy excitations of such ground states are described by the afore elaborated concept of topological quantum field theories (TQFT) [116]. A local order parameter

characterization is not available which implies that in general no long-ranged correlations of any physical observable are present in the state. However, the relation between topology and degeneracy as a property of the ground state indicates that there must be some kind of a global structure. This structure is established via *long-ranged entanglement* [117]. An entanglement entropy analysis of topologically ordered states is hence an obvious endeavor.

Characterizing topological order as a property of the ground state is to some extent unsatisfactory because it depends on the specific details of the interactions and is hence not universal. We therefore consider instead how entanglement entropies of an arbitrary bipartition provide signatures of topological order. In Sec. 2.2.3 we have presented the intuitive picture for why a boundary law is expected by assuming that entanglement is created between neighboring sites via interactions of the (local) Hamiltonian. This insight needs to be refined here because we expect a local Hamiltonian to create *non-local* entanglement. An illustrative picture of ‘dancing patterns’ [114] helps understanding the wanted mechanism: In the ground state all local interactions seek for minimizing the energy and thereby impose local ‘dancing rules’ on the degrees of freedom. These rules lead to global patterns which are interpreted as quantum fluctuations corresponding to long-ranged entanglement. Nevertheless, we consider the establishment of long-ranged entanglement between distant particles to happen in a sequential way via chains of direct neighbors. Hence, the procedure of cutting the system into two parts and tracing out one part still produces an amount of mixedness found to be proportional to the boundary size. But

¹A second consequence of topological order is the existence of non-Abelian geometric phases [112].

the enforced existence of global patterns suggests that bipartite entanglement entropies perceive an *additional* piece of information about subsystem A from tracing out part B . To put it differently, the individual contributions to the entropy of all cut interactions along the boundary are not independent. This manifests itself through a *reduction* of the boundary term by a constant amount γ [58, 59], originating from the macroscopic entanglement. For a d -dimensional system with a subsystem A of linear size L_A the generalization of this statement to Rényi entropies reads

$$S_\alpha(A) = \mathcal{A}L_A^d - \gamma + \dots, \quad (8.1)$$

with further subleading terms vanishing in the thermodynamic limit, i.e. scaling at most as L_A^{-1} . In general, γ could depend on the Rényi order α . We will, however, ignore this subtlety because in our context the amount of information gained by the additional knowledge about the boundary is quantified to the same value by all Rényi entropies. The existence of such a constant correction γ has an immense value: It *identifies* the presence of topological order in the ground state of a Hamiltonian and is often the only available quantity which does this. This seminal result has been established for the toric code model (Chapter 9) in Ref. [118]. Moreover, γ is a universal quantity which also *detects* the type of topological order by the so-called total quantum dimension \mathcal{D} of its elementary excitations, $\gamma = \ln \mathcal{D}$. Motivated by its inducing phenomenon, γ is referred to as *topological entanglement entropy* [58, 59].

We comment on a potential pitfall — the false conclusion that long-ranged entanglement is less or weaker in a physical sense than local entanglement: The reduction refers not to absolute values of the entropy but only to the boundary term which is intimately related to the technical definition of entanglement entropies.

So far, the presentation of the phenomenon of topological order has been rather abstract and general. We want to take the perspective of string-net condensates [120] in order to gain a more concrete and graphic perception of topological order. The formalism of string-net condensates is suitable for a particular class of topological order, among them discrete gauge theories to which the toric code model belongs. String-nets can be understood as lattice mod-

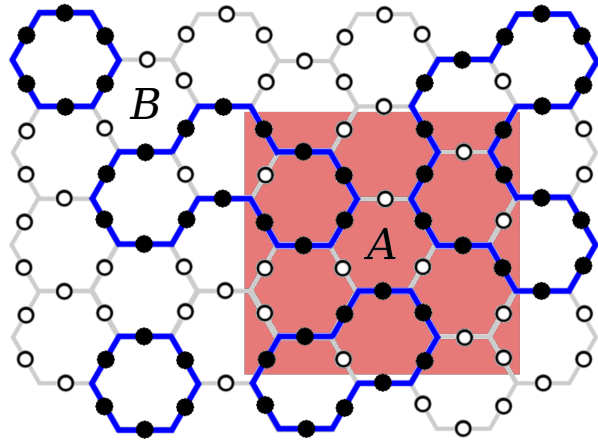


Figure 8.2.: String-nets are a representation of models with degrees of freedom located on the edges of the lattice. In this example we have \mathbb{Z}_2 particles (with orientation \circ and \bullet) on a honeycomb lattice. Strings are formed by the edges which have an \bullet -particle via rules imposed on the vertices. An entanglement entropy reduction for a bipartition into A and B can be understood from constraints on the number of strings which cross the boundary of A and thereby provide additional information. This picture is adapted from Ref. [119].

8. Topological entanglement entropy

els where the *edges* carry degrees of freedom, see Fig. 8.2. A particular set of rules (Fig. 8.3) at the vertices of the lattice constrains possible values of the adjacent degrees of freedom. These rules are imposed by the Hamiltonian at zero temperature and correspond to the ‘dancing rules’ of the vertices above. A global pattern of strings of edges with identical orientation is one aspect of the resulting long-ranged order. The second aspect is that the ground state is a superposition of all possible string states — therefore called a string-net *condensate*.

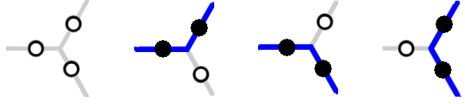


Figure 8.3.: Set of rules on the vertices inducing the string-net in Fig. 8.2.

In the specific example of the string-net condensate depicted in Figs. 8.2 and 8.3, spin-half degrees of freedom are located on the edges. Only closed loops are allowed by the rules which corresponds to the models we examine in this thesis. We will restrict our discussion to such *loopgases*². They provide a very nice understanding of the origin of the entropy reduction by γ in Eq. (8.1). We observe that the number of loops crossing the boundary between part *A* and *B* must be even, since no open strings are allowed. Considering the degrees of freedom at the cut edges along the boundary we see that each of them can take two values, up or down. The number of possible combinations thereof is precisely what the bipartite entanglement entropy measures. However, given that we have measured all edges except for the last one, we already know the state of the last one with certainty due to the constraint of an even number of loop passages across the boundary. The entropy is therefore $\ln 2^{\ell-1} = \ell \ln 2 - \ln 2$ for a boundary length ℓ and \mathbb{Z}_2 degrees of freedom. Hence we have $\gamma = \ln 2$ in this case due to the knowledge that only closed loops are allowed in the ground state.

8.2. Addition schemes

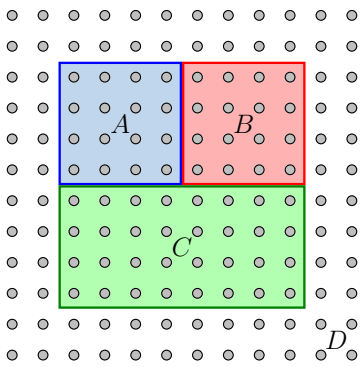


Figure 8.4.: Compact representation of a scheme inspired by Kitaev and Preskill.

The notion of topological entanglement entropy opens up a way to detect topological order in a given Hamiltonian of a many-body system. But provided we have numerical tools to compute the entanglement entropy of the ground state it is still not a trivial task to extract the topological part γ from it. One approach would be to determine the entanglement entropy for a range of subsystem sizes L_A and perform a linear regression to these data. We would obtain γ as the constant coefficient from this regression. Such a method requires many entanglement entropy computations of sufficiently large boundary sizes in order to get one value for γ .

A better technique is proposed in the two pub-

²More generally, string-nets are configurations for non-Abelian topological quantum field theories (TQFT) while loopgases represent Abelian TQFTs [119].

lications in which the concept of topological entanglement entropy has been introduced [58, 59]. The authors design *schemes* consisting of several bipartitions of the same total system and summation formulae which enable a direct extraction of γ . We present the two alternative schemes, the Kitaev-Preskill [58] and the Levin-Wen [59] construction. Both schemes have in common that they eliminate all contributions of the entanglement entropy which are induced by geometric elements of the bipartition, such as volume, boundaries and corners.

The approach followed by Kitaev and Preskill is to define three parts A , B and C similar to the ones shown in Fig. 8.4 which are combined in all possible ways to form one subsystem of a bipartition. For each of the seven combinations the entanglement entropy is computed and the results are added and subtracted according to³

$$\begin{aligned} -S_{\alpha,\text{top}} = & S_{\alpha}(A) + S_{\alpha}(B) + S_{\alpha}(C) \\ & - S_{\alpha}(AB) - S_{\alpha}(AC) - S_{\alpha}(BC) \\ & + S_{\alpha}(ABC). \end{aligned} \quad (8.2)$$

Since all subsystems created that way are topologically equivalent in the sense that they are simply connected, we expected all corresponding entanglement entropies to exhibit the same constant contribution, such that $S_{\alpha,\text{topo}} = \gamma$. We note, that in the specific example given in Fig. 8.4, some combinations are equivalent, specifically A and B , AC and BC , AB and C . Hence only four instead of seven computations have to be made. However, this construction holds a potential deficiency: The bipartitions AC and BC are concave with a corner of opening angle $3\pi/2$ which only appears with a minus sign in Eq. (8.2). This conflicts with the general idea of this scheme to eliminate all contributions from corners and boundaries. Due to the symmetry of corner contributions about π (Sec. 4.2) we can assume them to be annihilated by the right-angled corners of A and B at the same location, appearing with plus signs in the scheme⁴.

In the second proposal, Levin and Wen exploit that the constant correction to the boundary law depends also on the topology of the subsystem. To wit, the additional information provided by the global structure concerns *every closed* boundary of the bipartition. If one subsystem is disconnected, more than one closed boundary is present. In terms of the string-net perspective, the number of loops across each closed boundary must be even. Hence, the boundary law undergoes a constant reduction *per* closed boundary. The Levin-Wen scheme consists of the four bipartitions shown in Fig. 8.5. Subsystems A_1 and A_4 have two closed boundaries and therefore both have a topological term of two units in the boundary law as opposed to one unit γ for A_2 and A_3 . The extraction of the one-boundary γ is hence achieved by

$$S_{\alpha,\text{top}} = \frac{1}{2} (-S_{\alpha}(A_1) + S_{\alpha}(A_2) + S_{\alpha}(A_3) - S_{\alpha}(A_4)). \quad (8.3)$$

³We deviate from the original work [58] in the sign in the definition of S_{top} and hence define the topological entanglement entropy to be a positive quantity, in accordance with Levin and Wen.

⁴There are situations [121] in which this annihilation does not work and thereby singularities due to the concave corners appear in $S_{\alpha,\text{top}}$.

8. Topological entanglement entropy

In the example of a \mathbb{Z}_2 string-net condensate, we have $\gamma = 2 \ln 2$ for $A_{1/4}$ and $\gamma = \ln 2$ for $A_{2/3}$. We note that A_2 and A_3 are equivalent and therefore only three different entanglement entropy computations have to be carried out in order to obtain γ . In the original work [59], an additional interpretation of the scheme is given: The respective geometric differences of the bipartitions in $(S_\alpha(A_2) - S_\alpha(A_1))$ as well as in $(S_\alpha(A_3) - S_\alpha(A_4))$ are identical, namely the connecting bar at the bottom. Thus, $S_{\alpha, \text{top}}$ measures the entropic difference between the two connections at the bottom which should have the same effect if only local entanglement was present. On the other hand, a non-zero value of $S_{\alpha, \text{top}}$ indicates that the completion of an annular region ($A_3 \rightarrow A_4$) provides additional entropy compared to linking two disconnected parts of the subsystem ($A_1 \rightarrow A_2$). This is caused by the long-ranged nature of the entanglement in a topologically ordered state.

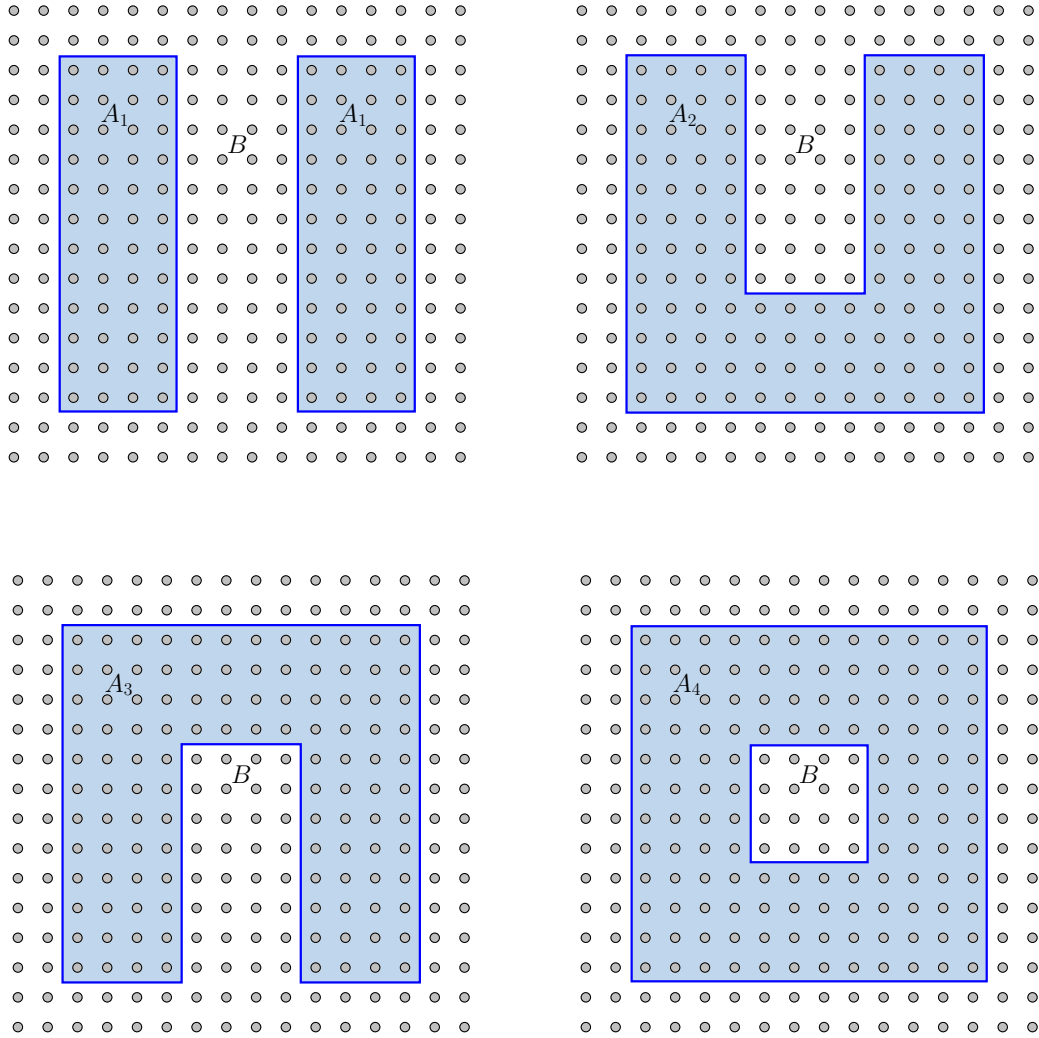


Figure 8.5.: Levin-Wen construction scheme for the extraction of a topological entropy γ .

8.3. Classical analogue of entanglement entropy

We have argued above that in string-net condensates the emergence of a topologically induced reduction of the entanglement entropy results from the constraint that the number of strings crossing the boundary must even. The nature of this argument is combinatorial and hence rooted in a classical statistical mechanics perspective. This insight raises the question whether such topological [entanglement] entropies can be studied in a purely classical context. Of course, there is no entanglement in classical physics so that we will avoid this word whenever we refer to a classical study in this thesis. Such an approach has indeed been successfully carried out on toric code models [122] and on general string-net models [119]. The numerical computation of such classical entropies using Monte Carlo methods has been worked out in Ref. [123].

In statistical mechanics, entropy refers to an ensemble of possible configurations of our system. Therefore, we first specify such an ensemble for (classical) loop-gases. The ground state of the quantum system is a superposition of all possible loops obeying the rules on the vertices, as discussed above. A classical analogue thereof is obtained by putting classical degrees of freedom such as Ising spins on the edges and defining the configuration space \mathcal{L} to be constituted exactly by all allowed closed-loop states \mathfrak{o} . In order to interpret the configuration space as an ensemble, we have to assign a weight $w_{\mathfrak{o}}$ to every configuration which we set to $w_{\mathfrak{o}} = 1$. All closed-loop configuration hence occur with equal probability in the ensemble. We note, that from the perspective of a microcanonical ensemble obeying a Boltzmann distribution, i.e. $w_{\mathfrak{o}} = \exp[-\beta E(\mathfrak{o})]$ with an associated energy $E(\mathfrak{o})$, we have assumed the limit of $\beta = 0$ for the inverse temperature. The probability for a particular configuration of the total system is given by $p_{\mathfrak{o}} = w_{\mathfrak{o}}/Z$, where $Z = \sum_{\mathfrak{o} \in \mathcal{L}} w_{\mathfrak{o}}$ is the partition function. The well-known Shannon entropy of such a probability distribution is given by

$$S = - \sum_{\mathfrak{o} \in \mathcal{L}} p_{\mathfrak{o}} \ln p_{\mathfrak{o}}. \quad (8.4)$$

We want to draw up an entropy analysis on our classical ensembles of many-body systems which is completely analogue to the bipartite entanglement entropies. Thus, we keep the concept of bipartitioning the many-body configuration. Instead of the reduced density matrices in quantum mechanics we can define the probability to find subsystem A in a state \mathfrak{o}_A by “tracing out” part B [119], that is,

$$p_{\mathfrak{o}_A} = \frac{1}{Z} \sum_{\mathfrak{o}_B \in \mathcal{L}_B} w_{\mathfrak{o}_{A \cup B}}, \quad (8.5)$$

where the sum runs over all possible remaining configurations of the degrees of freedom in part B while fixing those in part A . Finally, we can define classical bipartite entropies analogously to Eqs. (2.6) and (2.7) as

$$S_1(A) = - \sum_{\mathfrak{o}_A \in \mathcal{L}_A} p_{\mathfrak{o}_A} \ln p_{\mathfrak{o}_A} \quad (8.6)$$

8. Topological entanglement entropy

for the Shannon entropy and

$$S_\alpha(A) = \frac{1}{1-\alpha} \ln \left(\sum_{\sigma_A \in \mathcal{L}_A} p_{\sigma_A}^\alpha \right) \quad (8.7)$$

for the Rényi entropies of order α which recover the Shannon entropy in the limit $\alpha \rightarrow 1$. So far, we have assumed equal probabilities for all allowed closed-loop states. The resulting entropy computation is hence a combinatorial problem. In order to go further, we can introduce a finite temperature in the Boltzmann weights determining the probabilities and thereby investigate thermal transitions of the classical system.

8.3.1. Volume law

The crucial difference between the classical and the quantum bipartite entropies is the fact that we generically expect a scaling of the classical entropies to leading order with the *volume* of subsystem A [122]. This dependence can be understood by remarking that the degrees of freedom in the bulk of part A can fluctuate individually which leads to a number of possible configurations exponential in the volume. However, the fluctuations are not free but have to take place within the limits of the required global patterns, i.e. closed loops. The bipartite entropy of part A measures this number of configurations of the bulk logarithmically which yields the volume law. In the quantum case this picture fails because after tracing out part B we are left with a mixture of configurations of part A where each of them has fixed values at the boundary. The bulk of part A of every single element in this mixture is (almost) unchanged compared to the ground state of the total system and does hence not contribute to the entropy⁵. Thus, only the mixture of boundary configurations is measured by the entanglement entropies.

In the classical case, a further correction scaling with the size of the boundary between parts A and B is generally expected below the leading scaling with the volume. Furthermore, a reduction by a constant amount for a classical loopgas can be presumed due to the well-known reason — an even number of string passages of the boundary. Summing up, the classical bipartite entropies for a d -dimensional system A of linear size L_A follow the general form [119]

$$S_\alpha(A) = \mathcal{V}L_A^d + \mathcal{A}L_A^{d-1} - \gamma_{\text{cl}}, \quad (8.8)$$

with non-universal coefficients \mathcal{V} , \mathcal{A} and the *classical topological entropy* γ_{cl} .

8.3.2. Classical topological order

The emergence of a topological correction in the boundary law, Eq. (8.8), due to the constraint on the boundary, provides the notion of *classical topological order* for statistical mechanics ensembles. A partitioning of the ensemble into disjoint sectors replaces the quantum mechanical concept of ground state degeneracy. The

⁵This is different at finite temperatures: The quantum state *has* thermal fluctuations such that the entanglement entropy likewise follows a volume law in this case.

8.3. Classical analogue of entanglement entropy

sectors are segregated from each other in that local changes to a configuration cannot result in a configuration from another sector. This classical phenomenon is called *topological ergodicity breaking* [122]. Conversely, all configurations *within* a sector are linked ergodically, i.e. by subsequent local manipulations. The number of such sectors depends on the topology of the configuration space of the ensemble. For example, one sector of a loopgas defined on a torus (with genus $g = 1$) is given by the global property that it has an odd number of loops winding around one of the periodic lattice directions. It is impossible to obtain a configuration with an even number of windings only by local deformations of loops.

In order to extract the topological entropy γ_{cl} from the entropy, we are naturally inclined to apply the addition schemes from Sec. 8.2 used for the quantum case. However, the situation is slightly different: Consider all combinations of the values of the degrees of freedom on the edges in the bulk. The number of these combinations — exponential in the number of edges — is reduced by the constraints on the vertices which likewise scale with the volume. The very last constraint, however, is redundant and already ensured by all other vertex constraints. Hence, the reduction by the vertex constraints is itself diminished by one, thereby leaving one more degree of freedom for the bulk than expected from the number of vertices. The local possible states of all degrees of freedom in the bulk are responsible for the volume term. Indeed, as proven in Ref. [119], for the bipartite entropy of a simply connected subsystem A (such as all bipartition in the Kitaev-Preskill construction or A_2 and A_3 of the Levin-Wen construction) the constant correction vanishes because the reduction from the boundary constraint and the increment by the bulk compensate each other. Hence, the Kitaev-Preskill construction is blind for classical topological corrections. Only if the number of closed boundaries n_b is different from the number of bulks n_v of the respective subsystem we have a finite classical topological entropy scaling as $\gamma \sim (n_b - n_v)$. In contrast to the quantum case, the entropies are hence in general not symmetric under exchange of the subsystems, $S_\alpha(A) \neq S_\alpha(B)$. We observe that A_1 from the Levin-Wen construction has a non-vanishing $\gamma_{\text{cl}}^{(B)}$ and A_4 has a non-vanishing $\gamma_{\text{cl}}^{(A)}$. The very important conclusion from this discussion is, that we have to use the addition scheme of Levin and Wen⁶, i.e. generate different subsystem topologies in order to detect a topological entropy.

⁶In fact, Kitaev and Prekill provide a second construction, which is very similar to the one of Levin and Wen.

9. Quantum error-correcting codes

In a stroke of genius Alexei Kitaev laid out [10] that topological order in quantum many-body states can be exploited to help overcome an important issue in the rising field of quantum computation: The establishment of a quantum memory in which computational errors can be efficiently detected and corrected. This idea led to the conception of a number of so-called *codes* which in principle implement such a quantum memory, among them the central object of study in this part of the thesis — the toric code model.

In order to thoroughly introduce the toric code and related other models we prepend their presentation by a brief outline of the concept of error correcting codes in Sec. 9.1. As a part of it, we discuss fault-tolerant quantum computation and the idea of *self*-correcting quantum codes. Further, the toric code is extensively presented in Sec. 9.2 and highlighted from the perspective of quantum computation as a model on which fault-tolerant computation is possible as well as from a condensed-matter perspective as a model embodying dual aspects of the well-known Ising model. Two three-dimensional adaptations are subsequently introduced in Secs. 9.3 and 9.4. It is known that a four-dimensional variant of the toric code would be necessary to constitute a self-correcting code at finite temperature [124]. The cubic code (Sec. 9.5), also known as Haah’s Code, is an attempt to provide this feature in three dimensions. By the time of writing of this thesis, it seems however, that any proposals for a self-correcting in less than four spatial dimensions fall short [125].

9.1. Error correction in quantum computation

Any procedure involving the processing of information is susceptible to errors which can occur in the communication or at operations on the information. In order to set up a stable procedure, the ability to detect and correct such errors is necessary. This can be established by augmenting the amount of information by redundant elements.

The resulting total information must have a well-defined structure denoted as the *code space*. If a message violates the code space, an error detection procedure should be able to spot the corrupted piece of information. Considering the real-world example of communication between humans by spoken or written language, errors in the transmittal of the information may occur due to (actual) noise or dirt. However, human languages are structures that encode information in a very redundant way, that is, the receiver of the text can mostly infer missing words or parts of words. This redundancy can be further enhanced by the sender of the information, e.g. by repeating essential parts of the message.

9. Quantum error-correcting codes

In abstract terms of information given in (qu)bits, we can add redundant (qu)bits and possibly perform a mapping of the obtained (qu)bit string to one or several others in which the original information is not directly recognizable. Such a way of mapping the information is called a *code*. The following introduction to error-correcting codes is adapted from Chapter 10 of Ref. [60]. A comprehensive review article has been written by B. Terhal [126].

Classical error correction

An extremely simple example of a classical code is the repetition code and accounts for the prototypical error in classical systems, namely the erroneous flip of a bit. It is constructed by replacing every bit by three copies of itself

$$0 \rightarrow 000 \quad \text{and} \quad 1 \rightarrow 111.$$

Obviously, the decoding works by a majority voting, i.e. the two or three bits of the encoded string which have the same value are assumed to carry the correct value. This protocol fails if two or more bits are flipped. But for a sufficiently low single-bit-flip probability p this code increases the reliability of the transmission. It also reveals the important distinction between *physical* bits and *logical* bits. In this example, a logical bit with value 0 is given by the code words 000, 001, 010, 100.

Simple quantum codes

When trying to adapt such a classical code to quantum information stored in qubits, we are confronted with three problems. Specifically, (i) a simple copying of a quantum state is forbidden by the no-cloning theorem [60]. Further, (ii) errors occurring on a qubit $\alpha|0\rangle + \beta|1\rangle$ are not discrete like classical bit flips but continuous. The identification of such an error would require infinite resources. Finally, (iii) the decoding involves a quantum-mechanical measurement which destroys the information. But these issues can be overcome as demonstrated in the next paragraphs.

Bit flip errors can also happen to qubits and correspond to the result of applying the σ_x Pauli operator, often denoted by X in the context of quantum computation. A straightforward adaption of the repetition code to qubits is given by an encoding $\alpha|0\rangle + \beta|1\rangle \rightarrow \alpha|000\rangle + \beta|111\rangle$. This operation does not violate the no-cloning theorem and can be performed using the fundamental CNOT gate [60] — resolving issue (i). The kinds of errors that can be recovered using this code are zero or one bit flip on one of the qubits. For example, if a bit flip on the second qubit occurs, the state is $\alpha|010\rangle + \beta|101\rangle$. A measurement of the projection operator $|010\rangle\langle 010| + |101\rangle\langle 101|$ would return 1 with certainty and leave the state untouched. Hence, a so-called *syndrome measurement* can be performed using a measurement $\{P_m\}$ with projection operators

$$\begin{aligned} P_0 &= |000\rangle\langle 000| + |111\rangle\langle 111| \\ P_1 &= |100\rangle\langle 100| + |011\rangle\langle 011| \\ P_2 &= |010\rangle\langle 010| + |101\rangle\langle 101| \\ P_3 &= |001\rangle\langle 001| + |110\rangle\langle 110| \end{aligned}$$

so that issue (iii) is resolved. Since a potential single-bit flip is unambiguously identified using this measurement, it can be cured by applying an X operation on the affected qubit. In order to approach problem (ii), we first note that another elementary type of errors unique to the quantum case are *phase* flips — induced by σ_z (denoted by Z), i.e. $\alpha|0\rangle + \beta|1\rangle \rightarrow \alpha|0\rangle - \beta|1\rangle$. A code similar to the three qubit flip code can be constructed for the detection of phase flips. All we have to do is to go from the σ^z to the σ^x eigenbasis $\{|+\rangle, |-\rangle\}$. This basis change can be performed by the use of the Hadamard gate [60].

A combination of the quantum three qubit bit flip and phase flip codes is the *Shor code* [127], a nine qubit code. The important feature of the Shor code is that it detects *arbitrary* errors, not only pure bit and phase flips — provided the error occurs on one qubit only [60]. Thus, also issue (ii) is resolved. We conclude, that specifically designed quantum codes enable error-correction by a standard procedure consisting of two steps, syndrome measurement and recovery.

Stabilizer formalism

The elegant formalism of *stabilizers*, developed by D. Gottesman [128] engenders the class of *stabilizer codes* to which all codes discussed in this thesis belong. A quantum state $|\psi\rangle$ is *stabilized* by a set of quantum operators $\{S_1, S_2, \dots\}$ if $|\psi\rangle$ is invariant under the action of any of these operators, i.e. $S_k|\psi\rangle = |\psi\rangle \forall k$. We note that a quantum code resides in a *code space*, that is, a vector space that spans all possible code words, e.g. $\{|000\rangle, |111\rangle\}$ for the three qubit flip code. The essential idea of the stabilizer formalism is to describe this vector space by stabilizing operators instead of quantum states. Moreover, the structure of the set of stabilizing operators $\{S_1, S_2, \dots\}$ suggests a treatment with *group theory* since, for example, the identity operator $\mathbb{1}$ is trivially part of it and compositions of the S_k also stabilize a particular state. Specifically, a stabilizer is defined as a subgroup S of the Pauli group G_n for n qubits. For one qubit, the Pauli group is given by

$$G_1 \equiv \{\pm\mathbb{1}, \pm i\mathbb{1}, \pm i\sigma_x, \pm\sigma_x, \pm i\sigma_y, \pm\sigma_y, \pm i\sigma_z, \pm\sigma_z\}. \quad (9.1)$$

Further, S defines the vector space V_S by its constituting property that it contains all states that are stabilized by (all elements of) S . Hence, V_S is a subspace of the n qubit state space. It is obvious, that the element $-\mathbb{1}$ cannot not be part of any non-trivial stabilizer. Without proof, we mention another very important condition of a stabilizer S , namely that all its elements *commute* [60]. These two conditions carry an immense benefit for a local Hamiltonian-based description of such quantum codes and its simulatability: The ground state of a corresponding Hamiltonian is (i) frustration free and (ii) exactly solvable via a decomposition of the eigenspace into local subspaces [129].

We add an additional level of compactification in the description of stabilizer codes by noting that groups can be described by *generators*. A group G is generated by a subset g_1, \dots, g_l of its elements if all elements of G can be written as a product of the g_k . Another advantage of this description — denoted by $G = \langle g_1, \dots, g_l \rangle$ — is that in order to verify whether a certain state is stabilized by S , it is sufficient to check if the generators stabilize that state. We are now in a position to determine

9. Quantum error-correcting codes

which errors can be detected in a stabilizer code. A measurement of a generator g_k in a correct code state would yield $+1$ with certainty and would hence not disturb the state. If we perform a measurement of all generators and obtain -1 as a measurement result for one g_k we can infer that an error E_k has occurred and that E_k *anti-commutes* with g_k . This is precisely how error-correction in a stabilizer code works. However, only errors which anti-commute¹ with one of the generators can be detected and form the so-called correctable set of errors $E = \{E_1, E_2, \dots\}$.

We close this explanation by illustrating the stabilizer formalism for the three qubit flip code. Its stabilizer is $S = \{\mathbb{1}, Z_1 Z_2, Z_2 Z_3, Z_1 Z_3\} \in G_3$ as it fixes the subspace of 3 qubit states to the one spanned by $|000\rangle$ and $|111\rangle$. Due to $Z_1 Z_3 = (Z_1 Z_2)(Z_2 Z_3)$ and $\mathbb{1} = (Z_1 Z_2)^2$ we can write S using generators as $S = \langle Z_1 Z_2, Z_2 Z_3 \rangle$. This code is able to correct bit flips, represented by the operators X_1, X_2, X_3 . Indeed, if error X_1 occurs, a syndrome measurement of the generators yields -1 ($+1$) for $Z_1 Z_2$ ($Z_2 Z_3$) respectively. The set of correctable errors includes the ‘no error’ event, i.e. $E = \{\mathbb{1}, X_1, X_2, X_3\}$.

In anticipation of the specific codes discussed below, we remark that stabilizers involving only Z operators identify bit flips. Conversely, phase flips are identified by X stabilizers. In the Shor code, we have seen that a combination thereof leads to a code that can correct arbitrary errors on qubits. Hence, it appears natural that our more sophisticated codes consists of separate multiple X and Z stabilizer elements.

Fault-tolerant quantum computation

The procedure of syndrome measurement with subsequent error correction elucidated above might suggest that the actual quantum computational operations using quantum gates are performed on decoded single physical qubits. However, the encoding and decoding itself is generally afflicted with errors due to noise which hampers the set-up of a reliable quantum circuit. The crucial idea to circumvent this Sisyphean labor is to perform the quantum computation on the *encoded* state, i.e. on the code words. In other words, the gates have to be designed in order to work on the *logical* qubits of the specific code which yields an *encoded quantum gate*. Repeated error-correction between components of the quantum circuit prevents the accumulation of errors but does not suppress error propagation. As a remedy, we have to enhance the concept of error correction by *fault-tolerant* quantum computation [130] adopted from considerations on classical fault-tolerance [131]. Fault-tolerance means that a sufficiently accurate result of the quantum computation can be obtained even though the used gates and the quantum wires have a finite error probability p . Specifically, we require that if one failure in an encoded quantum gate occurs, at most *one* qubit of its output is faulty. For measurement processes we demand that a failure of a component yields an error probability for the measurement result scaling with $\mathcal{O}(p^2)$. We will not elaborate this concept beyond these requirements but solely point out the existence of the important *threshold theorem* [132]. Its essence is that the scaling of the number of gates needed in a fault-tolerant quantum circuit with the ‘size’ n of some problem is well behaved. The crucial condition

¹To be more accurate, any combination $E_k^\dagger E_j$ must anti-commute with at least one of the generators, cf. Theorem 10.8 in Ref [60].

for this theorem to hold is that the failure probability of all hardware components is below a certain threshold, i.e. $p < p_{\text{th}}$. For a desired finite accuracy ε the scaling of the size of the circuit is only polylogarithmically in the size $s(n)$ of a corresponding (theoretic) error-free circuit which in turn is polynomial in the problem size n , see Ref. [60].

This result provides a huge step towards the practical implementation of quantum computation. The success of the concept of fault-tolerant quantum computation proves that no physical limitation prevents the construction of quantum computers. Without this concept the framework of error-correcting quantum codes would be of a rather academic interest as it cannot ensure *error-free* computation.

Self-correcting codes

So far, we have considered an *active* error correction approach, i.e. errors have to be detected and corrected by specifically designed quantum operations. Also, we have ignored the role of time in our considerations about failures of gates and wires. Especially when it comes to *quantum memories*, the stability of the information against decoherence due to the unavoidable coupling with the environment is focussed on. Active error correction would have to be performed on the stored information repeatedly within the *memory time*, i.e. the time within which the state of the memory is assumed to be stable. A more promising ansatz is to design the quantum code in a way that it is *self-correcting* [133].

The idea to use the phenomenon of topological order for quantum computing is based on ground states of appropriate local gapped Hamiltonians. The eigenspace of a ground state represent the code space. Since topologically ordered states have a topology-dependent degeneracy, distinct orthogonal subspaces of the eigenspace can be used to represent one logical qubit state each. A local perturbation does not cause a transition to another subspace as these subspaces are locally indistinguishable [134]. An occurring error on a *physical* qubit in the code corresponds to a gapped excitation of the ground state. This relation paves the way for a self-correcting mechanism of the quantum code: Coupling the system to a thermal bath at a very low temperature results in the effort to annihilate emergent excitations and thereby correct the error. However, a sufficiently large number of excitations could yield a self-correction onto the ‘wrong’ subspace, that is, a different subspace than the one on which the excitations occurred. In this case, topological order is destroyed by thermal fluctuations. Thus, the information is not expected to be stored longer than the average time until such an event happens. Obviously, the memory time depends on the temperature of the bath and the size of the system. In order to achieve macroscopic memory times, it must hence be ensured that the system exhibits remnants of topological order even at finite temperature. We will see in Sec. 11.1.1 out that if excitations are deconfined, topological order does not survive at finite temperature in the thermodynamic limit. Hence, self-correcting quantum codes must be designed in a way that their excitations are confined [124, 134].

9.2. Toric code

In the domain of theoretical many-body physics the intense study of colloquially dubbed *toy models* is very popular. Such systems are not designed to accurately model a real material with respect to all details but to incorporate rather abstract and idealized assumptions which allow for a thorough and undisturbed investigation of a special phenomenon. From the point of view of the phenomenon a particularly suitable toy model may be said to be its “drosophila” — a naming borrowed from genetics which emphasizes the simplicity and generality of the model. A famous example is the Ising model describing phase transitions of magnetism and conventional order in classical statistical mechanics.

The celebrated *toric code model* can veritably be called the drosophila of topological order. It has been invented by A. Kitaev [10] as an error-correcting quantum code that enables fault-tolerant quantum computation. This Section is intended to introduce this model and is organized as follows. First, we define this model in a condensed matter fashion, i.e. via its Hamiltonian. As this Hamiltonian is a so-called *commuting Pauli Hamiltonian* it is equivalent to a stabilizer code defined by generators. Further, we focus on the ground state of the toric code and discuss its properties. If we apply an external longitudinal magnetic field to the model, we can map the resulting Hamiltonian in the ground state to an Ising model in a transverse field. This mapping is discussed hereafter. Finally, it is possible to formulate a classical variant of the quantum model and study classical topological order therein. This approach is covered in the last Subsection.

9.2.1. Definition

The toric code model is defined on a two-dimensional square lattice with spin-half degrees of freedom located on the edges of the lattice, see Fig. 9.1. Periodic boundary conditions are employed on the lattice leading to a toroidal structure — hence the name toric code. Vertices (stars) and plaquettes (squares) of the lattice each have four adjacent spins. We define four-body operators on the vertices and plaquettes by multiplying one spin component over the four adjacent spins. In our convention, the plaquette operators are given by $A_p = \sigma_{p_1}^x \sigma_{p_2}^x \sigma_{p_3}^x \sigma_{p_4}^x$ and the vertex operators by $B_v = \sigma_{v_1}^z \sigma_{v_2}^z \sigma_{v_3}^z \sigma_{v_4}^z$. The Hamiltonian is then given by the sum of all plaquette and vertex operators

$$H = -J_p \sum_{p \in P} A_p - J_v \sum_{v \in V} B_v, \quad (9.2)$$

with coupling constants $J_p, J_v \geq 0$. The set of all plaquettes (vertices) is denoted by P (V), respectively. A pair of two plaquette or two vertex operators in this Hamiltonian share either zero or one spin. For mixed pairs of two four-body interactions either zero or two spins are common to them. For zero overlap, the commutator between the operator trivially vanishes. Also for a common identical spin component, we have $[\sigma_i^x, \sigma_i^x] = [\sigma_i^z, \sigma_i^z] = 0$. Otherwise, due to the anti-commutation of

fermionic operators $\{\sigma_i^z, \sigma_j^x\} = 0$, we have

$$\begin{aligned}
& [\sigma_i^z \sigma_j^z \sigma_k^z \sigma_l^z, \sigma_k^x \sigma_l^x \sigma_m^x \sigma_n^x] \\
&= \sigma_i^z \sigma_j^z [\sigma_k^z \sigma_l^z, \sigma_k^x \sigma_l^x] \sigma_m^x \sigma_n^x \\
&= \sigma_i^z \sigma_j^z (\sigma_k^z \sigma_k^x \sigma_l^z \sigma_l^x - \sigma_k^x \sigma_k^z \sigma_l^x \sigma_l^z) \sigma_m^x \sigma_n^x \\
&= \sigma_i^z \sigma_j^z (\sigma_k^x \sigma_k^z \sigma_l^x \sigma_l^z - \sigma_k^z \sigma_k^x \sigma_l^z \sigma_l^x) \sigma_m^x \sigma_n^x \\
&= 0.
\end{aligned} \tag{9.3}$$

As all interactions in the Hamiltonian (9.2) consist of Pauli matrices and mutually commute, it is called a *commuting Pauli Hamiltonian*. Basic quantum mechanics tells us that it is possible to construct a basis of the total Hilbert space from the eigenspaces of local commuting plaquette and vertex operators. Since the Pauli matrices σ^x and σ^z have eigenvalues ± 1 , it follows for the vertex operators B_v that they likewise have these two eigenvalues, in particular it is $+1$ if an *even* number of the four associated spins point downwards (in the z -direction) and -1 otherwise. The same is true for plaquette operators, up to the fact that spin orientations are considered with respect to the x -direction². The eigenvalues are eight-fold degenerate as a result of the number of possibilities to orient the individual spins at a specific vertex or plaquette in order to have an even or odd total number of equally oriented spins. We can write down the eigenvectors for the four-body terms in the σ^z basis. Denoting a spin up by a lightgray edge and a spin down by a black edge we have for the eigenspaces of the vertex operator with eigenvalue b_v

$$\begin{aligned}
b_v = +1 : & \quad \{ | \begin{array}{c} \text{lightgray} \\ \text{lightgray} \\ \text{lightgray} \\ \text{lightgray} \end{array} \rangle, | \begin{array}{c} \text{lightgray} \\ \text{lightgray} \\ \text{black} \\ \text{black} \end{array} \rangle, | \begin{array}{c} \text{lightgray} \\ \text{black} \\ \text{lightgray} \\ \text{black} \end{array} \rangle, | \begin{array}{c} \text{lightgray} \\ \text{black} \\ \text{black} \\ \text{lightgray} \end{array} \rangle, | \begin{array}{c} \text{black} \\ \text{lightgray} \\ \text{lightgray} \\ \text{lightgray} \end{array} \rangle, | \begin{array}{c} \text{black} \\ \text{lightgray} \\ \text{black} \\ \text{black} \end{array} \rangle, | \begin{array}{c} \text{black} \\ \text{black} \\ \text{lightgray} \\ \text{lightgray} \end{array} \rangle, | \begin{array}{c} \text{black} \\ \text{black} \\ \text{black} \\ \text{lightgray} \end{array} \rangle \} \\
b_v = -1 : & \quad \{ | \begin{array}{c} \text{lightgray} \\ \text{black} \\ \text{black} \\ \text{black} \end{array} \rangle, | \begin{array}{c} \text{lightgray} \\ \text{black} \\ \text{lightgray} \\ \text{lightgray} \end{array} \rangle, | \begin{array}{c} \text{lightgray} \\ \text{lightgray} \\ \text{black} \\ \text{black} \end{array} \rangle, | \begin{array}{c} \text{lightgray} \\ \text{lightgray} \\ \text{lightgray} \\ \text{black} \end{array} \rangle, | \begin{array}{c} \text{black} \\ \text{lightgray} \\ \text{lightgray} \\ \text{lightgray} \end{array} \rangle, | \begin{array}{c} \text{black} \\ \text{lightgray} \\ \text{black} \\ \text{black} \end{array} \rangle, | \begin{array}{c} \text{black} \\ \text{black} \\ \text{lightgray} \\ \text{lightgray} \end{array} \rangle, | \begin{array}{c} \text{black} \\ \text{black} \\ \text{black} \\ \text{lightgray} \end{array} \rangle \}.
\end{aligned} \tag{9.4}$$

The basis of the eigenspaces for an eigenvalue a_p of the plaquette operators reads in superposed notation

$$\begin{aligned}
a_p = \pm 1 : & \quad \left\{ \frac{| \begin{array}{|c|} \hline \text{lightgray} \\ \hline \end{array} \rangle \pm | \begin{array}{|c|} \hline \text{black} \\ \hline \end{array} \rangle}{\sqrt{2}}, \frac{| \begin{array}{|c|} \hline \text{lightgray} \\ \hline \end{array} \rangle \pm | \begin{array}{|c|} \hline \text{black} \\ \hline \end{array} \rangle}{\sqrt{2}}, \frac{| \begin{array}{|c|} \hline \text{lightgray} \\ \hline \end{array} \rangle \pm | \begin{array}{|c|} \hline \text{black} \\ \hline \end{array} \rangle}{\sqrt{2}}, \frac{| \begin{array}{|c|} \hline \text{lightgray} \\ \hline \end{array} \rangle \pm | \begin{array}{|c|} \hline \text{black} \\ \hline \end{array} \rangle}{\sqrt{2}}, \right. \\
& \quad \left. \frac{| \begin{array}{|c|} \hline \text{lightgray} \\ \hline \end{array} \rangle \pm | \begin{array}{|c|} \hline \text{black} \\ \hline \end{array} \rangle}{\sqrt{2}}, \frac{| \begin{array}{|c|} \hline \text{lightgray} \\ \hline \end{array} \rangle \pm | \begin{array}{|c|} \hline \text{black} \\ \hline \end{array} \rangle}{\sqrt{2}}, \frac{| \begin{array}{|c|} \hline \text{lightgray} \\ \hline \end{array} \rangle \pm | \begin{array}{|c|} \hline \text{black} \\ \hline \end{array} \rangle}{\sqrt{2}}, \frac{| \begin{array}{|c|} \hline \text{lightgray} \\ \hline \end{array} \rangle \pm | \begin{array}{|c|} \hline \text{black} \\ \hline \end{array} \rangle}{\sqrt{2}} \right\}.
\end{aligned} \tag{9.5}$$

A very important consequence of the decomposition of the eigenvalue problem onto the local interaction is that the eigenvalues of the Hamiltonian (9.2) are simply the sums of the eigenvalues a_p and b_v for all plaquettes and vertices. It is hence easy to see, that the Hamiltonian is *gapped* since the energy levels are separated by multiples of $\Delta E = 2 \min(J_p, J_v)$ which corresponds to replacements $+1 \rightarrow -1$ for local eigenvalues a_p or b_v in the sum. Moreover, as no continuous symmetry of an order parameter can be broken in this system, no gapless Goldstone modes can

²Strictly speaking, this derivation of the eigenvalues for the B_v and A_p uses the statement about commuting observables *again* on the local level. Both four-body interactions consist of four mutually commuting single-spin operators which enables the factorization of the eigenvalue problem.

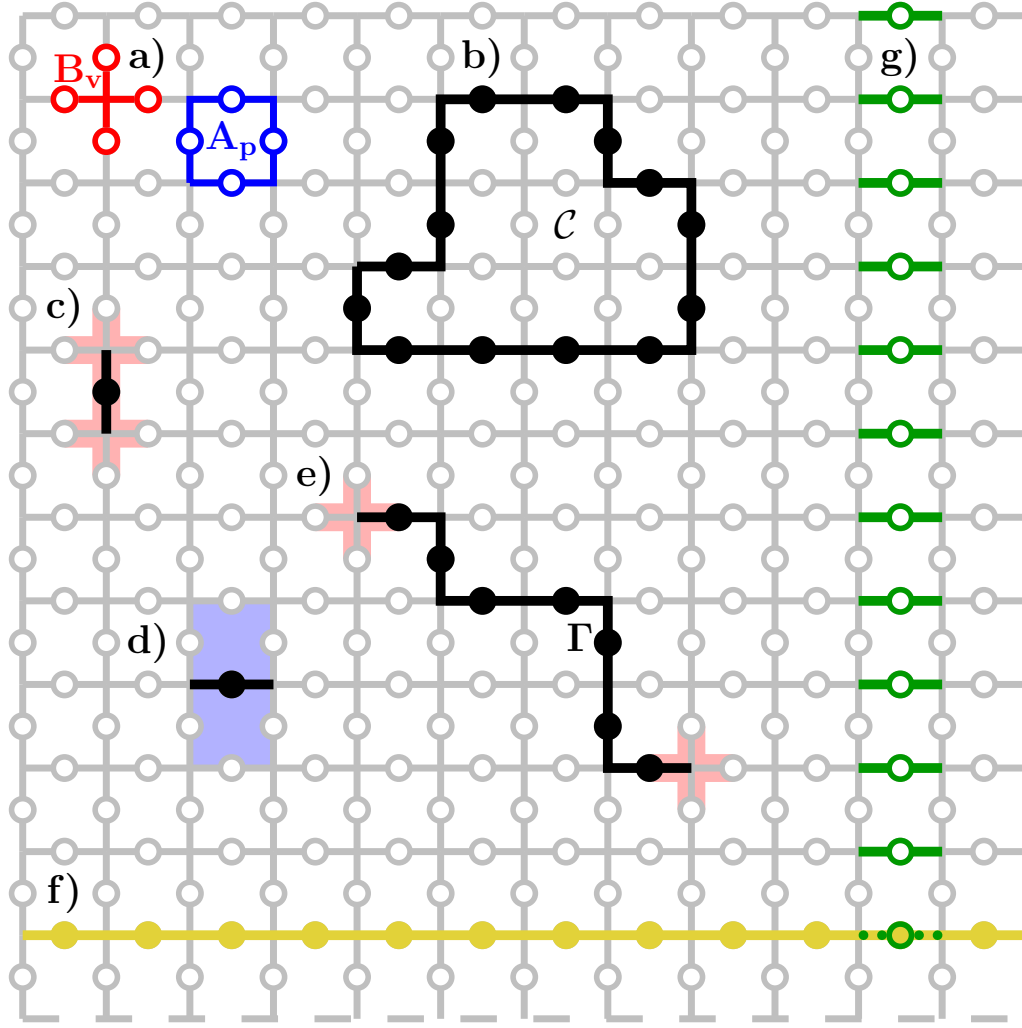


Figure 9.1.: Illustration of the toric code model. Spin degrees of freedom are located on the edges of a square lattice and can point upwards (empty circles) or downwards (solid circles) with respect to the σ^z basis. The interactions of the Hamiltonian (a) act on the four sites of vertices (red) and plaquettes (blue). In the ground state, only closed loops (b) of spins down are allowed. At finite temperature, single-spin flips result in pairs of excited vertices (c) or plaquettes (d) — depending on the basis in which the flip is considered. Pairs of such defects can be moved apart from each other without exciting further operators, a procedure represented by non-local string operators Γ (e). So-called non-contractible winding loops (f) cannot be created or removed by local operations and identify the ground state manifold. They can be detected by string-like Wilson loop operators (g). If one changes to the σ^x basis, the figure objects (f) and (g) switch roles.

emerge. The eigenvectors in Eqs. (9.4) and (9.5) reveal the structure of eigenvectors of the total system, written in the single-spin σ^z -basis. To elucidate this we adopt the string-net concept [120], that is, we refer to an uninterrupted string of edges carrying a down spin as a *loop*. A positive local eigenvalue ($b_v = +1$) on a vertex imposes that a loop does not end at that vertex, whereas the energetically costly $b_v = -1$ implies the end of a loop at v . The plaquette terms enforce a *superposition* between global loop configurations in the σ^z basis in order for the state to be an eigenstate of Eq. (9.2). The sign of a plaquette eigenvalues a_p , has an effect on the

relative phase of the superposed configurations, where the phase likewise can be $+1$ or -1 . This insight is of great use for the following two Subsections, in which the ground state and excitations are discussed respectively.

We note, that the underlying idea of the design which led to Kitaev's clever combination of vertex and plaquette terms predates the era of quantum information theory and topological order. The degrees of freedom on the edges emerge from formulating a dual description of a conventional square lattice which has been used in classical statistical mechanics in order to solve the two-dimensional Ising model [135]. More generally, this dual description gives rise to a \mathbb{Z}_2 lattice gauge theory [136, 137] defined by the existence of a gauge symmetry. By defining classical variant of the toric code model further below, we reobtain precisely this gauge theory in a roundabout way.

Finally, we remark that the (quantum) toric code is *self-dual* under exchange of $\sigma_i^x \leftrightarrow \sigma_i^z$. The dual description can alternatively be obtained by switching plaquettes and vertices, i.e. through shifting the lattice diagonally by half the size of a plaquette.

9.2.2. Ground state

It is straightforward to derive the ground state of the toric code model from the above introduction. The Hamiltonian (9.2) takes the lowest possible value, if and only if all plaquette and vertex operators have eigenvalues $a_p = b_v = 1$, $\forall p \in P, v \in V$. Its energy is hence $E_{\text{gs}} = -N_p J_p - N_v J_v$, where N_p (N_v) denotes the total number of plaquettes (vertices). For the eigenstate, it follows from Eq. (9.4) that all loops in the configuration must be closed. In addition, Eq. (9.5) forces all closed-loop configurations which are related to each other by an arbitrary number of *plaquette flips* into a superposition with relative phase 1. Note, that plaquette flips do not violate the closed loops condition. We can write such an eigenstate as

$$|\Psi\rangle = \sum_{o \in \mathcal{L}_i} |o\rangle, \quad (9.6)$$

where \mathcal{L}_i denotes a set of closed loop configurations linked by plaquette flips. The subscript anticipates that on a torus, there are pairs of closed-loop configurations which are *not* linked in such a way. These have to be associated to two different $\mathcal{L}_i \neq \mathcal{L}_j$. Consider, for example, a single closed loop winding around the periodic lattice as in Fig. 9.2b. Such a loop cannot be eliminated by applying plaquette flips and the configuration must hence belong to another set \mathcal{L}_j . This argument can be repeated for single closed loops winding around the other lattice dimension or around both of them. We hence obtain four different sets which implies a *degeneracy* of four for the ground state of the toric code, see Fig. 9.2. Noting that *pairs* of winding loops can be annihilated by local plaquette flips, we formulate the distinction between different ground states in more general terms by their *winding number parity*. Two closed-loop configurations belong to the same ground state, if their respective number of winding loops has the same parity for both lattice dimensions. In order to determine the winding number parity, so-called *Wilson loop operators* can be used as shown in Fig. 9.1. The ground state degeneracy depends on the genus g of the space on which

9. Quantum error-correcting codes

the Hamiltonian (9.2) is defined, specifically it is 4^g . This value of the degeneracy can also be obtained by counting the degrees of freedom. A toric code on an $L \times L$ square lattice as $N = L^2$ vertices, N plaquettes and $2N$ spins. Without constraints there would be 2^{2N} possible spin configurations. However, each of the N vertices imposes a constraint on the configuration and effectively divides the number of possible configurations by two, see Eq. (9.4). However, the constraint of the *last* vertex considered is already implemented by the surrounding vertices. The same argument holds for the plaquettes, such that the remaining number of configurations is $2^{2N-(N-1)-(N-1)} = 4$.

Another notation of the ground state is based on *representatives* of the superposition which forms the ground state. Any configuration can be taken as such a representative $|\text{rep}_i\rangle$ and all other configurations are included by applying all combinations of plaquette flips through the σ^x -operations in A_p , i.e.

$$|\Psi_i\rangle = \left(\prod_{p \in P} \frac{1 + A_p}{\sqrt{2}} \right) |\text{rep}_i\rangle \quad i = 1, \dots, 4. \quad (9.7)$$

This notation emphasizes that graphic illustrations of configurations of the toric code solely show one representative but not an eigenstate of the system. Fig. 9.2 depicts four representatives for the distinct degenerate eigenstates.

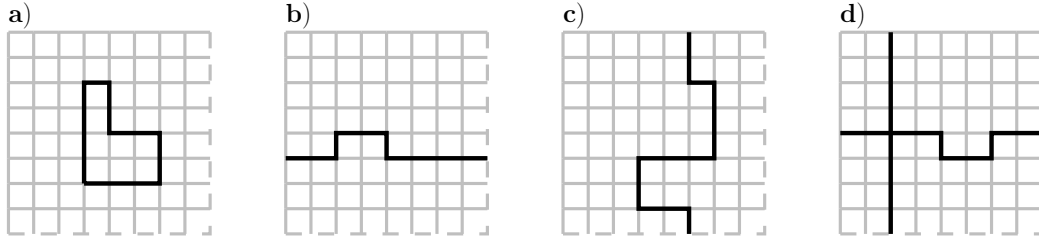


Figure 9.2.: Graphic illustration of the four-fold degeneracy of the toric code in the string-net picture. Black edges correspond to spins pointing down. Dashed lines of the lattice indicate the repetition due to the periodic boundary conditions. Each loop configuration shows one representative of the corresponding ground state, separated by a different winding number parity for both lattice dimensions.

The understanding of the ground state of the toric code allows for revisiting the stabilizer formalism from the previous section. Since the ground state is also an eigenstate of the local four-body operators and compositions thereof, they can be said to stabilize the state. We can consider the ground state as a stabilizer code S_{TC} generated by all local plaquette and vertex operators,

$$S_{\text{TC}} = \langle A_{p_1}, A_{p_2}, \dots, B_{v_1}, B_{v_2}, \dots \rangle. \quad (9.8)$$

The number of physical qubits of this code is $2L^2$ for a square lattice of linear dimension L . They encode two logical qubits by the four degenerate ground states. As we will see in the next Subsection, correctable errors correspond to excitations of the ground state. Such errors can be bit flips which are represented by σ^x or phase flips — represented by σ^z . This approach hints at the equivalence between commuting Pauli Hamiltonians and the stabilizer formalism.

9.2.3. Excitations

An excitation of the ground state of the toric code is characterized by a finite number of vertex or plaquette operators in Eq. (9.2) having an eigenvalue of -1 . The simplest example of such an excitation is a flip of a single spin in its σ^z basis, see Fig. 9.1e. It results in a violation of the closed loop condition of the ground state at the two vertices that share the pertaining spin. Hence, the two corresponding vertex operators measure a value of -1 which is why we dub them a pair of *electric charges*. We conclude that these excitations always emerge *pairwise* and the energy gap is $\Delta E = 4J_v$. A single flip of one vertex eigenvalue b_v would not yield an eigenstate of the Hamiltonian (9.2). Albeit being less figurative in the σ_z basis for the total configurations, a flip of a single spin in its σ_x basis is completely equivalent and causes the two adjacent plaquettes to flip their eigenvalue. The resulting total state can be understood in the representation (9.7) where it corresponds to a minus sign in the two factors $(\mathbb{1} - A_p)$ of the relevant plaquette operators. Such excitations are referred to as *magnetic vortices*.

A very important observation about the relative position of a pair of excitations is that they can be moved away from each other without applying energy. To see this, consider flipping a spin shared by an already excited and a non-excited vertex. The energy difference to the state after this flip is $2J_p - 2J_p = 0$ and the excitation has effectively been moved. Hence, the excitations are *deconfined*. Together with the notion that such spin flips are obtained by applying the σ^x operator to the spin we can find an alternative creation of excitations, namely by *string operators* either for electric charges (e) or for magnetic vortices (m)

$$S_\Gamma^{(e)} = \prod_{i \in \Gamma} \sigma_i^x \quad \text{and} \quad S_\Gamma^{(m)} = \prod_{i \in \Gamma} \sigma_i^z, \quad (9.9)$$

where Γ describes some path in the lattice, see Fig. 9.1. The excitations are located at the end points of the path. An annihilation of such a pair of excitations is achieved by a string operator on an arbitrary path Γ' that links the same endpoints. We note, that such string operators are non-local objects and can also be used to engender a transition between different ground states if their path winds around the lattice.

From the perspective of quantum stabilizer codes, excitations are errors of the code which can occur in a quantum circuit. In the toric code, self-correction is not possible at finite temperatures but we can apply an active error correction protocol [129]. The syndrome measurement can safely be performed by measuring all plaquette A_p and vertex operators B_v since they commute with the Hamiltonian (9.2). Errors will be detected since those four-body terms which yield a -1 in this measurement are defective. An appropriate string operator as in Eq. (9.9) can be calculated by the decoding software and annihilates the pair of errors. Obviously, there are many possible paths to connect the excitations. The application of two equivalent string operators could differ in the resulting winding number parity. If the decoder takes the shortest possible path for the error-correction, any pair of excitations which has split over a distance larger than half the lattice size will be corrected to the ‘wrong’ logical qubit state, e.g. to another ground state. We conclude that the ability to logically correct emergent errors in the two-dimensional

9. Quantum error-correcting codes

toric code by such a protocol is limited, since the defects are deconfined, i.e. they can have an arbitrary distance.

Regarding the statistics of the excitations of both types e and m we can convince ourselves that they both represent *hard-core bosons* if separately considered. This can be understood from the fact that two string operators of the same type commute with each other, $[S_\Gamma^{(e)}, S_{\Gamma'}^{(e)}] = [S_\Gamma^{(m)}, S_{\Gamma'}^{(m)}] = 0$. Hence, an exchange of two excitations of the same kind does not induce a change in the phase of the total state qualifying them as bosonic³. The situation is different if we want to swap an

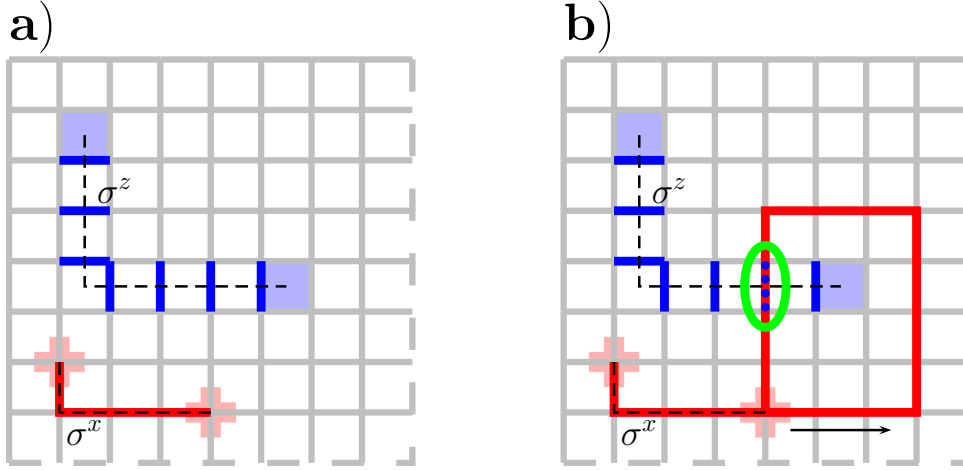


Figure 9.3.: Example of braiding between a charge excitation (red shaded vertices) and a flux excitation (blue shaded plaquettes). Initially (a) two pairs of either excitation are created via string operators of the corresponding Pauli matrices. Braiding (b) is effected by moving one charge around a flux and back to its original position. The spin configuration is the same before and after the braiding but due to the combined action exerted on one spin (green ellipse) it acquires a phase of -1 .

e with an m excitation. This operation cannot be carried out exactly as plaquettes and vertices are not located at the same places. However, we can consider a *double* exchange thereof which is topologically equivalent to moving an electric charge *around* a magnetic vortex (or vice versa) — also referred to as *braiding*. As depicted in Fig. 9.3 this movement corresponds to applying a closed-string operator enclosing one magnetic vortex. The procedure results in a phase of -1 acquired by the total state. To see this, we note that precisely one spin is affected by *two* string operators — the open string creating the pair of magnetic vortices and the closed string performing the double exchange. The first action on the ground state is a σ^z operator, yielding the initial state before the braiding $|\text{init}\rangle = \sigma_i^z |\Psi_{\text{GS}}\rangle$. Using the anti-commutation relation $\{\sigma_i^x, \sigma_i^z\} = 0$ we obtain after applying the closed string operator for the closed string \mathcal{C} which contains σ_i^x

$$S_{\mathcal{C}}^{(e)} |\text{init}\rangle = S_{\mathcal{C}}^{(e)} \sigma_i^z |\Psi_{\text{GS}}\rangle = -\sigma_i^z S_{\mathcal{C}}^{(e)} |\Psi_{\text{GS}}\rangle = -|\text{init}\rangle, \quad (9.10)$$

because the closed string operator commutes with the Hamiltonian and therefore stabilizes the ground state. Thus, we get the total phase of -1 for the double

³Since no two excitations can be located at the same four-body operator they can be described as *hard-core* bosons.

exchange. The relative phase R_{em} of a single exchange $e \longleftrightarrow m$ must satisfy $R_{\text{em}}^2 = -1$ which implies $R_{\text{em}} = \pm i$ — being neither bosonic nor fermionic. We conclude that the quasiparticles corresponding to the electric and magnetic excitations are so-called *mutual anyons*⁴, i.e., they can have *any* statistics with $|R| = 1$. The fact that braiding of anyonic quasiparticles can produce non-trivial phases is a characteristic feature of anyons and opens up an approach to not only *store* but also perform quantum *computations* on the encoded qubit [10, 138]. However, this feature immediately disqualifies the two-dimensional toric code model as a quantum memory: Suppose, we have a pair of electric defects in our configuration. Two different Wilson-loop operators in the same spatial direction with one of the defects between them read off *different* winding number parities which means that the stored information is inconsistent, i.e. lost [139]. This braiding phenomenon is unique to two-dimensional systems as in higher dimensions, the paths of quasiparticles winding around each other can smoothly be transformed into non-braiding paths.

9.2.4. Loop tension

Energetic excitations cause the system to leave the ground state representing the code space. Another such violation of the code can be induced by external perturbations of the Hamiltonian (9.2). We discuss a longitudinal magnetic field in the σ^z direction leading to a modified Hamiltonian

$$H = -J_p \sum_{p \in P} A_p - J_v \sum_{v \in V} B_v - h_z \sum_i \sigma_i^z, \quad (9.11)$$

for a field strength $h \geq 0$. Due to the duality of plaquettes and vertices in the Hamiltonian, a field h_x in the σ^x direction would represent an equivalent perturbation. This problem has been considered in Ref. [140]. The effect of such an external field at low temperatures is that loops of spins pointing down with respect to the σ^z direction are energetically hindered. Upon increasing the field strengths, such loops will hence be further and further contracted which is why we can also dub h as the *loop tension*.

The ground state of the Hamiltonian (9.11) can be mapped onto a two-dimensional Ising model in a transverse field on a square lattice if we consider a large charge gap, i.e. $J_v \gg J_p$. Charge excitations are hence ‘frozen out’ such that only closed loops of σ^z spins up are possible. These loops are mapped to domain walls in the corresponding Ising model. To this end, we place Ising degrees of freedom — labeled by $\mu_i^{x/z}$ — in the centers of the plaquettes and choose their value according to $\mu_i^z \mu_j^z = \sigma_k^z$, where k is the edge in the toric code model separating the Ising sites i and j . Every plaquette term in Hamiltonian (9.11) is represented by the σ^x component μ_p^x of the Ising spins since flipping a whole plaquette in the toric code corresponds to flipping a single spin in the Ising model. The Hamiltonian for the

⁴In the special case, where a double exchange yields an ‘ordinary’ statistics of ± 1 this kind of quasiparticles are dubbed *mutual semions*.

9. Quantum error-correcting codes

Ising model in a transverse field reads

$$H_{\text{TFIM}} = -J^{(\text{Is})} \sum_{\langle i,j \rangle} \mu_i^z \mu_j^z - h_x^{(\text{Is})} \sum_i \mu_i^x, \quad (9.12)$$

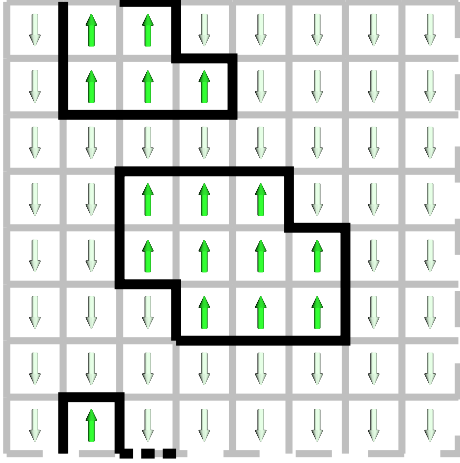


Figure 9.4.: Mapping between the toric code model (edges) with a longitudinal loop tension and the two-dimensional Ising model (green spins) in a transverse field. Loops in the toric code (thick black edges) are translated to domain walls in the Ising model. Two neighboring Ising spins μ_i, μ_j have opposite orientation, if the spin on the toric code edge separating them points down.

polarized with respect to the σ^x basis. This transition occurs at a critical ratio $(J^{(\text{Is})}/h_x^{(\text{Is})})_c = 0.65695(2)$ determined in Ref. [141]. Ferromagnetic order in the Ising model corresponds to the absence of spin down loops in the toric code model. This phase is hence trivial in the toric code, that is, polarized to spin up. Its ground state is not degenerate as a state with a single winding loop would have an energy difference of at least $\Delta E = 2Lh_z$ to the ground state, L being the linear size of the system. The disordered phase of the Ising model, however, translates to a loopgas of the toric code — which is the topologically ordered phase. Setting $h_x^{(\text{Is})} = J_p = 1$ for simplicity, we can sketch the phase transition in the one-dimensional phase diagram shown in Fig. 9.5. The two-dimensional Ising model with a transverse field is equivalent to a 3D classical Ising model with anisotropic interaction in one dimension [142]. Thus, a full characterization of the discussed phase transition is known in terms of a local order parameter and critical exponents. Using topological entanglement entropies, this phase transition⁶ can be complementary studied from the perspective of topological order.

which reveals that loop tension and interaction terms have switched roles, $J^{(\text{Is})} = h_z$ and $h_x^{(\text{Is})} = J_p$. The mapping is depicted in Fig. 9.4. It is clear that one specific toric code configuration is represented by *two* Ising configurations related by a global flip of all Ising spins. Hence, the \mathbb{Z}_2 symmetry of the Ising model is not present in the toric code. We note that only the ground state without odd winding numbers is captured by this mapping. Separate mappings would have to be defined for the other three ground states of the toric code model by introducing *anti*-periodic boundary conditions in the appropriate lattice dimension(s). Hence, as expected, the mapped Ising model does not contain topological order⁵.

Upon increasing $h_x^{(\text{Is})}$, the Ising model in a transverse field undergoes a quantum phase transition from a ferromagnetically ordered phase of the σ^z spins to a paramagnetic phase which is

⁵One can argue that topological order is hidden in the domain walls of the Ising configuration.

⁶To avoid confusion, we note that this phase transition is not what is meant by *topological phase transitions*. The latter are transitions between different topologically ordered phases but not to topologically trivial phases like in our case.

We note that more general forms for the external field have been considered. For the toric code in a two-component parallel field (h_x, h_z) a phase diagram in the h_x - h_z -plane has been obtained in Ref. [143]. Beyond a topologically ordered phase for low- h_x and low- h_z there are two other phases — one for low- h_x and large- h_z and vice versa. These phases are characterized by spin-flip excitations either in the σ^x or the σ^z direction. They are separated by a first-order transition line at $h_x = h_z$ ending in a critical point. A transverse external field (σ^y) has been considered in Ref. [144]. Its presence deprives the Hamiltonian of its solvability via local eigenspaces of the four-body operators since they no longer commute with the Hamiltonian.

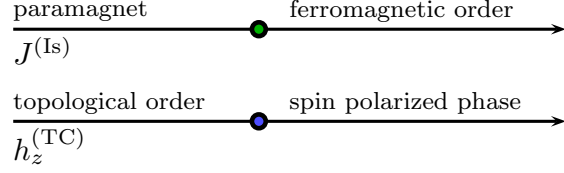


Figure 9.5.: One-dimensional phase diagram for the transverse field Ising model (top arrow) upon increasing the coupling $J^{(\text{Is})}$ at fixed transverse field. The same transition occurs in the mapped toric code (bottom arrow) upon increasing the external field $h_z^{(\text{TC})}$.

9.2.5. Classical variant

The fact that the ground state is exactly solvable and can be represented in the product basis of σ^z eigenstates of single degrees of freedom opens up the possibility to define a classical analogue of the toric code model [122]. Moreover, the topological nature of the ground state can be perceived in the entirety of allowed closed-loop states in the σ^z representation. It is hence obvious that a classical perspective likewise reflects some sort of topological order.

We obtain the classical toric code model by taking Ising spins $\sigma_i = \pm 1$ as our classical degrees of freedom instead of quantum spins. The ground state condition of closed loops is translated to a hard constraint on the allowed spin configurations of the classical spins. Additionally, the superposition of the ground state, Eq. (9.6), induced by the σ^x plaquette terms in the Hamiltonian (9.2) is accounted for by defining a *statistical mechanics ensemble* of all allowed loop states — all equally weighted. In this ensemble, we do not distinguish between loop states with different winding number parities such that the classical partition function is simply given by

$$Z = \sum_{\sigma \in \mathcal{L}} 1, \quad (9.13)$$

where \mathcal{L} denotes the set of all closed-loop configurations of Ising spins. Nevertheless, this ensemble is partitioned into the same four sectors as the ground state of the quantum toric code. The sectors are separated by the impossibility of a transition between them by local changes of the configuration — *topological ergodicity breaking* [122]. In this classical adaptation we have directly translated the vertex operators $\sigma_{v_1}^z \sigma_{v_2}^z \sigma_{v_3}^z \sigma_{v_4}^z \rightarrow \sigma_{v_1} \sigma_{v_2} \sigma_{v_3} \sigma_{v_4}$ at $T = 0$. Alternatively, we could have done this procedure with the plaquette operators which yields a completely equivalent classical model due to the self-duality of the quantum toric code. Sticking with our choice, we further find that charge excitations of the quantum system are

9. Quantum error-correcting codes

representable by extending the ensemble to configurations $\mathfrak{s} \in \mathcal{S}$ with open strings. We assign variable weights to these configurations according to

$$w(\mathfrak{s}) = \exp(-\beta J_v N_e), \quad (9.14)$$

where N_e is the (even) number of charges in the configuration \mathfrak{s} . The other type of excitations — magnetic vortices — is *not* captured by our classical variant. Remembering that these excitations are represented in the quantum case by minus signs in Eq. (9.6), i.e. by relative phases of the configurations written in the σ^z representation, we understand that we cannot keep them when going to the classical toric code: We cannot assign negative weights to configurations in a statistical mechanics ensemble. Hence, in a certain way, the classical variant reflects ‘half’ of the quantum case (the other half exhibiting the same physics). Together with the realization [11] that each of the two types of excitations is responsible for half of the topological entanglement entropy $S_{\text{topo}}^{(\text{quantum})}$ in the ground state, we conclude for the classical variant $S_{\text{topo}}^{(\text{classical})} = S_{\text{topo}}^{(\text{quantum})}/2$. We can use the classical variant to study the finite-temperature behaviour of S_{topo} .

Applying a finite loop tension h to the classical toric code model at zero temperature, leads to a Hamiltonian

$$H^{(\text{cl})} = -J_v \sum_v \sigma_{v_1} \sigma_{v_2} \sigma_{v_3} \sigma_{v_4} - h \sum_i \sigma_i. \quad (9.15)$$

As any finite temperature $T > 0$ would immediately polarize the resulting model we exclude the temperature from the weights in our ensemble. In this scenario, again only closed loops are allowed but this time with variable weights

$$w(\mathfrak{o}) = \exp(-hm_o), \quad (9.16)$$

where m_o is the total loop length of all loops consisting of spins down. This choice implicitly assumes a non-zero temperature T with $J_v \ll T \ll h$ such that the constraint to closed loops is implemented but the loop tension does not freeze the state in a polarized configuration. This model can be mapped in the same manner as shown in Fig. 9.4 to a two-dimensional *classical* Ising model at finite (inverse) temperature β without perturbations. We have the analogies $h^{(\text{TC})} \leftrightarrow J^{(\text{Ising})}$ and $m_o^{(\text{TC})} \leftrightarrow E^{(\text{Ising})}$. Again, the mapping is restricted to the sector of the ensemble which has an even parity for the winding number in both lattice dimensions. The mapped Ising model is known [135] to have a phase transition at $\beta_c = \ln(1 + \sqrt{2})/2 \approx 0.44069$ which maps directly to the critical loop tension h_c for the classical toric code model. This mapping allows us to investigate this known phase transition in terms of topological entanglement entropies of its dual system.

9.3. Three-dimensional ‘toric’ code

When defining a three-dimensional variant of the toric code model we can straightforwardly adapt an appropriate lattice structure — a simple cubic lattice with degrees of freedom located on the edges. A suitable Hamiltonian on an lattice of size

$N = L \times L \times L$ has been defined by Castelnovo and Chamon [139] and — written in terms of vertices and plaquettes — is identical to the two-dimensional Hamiltonian (9.2). However, the N vertices have *six* spins in this case and the $3N$ plaquettes exist in three different orientations according to the three planes $\langle xy \rangle, \langle xz \rangle, \langle yz \rangle$, see Fig. 9.6. The Hamiltonian hence reads

$$H = -J_p \sum_{\substack{e \in \{\langle xy \rangle, \langle xz \rangle, \langle yz \rangle\} \\ p \in P}} \sum_{p \in P} A_p^{(e)} - J_v \sum_{v \in V} B_v, \quad (9.17)$$

with $A_p^{(e)} = \sigma_{p_1}^x \sigma_{p_2}^x \sigma_{p_3}^x \sigma_{p_4}^x$ and $B_v = \sigma_{v_1}^z \sigma_{v_2}^z \sigma_{v_3}^z \sigma_{v_4}^z \sigma_{v_5}^z \sigma_{v_6}^z$.

We employ periodic boundary conditions in all dimensions. Just like in the two-dimensional case all vertex and plaquette operators commute and their quantum numbers are ± 1 . The states of the total system can be constructed using the local eigenstates of these operators and represented in a superposition of configurations in the σ^z eigenbasis. In terms of constraints on the possible states established by the multi-body operators $A_p^{(e)}$ and B_v once their quantum numbers are fixed, we count $N - 1$ independent vertex operators since the quantum number of the last one is already determined by all others. The interdependency of the plaquette operators is higher: The product of the six plaquette operators around every cube must be unity which introduces one constraint per cube except for the last cube which is satisfied through the others. In addition, the remaining $3N - (N - 1)$ plaquette operators must be further reduced by three due to the global constraints that all plaquette operators belonging to one plane ($d = x, y, z$) likewise multiply to unity. Hence, there are $2N - 2$ independent plaquette operators in the three-dimensional toric code.

The ground state is given by setting all vertex and plaquette operator eigenvalues to 1. This results in closed σ^z loops enforced by the vertex terms in possible spin configurations. Superpositions thereof are required to satisfy the plaquette terms of the Hamiltonian (9.17). The ground state degeneracy is 2^3 which can be understood from the presence or absence of non-contractible loops winding around one of the three lattice directions. Alternatively, counting the remaining possible states of the $3N$ degrees of freedom also yields $2^{3N - (N - 1) - (2N - 2)} = 8$. The detection of the winding number parity determining the ground state is enabled by non-local winding *plane* operators, see Fig. 9.6. In the σ^x basis, the characterization of the degenerate ground states is ‘dual’ to the picture in the σ^z basis. To see this, note that a common flip of all (equally oriented) edges in a plane of the lattice does not change the quantum number of any plaquette operator. This operation, however, cannot be obtained by a series of local operations leaving the Hamiltonian invariant — vertex flips. Thus, the presence or absence of winding planes of σ^x spins separates the eight degenerate ground states and they are identified by winding *loops*.

We have already seen that in the ground state the global structures (or ‘patterns’ in the sense of Sec. 8.1) of the spin configurations represented in the σ^z basis are closed loops along edges of the lattice. These loops can be created and annihilated by applying the plaquette terms $A_p^{(e)}$ to a spin configuration. In the σ^x basis, energy-preserving modifications of the spin configuration are obtained by applying the vertex operators B_v . This results in flipping all six spins at the corresponding vertex. Hence, the underlying structure in this basis are *membranes* of spins having

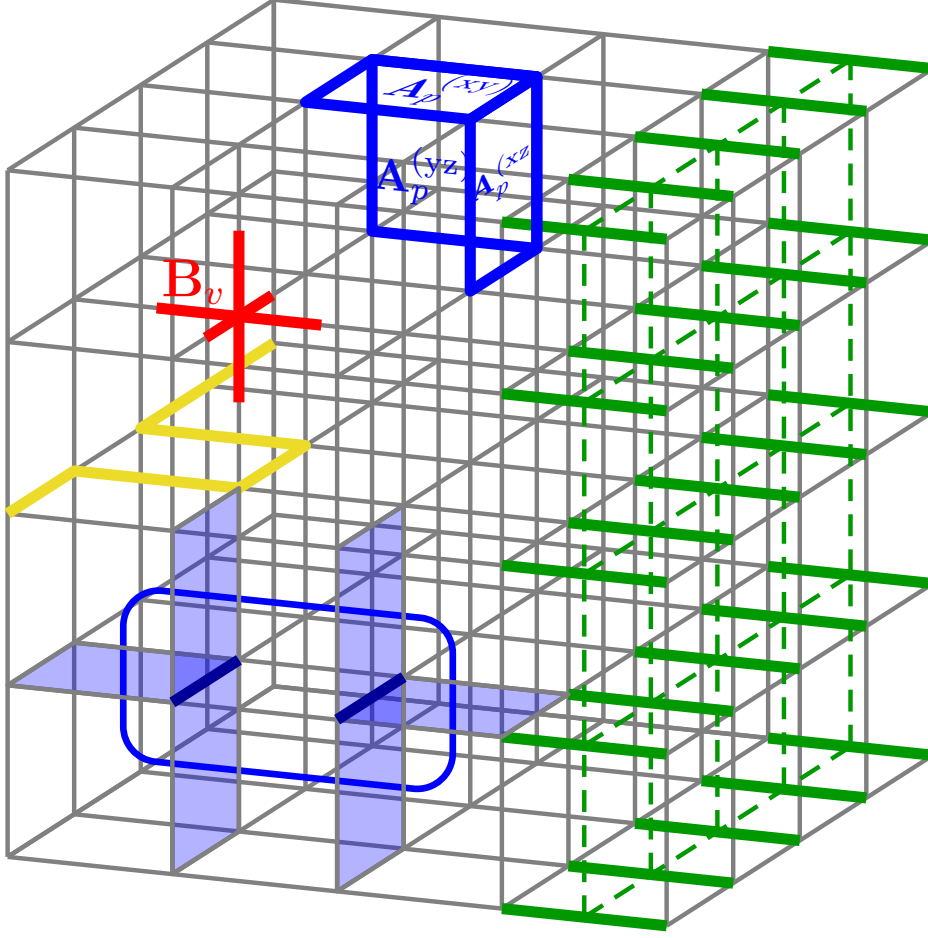


Figure 9.6.: Illustration of the three-dimensional toric code model. Vertex operators (red) are products over the σ^z component of six edges. Plaquettes (blue) appear in three different orientations and each are products over four σ^x components. The vertex constraints gives rise to closed loops, among them winding loops (yellow). The green edges represent Wilson planes for the identification of the topological sector from winding loops. At the same time, if interpreted in the σ^x basis, they depict the winding membranes of the plaquette constraints. Excitations of the plaquettes (blue shaded squares) result in loop-like objects if they are connected by a line which orthogonally crosses the plaquettes. Point-like excitations of the vertex operators B_p are not shown.

the same (x -)orientation.

Beyond the ground state, energetic excitations of the Hamiltonian (9.17) come in two forms: Pairs of vertices can have a quantum number -1 which are connected by an open string of equally-oriented spins in the σ^z basis. These excitations are point-like and can be created by single-spin flips and moved apart from each other without the investment of additional energy. As a consequence, such a pair of excitations can move around the lattice at any finite temperature, mutually annihilate and thereby leave the state in another ground state. Hence, the point-like excitations are deconfined. This is different for the excitation of plaquette operators. A single-spin flip of a σ^x -spin (effected by the application of a σ^z spin operator) switches the quantum numbers of the *four* plaquettes that this spin is part of. Moreover,

the excited plaquettes can only be moved apart at the cost of *additional* plaquette flips, such that flipped plaquettes fringe the trajectory of the separation. As seen in Fig. 9.6, the structure of these excitations is hence *loop-like* and the excitations are *confined*, i.e. the loops tend to contract at lowering the energy. In contrast to the point-like excitations, the emergence of a single winding plane as a result of increasing the loop-like excitation is energetically suppressed at sufficiently low *but finite* temperature. This gives rise to a survival of topological order above zero temperature [139].

9.3.1. Classical variants

Two different classical variants can be formulated from Eq. (9.17). Either the plaquette or the vertex terms are written in terms of Ising spins $\sigma_i = \pm 1$, yielding

$$H_{(\text{plaq})}^{(\text{cl})} = -J_p \sum_{p \in P} \sigma_{p_1} \sigma_{p_2} \sigma_{p_3} \sigma_{p_4}, \quad (9.18)$$

$$H_{(\text{vert})}^{(\text{cl})} = -J_v \sum_{v \in V} \sigma_{v_1} \sigma_{v_2} \sigma_{v_3} \sigma_{v_4} \sigma_{v_5} \sigma_{v_6}. \quad (9.19)$$

The respective abandoned interaction term is translated into the statistical ensemble where all allowed spin configurations have the same weight, in complete analogy with the two-dimensional case, see above. A finite temperature $T > 0$ in the classical systems introduces point-like (loop-like) excitations in the spin configurations for the vertex (plaquette) variant, respectively. Using the classical topological entropy (8.3), we can investigate whether topological order is present above zero temperature. The classical plaquette variant is a known 3d gauge Ising model [145] at finite temperature, which has a phase transition at $\beta_c \approx 0.76141$. We hence expect the classical topological entropy to leave a signature at this critical inverse temperature.

Further, we have discussed above that the plaquette terms impose a membrane structure on the spin configurations. This insight suggest to identify such a toric code configuration with a three-dimensional Ising model configuration via a mapping from membrane surfaces to domain walls of Ising spins. The Ising spins are located at the vertices of the three-dimensional lattice, see Fig. 9.7. The equivalence of all possible membranes in the ground state of the toric code corresponds to the Ising model at infinite temperature, that is, $\beta^{(\text{Is})} = 0$. Hence, it is worthwhile to consider a modified classical plaquette

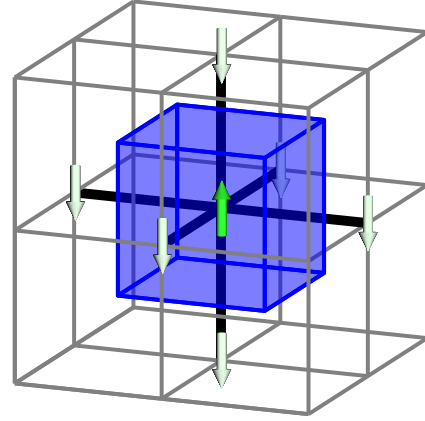


Figure 9.7.: Mapping of the three-dimensional toric code model to a three-dimensional Ising model with spins (green) located at the vertices. The energetic cost of a toric code spin oriented against the external field (black edges) corresponds to a domain wall (blue surfaces) in the Ising model.

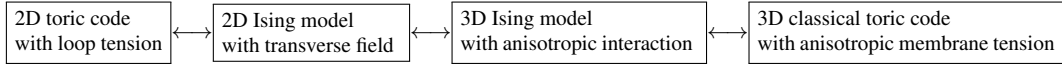
9. Quantum error-correcting codes

variant of the toric code which exhibits an external magnetic field, appropriately dubbed *membrane tension* h ,

$$H_{(\text{plaq})}^{(\text{cl})} = -J_p \sum_{p \in P} \sigma_{p_1} \sigma_{p_2} \sigma_{p_3} \sigma_{p_4} - h \sum_i \sigma_i. \quad (9.20)$$

Assuming $J_p \gg h$, we construct the statistical mechanics ensemble for Eq. (9.20) with Boltzmann weights $w(\mathbf{m}) = \exp(-hm_{\mathbf{m}})$, where \mathbf{m} represents a closed-membrane configuration and $m_{\mathbf{m}}$ is the associated total magnetization. In the mapping to the three-dimensional Ising model we can identify a *finite* temperature with the membrane tension, $\beta^{(\text{Is})} \leftrightarrow h$. The three-dimensional Ising model has a phase transition at $\beta_c^{(\text{Is})} \approx 0.221656(3)$, determined in Ref. [146]. Accordingly, the Hamiltonian (9.20) undergoes a phase transition for $h_c = \beta_c^{(\text{Is})}$ from the topologically ordered low- h phase to a trivial polarized phase.

We can easily add one more level of complexity in the Hamiltonian (9.20) by making the membrane tension h anisotropic, i.e. dependent on the orientation of the edge in the toric code model. In particular, we apply a different membrane tension h_z on the spins on the vertical edges in the three-dimensional toric code than on those spins in the x - y -plane. The motivation for this is that the corresponding mapped Ising model has anisotropic interactions and represents at the same time the quantum-to-classical mapping of a two-dimensional (quantum) Ising model in a transverse field. As we have seen above in Eq. (9.12), this model then again is equivalent to the two-dimensional toric code model at the ground state with a finite loop tension, Eq. (9.11). To sum up the series of mappings we have:



Since the toric code models in these mappings both exhibit topological order, we can investigate the quantum phase transition of the two-dimensional toric code model with a finite loop tension using the topological entropy analysis in a classical three-dimensional toric code. To do so, we adapt the quantum-to-classical mapping of the Ising model [142] to our needs. The lattice spacing in the additional (imaginary-time) dimension of size L_τ of the classical system is $\Delta\tau = L_\tau/\beta$. We obtain for a loop tension $h^{2\text{D-TC}}$ in the two-dimensional toric code

$$h_{xy}^{3\text{D-TC}} = \frac{1}{2} \Delta\tau h^{2\text{D-TC}} \quad \text{and} \quad h_z^{3\text{D-TC}} = -\frac{1}{2} \ln \tanh(\Delta\tau) \quad (9.21)$$

for the classical three-dimensional toric code with anisotropic membrane tension. We further use the simplification employed in Ref. [140], namely fixing $\Delta\tau \approx 0.76141$ which satisfies $h_{xy}^{3\text{D-TC}} = h_z^{3\text{D-TC}} = \beta_c^{(\text{Is})} \approx 0.221656$, such that the critical behavior is represented by the *isotropic* case. The resulting critical loop tension is slightly below the exact value of the transverse field Ising model, $h^{2\text{D-TC}} \approx 0.5822 < 0.65695$ but the long-distance physics is the same [140]. We can hence tune $h^{2\text{D-TC}}$ through the quantum phase transition by means of the correspondence in Eq. (9.21) using a classical system and effectively tune $h_{xy}^{3\text{D-TC}}$.

9.4. X-cube code

We present another commuting Pauli Hamiltonian defined on the same three-dimensional lattice as before — a simple cubic lattice with degrees of freedom located on the edges. The *X-cube* code has been proposed by Vijay *et al.* [147] and involves four-body vertex terms $B_v^{(e)}$ of σ^z operators coming in three different orientations as well as twelve-body cube terms A_c of σ^x operators, see Fig. 9.8. Its Hamiltonian is hence given by

$$H = -J_c \sum_{c \in C} A_c - J_v \sum_{\substack{e \in \{\langle xy \rangle, \langle xz \rangle, \langle yz \rangle\} \\ v \in V}} B_v^{(e)}, \quad (9.22)$$

with $A_c = \prod_{i \in \partial c} \sigma_i^x$ and $B_v^{(e)} = \sigma_{v_1}^z \sigma_{v_2}^z \sigma_{v_3}^z \sigma_{v_4}^z,$

where C is the set of all cubes in the lattice and ∂c denotes the twelve spins belonging to cube c . We observe that any pair of vertex and cube operators share either zero or two spins and hence commute. Exactly as in the previously discussed models it is possible to solve the X-cube in terms of eigenvalues ± 1 and eigenstates of the local multi-body operators. A classical variant using Ising spins can be derived from either type of operators and considered separately — yielding a cube and a vertex variant.

In the following consideration of the excitations of the X-cube model we adopt the bisected classical perspective. For simplicity, let us start from the ground state, i.e. all cubes or vertices are in their $+1$ state. At first, we see that flipping a single spin in the *cube variant* induces an excitation of the four cubes that the spin is part of. The four excited cubes can be moved apart by flipping additional spins that belong to at least one of them. Here, we can distinguish between energetically neutral movements (exciting two and relaxing two cubes) and those accompanied by a net change of the energy (exciting three and relaxing one cube or vice versa). It is possible to move pairs of excited cubes around the periodic lattice and annihilate them — thereby creating a winding loop of spins down. In addition, the cube variant also allows for winding planes which have exactly the same form as the green edges in Fig. 9.6. This occurrence of both non-contractible loops and planes for the cube term is a remarkable feature of the X-cube model. In the *vertex variant*, a single spin flip likewise switches the four corresponding vertices.

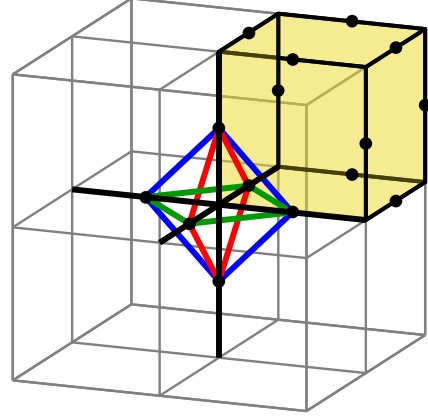


Figure 9.8.: The X-cube model is defined on a cubic lattice with spin-half degrees of freedom located on the edges. It exhibits a cube interaction term (yellow) multiplying the twelve σ^x components of the spins and three differently oriented vertex terms (blue, red, green) of four σ^z components. Flipping single spin excites four cubes (vertices), if the flip is considered in the σ^x (σ^z) basis, respectively.

9. Quantum error-correcting codes

Moving them pairwise apart without additional energy is possible but only along one axis of the lattice. ‘Turnings’ of such strings leave behind a pair of excited vertices at the resulting corner of the string, which implies a change in the energy of the string.

We conclude that the structure of the excitations of the X-cube model is richer than in the three-dimensional toric code discussed above. However, the fact that the topological sectors of the σ^x basis have to be read out by string operators disqualifies the X-cube model to be a self-correcting quantum memory according to the no-go theorem [148].

9.5. Cubic code

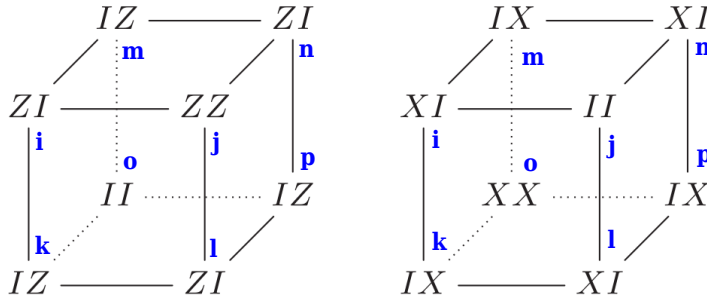


Figure 9.9.: Representation of the cubic code by Haah. Each cube displays one of the eight-body interactions. The two upper-case letters at every corner of the cube denote the Pauli matrix for the σ_i (left letter) and the ρ_i (right letter) spin type. I is the identity matrix, i.e. the respective spin does not show up in the interaction. The blue letters label the indices with respect to the shown cube c used in the explicit Hamiltonian formulation (9.23).

An attempt to design a self-correcting quantum memory in three dimension has been made by Haah [149] who defined a stabilizer code which does not exhibit string logical operators such that a no-go theorem [148] is not applicable. We introduce this *cubic code* model very briefly and refer to Refs. [125, 134, 147] for a more detailed discussion regarding its (un)ability

to be a self-correcting quantum memory.

The cubic code is defined on a regular cubic lattice with *two* spin-half degrees of freedom (σ_i, ρ_i) located at every vertex. Its Hamiltonian consists of one eight-body operator of σ^x and one of σ^z matrices and can be sketched as in Fig. 9.9. This representation translates to

$$H = -J_1 \sum_{c \in C} \sigma_i^z \sigma_j^z \sigma_l^z \sigma_n^z \rho_j^z \rho_k^z \rho_m^z \rho_p^z - J_2 \sum_{c \in C} \sigma_i^x \sigma_l^x \sigma_n^x \sigma_o^x \rho_k^x \rho_m^x \rho_o^x \rho_p^x, \quad (9.23)$$

where the indices of the Pauli operators follow from setting each cube c to the one shown in Fig. 9.9.

In contrast to the previously discussed models, the ground state degeneracy $g(L)$ of the cubic code strongly depends on the linear system size L of the lattice. We have $g(L) = 2^{k(L)}$ for the number of encoded qubits $k(L)$ in the model

$$k(L) = 2 \left[1 - 2q_2 + 2^{r+1}(q_2 + 12q_{15} + 60q_{63}) \right],$$

where r is the largest integer such that 2^r divides L and $q_n(L)$ is the divisibility function (1 if n divides L and zero otherwise) [149]. Obviously, any odd L has the

9.5. Cubic code

lowest possible degeneracy of 2^2 , whereas if L is a power of two, the degeneracy is large (compared to L), see Tab. 9.1.

L	2	3	4	5	6	7	8	9	10	11	12
$g(L)$	64	4	16,384	4	64	4	1,073,741,824	4	64	4	16,384

Table 9.1.: Degeneracies of the ground state of the cubic code for the system sizes $L \leq 12$.

10. Monte Carlo approach

The determination of expectation values of observables in a statistical mechanics ensemble in general implies the computation of a thermal average and the corresponding partition function. For discrete lattice systems, such an average is simply a sum over the usually very large configuration space. Often, the exact calculation of the sum is computationally inaccessible within an acceptable time due to the sheer multitude of summands. *Monte Carlo simulations* constitute an approximative method to this endeavor which estimates the thermal average from a significantly smaller subset of configurations carefully selected such that they adequately represent the total configuration space. The selection of configurations is carried out in a sequential way via a *Markov chain* of configurations — a random process generated on a computer by (*pseudo*)random numbers. For every visited configuration in the Markov chain the observable of interest is *measured*. Finally, the statistical average of these measurements is computed and represents the simulation result of the physical observable.

In this Chapter, we present the Monte Carlo approach that we employ in order to compute the specific heat and the topological Rényi entropies of the classical code models introduced in the previous Chapter. We first discuss in Sec. 10.1 how the two quantities can be measured and how the inevitable replica trick is implemented. After having chosen an appropriate representation of the configuration on the computer, a major challenge in the conception of a Monte Carlo algorithm is to design an *update scheme*, that is, a recipe for the proposal of a new configuration to be adopted next in the Markov chain. In Sec. 10.2 we briefly introduce conditions on this update before turning to the discussion of various forms — of both local and global nature — specifically adapted to the codes and to the replicated system.

10.1. Representation and measurement

We first explain how the specific heat can be obtained using local energy measurements on the original lattice of the code models. Subsequently, we turn to the topological entropies, which are non-local concepts. Their measurement is more complex and requires resorting to partition functions incorporating the replica trick (see Section 2.2.2.1). Having modified the lattice appropriately we clarify how the resulting partition function is measured. Finally, we discuss addition schemes to extract the constant correction γ of the Rényi entropies.

10.1.1. Specific heat

Continuous phase transitions in the Landau paradigm are manifested in a universal divergence of the *specific heat*, defined as $C_v = \partial \langle E \rangle / \partial T$. Therefore, we are

10. Monte Carlo approach

interested in measuring this quantity in the finite-temperature investigations of our models. A brute force approach to this endeavor would be to measure the energy E for a dense range of temperatures in a simple¹ representation of the model and numerically perform the above derivative. A more direct measurement is enabled by using $\langle E \rangle = -\partial \ln Z / \partial \beta$ and observing

$$\begin{aligned}
 C_v &= -\beta^2 \frac{\partial \langle E \rangle}{\partial \beta} \\
 &= \beta^2 \frac{\partial^2 \ln Z}{\partial \beta^2} \\
 &= \beta^2 \left[\frac{1}{Z} \frac{\partial^2 Z}{\partial \beta^2} - \frac{1}{Z^2} \left(\frac{\partial Z}{\partial \beta} \right)^2 \right] \\
 &= \beta^2 (\langle E^2 \rangle - \langle E \rangle^2).
 \end{aligned} \tag{10.1}$$

Hence, it is sufficient to measure E and E^2 in the Monte Carlo simulation to obtain the specific heat. In practice, we compute the expectation value of C_v and its statistical error from the Monte Carlo data using bootstrapping².

10.1.2. Topological entropy

The approximative computation of the classical Rényi entropies with $\alpha = 2$, defined in Eq. (8.7), is possible without explicitly determining *all* subsystem probabilities p_A of the states. To this end, two obstacles have to be overcome. First, the entropies are not thermally weighted averages of an observable but sums of the probabilities (weights) alone. As we will see below these sums can be turned into the partition function of a modified system, via a classical variant of the replica trick. This resort entails the second obstacle, namely that Monte Carlo simulations cannot access partition functions directly. However, a thermodynamic integration from energy measurements can recover the partition function. Finally, we have to extract the constant contribution from the Rényi entropy. The general strategy how this is done has been discussed in Sec. 8.2. In this Section, we will upgrade the procedure to the three-dimensional cases.

10.1.2.1. Replica trick

For classical Rényi entropies of integer order α , the replica trick (Sec. 2.2.2.1) is conceptually simpler than for the quantum case. Its adaptation has been worked out in Ref. [123]. Taking $\alpha = 2$, it is implemented by considering two copies of the system and *identifying* all degrees of freedom in subsystem A , see Fig. 10.1. As a consequence, a local change of the configuration in subsystem A induces twice the energetic or magnetic difference than the same change in subsystem B . To put

¹By ‘simple’ we mean the absence of any replica trick related modifications of the model.

²The resampling technique of bootstrapping [150] simply generates N normal distributed samples of E and E^2 based on the mean and variance returned by the Monte Carlo simulation. N samples of the specific heat are then computed using Eq. (10.1) and all energy samples. The mean and variance of this set of specific heat samples is taken as our measurement result.

it differently, subsystem A is effectively held at twice the inverse temperature β or loop tension h considered. The partition function associated with this system is denoted by $Z[A, \alpha, \beta]$ or $Z[A, \alpha, h]$ and together with the ordinary partition function Z of the unaltered system, we obtain the Rényi entropy as in Eq. (2.8). The imposed synchronization of the spins in subsystem A entails possible complications for all Monte Carlo updates in closed-loop states since they may affect spins in both parts.

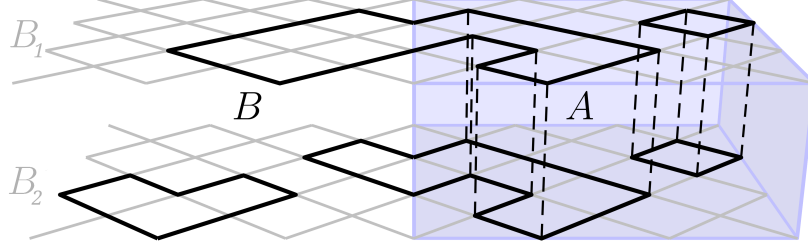


Figure 10.1.: Representation of the replicated systems on which the modified partition function is defined. In the depicted case of $\alpha = 2$, we have two copies of the system. The degrees of freedom in part B are independent over the replicas, while those in part A have to be the same.

10.1.2.2. Thermodynamic integration

The replica trick transfers the problem of computing the Rényi entropies to the computation of partition functions. As pointed out, they are not directly accessible in a Monte Carlo measurement. However, thanks to the previously used identity $\langle E \rangle = -\partial \ln Z / \partial \beta$, we can perform a thermodynamic integration [27] over β to obtain $\ln Z$ for finite temperature studies. We write the Rényi entropies as

$$\begin{aligned} S_\alpha(A) &= \frac{1}{1-\alpha} [-\ln Z[A, \alpha, \beta] + \alpha \ln Z(\beta)] \\ &= \frac{1}{1-\alpha} \left[\ln Z[A, \alpha, 0] + \int_0^\beta \langle E \rangle_{A, \beta'} d\beta' - \alpha \ln Z(0) - \alpha \int_0^\beta \langle E \rangle_{0, \beta'} d\beta' \right]. \end{aligned} \quad (10.2)$$

Hence, we can measure the *energy* in our Monte Carlo simulations for a sufficiently dense range of inverse temperatures β and numerically perform the integration. Additionally, the knowledge of the Rényi entropy at infinite temperature, $S_\alpha(A)|_{\beta=0} = (-\ln Z[A, \alpha, 0] + \alpha \ln Z(0))/(1-\alpha)$ is necessary in order to obtain our finite temperature values of $S_\alpha(A)$. This is in general not a serious issue since the entropy mostly vanishes either for $\beta = 0$ or for $\beta = \infty$. In the latter case $S_\alpha(A)|_{\beta=0}$ can be reverse engineered by performing the integration with an initial guess and subsequently adapting it such that the data for large β approach zero.

The thermodynamic integration for the cases where we consider the behavior for finite isotropic loop tension is completely analogue. We have $\langle m \rangle = -\partial \ln Z / \partial h$ such that we simply have to replace the energy E by the magnetization m and

10. Monte Carlo approach

perform the integration over a range of loop tensions h . A special situation arises for anisotropic loop tensions, i.e. $h_x = h_y \neq h_z$, as considered in Eq. (9.21). The derivative of $\ln Z$ with respect to the parameter h_x , which we want to manipulate, only affects one part of the Boltzmann weights $\exp(-\mathbf{h}\mathbf{m}) = \exp[-h_x(m_x + m_y) - h_z m_z]$. However, the unaffected part $\exp[-h_z m_z]$ is not necessarily a constant over the range of values for h_x and hence needs to be considered for a computation of Z . We therefore have to carry out simulations for a range of h_z values as well, such that we can use

$$\begin{aligned} \frac{\partial^2 \ln Z}{\partial h_z \partial h_x} &= -\frac{\partial}{\partial h_z} \left(\frac{1}{Z} \sum_{\mathbf{o} \in \mathcal{L}} m_{xy}(\mathbf{o}) e^{-\mathbf{h}\mathbf{m}(\mathbf{o})} \right) \\ &= \frac{1}{Z} \left(\frac{\partial Z}{\partial h_z} \right) \langle m_{xy} \rangle + \frac{1}{Z} \sum_{\mathbf{o} \in \mathcal{L}} m_{xy}(\mathbf{o}) m_z(\mathbf{o}) e^{-\mathbf{h}\mathbf{m}(\mathbf{o})} \\ &= \langle m_{xy} m_z \rangle - \langle m_{xy} \rangle \langle m_z \rangle, \end{aligned} \quad (10.3)$$

where m_{xy} denotes the magnetization of all edges in the xy -planes of the model. The thermodynamic integration consequently has to be performed for a dense grid of longitudinal and transverse loop tensions over the averages of the individual magnetizations and their product, i.e.

$$\begin{aligned} S_\alpha(A) &= S_\alpha(A) \Big|_{\mathbf{h}=0} \\ &+ \frac{1}{1-\alpha} \left[- \int_0^{h_z} dh'_z \int_0^{h_x} dh'_x (\langle m_{xy} m_z \rangle_{A, \mathbf{h}'} - \langle m_{xy} \rangle_{A, \mathbf{h}'} \langle m_z \rangle_{A, \mathbf{h}'}) \right. \\ &\quad \left. + \alpha \int_0^{h_z} dh'_z \int_0^{h_x} dh'_x (\langle m_{xy} m_z \rangle_{0, \mathbf{h}'} - \langle m_{xy} \rangle_{0, \mathbf{h}'} \langle m_z \rangle_{0, \mathbf{h}'}) \right]. \end{aligned} \quad (10.4)$$

The method of thermodynamic integration is a convenient way to compute Rényi entropies since the energy or magnetization is efficiently measured in classical Monte Carlo simulations. Care needs to be taken in the selection of the resolution of the range of temperatures or loop tensions simulated as it has to be adapted to the variation of the final entropy function. For example, sharp peaks require a fine grid of parameter values (β or h). Otherwise, errors due to the numerical integration accumulate and cause a systematic error in the highest parameter values considered. As for the specific heat, we use bootstrapping for the computation of a well-defined mean and statistical error on the Rényi entropies.

10.1.2.3. Addition schemes

In Sec. 8.2 we have already discussed schemes for the extraction of a constant topological term γ from Eq. (8.1) for two-dimensional systems. We emphasize that in the classical variants, it is not only the purpose of the bipartitions to *extract* γ but also to *exhibit* a finite γ at all in at least one of them. Only the construction by Levin and Wen [59] fulfils this requirement. Naively, one might think that five independent simulations have to be performed in order to compute the sum (8.3)

for $\alpha = 2$: Using typographic representations for the bipartitions (Fig. 8.5), we need $Z[\sqcup, 2, \beta]$, $Z[\sqcap, 2, \beta]$, $Z[\sqcup, 2, \beta]$, $Z[\sqcap, 2, \beta]$ and their common partition function $Z(\beta)$ of the unmodified system. However, it turns out that the latter cancels in the addition,

$$\begin{aligned} S_{2,top} &= \ln \frac{Z[\sqcup, 2, \beta]}{Z(\beta)^2} - \ln \frac{Z[\sqcap, 2, \beta]}{Z(\beta)^2} - \ln \frac{Z[\sqcup, 2, \beta]}{Z(\beta)^2} + \ln \frac{Z[\sqcap, 2, \beta]}{Z(\beta)^2} \\ &= \ln \frac{Z[\sqcup, 2, \beta]}{Z[\sqcap, 2, \beta]} - \ln \frac{Z[\sqcup, 2, \beta]}{Z[\sqcap, 2, \beta]}, \end{aligned} \quad (10.5)$$

and therefore needs not be simulated. The form of the last line in Eq. (10.5) reflects Levin and Wen's interpretation of the topological entropy, namely that it is the additional entropy associated with closing an annular region at the top, compared to the same closing for disconnected parts.

In three dimensions, two suitable schemes implementing Levin's and Wen's idea have been proposed in Ref. [139]. One of them, depicted in Fig. 10.2a, is appropriate for our classical toric code model in three dimensions since in A_4 , part B has two disconnected regions. These bipartitions are embedded in a cubic lattice of linear extent L with periodic boundary conditions in all dimensions. We see that all contributions from the volume, surfaces, edges and corners vanish in the addition (8.3). This scheme is able to detect the topological contribution from the degeneracy in the groundstate induced by winding *string* operators. To see this, we can recycle the argument used earlier in the two-dimensional case, namely that every surface of part A has an even number of piercing strings due to the closed-loop constraint. This constraint reduces the entropy of the states on the boundary. Taking into account the particularity of classical topological order that the number of disconnected parts of subsystem B also influences the value of γ , we can conclude again that bipartition A_4 provides a finite value for γ . However, only the classical *vertex* variant of the three-dimensional toric code model, Eq. (9.19), has winding strings.

It turns out that topological order from winding planes is not identified by the scheme in Fig. 10.2a, as will be revealed in Chapter 11. The problem is that the intersection of a closed membrane with a three-dimensional subsystem is not a single point but a loop on the boundary of part A . Hence, the parity constraint of the number of string piercings does not apply. As a consequence, for the study of the plaquette variant (9.18) and its alterations with a finite loop tension (9.20) we have to design a modified scheme. An idea to detect closed membranes — being three-dimensional objects — is to take *two*-dimensional subsystems A , i.e. by an embedding of the original two-dimensional Levin-Wen construction in a cube. The intersection of a membrane with such a sheet is a loop segment. This loop segment has two crossings with the one-dimensional boundary of the sheet — reenabling the counting argument. In order to increase the statistical data basis, we embed the sheets in L layers of a cube with size $L \times L \times L$ as shown in Fig. 10.2b. We note that no sites on edges oriented in the z -direction are part of subsystem A . Every single layer measures a topological contribution so that we compute γ/L for this scheme for consistency.

Interestingly, the volume continuation of these layers, yielding the scheme in Fig. 10.2c, also exhibits a topological entropy. Just like the layers this scheme

10. Monte Carlo approach

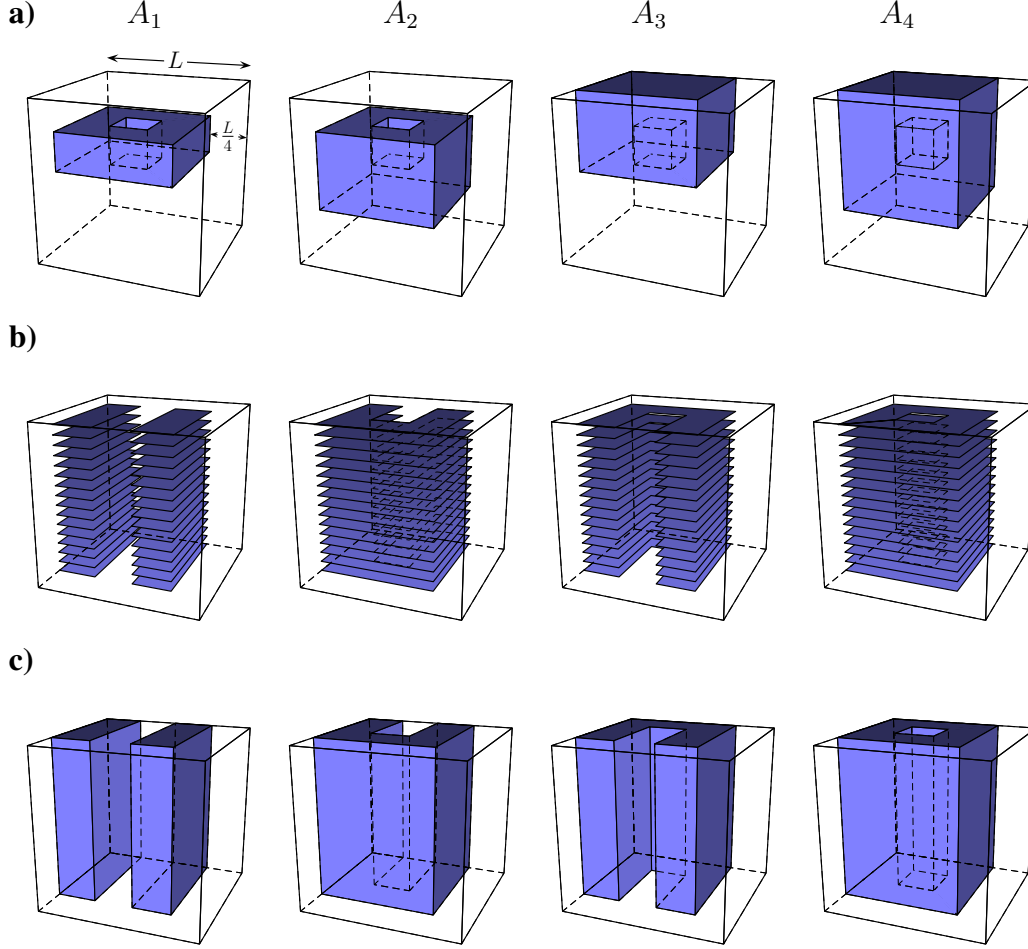


Figure 10.2.: Addition schemes for the three-dimensional toric code model. The authors of Ref. [139] propose scheme **a)** for the detection of topological order in the quantum model. In the classical variants, it only detects string-like structures. Schemes **b)** and **c)** provide a detection of membrane-like structures induced by the plaquette constraints in the three-dimensional toric code.

is translationally invariant in the z -direction which qualifies it to be used for the anisotropic loop tension variant. The z -direction represents the imaginary time dimension of the underlying two-dimensional quantum system and we do not intend to capture topological effects in this dimension which would possibly happen if we used scheme **a)**.

We have uniformly chosen the distances between two boundaries separating the subsystems to be $L/4$ in the xy -plane along the main axes in all our bipartitions. The reason for this choice is that we expect a reduction of finite-size effects from asymmetries and avoid the mixing of geometric dependencies in the boundary law. It should be noted that the truly three-dimensional addition schemes (Fig. 10.2a and c) lack a property of the two-dimensional Levin Wen scheme unmentioned so far: Beyond the fact that the boundary contributions vanish in the addition, all four boundaries in the bipartitions of Fig. 8.5 have the same size. This is not true for the surface-like boundaries in the present three-dimensional cases. We emphasize this detail because it is possibly responsible for increased finite-size effects in the three-

dimensional results for γ if we assume further non-linear subleading dependencies of $S_\alpha(A)$ on the boundary size in Eq. (8.1). Such terms could still cancel in the addition if they are identical in all A_i like in the two-dimensional case.

10.2. Update algorithms

The Markov chain of configurations produced by the Monte Carlo algorithm starts with an arbitrary configuration C_0 . In our code models we choose this initial configuration to be the state where all spins point up. Subsequently, based on the respective current configuration $C^{(n)}$, a new configuration $C^{(n+1)}$ is *proposed* and possibly *accepted* according to an appropriate probabilistic decision. It is the purpose of this procedure that a configuration C is visited in the Markov chain with a frequency f_C corresponding to the (known) *weight* $w(C)$ of that configuration in the thermal average of an observable O ,

$$\langle O \rangle = \frac{1}{Z} \sum_C O_C w(C), \quad (10.6)$$

with the partition function $Z = \sum_C w(C)$. For a Markov chain of length M we thus aim at achieving $f_C/M \rightarrow w(C)/Z$ as $M \rightarrow \infty$. In our Monte Carlo simulation we hence obtain the expectation value of O as

$$\langle O \rangle = \lim_{M \rightarrow \infty} \frac{1}{M} \sum_C f_C O_C. \quad (10.7)$$

The frequency trivially has to satisfy $\sum_C f_C = M$. This strategy is called *importance sampling*³ since configurations with a high weight are visited more often than those with a low weight.

The probabilistic decision for the selection of the next configuration is based on a transition matrix containing the probabilities $W(C_i \rightarrow C_j)$ for choosing configuration C_j given that we are in configuration C_i . These probabilities have to satisfy the following three conditions

1. Normalization: For all configurations C_i , the probability to choose any of the available configuration as the next one must be unity, i.e. $\sum_j W(C_i \rightarrow C_j) = 1$.
2. Ergodicity: From any configuration C_i it must be possible to reach any other configuration C_j in a finite number of transitions, $\exists N \in \mathbb{N} : W(C_i \rightarrow C_{n_0}) \left[\prod_{k=0}^{N-1} W(C_{n_k} \rightarrow C_{n_{k+1}}) \right] W(C_{n_N} \rightarrow C_j) > 0$.

³More specifically, importance sampling is a Monte Carlo sampling technique applicable to sums or integrals of the form (10.6), i.e. a product of the quantity of interest and a known normalized weight function. The weight function is handled through the selection probability of the state and can hence be ignored in the measurement. Opposed to importance sampling is the concept of *simple sampling* for sums not exhibiting such a product form. In this case, configurations have to be selected uniformly.

10. Monte Carlo approach

3. Balance: The probability $P(C_i)$ to visit a configuration C_i is predetermined by the weights $w(C_i)/Z$ of the physical problem. In order for the transition probabilities to establish this distribution, the ‘incoming’ and ‘outgoing’ transitions to and from C_i must be in equilibrium, i.e. $\sum_j P(C_j)W(C_j \rightarrow C_i) = \sum_j P(C_i)W(C_i \rightarrow C_j)$.

One of the most simple strategies to satisfy the third condition is to require so-called *detailed balance* between any two configurations which means

$$\begin{aligned} P(C_j)W(C_j \rightarrow C_i) &= P(C_i)W(C_i \rightarrow C_j) \\ \Leftrightarrow \frac{P(C_j)}{P(C_i)} &= \frac{W(C_i \rightarrow C_j)}{W(C_j \rightarrow C_i)}, \end{aligned} \quad (10.8)$$

that is, to individually equalize the corresponding summands in the equilibrium equation. We employ this detailed balance condition in all our update algorithms. The left-hand-side of Eq. (10.8) corresponds to the ratio of the weights $w(C_j)/w(C_i)$ in the statistical mechanics ensemble. In the case of a thermal canonical ensemble it is $\exp[-\beta(E(C_j) - E(C_i))]$

The transition probability comprises the probability to select and the probability to accept C_j , i.e. $W(C_i \rightarrow C_j) = P_{\text{sel}}(C_i \rightarrow C_j)P_{\text{acc}}(C_i \rightarrow C_j)$. Most approaches for update algorithms decide to make one of the two types of probabilities symmetric under exchange of C_j and C_i , such that this type vanishes in the ratio on the right-hand-side of Eq. (10.8). The respective other type of probabilities alone implements the required ratio. *Local* updates, discussed in the following, typically set $P_{\text{sel}}(C_i \rightarrow C_j) = P_{\text{sel}}(C_j \rightarrow C_i)$ such that the equilibrium distribution is produced by the acceptance probabilities. In the subsequent Subsection introducing *global* updates we present two options on this issue. First, the same allocation of responsibilities between selection and acceptance as for local updates can be applied. A second approach has the generation of the correct probabilities $P(C_i)$ built in the selection probabilities such that the acceptance probability can be set to unity.

10.2.1. Local updates

An intuitive attempt to simulate a physical system at equilibrium is to approximately mimic its physical behavior. The latter can be thought of as small steady local fluctuations over the observation time due to thermal energy present in a system above zero temperature. Here, we describe Monte Carlo algorithms consisting of proposing local changes to the configuration such as single-spin flips or collective flips of a small number of spins belonging to a local operator. The (artificial) evolution of the configurations in the course of the simulation is hence similar to the microscopic physical evolution.

States of our classical models are represented by spin configurations. For the investigation of the finite-temperature behavior, flipping a single spin in a configuration leads to another allowed configuration. This is not true if we consider ground-states of our code models perturbed by external fields. In this case, excitations of the local interaction operators (plaquettes, vertices or cubes) are suppressed such that our local update must preserve the groundstate constraints induced on the spins

by the operators. It is straightforward to see for each model, how this local update must be constructed: The classical variants of the underlying quantum models were defined by translating the superposition induced by the flip operators to the classical ensemble. Hence, a transition between configuration in the classical ensemble is performed by such a flip of one of the corresponding operators. These operators are *dual* to the actual operators appearing in the Hamiltonian which impose the classical constraints. For example, local updates for the two-dimensional *vertex* classical toric code model are simultaneous flips of the four spins of a *plaquette* and vice versa. The same is true for the other pairs of classical variants of the commuting Pauli Hamiltonians.

Having identified the appropriate local update, we are in a position to define the algorithm which we choose to be the *Metropolis* [151] algorithm:

1. Selection: Pick a single object considered for flipping at random (uniformly).
2. Acceptance: Compute the weights of the current configuration $w(C_i)$ and of the configuration resulting from the proposed flip $w(C_j)$. The probability to accept the flip is then given by $P_{\text{acc}}(C_i \rightarrow C_j) = \min(1, w(C_j)/w(C_i))$ which satisfies Eq. (10.8). This decision is realized by producing a uniformly distributed random number in the range $[0, 1)$ and performing the flip if it is smaller than $P_{\text{acc}}(C_i \rightarrow C_j)$.

For a system of N spins, N repetitions of this procedure are performed for a complete Monte Carlo *sweep*, i.e. a transition to the next configuration in the Markov chain, $C^{(n)} \xrightarrow{N \text{ flip attempts}} C^{(n+1)}$. Measurements are performed only after complete sweeps. The repetition has two advantages: If ergodicity is satisfied by the update in general, it is already ensured between two sweeps since it is possible to obtain any other reachable configuration immediately. Moreover, the so-called *autocorrelation time*⁴ is significantly lower on the full sweeps compared to defining a single flip as a full sweep.

The single-spin flips for finite-temperature simulations lead to toggling the quantum number $\pm 1 \rightarrow \mp 1$ of the local operators that the spin is part of. This event would possibly induce a change in the energy such that according to Eq. (9.14), we have $P_{\text{acc}}(C_i \rightarrow C_j) = \min[1, \exp(-\beta \Delta_{ij} E)]$. We note, that these updates provide ergodicity of the Markov chain. Furthermore, as spins unambiguously belong to either part A or part B of the system, no particularities need to be considered at the boundary for the replica trick. A factor of α appears in the energy change $\Delta_{ij} E$ if the spin is in part A .

Single-plaquette or single-vertex flips are used for simulations of classical toric codes with a finite loop tension h . We have $P_{\text{acc}}(C_i \rightarrow C_j) = \min[1, \exp(-h \Delta_{ij} m)]$, in this case, following Eq. (9.16), such that the magnetization possibly changes. If

⁴In general, consecutive configurations produced by Monte Carlo updates are correlated and so are the measurements in these configurations. When computing the statistical error on the average of the measurement results one must consider these correlations. A measure for the correlations between consecutive configurations is given by the autocorrelation time of the simulation. It is defined as the average minimal length l of a series of configurations $C^{(n)}, C^{(n+1)}, \dots, C^{(n+l)}$ such that correlations between the first and the last element vanish, $\langle C^{(n)} C^{(n+l)} \rangle \approx 0$.

10. Monte Carlo approach

the plaquette or vertex to be flipped is located on the boundary between the subsystems A and B , we have to flip it in all replicas in order to maintain the equality of all spins in subsystem A . These kinds of updates, however, are *not* ergodic as they cannot induce changes between the different sectors of the ensemble that are separated by differing winding number parities. The reason for this shortcoming is, that a single winding loop cannot be created by consecutive plaquette flips. In order to simulate the full configuration space, these local updates have to be complemented by *global* winding loop flips.

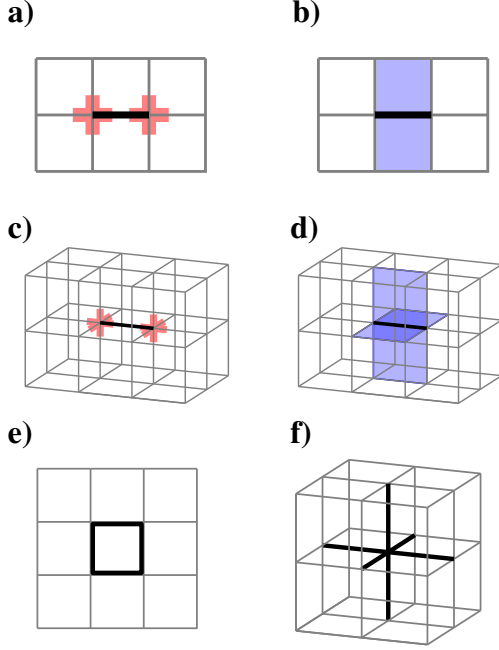


Figure 10.3.: Local updates by flips of single objects (black edges) performed on an ‘empty’ configuration. The left column corresponds to the vertex variants of the toric code and the right column to plaquette variants. Single spin updates **a)**–**d)** are used for finite-temperature simulations and create excited operators (shaded objects). The operator updates **e)** and **f)** preserve the groundstate constraint but have an effect on the magnetization.

Fig. 10.3 illustrates a collection of the local updates used in our Monte Carlo simulations for the two- and three-dimensional toric code models.

We finally remark that for finite-temperature simulations of deconfined (point-like) excitations, the *states* of the single spins are entirely irrelevant as we are only interested in the energy of a configuration and hence in the excited *vertices*. In more physical terms, it is superfluous to simulate more than one representative of gauge invariant states. It is hence not necessary to actually perform the spin flip but only the flips of the corresponding pair of vertices. Expanding this idea, we have constructed and used an algorithm which picks two independent vertices at random instead of a single spin. Their quantum numbers are flipped if accepted according to the Metropolis probability, but the spin values are not changed. Embedding this algorithm in the replicated system is non-trivial: Two random vertices may perhaps not be linkable⁵ by strings if they are in different subsystems or in disconnected parts of one subsystem. It is hence necessary to consider picking more than two vertices and to check if

they constitute a set which is connectable by strings. Since the positions of the chosen vertices are not correlated and can be anywhere in the system, we thereby shorten the autocorrelation time because a sequence of single-spin flips would be necessary to obtain the same update.

⁵The problem is, that a string which traverses part A must be copied to all other replicas — causing additional open ends there.

10.2.2. Global pattern updates

For the toric code models subjected to a finite loop tension we have realized that local operator updates are not ergodic as they cannot establish a transition to another sector of the groundstate ensemble. Moreover, since the phase transitions occurring at a critical loop tension h_c have been shown to correspond to those of an Ising ferromagnet, they may be affected by critical slowing down, i.e. a low efficiency near h_c in simulations based on local updates. We present *global* updates as a remedy for these two issues. The particular difficulty in the design of such update algorithms is to take into account the replica states with independent parts B and a common part A .

10.2.2.1. Winding operator updates

The different sectors of the groundstate ensemble are distinguished by winding loops (or planes) which can only be created or removed at once if we exclude energetic excitations. In order to enable a transition between them we can in a most simple approach propose such winding loops to be flipped *as a whole* and accept this modification with Metropolis probability as above. To select such a loop for a vertex groundstate we pick a single edge of the toric code lattice at random and follow the straight grid line of this edge around the periodic lattice. As we do not consider corners in our winding loop, the initial edge completely determines the loop. For a plaquette groundstate we have to follow the edges which are parallel to the initial one, yielding a ‘dual’ loop in two dimensions and a plane in three dimensions (see the green edges in Fig. 9.6). If any of the spins along the winding object belong to part A , we have to consider this object in all replicas, i.e. either all of them are flipped or none. To avoid confusion, we emphasize that the proposed winding loop or plane is a geometric object in the lattice which is independent and ignorant of the actual spin configuration of its elements. We therefore denote it as a *template loop* in order to distinguish it from the loops of down-pointing spins in a particular configuration. The winding operator update is an extension of the local plaquette or vertex flip algorithm — it is not meant to be used as a standalone algorithm because its updates generate highly patterned changes (straight lines or planes).

10.2.2.2. Cluster-like updates

A well-known Monte Carlo algorithm for the remedy of critical slowing down in the Ising model is the so-called *Wolff* algorithm [152]. Its idea is to identify stochastic *clusters* of Ising spins which point all in the same direction and flip them collectively. As we have seen in the mapping from the toric code model in a finite loop tension to the Ising model, Ising cluster domain walls correspond to closed loops or membranes in the toric code. Hence, the algorithm can straightforwardly be adapted to the toric code models. For its explanation we restrict ourselves to the groundstate of the two-dimensional vertex variant (9.15) which is left invariant by plaquette flips. Initially, we pick a plaquette at random. The algorithm reads:

1. Flip the spins of the plaquette. If some of them belong to subsystem A , flip **all** of them in all other replicas.

10. Monte Carlo approach

2. For all edges limiting the plaquette(s) whose spin points **down** we traverse this edge to the neighboring plaquette and include this plaquette with probability

$$p = \begin{cases} 1 - e^{-2\alpha h}, & \text{if the edge is in subsystem } A, \\ 1 - e^{-2h}, & \text{else,} \end{cases}$$

in the cluster.

3. **Check** if we have not flipped this plaquette already. If not, we continue at (1.) with this plaquette.

One might wonder why the check (3.) is performed. It is unnecessary in the Wolff algorithm for the Ising model because the information on which plaquettes to follow is contained in their orientation already. This is different in the dual description of closed loops instead of domain walls: The presence of a single winding loop may lead to trying to cross it from both sides during the cluster creation. This scenario is illustrated in Fig. 10.4 and necessitates the check. At the same time, we note that also these cluster updates are unable to switch between the groundstate sectors. We must hence add the winding operators updates introduced above to our simulation.

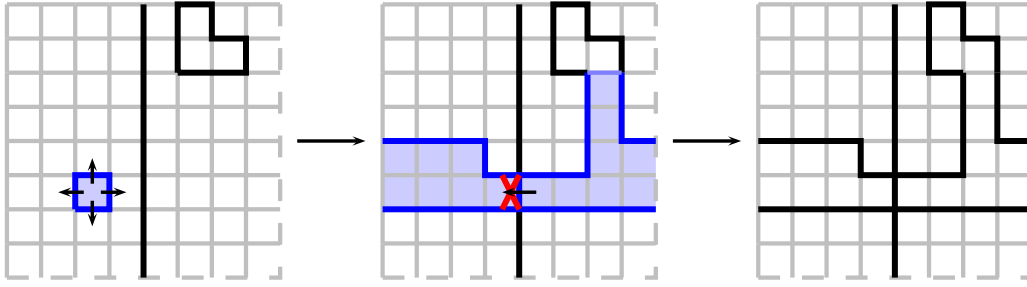


Figure 10.4.: Cluster update in the classical toric code model. In the left picture, the initial plaquette is chosen and the cluster growth begins. It stops at existing loops, thereby annexing them. A winding loop may cause the cluster to try to overlap itself which needs to be interrupted by an additional check for such an event. The final configuration in the right picture has the same winding number parities as the initial configuration.

It is important to respect the replica-trick structure of the modified partition functions, see Fig. 10.1. A single cluster may spread over a part of subsystem A and independently over parts in all replicas of subsystem B . Thus, if the cluster grows within subsystem A and reaches the boundary to subsystem B it is important to check for all neighboring plaquettes in all replicas. Also, if a plaquette touching the boundary between A and B (that is, having A -spin edges) is initially selected, it must be flipped in all replicas.

10.2.2.3. Lattice walk updates⁶

The resulting update from the cluster generation in the previous paragraph is the collective flip of a template loop. To arrive at this loop, its entire bulk has been

⁶This subsection about lattice walk updates is largely identical to the Appendix of our publication in Physical Review B [153].

considered. A more elegant way of generating the loop can be designed for the two-dimensional classical toric code model in a loop tension with vertex constraints. It is based on performing a one-dimensional walk from vertex to vertex along edges in the lattice and wait for the walk to run into itself. The trace of this walk is (a candidate for) the template loop. During the algorithmic creation of the walk it has a *head* which is the last appended vertex. This head “decides” which vertex (and thereby which edge) to append next. If accepted according to the detailed balance condition, the template loop will be applied to the spins along this loop by flipping them. This procedure is shown in Fig. 10.5. Sampling a template loop is particularly challenging if it crosses part *A* since its degrees of freedom are identified with those in the other replica. Thus, two additional open loop ends are generated in the other replica at the boundary between *A* and *B*. These two ends need to be linked in part *B* of the other replica as well. Trying this, it is possible to cross part *A* again. Obviously this procedure can easily result in a seesaw of linking two open loop legs in part *B* of either replica.

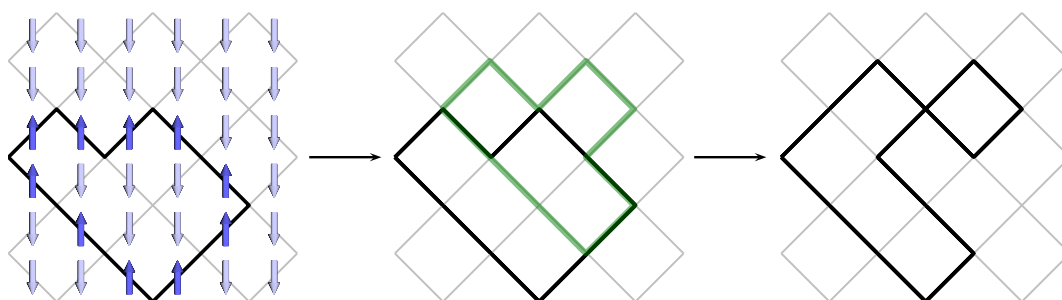


Figure 10.5.: A loop update is performed by creating a template loop (green) in the lattice and applying it to the spin configuration with its spin loops (black) if the resulting energy change is accepted.

For the actual procedure of choosing the template loop a first approach is to perform a *random walk* through the lattice. Once a valid loop is found, we apply a Metropolis probability between the current and the potential next state to decide on its acceptance. Later we will present a more advanced algorithm which unifies the selection and acceptance step in a so-called *directed walk*.

Random walk The random walk is started at an arbitrary vertex of the toric code lattice and proceeds with equal probability of $\frac{1}{4}$ to one of the four neighboring vertices⁷. Once a vertex is visited a second time, we can stop the walk and discard the first segment of the loop up to the first visit of this vertex. Possibly, the random walk has entered one or more times the connected subregion *A* so that its segments in *A* in the other replica also have to be included in the template loop. Thus, an even number of open template loop ends is created in the other replica at the boundary to part *B*. To match these ends, it is efficient to start individual random walks at every open end simultaneously. If the head of one of the walks hits a vertex already

⁷ For completeness, it should be mentioned that this mapping is strictly defined for the even parity sector of the toric code model. Other parity sectors of the toric code would necessitate the definition of antiperiodic boundary conditions in the Ising model for every odd winding number in the toric code model.

10. Monte Carlo approach

visited by a different walk we have created a linking loop between the two open ends so that these two are *healed*. Most likely, the two loops do not meet precisely at their heads so that a superfluous part between the meeting point and one of the heads arises. This part of the template loop is discarded, see Fig. 10.6. It may also happen, that a specific random walk head hits a vertex twice. In this case, we can discard the resulting *internal* loop of this walk since it does not help in linking open ends. Moreover, the general strategy is to keep the total length of the template loop as short as possible.

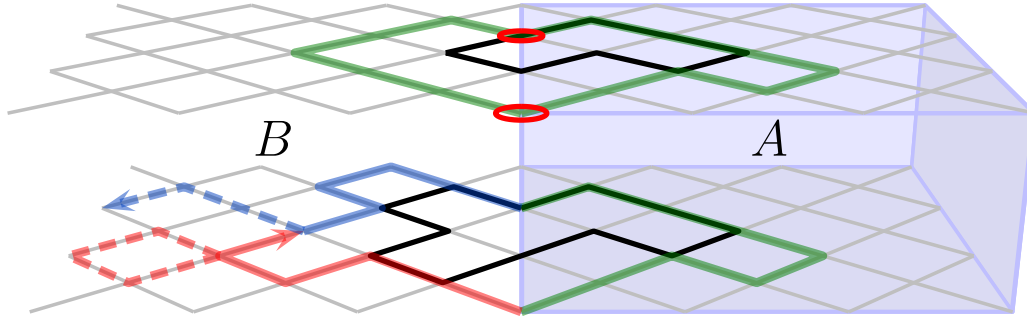


Figure 10.6.: Visualization of the healing process. On top, a template loop (green) is sampled within the first replica. It leaves behind two open loop ends (red circles) at the boundary between A and B in the other replica. The right sketch depicts the healing processes: Two random walks (blue and red) simultaneously try to meet each other. The dashed segments indicate parts of the template loops which are discarded. Internal loops (dashed red) would be allowed but are contracted in order to shorten the total template loop.

In Monte Carlo parlance, this procedure is responsible for ensuring ergodicity in our simulation. What remains is to fulfill also detailed balance. Since we have only generated a template loop so far, we can compare the total weight of the configuration prior to the application of this template loop and after it. In our special case we need to determine the magnetizations m_{before} and m_{after} . The acceptance is then decided on by the Metropolis probability

$$p(\sigma \rightarrow \sigma \circ \text{template loop}) = \min(1, e^{-h(m_{\text{after}} - m_{\text{before}})}), \quad (10.9)$$

where the function composition symbol \circ is used to denote the application of the template loop on the current configuration.

Since this implementation of the Markov chain separates the selection and acceptance of new configuration we can almost freely design the random walk procedure as long as we guarantee ergodicity. A shortcoming of it appears at higher loop tension h where the acceptance of an energetically less favourable configuration is low. In addition, for relatively large sizes of the subsystem A , the healing of all open loop ends can entail many random walks back and forth between the replicas. This makes the algorithm less efficient, especially for parameter settings ($h \approx 0.44$, L large) we want to investigate to track the phase transitions.

Directed walk A substantially different and more efficient approach for the Monte Carlo update scheme is implemented by unifying selection and acceptance. The

idea is to ensure detailed balance on-the-fly while choosing the template loop. Strictly speaking it is no longer a *template* loop since all spins along this loop are flipped with probability 1, i.e. they can (and have to) be flipped directly. The walk that the head of the loop performs is not at random but obeys probability rules depending on the value of the potential next spins to be visited. In general, the rule is to select the next spin (which unambiguously selects the next vertex) with so-called heat bath probability. This means, the microscopic weights w_i of all candidates for the next head of the loop are added up to a normalization constant n . In the toric code model the head has four possibilities to choose the next spin because bouncing must now be included. The only possible values for the weights are $w_i \in \{\exp(h), \exp(-h), \exp(2h), \exp(-2h)\}$, where the factor of two in the exponent applies in the connected part A which is simulated at an effective loop tension of $2h$ as discussed above. With the constant $n = \sum_{i=1}^4 w_i$ the heat bath probabilities for the four directions are defined as

$$\frac{w_1}{n}, \frac{w_2}{n}, \frac{w_3}{n}, \frac{w_4}{n}. \quad (10.10)$$

It is not obvious to see whether this rule generates an update which obeys the detailed balance condition. To check it we need to identify a reverse update to any (completed) update and compare the probabilities of their occurrence. If we now try to fractionize this update into its individual moves according to the heat bath rule and compare it to its reverse move, cf. Fig. 10.8, we see that the normalization constants thwart the analysis: A specific spin at position j in the loop was chosen to be visited (and flipped) with probability w_j/n_j in the original update. Doing its reverse, we would have the probability w_j^{-1}/n'_{j+1} to reflip it. The ratio of the two probabilities is in general not w_j/w_j^{-1} as they should be from the ratio of the weights of the configurations that differ by flipping spin j . Two facts about the involved normalization constants annoy: (i) they originate from different configurations and (ii) they are shifted by a lattice position.

We see that that issue (i) is not a problem by realizing that the value of normalization constant at a specific vertex at the moment when it is the head is the same for both — the original and its reverse — update is the same, i.e. $n_j = n'_j$. This can be understood from Fig. 10.7 where we see that the coming-from and the going-to spin switch roles (and weights) in both situations.

The other issue (ii) can be resolved by leaving the local perspective from the loop head and regarding the entire loop update. If we consider a chain of moves and its reversion, we have to multiply all probabilities to obtain the total probability for the walk. In the ratio of the total probabilities for the walk and its revers, we realize that all normalization constants vanish. Since their respective numerator-denominator pairing is shifted by one in the product, we dub this feature of the microscopic rule

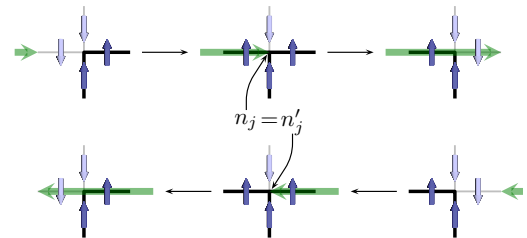


Figure 10.7.: Passing of the directed walk (green) at vertex j . The normalization constants for inverse loop update walks agree. In this example they both have the value of $n_j = 3 \exp(-h) + \exp(h)$.

10. Monte Carlo approach

staggered detailed balance. The staggering can be seen in Fig. 10.8 and the ratio between a loop update and its reverse is given later in Eq. (10.12).

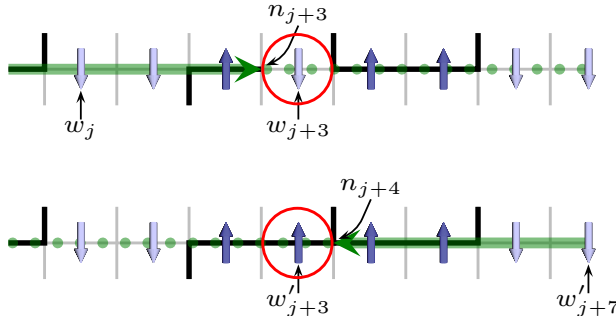


Figure 10.8.: Formation of the probabilities of two reversing update loops at a specific intermediate position $j + 3$ of the walk using heat bath probabilities. We compare the probabilities of selecting the encircled spin in the right moving loop and in its reversal left moving counterpart. The probability in the right moving case is $w_{j+3}/n_{j+3} = \exp(h)/(\exp(-h) + 3\exp(h))$. Note that spins at $j \dots j + 2$ are already flipped when the loop does this selection at n_{j+3} since we perform the update in-place. For the reverse move the selection probability is $w'_{j+3}/n_{j+4} = \exp(-h)/(3\exp(-h) + \exp(h))$. In particular, the ratio of these to probabilities is *not* $\exp(2h)$ as it should be if we wanted a microscopic detailed balance for the spin flip at $j + 3$.

We have seen that detailed balance can be satisfied in principle by the design of the walk but crucial aspects have not been discussed yet: How is a loop initiated and finished and what are the decision rules for choosing the next spin at the boundary between A and B ? It is clear that a loop must bifurcate when leaving part A but how is a reunification at another site at the boundary accepted? The latter may fail such that the update is discarded for technical reasons (as opposed to probabilistic reasons).

For the start of a loop update, a random spin in a random replica is chosen and one of its adjacent vertices is selected with probability of $\frac{1}{2}$. This spin is immediately flipped and the walk continues

at the selected vertices following the heat bath rule. It is instructive to note at this point that we have not “paid” the flipping of this first spin in terms of acceptance probabilities. This will be caught up at the decision to end the loop. The probability to start the loop at a particular pair of a spin and a vertex is thus simply

$$p_{\text{init}} = \frac{1}{4N}, \quad (10.11)$$

where N is the total number of spins in the lattice.

In order to finish the walk it is first of all necessary that the loop is closed, i.e. that the head reaches precisely the other vertex at the initial spin — the vertex that was *not* chosen to start with. This is not sufficient, since just like anywhere the head is free at this vertex to choose any of the adjacent spins — among them the initial spin. Before we determine the heat bath probabilities and normalization constant we have to flip the initial spin once again. The loop head thus “sees” the original orientation of this spin before the whole loop update was started. Afterwards the heat bath selection is performed and in the case, the initial spin is chosen, it is flipped a third time and the loop update is successfully finished. Only now, the flipping of the initial spin is justified (“paid”) by a probabilistic selection according to its weight. If another but the initial is chosen, the loop continues and we must not forget to flip the initial spin again.

We have now explained the algorithm for non-boundary-crossing loops. Fig. 10.9 and the following equation prove that the detailed balance condition is fulfilled.

$$\begin{aligned} \frac{p(\sigma \rightarrow \sigma')}{p(\sigma' \rightarrow \sigma)} &= \frac{p_{\text{init},s_0} \cdot \frac{w_{s_1}}{n_1} \frac{w_{s_2}}{n_2} \cdots \frac{w_{s_{l-1}}}{n_{l-1}} \frac{w_{s_0}}{n_l}}{\frac{w_{s_0}^{-1}}{n_1} \frac{w_{s_1}^{-1}}{n_2} \cdots \frac{w_{s_{l-2}}^{-1}}{n_{l-1}} \frac{w_{s_{l-1}}^{-1}}{n_l} \cdot p_{\text{init},s_0}} \\ &= \frac{w(\sigma')}{w(\sigma)}. \end{aligned} \quad (10.12)$$

The relative shift of the numerators again demonstrates what we mean by staggered detailed balance for the loop steps. The chronological order of the appearance of the probabilities is from left to right in the main numerator but from right to left in the main denominator. We chose write the equation in this way to emphasize the reversing effect of factors that are written one below the other.

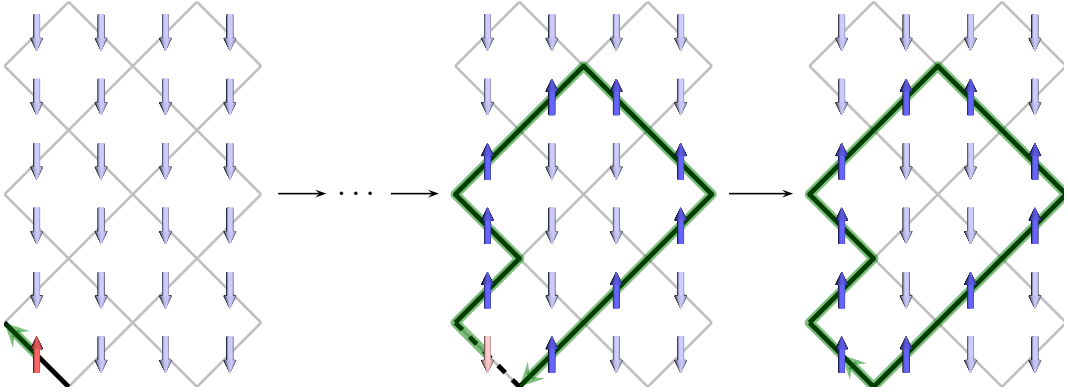


Figure 10.9.: Completing a loop by catching up the probabilistic choice of the initial spin as part of the loop. The initial spin is drawn red in order to emphasize that it was not *paid* in terms of probabilistic weight selection until the last step. In the middle sketch it is temporarily flipped back since the loop head must choose it as if it was never flipped.

It remains to define rules how to deal with boundary crossings and its resulting bifurcations of the loop. In order to justify the probabilities for the direction of the walk we need to ensure reversibility of any moves we allow. This is the reason why we only allow a single bifurcation of the loop and hope for its reunification. In case the reunification fails, the update is aborted and the original configuration is restored. We will elucidate this point further at the end of this section. The vertices of interest for the treatment of boundary crossings are those which have adjacent spins in either of the bipartitions — subsequently called *boundary vertices*. In general we will never set a heat bath normalization constant at a vertex using weights from both parts, i.e. both $\exp(\pm h)$ and $\exp(\pm 2h)$. In other words, a drift to or away from the connected part A is avoided.

We first describe the update for the case of an initial spin somewhere in part B . If a boundary vertex is visited coming from the disconnected part B we treat all four spins as if they were in part B (although at least one is in part A) for the calculation of the heat bath weights. In other words, the head does not *see* the boundary. If the head selects a spin in part A , also its counterpart in the other replica is flipped. However, the flipping of this counterpart is at that state not paid in terms

10. Monte Carlo approach

of acceptance probability just as we used this wording above. The loop continues in part *A* where it uses the weights $\exp(\pm 2h)$ until it reaches again a boundary vertex. At such an occurrence we have to perform the mentioned bifurcation: First, a loop is continued in the initially chosen replica only. This loop should now rejoin the initial spin in the same way we described above for the simpler case devoid of a connected part *A*. Trying this, the loop must not enter part *A* again. If it does, we have to abort the entire update. Second, another loop is continued in the respective other replica. In the same manner, this loop is expected to rejoin the by then unpaid spin in part *A* at the entering boundary spin. To successfully finish the total loop update, this unification must happen without a prior visit of part *A* again. Fig. 10.10 illustrates the described procedure.

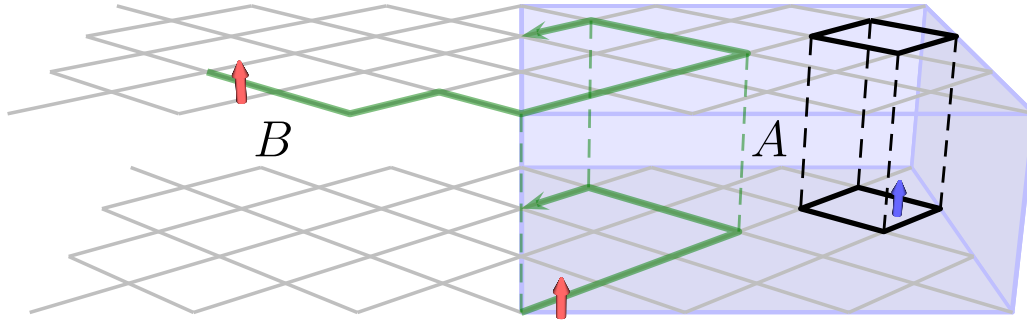


Figure 10.10.: In the presence of a connected subsystem *A* loops need to bifurcate. After entering part *A*, all weights have to be taken using the effective loop tension of $2h$ and flipped in both replicas. The first spin in part *A* in the other at the entrance is unpaid (drawn red), just like the initial spin in part *B*. The bifurcation happens when the loop leaves part *A* again and must be finished individually in both replicas by joining the red spins.

A slight difference needs to be made if the initial spin of the update is part *A*. In this case, the first visit of a boundary vertex leads to bifurcation and the first bifurcated loop in one of the replicas in part *B* is free to reenter part *A* at any boundary vertex. Not before the second bifurcated loop in part *A* is performed and rejoins the unpaid boundary spin that its counterpart has been selected for reentering part *A*, the subsequent loop in part *A* is continued and hopefully rejoins the initial spin.

Our implementation of the Monte Carlo algorithm resigns to allow multiple temporary open loops in part *B* in one of the replicas alone. In principle one could allow more than one open loop and perform the loop update in the initial replica until it rejoins the initial spin. Subsequently one could start to connect all $2n_o$ open ends in part *B* of the other replica. Doing so it would be important to start the connecting walks only at those n_o ends that arose from *leaving* part *A* in the initial replica. Special care must be taken in this approach to not mix the order of the start spins of the healing walks in part *B* of the other replica. They must be started in the same order the arose from the initial loop. This is due to the ambiguity of possible paths that lead to the same loop update. Mixing the order of starting spins would violate the detailed balance condition because the reversal loop of a loop could then

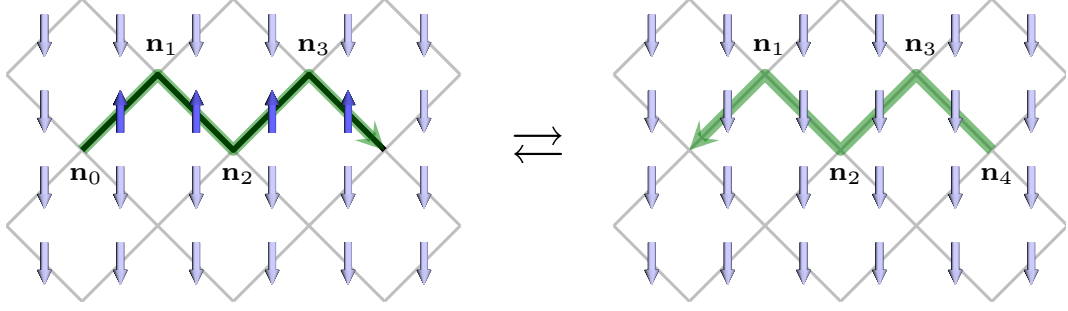


Figure 10.11.: Two mutually reversing open loop updates including the normalization constants used for the respective choice of the next direction of the walk. The last normalization n_4 (resp. n_0) is missing and therefore will be included artificially in the decision to stop the loop.

be achieved through more than one move.

We decided to allow only a single pair of bifurcations of the loop and avoid long seesaw healing processes for a single update step.

Finite-temperature simulations So far, we have considered the classical toric code at zero temperature, i.e. the system subjected to the loopgas constraint. By releasing this constraint and activating the vertex terms in the Hamiltonian (9.11) we investigate the toric code at finite temperature. In this situation pairs of open loop ends are permitted at the energetical cost of two times the vertex coefficient J_v . In practice we set $J_v = 1$ since only the ratio between J_v and h is important. A loop update in our Monte Carlo simulation must therefore be able to introduce open loops. Once again we propose two strategies.

Our first approach consists of separating the operations of the loop update and the introduction of loop excitations. We pick two vertices of the total system at random and have the algorithm perform a random walk between them. At $h = 0$ we only need to determine an acceptance probability for the open ends, which we set to Boltzmann weights $\exp(\pm J_v)$ or $\exp(\pm 2J_v)$ depending on the subsystem where the open end is introduced. In case one of the vertices is in part A and the other in part B we need a third vertex in part B of the respective other replica and thus create a “double-tongued” open loop. Also at finite loop tension we can apply Metropolis probabilities to the acceptance of a sampled open loop by balancing both the change in energy and in magnetization between the current and the proposed configuration.

Going beyond the simple sampling technique we also present an algorithm that again includes the acceptance probability in the selection of the subsequent configuration. We therefore extend our zero energy algorithm based on heat bath selections for the random walk at every vertex in the lattice. The head of the loop may take four different directions at a specific vertex. We add a fifth event to these four, namely stopping the loop and thereby creating (or annihilating) an open loop end in the spin configuration. However, we will not include the decision of stopping the loop in the heat bath sum but perform it separately using the Boltzmann weight of an open loop end. This decision is made prior to the selection of the next bond to walk on. There is one issue concerning the detailed balance between an open loop update and its reversal update: Due to the staggered detailed balance philosophy the

10. Monte Carlo approach

last heat bath normalization constant of the walk does not enter any of the probabilities for the loop continuation but the first one does, see Fig. 10.11. Roles are switched in the reversal update, which implies that the two normalization constants at the edges do not vanish in the ratio between the opposite loop updates.

Our workaround is to artificially include every heat bath normalization constant (and thus also the last one) into the decision of stopping the loop. The probability to stop at the j th vertex of the loop is thus $\frac{\exp(\pm J_v)}{n_j}$. Since in our model $n_j > 1$ in any case it cannot happen that this alteration of the pure Boltzmann constant leads to trivial probabilities (> 1) for stopping the loop. In formulas the ratio between two opposing loop updates is given by

$$\begin{aligned}
 & \frac{p(\sigma \rightarrow \sigma')}{p(\sigma' \rightarrow \sigma)} \\
 &= \frac{p_{\text{init},v_0} \cdot w_{v_0} \frac{w_{s_0}}{n_0} (1 - w_{v_1}) \frac{w_{s_1}}{n_1} (1 - w_{v_2}) \dots (1 - w_{v_{l-1}}) \frac{w_{s_{l-1}}}{n_{l-1}} \frac{w_{v_l}}{n_l}}{\frac{w_{v_0}^{-1}}{n_0} \frac{w_{s_0}^{-1}}{n_1} (1 - w_{v_1}) \frac{w_{s_1}^{-1}}{n_2} (1 - w_{v_2}) \dots (1 - w_{v_{l-1}}) \frac{w_{s_{l-1}}^{-1}}{n_l} \cdot w_{v_l}^{-1} \cdot p_{\text{init},v_l}} \\
 &= \frac{w(\sigma')}{w(\sigma)}. \tag{10.13}
 \end{aligned}$$

Until now we have neglected again the bipartition and replication of the lattice. But surprisingly the situation becomes easier if open loops are allowed. We can simply forbid boundary crossings of open loops i.e. abort a loop update which tries it. The algorithm is nevertheless ergodic since an arbitrary loop update (including a boundary crossing) can be generated by two non-crossing open loops which share one of their ends at the boundary. Moreover, also closed loops can be created that way by creating an open loop whose starting and ending vertex coincide. This does not make the closed loop algorithm superfluous since it is indispensable at the hard loopgas constraint and more efficient for very low temperature in combination with the open loop algorithm.

11. Results for stabilizer codes

We employ the Monte Carlo simulations developed in the previous Chapter in order to numerically study the topological entropy in the multiple classical variants of the quantum error-correcting codes introduced in Chapter 9. First, we provide a thorough study of the two-dimensional toric code in Sec. 11.1, where we focus on the finite-temperature behavior of the topological entropy as well as the effect of a finite loop tension. One of the main interests in the extension to three spatial dimensions is the quest for a thermally stable self-correcting code, i.e. a code in which topological order survives up to a finite temperature. For this reason, we begin the investigation of a series of three-dimensional codes in Sec. 11.2 with an analysis of the specific heat — a common approach in conventionally ordered systems. The perspective of topological entropy is then adopted again for the classical variants of the three-dimensional toric code.

11.1. Two-dimensional classical toric code

We present results from Monte Carlo simulations of the classical toric code in two dimensions with vertex terms. Our first numerical study confirms the expected fate of groundstate topological order upon cranking up temperature. Further, we investigate the well-known Ising phase transition induced by an external loop tension in Hamiltonian (9.15) from the perspective of topological Rényi entropies.

11.1.1. Finite temperature crossover

In Ref. [11] it has been pointed out that exceeding a certain finite temperature in the toric code leads to a size-dependent vanishing of the topological entropy γ . Excitations of the closed-loop constrained groundstate are thermally activated and cause the emergence of open strings, i.e. pairs of *defects*. Hence, a transition between the degenerate sectors of the ensemble with different winding parities becomes possible for sufficiently large temperatures. This lifting of the topological ergodicity breaking takes away the topological order. The *crossover* temperature is predicted [139] to scale as $T_{\text{co}}(L) \sim (\ln L)^{-1}$, i.e. it approaches zero in the thermodynamic limit, which implies that no topological survives above the groundstate.

Our Monte Carlo simulations using single-spin flips and directed walk global updates allow us to determine the topological entropy γ from the second ($\alpha = 2$) Rényi entropy. We employ the addition scheme of Levin and Wen for the extraction of the topological term. The results are shown in the top panel of Fig. 11.1 and confirm that γ smoothly vanishes as soon as some crossover temperature is surpassed. At very low temperatures we have $\gamma = \ln 2$, in agreement with the expected entropy reduction due to the even number of boundary crossings by closed loops [119].

11. Results for stabilizer codes

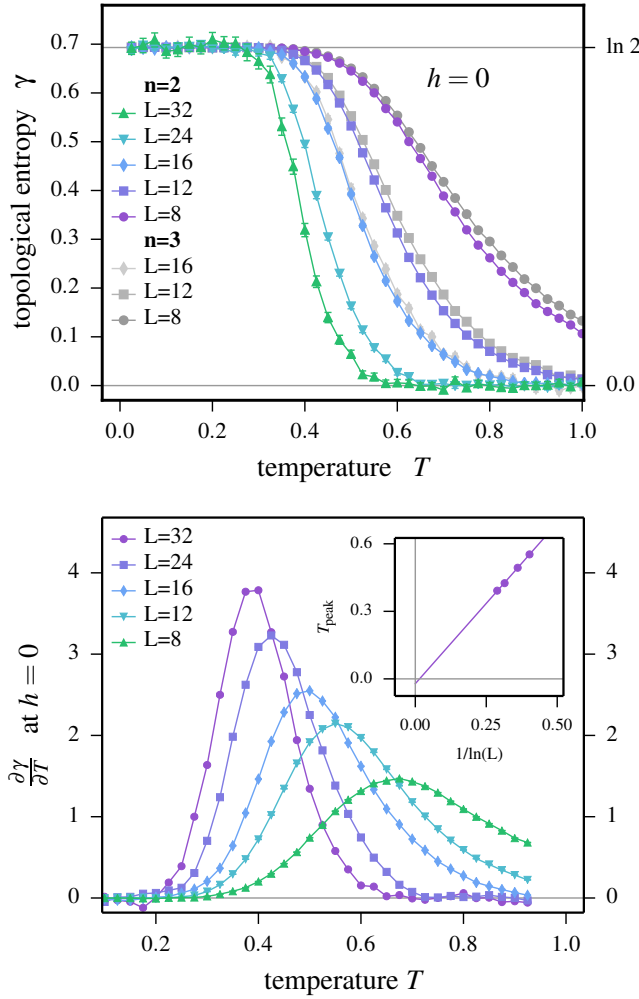


Figure 11.1.: Top panel: finite-temperature behavior of topological entropy for the classical toric code model indicating the thermal transition from the low-temperature topologically ordered phase to the high-temperature paramagnet for various system sizes. Bottom panel: identification of the transition temperature into the topologically trivial phase by determining the peak position of the derivative $\partial\gamma/\partial T$ for various system sizes. The scaling of the so- determined temperatures shows the expected logarithmic scaling with system size.

behavior. However, we see that the low-temperature and high-temperature values for γ are invariant, solely a slightly different curve is obtained in the crossover regime. The discrepancy is sufficiently explained by the ‘natural’ α -dependence of Rényi entropies, see Fig. 2.3 and provides reason to believe that also the canonical von Neumann entropy would show a very similar behavior to that of Fig. 11.1.

11.1.2. Connectivity contribution

Applying a finite loop tension h to the groundstate of the classical toric code with Hamiltonian (9.15), we implicitly have to assume a finite temperature T with $h \ll$

We observe, that this crossover temperature decreases upon increasing the system size L . In order to provide a quantitative analysis of this decrease we have chosen the inflection point of the curve as the indicator for a precise value of $T_{\text{co}}(L)$. It can be determined by numerically computing the derivative $\partial\gamma/\partial T$ and identifying its local maximum, see the bottom panel of Fig. 11.1. A scaling plot of these maxima with an ansatz of the predicted logarithmic behavior clearly verifies that (i) the above scaling holds and that (ii) the crossover temperature in the thermodynamic limit is zero.

Additionally, we have simulated the third Rényi entropy for the smallest system sizes considered. The purpose of this computationally more laborious study is to test the topological entropy for an α -dependence or artifactual behavior.

$T \ll J_v$. If the temperature was too low, no loop of down-pointing spins would be possible. We ignore the temperature in the ensemble weights $\exp(-hm_o)$ of a closed-loop configuration σ . The implicit finite temperature is not a contradiction to the groundstate phase since we do not consider thermal effects in our ensemble weights and freeze out thermal excitations by setting $J_v \rightarrow \infty$.

Mutual information We have pointed out in Section 9.2 that the classical toric code with external is dual to a two-dimensional Ising model at finite temperature *without* external field. Hence, we expect a phase transition [135] to occur in our toric code model at $h_c \approx 0.44069$. A first examination of the h -dependent behavior of the model can be done using the mutual information $I_2(A : B)$ based on the second Rényi entropy, see Sec. 2.3. This quantity has already been used successfully as an indicator for phase transitions [123] since it tracks long-ranged correlations. In a *conventional* order context, we expect the mutual information to be finite in ordered phases and to vanish in the disordered regime. It is interesting to investigate whether this behavior also holds for topological order where no local order parameter is available.

In order to determine the mutual information we have to bipartition the system into parts A and B . For a quadratic lattice of $L \times L$ plaquettes with periodic boundary conditions we choose part A to be exactly one half of the torus. Hence, its boundary has two straight lines of total length $\ell = L_A = 2L$ separated by a distance of $L/2$. It follows that part B has exactly the same form and $S_2(A) = S_2(B)$.

Fig. 11.2 shows our results for the mutual information plotted over a range of values h for the loop tension. It turns out that a division by $(\ell - 1)$ leads to a collapse of the curves for different system sizes in the topologically ordered low- h regime. The obvious conclusion that the mutual information scales as

$$I_2(A : B) = a_\ell \cdot (\ell - 1) + D, \quad (11.1)$$

can be understood from a familiar counting argument for closed-loop constrained configurations: Due to the defining addition of the mutual information, Eq. (2.12), bulk contributions vanish — unlike the boundary contributions. The reason for the reduced scaling in $(\ell - 1)$ instead of ℓ follows from the imposed even number of boundary crossings of the closed loops. Knowing the state of $\ell - 1$ boundary segments we can deduce the remaining boundary segment state which reduces the lack of information by one unit. Since the information is binary for every boundary segment (spin up or down) we can also determine $a_\ell = \ln 2$ which is confirmed by our numerical data, see also Ref. [119]. Continuing our analysis of Fig. 11.2 we observe that $I_2(A : B)$ vanishes in the topologically trivial phase where $h > h_c$. The mutual information hence is apt to capture a phase transition from a topologically ordered phase to a paramagnet. An interesting behavior of $I_2(A : B)/(\ell - 1)$ appears in the intermediate regime of $h_c/2 \leq h \leq h_c$. The curves for the different system sizes undergo a *splitting* at $h \approx h_c/2$ and overshoot the value of $\ln 2$ before sharply decreasing and exhibiting *crossing points* near the phase transition at h_c . The crossing points of subsequent system sizes L convincingly approach the known value of the phase transition with a scaling of $1/L$, as shown in the bottom panel of Fig. 11.2.

11. Results for stabilizer codes

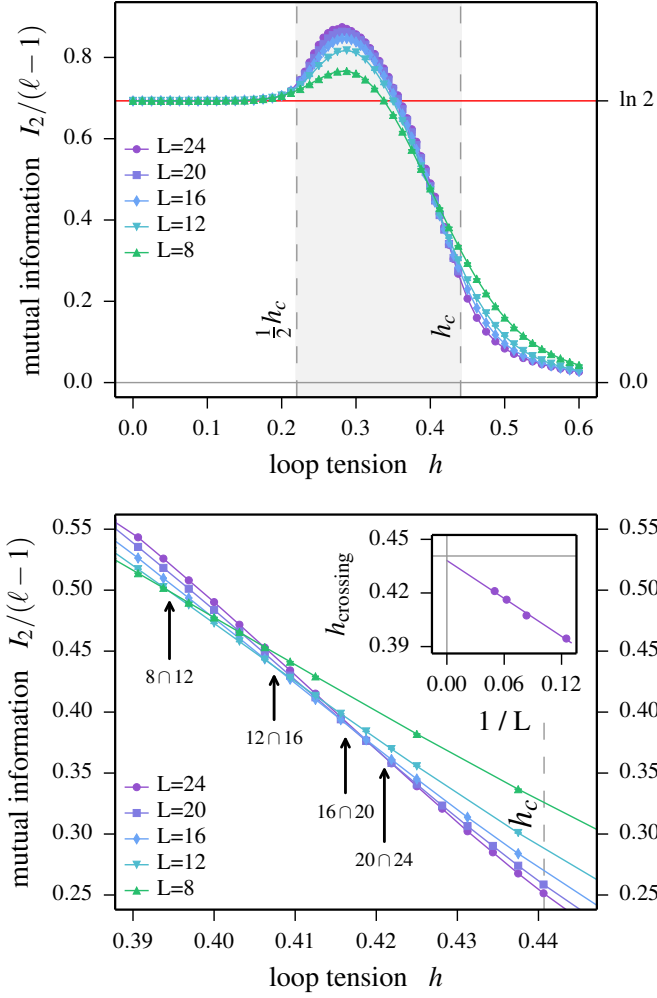


Figure 11.2.: Top panel: mutual information I_2 of the classical toric code model with a loop tension h for varying system sizes. The gray shaded area indicates the intermediate regime $h_c/2 \leq h \leq h_c$. Bottom panel: Zoom of the data near h_c illustrating the crossing points for different system sizes. The inset shows a scaling of the crossing points with inverse system size $1/L$ extrapolating well to the expected value of $h_c = 0.44069$ in the thermodynamic limit

Fig. 11.2. This insight about the subleading constant contribution D of the mutual information in Eq. (11.1) also provides access to understanding the crossing points near h_c . As partly pointed out, we expect a behavior

$$D = \begin{cases} 0, & h < h_c/2 \\ -\ln 2, & h_c/2 < h < h_c \\ 0, & h > h_c \end{cases} \quad (11.2)$$

where the parameter regions in which D vanishes are either fully topologically ordered ($h < h_c/2$) but do not exhibit a topological term due to the simple-connectedness, or fully polarized such that the mutual information entirely vanishes

An explanation for the behavior in the intermediate regime is found by observing that order in subsystem A is established at a *different* critical loop tension than in subsystem B . To wit, remembering that subsystem A is *effectively* simulated at $2h$, its critical loop tension is $h_c/2$. Subsystem A is hence in a polarized state in the intermediate region such that its bulk entropy vanishes. As a consequence, also a *simple* bipartition such as the presently considered half-torus (or bipartitions A_2 and A_3 of the Levin Wen scheme, see Fig. 8.5) exhibits a reduction of the entropy $S_2(A)$ by a constant of $\ln 2$ from the closed loop crossing the boundary since its compensation by the bulk lapses. The division by $(\ell - 1)$ of an emerging negative constant leads to the splitting because lower- ℓ curves undergo a stronger reduction, see

($h > h_c$).

Fitting our numerical results for the mutual information to the scaling behavior (11.1) we obtain data for the boundary coefficient a_ℓ as well as the constant D , which are shown in Fig. 11.3. As expected, we see that the boundary coefficient represents the limiting behavior of the mutual information in the thermodynamic limit. The overshooting of a_ℓ between $h_c/2$ and h_c can be interpreted as an over-estimation of the knowledge about subsystem A from the perspective of subsystem B . In the more interesting behavior of the fitted constant D we can find the reason for the crossing points near h_c . We first observe that our predicted values for D from Eq. (11.2) are approximately taken by the numerical data but transitions between the different regimes are accompanied by strong finite-size effects. The latter are responsible for the *sign change* of D slightly below h_c whose location approaches h_c upon excluding the smaller system sizes. Such a sign change precisely causes the crossing points of $I_2(A : B)$. Further, its absence close to $h_c/2$ where D jumps from zero to a negative value, explains why we obtain a splitting instead of a crossing point in Fig. 11.2.

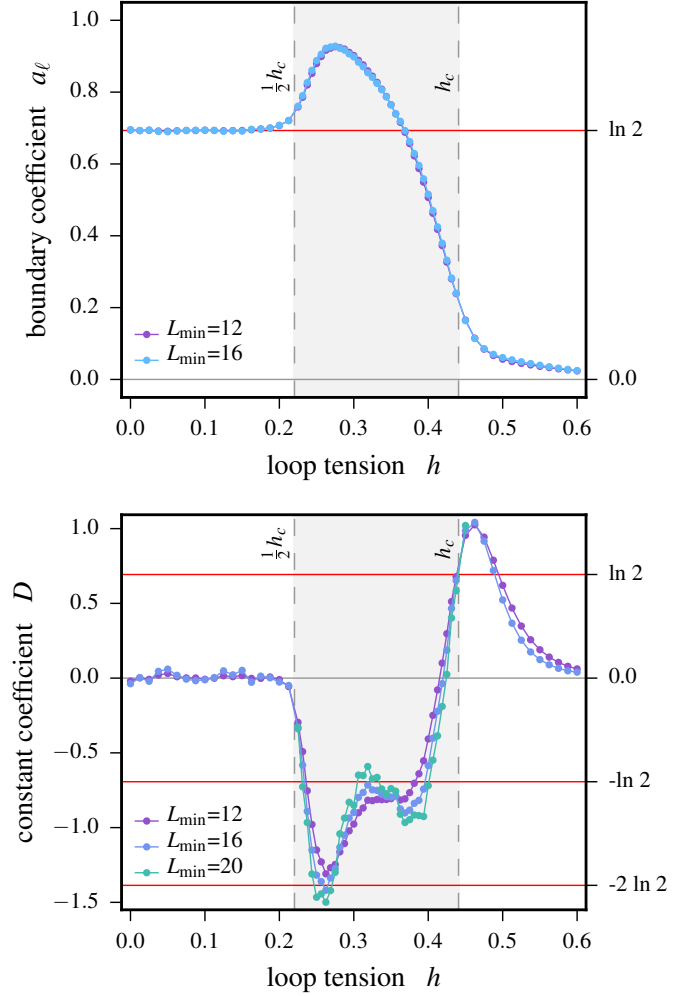


Figure 11.3.: Contributions to the finite-size scaling of the mutual information for the classical toric code model with loop tension h . The top panel shows the boundary coefficient a_ℓ and the bottom panel the constant contribution D of this fit. Data is obtained from fitting system sizes $L_{\min} = 12$ to $L_{\max} = 24$ and $L_{\min} = 16$ to $L_{\max} = 24$, respectively.

Topological entropy In order to obtain a clear signature of the topologically ordered phase, we compute our main quantity of interest — the topological Rényi entropy. We use the Levin-Wen scheme to induce and extract this quantity. The insight about the particularity of an intermediate region for Rényi entropies that we

11. Results for stabilizer codes

gained from the mutual information applies to this case as well. Let us expose in detail the consequences for the quantity

$$\Delta S = -S_2(A_1) + S_2(A_2) + S_2(A_3) - S_2(A_4), \quad (11.3)$$

coming from the separated critical points of the loop tension of the subsystems — $h_c/2$ for A versus h_c for B — in the replica representation. ΔS precisely represents the $O(1)$ contribution to the entanglement entropy $S_2(A)$ as all volume, boundary and corner contributions are cancelled.

We first remind that only bipartition A_4 induces a non-vanishing subleading topological term $\gamma = \ln 2$ as pointed out in Section 8.3.2 and Ref. [119]. For $h < h_c/2$ the situation is hence clear for the second Rényi entropy: In our numerical analysis, we expect the $O(1)$ contribution ΔS to be exactly this topological entropy as both subsystems A and B are topologically ordered. Likewise, for $h > h_c$ there are no subtleties since most spins trivially point down in both subsystems. From the limiting case $h \rightarrow \infty$ we can conclude that all four contributions in Eq. (11.3) become identical such that ΔS vanishes. The interesting regime is $h_c/2 < h < h_c$ where part A is in the trivially ordered phase while both replicas of part B exhibit topological order. Bipartitions in which the subsystems are separated by a single boundary have a contribution of $\ln 2$ in this case due to the constraint of closed loops which is never broken in the finite- h study¹. Consequently, we have an $O(1)$ contribution of $2 \ln 2$ for the bipartitions A_1 and A_2 which feature *two* boundaries. Since these contributions in the intermediate regime are rather a signature of the connectedness of the bipartition than of topological order we name it *connectivity contribution*. We summarize the various contributions for each geometry of the

¹This is fundamentally different to the fully topologically ordered phase where such bipartitions do *not* induce an $O(1)$ contribution because the (in that case non-trivially ordered) bulk of A compensates the even-crossings entropy.

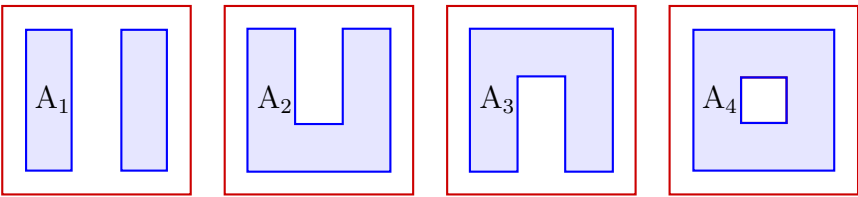
				
topological ($h < h_c/2$)				
γ^A	0	0	0	$\ln 2$
γ^B	$\ln 2$	0	0	0
connectivity ($h_c/2 < h < h_c$)				
γ^A	$2 \ln 2$	$\ln 2$	$\ln 2$	$2 \ln 2$
γ^B	$2 \ln 2$	$\ln 2$	$\ln 2$	$2 \ln 2$

Table 11.1.: Constant contributions to the second Rényi entropy in the topologically ordered phase of the classical toric code model in a loop tension of strength h for the different bipartitions in the Levin-Wen scheme.

11.1. Two-dimensional classical toric code

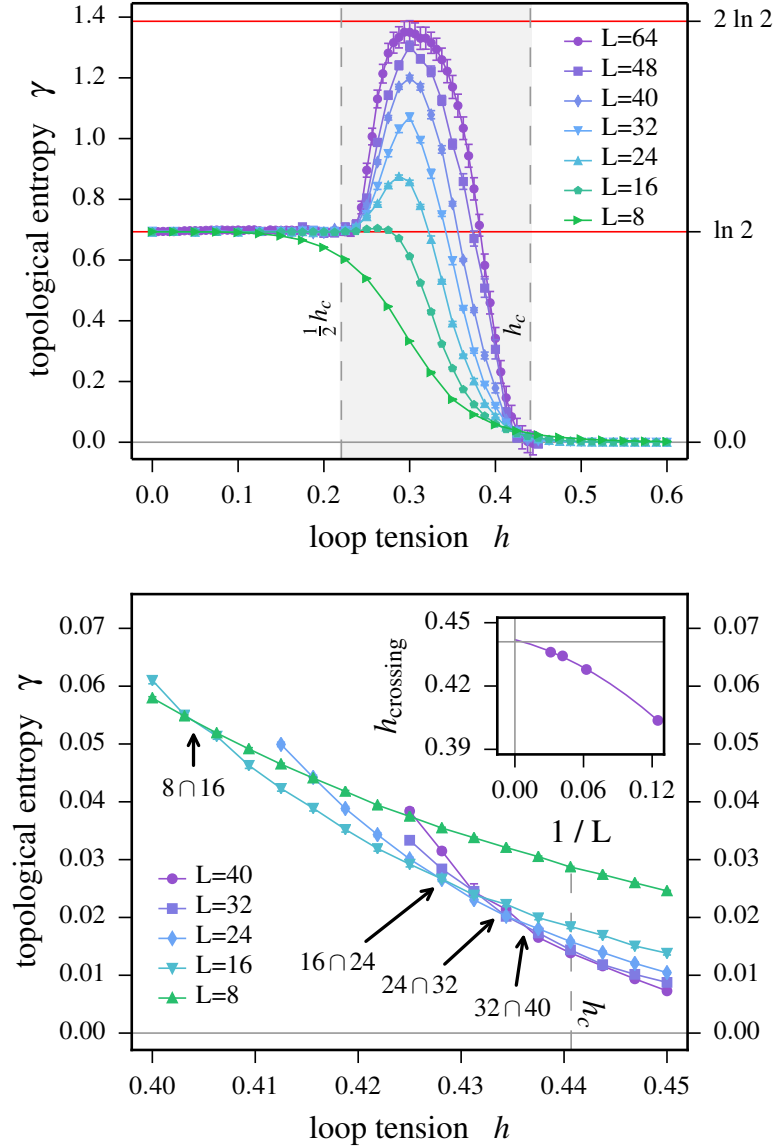


Figure 11.4.: Top panel: The $O(1)$ contribution to the Rényi entropy $S_2(A)$ of the classical toric code model versus loop tension h determined via the Levin-Wen summation scheme. The $O(1)$ contribution contains the expected universal topological contribution of $\gamma = \ln(2)$ in the regime $h \leq h_c$ as well as an additional connectivity contribution $\gamma = \ln(2)$ in the intermediate regime $h_c/2 \leq h \leq h_c$, in which for sufficiently large system sizes subsystem A already transitions into the paramagnetic phase. Bottom panel: Near the critical loop tension, crossing points between data curves of different linear system sizes L can be identified. While keeping the difference between crossing L 's constant ($\Delta L = 8$) a clear tendency towards the critical point can be observed upon increasing L . However, an extrapolation of the location of the crossing points is non-trivial because a subleading logarithmic contribution coming from corners of the subsystem is expected at criticality unlike in off-critical regions.

Levin-Wen scheme in Tab. 11.1. For the $O(1)$ contribution ΔS we hence obtain

$$\Delta S = \begin{cases} \ln 2, & h < h_c/2 \\ 2 \ln 2, & h_c/2 < h < h_c \\ 0, & h > h_c \end{cases} \quad (11.4)$$

11. Results for stabilizer codes

which we will check numerically in the following. We employ Monte Carlo simulations using lattice walk updates in order to efficiently sample the groundstate ensemble and to enable transitions between the degenerate sectors easily. It turns out that the *random* walk strategy is the better option for relatively low values of the loop tension $h \lesssim 0.3$, i.e. where loops are large. The acceptance probability of a large template loop decreases as we increase the loop tension such that the *directed* walk update algorithm outperforms the random walk at larger h . Our results for different system sizes L of the toric code are plotted in Fig. 11.4. The data convincingly confirm the expected behavior of the limiting cases $h \ll h_c$ and $h > h_c$, i.e. they show a constant contribution of $\ln 2$ in the topologically ordered phase which vanishes in the paramagnetic phase. An overshooting emerges upon increasing the system size in the intermediate regime, approaching a plateau at $2 \ln 2$ for large L . This behavior is perfectly consistent with Eq. (11.4). We emphasize that the overshooting is an artifact of the definition of the Rényi entropies which is most evidently understood in the replica-trick picture. A closer look on the data in the region close to the phase transition $h \approx h_c$ reveals that crossing points of consecutive subsystem size curves approach the known value of $h_c \approx 0.44069$. The bottom panel of Fig. 11.4 provides a zoom to this region and demonstrates that an extrapolation of the crossing points to h_c can be done.

While in the quantum case the topological entropy is found even if one restricts the computation to one of the groundstate sectors, this is not true for the classical analogue. Here, it is very important to simulate within the full ensemble of all degenerate sectors in order to find a non-vanishing topological entropy since the degeneracy is the only manifestation of classical topological order. We have verified this statement by simulating ΔS with a local update algorithm which we found to be zero for any value of the loop tension h .

Ising model The finding that the Rényi entropies exhibit non-topological constant subleading contributions leads to the questions whether such contributions can be detected in systems in which topological order is entirely absent. To shed light on this issue we apply our simulation of ΔS to the two-dimensional Ising model. For this model we use the Wolff cluster-flip algorithm which can be straightforwardly adapted to the replica representation since there are no winding objects in the Ising model.

The results of our computations of the $O(1)$ contribution using the Levin-Wen scheme are shown in Fig. 11.5 for tuning β through the thermal phase transition at $\beta_c \approx 0.44069$. Indeed, we observe the manifestation of a plateau at $\ln 2$ in the intermediate regime $\beta_c/2 < \beta < \beta_c$ upon increasing the system size. This feature is satisfyingly understood from considering the state of magnetic order in the two subsystems. In the intermediate temperature regime, subsystem A is magnetically ordered but part B is not. The two possible global orientations resulting from spontaneous symmetry breaking induce a constant entropy of $\ln 2$ *per disconnected part* of A since we allow for transitions between the global spin-up and spin-down phase in our simulation. Specifically, in bipartition A_1 of the Levin-Wen scheme, either of the two rectangles can collectively point up or down independently, yielding a total $O(1)$ contribution of $2 \ln 2$ while all other bipartitions only contribute $\ln 2$.

Hence, we obtain $\Delta S = \ln 2$ in this regime and zero elsewhere as the system is either fully disordered or polarized — leading to equal $O(1)$ contributions for all bipartitions. We note, that disconnected parts of subsystem A can only take their global orientation independently if they are separated from each other by a distance exceeding the correlation length ξ . This explains why the plateau only emerges for large system sizes. We confirm our statement that such connectivity contributions are not of topological origin but an artifact of the Rényi entropies.

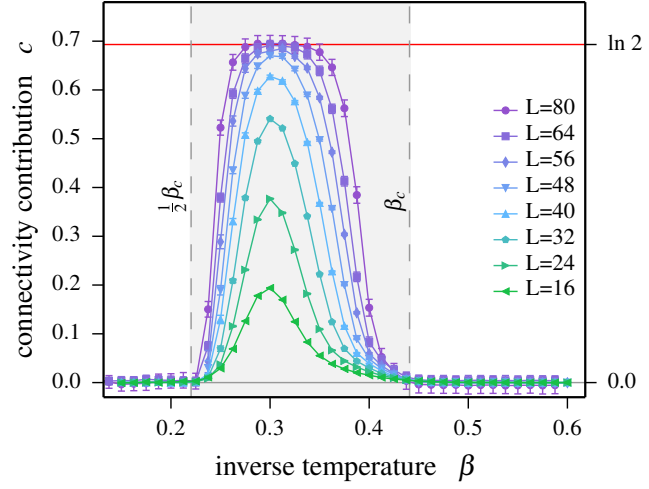


Figure 11.5.: The $O(1)$ contribution to the Rényi entropy $S_2(A)$ of the 2D Ising model versus inverse temperature β determined via the Levin-Wen summation scheme. While no topological contribution is expected, a finite $O(1)$ connectivity contribution of $c = \ln(2)$ is observed in the intermediate regime $\beta_c/2 \leq \beta \leq \beta_c$ (indicated by the grey shaded area), in which for sufficiently large system sizes subsystem A already transitions into the low-temperature ordered phase.

Finite temperature We finally combine our study of a finite loop tension with the preceding investigation of the effect of a finite temperature. Therefore, we have to introduce an *explicit* inverse temperature β in the statistical weights of (open and closed) string configurations \mathfrak{s} , i.e.

$$w(\mathfrak{s}) = \exp(-\beta J_v D_{\mathfrak{s}} - \beta h m_{\mathfrak{s}}), \quad (11.5)$$

where $D_{\mathfrak{s}}$ denotes the number of defects (open loop ends) on vertices of the configurations and $m_{\mathfrak{s}}$ is the total magnetization. The fact that we overlay the weights of the loop tension with a finite temperature implies that we cannot assess a finite topological entropy at very low temperatures since even at a small loop tension any loops with spins pointing down are immediately frozen out, i.e. the system is in a trivial state.

11. Results for stabilizer codes

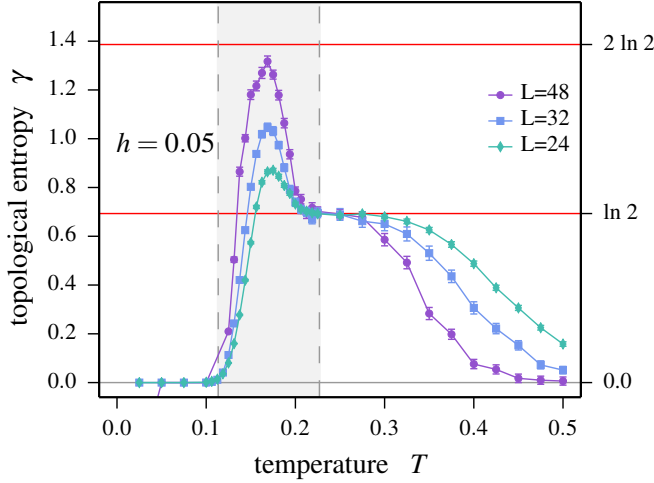


Figure 11.6.: Finite-temperature behavior of $O(1)$ contribution to the Rényi entropy S_2 of the classical toric code model in the presence of a finite loop tension $h = 0.05$. The $O(1)$ contribution exhibits the expected universal topological contribution $\gamma = \ln(2)$, which contributes for sufficiently large temperatures and vanishes at high temperatures. An additional connectivity contribution of $\gamma = \ln(2)$ is observed in an intermediate regime. It can be understood from noting that the *effective* field is $h_{\text{eff}} = \beta h$ as we introduced β in the Hamiltonian. Hence this field increases for $T \rightarrow 0$ and we observe the same behavior as in Fig. 11.4 – read from right to left. At very low temperature even a small field $h = 0.05$ leads to the frozen trivial phase so that no topological order is present and thus $\gamma = 0$.

Our numerical data for this combined study (Fig. 11.6) at a fixed loop tension $h = 0.05$ reflect this behavior at $T \lesssim 0.1$. As pointed out for the implicit temperature study above, only if $h \ll \beta^{-1} \ll J_v$ we can observe topological order. Thus, it is useful to introduce the notion of an effective loop tension $h_{\text{eff}} = \beta h$ to explain the behavior of γ from our simulations. The left half of Fig. 11.6 — seen from right to left, i.e. in the direction of increasing β — exhibits the same behavior as the top panel of Fig. 11.4, including the connectivity contribution in the intermediate regime $h_c/2 < h_{\text{eff}} < h_c$. Only if the temperature is increased to sufficiently high values

where the topological order breaks down (right half) we see the same vanishing of $\gamma \rightarrow 0$ as in Fig. 11.1.

11.2. Three-dimensional classical codes

We extend our numerical analysis of topological order to both classical variants of the three-dimensional toric code model. One of them, the plaquette variant (9.18), exhibits a finite-temperature phase transition, i.e. a finite value for the topological entropy γ below a critical temperature T_c independent of the system size. In the context of conventional order such transitions would be accompanied by a divergence in the specific heat C_v . This raises the questions whether the breakdown of topological order is likewise manifested in a singular behavior of C_v . We numerically investigate this issue not only for the toric code but — in the quest for truly self-correcting stabilizer codes — also for the X-cube and the cubic code model. Subsequently, we carry out a similar analysis to that of the two-dimensional case for the toric code in three dimensions. We first determine γ for a range of inverse temperatures before we place the plaquette Hamiltonian in an external membrane tension, Eq. (9.20), which we tune through a phase transition equivalent to the one

in the three-dimensional Ising model.

11.2.1. Specific heat

We solely employ single-spin flip updates for the simulations meant to measure the specific heat.

Toric code model

Our numerical results for the specific heat are shown in Fig. 11.7 for the classical vertex variant of the toric code model. As expected, it reveals no diverging behavior or movement of the peak position upon increasing the system size. The common broad maximum at $\beta \approx 1.2$ indicates a crossover behavior of the energy in the system but not a phase transition. In the regime of $\beta \gtrsim 2.5$ transient discrepancies between the different system sizes become appar-

ent. As will be seen in the next Subsection, these features correspond to the size-dependent breakdown of the topological entropy which occurs at crossover temperatures $T_{\text{co}}(L)$ precisely in this regime.

The specific heat of the plaquette variant of the three-dimensional toric code has a richer significance. It shows the typical behavior of a phase transition by exhibiting a peak which becomes sharper upon increasing the system size, see Fig. 11.8. We can understand this transition from considering the nature of the thermally induced excitations. An excitation consists of at least four excited plaquettes which form a loop (see Fig 9.6). Such a loop can be enlarged only at the cost of additional plaquette excitations. Hence, at low temperature, these loop-like excitations are energetically hindered and occur mainly as isolated single-spin flips. Surpassing a critical temperature T_c , longer loops become possible and constitute typical configurations. This so-called *deconfinement* transition is dual to the order-disorder transition of the three-dimensional Ising model [154]. Moreover, the classical plaquette variant of the three-dimensional toric code is precisely the mapping of the three-dimensional Ising model from the Kramers-Wannier duality. The phase transitions are linked via $\beta_c^{(\text{TC})} = -\frac{1}{2} \ln \tanh \beta_c^{(\text{Is})} \approx 0.76141$ [137, 145]. The low-temperature ferromagnetic phase in the Ising model corresponds to the high-temperature phase

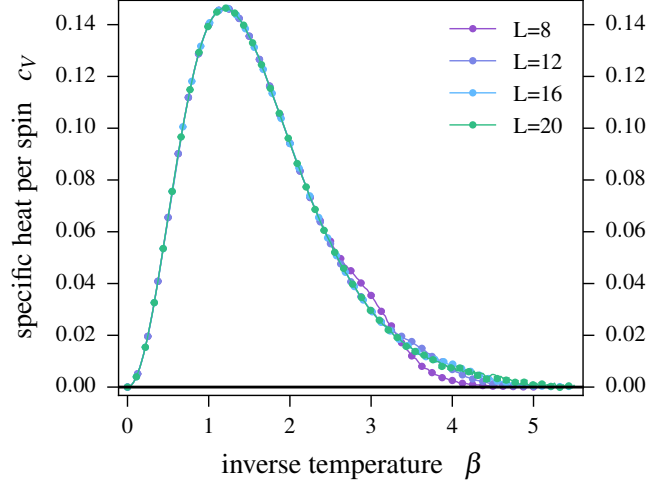


Figure 11.7.: Specific heat of the classical vertex variant of the three-dimensional toric code model as a function of the inverse temperature. The data for different system sizes mainly collapse and do not reveal a diverging behavior. Transient features at $\beta \approx 3.0$ correspond to the breakdown of topological order.

11. Results for stabilizer codes

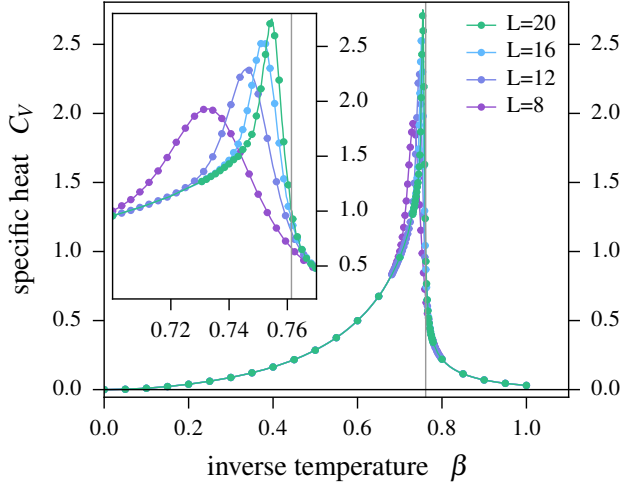


Figure 11.8.: Specific heat of the classical vertex variant of the three-dimensional toric code model as a function of the inverse temperature. A divergent peak close to the phase transition at $\beta_c \approx 0.76141$ emerges in the curves upon increasing the system size. The inset provides a close-up of the peaks slightly below β_c .

of the toric code. Conversely, the paramagnetic phase of the Ising model maps to the low-temperature phase of the toric code which reveals traces of topological order.

We further process our numerical data of the specific heat by considering the scaling behavior of the peak position and of its magnitude. As can be seen in Fig. 11.9 we recover very accurately the critical temperature $T_c \approx 1.31335$. Further, we obtain estimates for the critical exponents ν and

α of the three-dimensional Ising universality class which are — in light of the small number of data points entering the fit — surprisingly close to those in the literature. Specifically, we find for the exponent associated with the correlation length $\nu = 0.639(1)$ instead of $\nu^{(\text{Is } 3\text{d})} = 0.62997$ and for the exponent of the specific heat $\alpha = 0.15(1)$ instead of $\alpha^{(\text{Is } 3\text{d})} = 0.11008$. The quality of our numerical estimation of the critical temperature and the exponents is underlined by the fact that the data points in the scaling plots do not exhibit considerable deviations from the fitted curves.

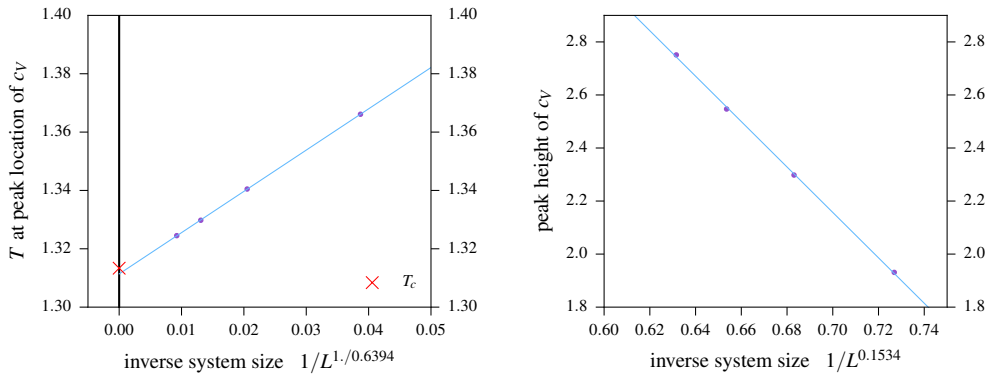


Figure 11.9.: Left panel: Fit of a power law of the inverse system size to the peak position of the specific heat of the plaquette variant, Fig. 11.8. The resulting exponent associated with the correlation length ν is close to the value in the literature (0.62997). Also the extrapolated value of the peak position in the thermodynamic limit is approximately the known critical temperature T_c . Right panel: Fit of the peak height of the same data. We obtain a value for the critical exponent α — describing the divergence of the specific heat — which is again in agreement with the value in the literature (0.11008).

X-cube model With regard to the finite-temperature behavior, the roles of the threesome²-type and the single-type classical variants are switched between the toric code and the X-cube model: There is no finite-temperature stability of topological order to be expected in the threesome vertex variant of the X-cube model as its excitations are open strings. However, in contrast to its non-stable toric code counterpart — the vertex variant (Fig. 11.7) — the specific heat of the X-cube *does* exhibit moving local maxima

upon increasing the system size, see Fig. 11.10. It becomes only apparent in a finite-size scaling ansatz of the peak location that the behavior vanishes in the thermodynamic limit and hence does not represent a phase transition. The form of the scaling is $1/\ln L$, just like in the toric code vertex variant and consistent with Ref. [139]. In addition, a crossover behavior at $\beta \approx 0.7$ is revealed by all curves — a common feature with the corresponding toric code.

The cube variant of the X-cube model, i.e. the classical system made from the twelve-body interactions A_c in Eq. (9.22) exhibits loop-like excitations. Similar to the arguments in the discussion of the plaquette terms in the three-dimensional toric code, enlarging an existing elementary excitation (four excited cubes) costs energy and appears only at sufficiently large temperatures. This observation constitutes our expectation for a finite-temperature phase transition in this model. Our simulation results are depicted in Fig. 11.11 and show narrow peaks which are considerably displaced between consecutive even system sizes. Indeed, a fit to a power law of the peak position yields a function which extrapolates to a finite value of $T_c = 0.294(1)$ for $\beta \rightarrow 0$. The corresponding fitted critical exponent $\nu^{-1} = 1.23(1)$ establishes a very strong alignment of the data points in the scaling plot.

Furthermore, we observe another interesting feature of the specific heat for the classical cube variant: Apart from the peaks, the data for different system sizes seem to have a common baseline for high temperatures — being precisely the curve of the three-dimensional toric code vertex variant in the thermodynamic limit, i.e.

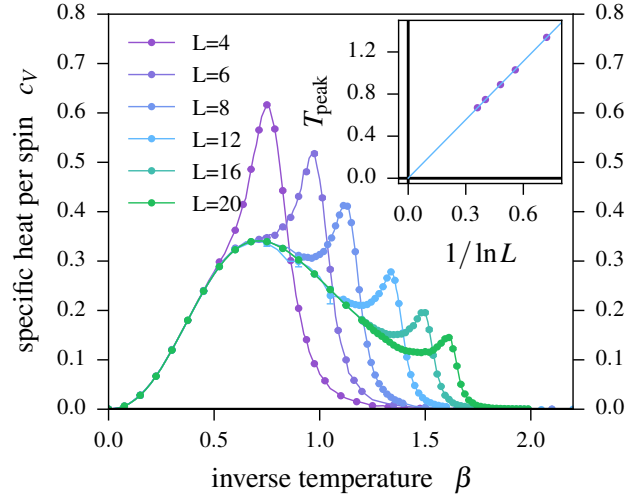


Figure 11.10.: Specific heat of the classical vertex variant of the X-cube model as a function of the inverse temperature. A shrinking peak moving towards lower temperatures can be identified upon increasing the system size. The curves for different system sizes have a common base which reveals a crossover behavior at $\beta \approx 0.6$. Inset: Scaling of the peak position as a function of the inverse logarithmic system size. The data points fall onto a straight line which extrapolates to zero in the thermodynamic limit — as expected.

²We mean by ‘threesome’ that the type of this interaction exists in three different orientations in the Hamiltonian.

11. Results for stabilizer codes

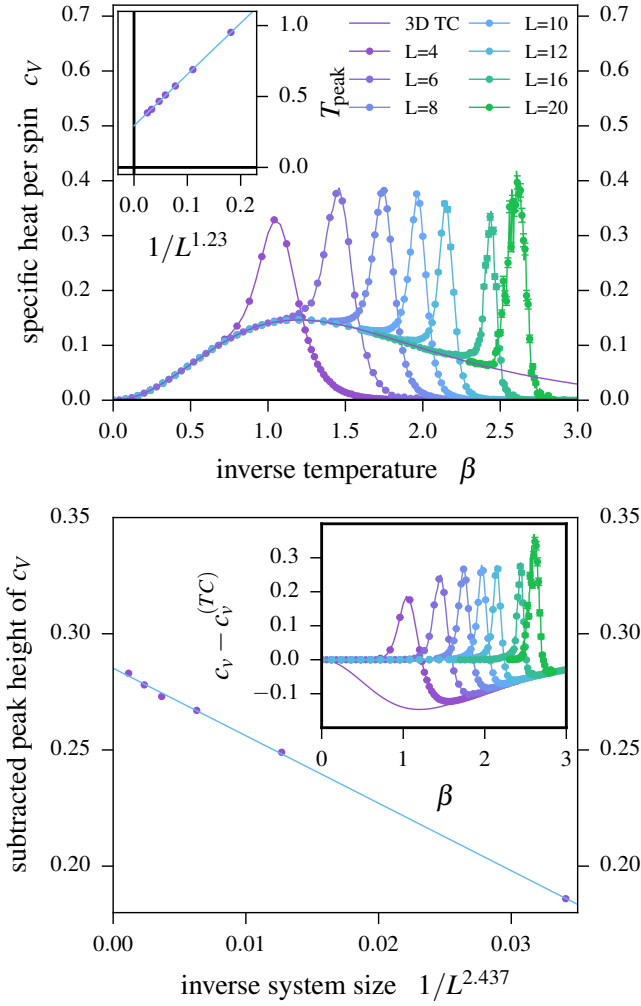


Figure 11.11.: Top panel: Specific heat of the cube variant of the X-cube model as a function of the inverse temperature. The data show a peak which moves towards lower temperature upon increasing the system size. All curves share a common baseline which is identical to the specific heat of the vertex variant of the three-dimensional toric code. Performing a fit of a power law to the peak position (inset) yields an exponent $\nu^{-1} = 1.23(1)$ and a finite temperature for the transition in the thermodynamic limit. Bottom panel: In order to fit a power law to the peak height we first subtract the common baseline from the data. The fit returns an exponent associated with the divergence of the specific heat $\alpha = 2.437(1)$.

Fig. 11.7. The reason for this behavior can be understood from a microscopic perspective, that is, to consider what energetic changes are induced by single spin-flips. If the temperature is sufficiently high such that the X-cube system is densely covered with excited cubes, it is very likely that a randomly picked spin is adjacent to one, two or three excited cubes (but rarely to zero or four). Hence, the energy change resulting from flipping this spin is $\Delta E \in \{-4J_c, 0, 4J_c\}$ just like in the vertex toric code model. The total energy can be assumed to be the same for these two models and therefore also the specific heat. We decide to *subtract* the common baseline in order to obtain adjusted peak heights which we subject to a scaling ansatz. As shown in the bottom panel of Fig. 11.11, we obtain a critical exponent $\alpha = 2.437(1)$. However, the numerical data points reveal a slight scattering around the fitted curve.

Cubic code Both classical variants of the cubic code, Eq. (9.23) are structurally identical. Since it is claimed that this code exhibits a thermal stability of the ground-state topological order, we expect the specific heat of its classical variant to reflect traces of a phase transition. However, the situation is more complex compared to the previously studied codes: First, the groundstate degeneracy which is broken at

the breakdown of topological order is not universal but depends non-trivially on the system size L , except for all odd L which have a common degeneracy of 4. Second, the underlying structure of groundstate configurations is *fractal* instead of loops or membranes, see Refs. [125, 147].

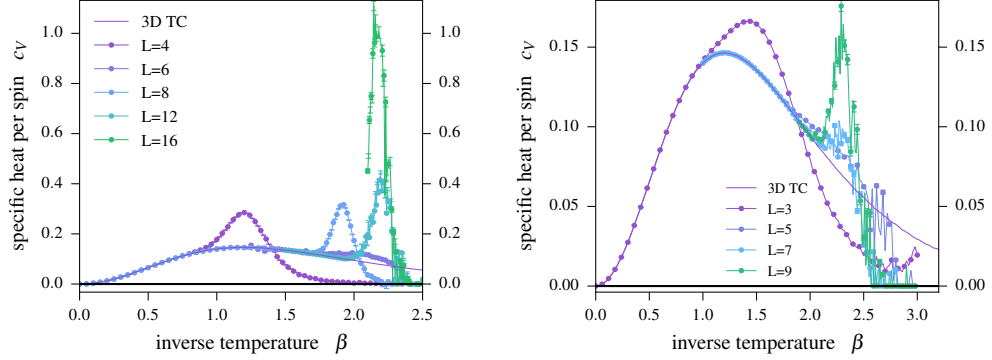


Figure 11.12.: Specific heat of the classical variant of cubic code model for even (left panel) and odd (right panel) system sizes. A movement of the peak position is only recognizable for the very small system sizes. The peak seems not to move further above $\beta \gtrsim 2.3$. Already for relatively small sizes of $L \geq 12$ ($L \geq 5$) in the even (odd) case, the data are affected by significant noise. All curves have a common baseline — the specific heat of the plaquette variant of the three-dimensional toric code.

We plot our numerical data for the specific of the cubic code separately for even and for odd system sizes in Fig. 11.12. The even system sizes exhibit broad peaks which initially show a tendency to move towards lower temperatures. For $L = 12$ and $L = 16$, however, the peak seems to be approximately at the same temperature. Again, all data have a common baseline for sufficiently low β which coincides with the specific heat of toric code vertex variant. The reason for this agreement in the behavior can again be understood heuristically from noting (cf. Fig. 9.9) that a single spin flip in the cubic code causes the switch of the quantum number of four cubes, just like in the X-cube code. For large enough temperatures, most spins belong to at least one cube which is already excited. Hence the energetic change induced by flipping such a spin is mostly the same as for the vertex variant of the three-dimensional toric code model, namely $\Delta E \in \{-4J_1, 0, 4J_1\}$. A fit to the peak positions in order to investigate the finite-size scaling behavior of the cubic code model is not reasonably possible since the peak does not reveal a clear shift upon increasing system size. For odd system sizes, the location of the peak seems to saturate at $\beta \approx 2.3$. We conclude that the perspective of a specific heat analysis seems not compatible with the fractal structures of the cubic code at low temperatures and thereby does not provide a clear signature of the expected transition from a topologically ordered to a trivial phase. Moreover, the power of the single-spin flip algorithm applied for this study is very limited for these fractal structures as can be seen in the large statistical errors on the data points.

11.2.2. Finite temperature

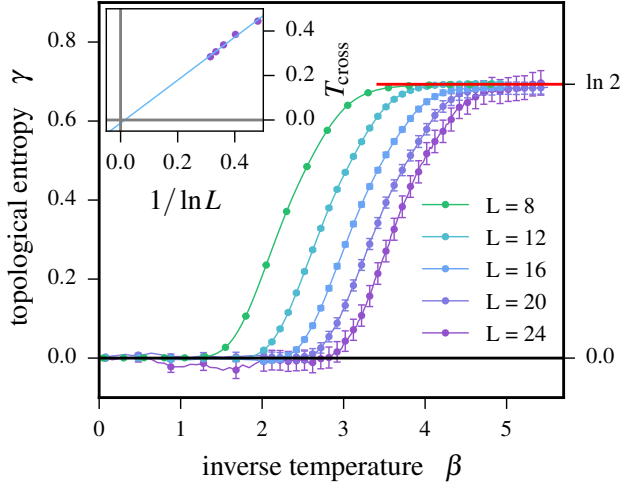


Figure 11.13.: Topological entropy of the vertex variant of the toric code model as a function of the inverse temperature. The topological entropy has a finite value of $\ln 2$ at low temperatures and vanishes upon increasing the temperature. The position of the vanishing depends on the system size L and approaches zero temperature upon increasing L . In the inset, we show the scaling of the temperature of the breakdown. We define the inflection points of the data as the precise locations of the breakdown and fit these locations to $1/\ln L$. As expected, the breakdown temperature vanishes in the thermodynamic limit.

from this simulation are shown in Fig. 11.13. As expected, the larger the system size, the lower is the temperature at which γ vanishes. A quantitative analysis of this relation is performed by identifying the inflection point of the curves to mark the breakdown. The inset of Fig. 11.13 demonstrates that the breakdown scales as $1/\ln L$ and extrapolates to zero in the thermodynamic limit, in agreement with Ref. [139].

For the plaquette variant of the toric code model, subjected to a finite temperature, single spin flips are the Monte Carlo method of our choice. In a first attempt, we use the same Levin-Wen type scheme as above, i.e. the cube-in-a-cube in Fig. 10.2a. Since this model has a phase transition we naively expect a finite value of γ for $\beta > \beta_c \approx 0.76141$. As seen in Fig. 11.14, this is not the case. In the other limit ($\beta \rightarrow 0$) the vanishing of γ reflects the expected behavior of thermal destruction of topological order. Hence, we learn that bipartition A_4 is not apt to produce a reduction in the entropy for systems which exhibit a closed-membrane structure. Nevertheless, the data feature a divergent peak approaching the phase transition from below (with regard to β). A simple linear fit of the locations of these peaks versus the inverse system size $1/L$ yields a curve which extrapolates to $\beta \approx 0.764$, that is, to a critical temperature close to the value from the literature. Moreover, we observe an interim behavior of γ between $\beta_c/2 < \beta < \beta_c$ which suggests that a

We turn to the perspective of the classical topological entropy γ in which we analyze the three-dimensional toric code model. For the simulation of the classical vertex variant we employ our advanced variant of a local update algorithm which randomly picks two or three vertices in the replica representation of the system. These vertices are flipped according to the Metropolis probabilities and the spins states are completely ignored in the simulation. In order to create and extract a topological term, we use the scheme in Fig. 10.2a, dubbed cube-in-a-cube. Our numerical results

value of $\gamma = \ln 2$ could be taken in the thermodynamic limit. As pointed out earlier, such a behavior is an artifact of the second Rényi entropy.

Our hypothesis for the above failure of the detection of a finite γ in the topologically ordered phase is, that we have tried to detect a membrane with another membrane (the bipartition). To cure this problem, we try to detect the membranes with two-dimensional slices via the ‘layers’ bipartition in Fig. 10.2b. Since we expect every set of equally positioned layers to detect the same topological contribution, we divide the obtained constant by the number of layers L . Fig. 11.15 shows the results from our Monte Carlo simulations. Indeed, we observe a contribution per

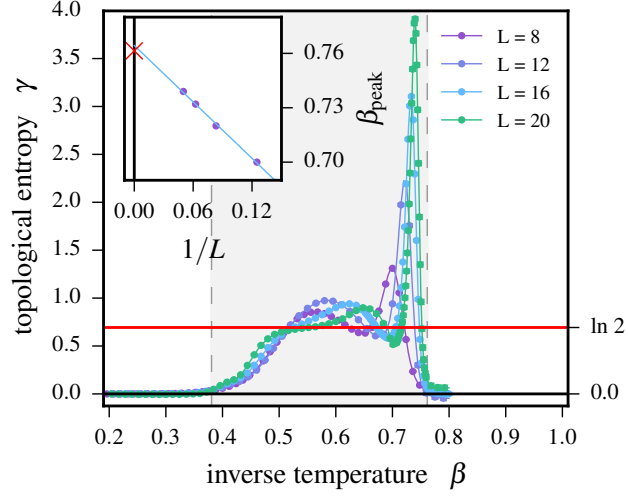


Figure 11.14.: Topological entropy of the plaquette variant of the three-dimensional toric code as a function of the inverse temperature using the cube-in-a-cube extraction. No finite value of γ is revealed in the topologically ordered phase for $\beta > \beta_c$. However, a divergent peak approaches the critical inverse temperature from above upon increasing the system size. A scaling of the peak position with the inverse system size is demonstrated in the inset. In the thermodynamic limit, this scaling extrapolates very accurately to the known critical β_c .

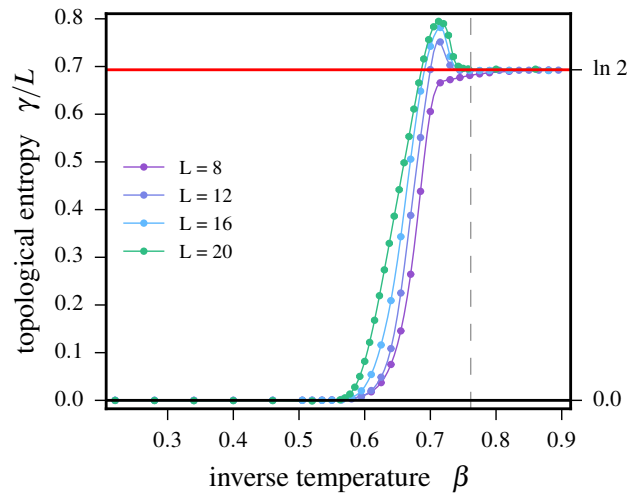


Figure 11.15.: Topological entropy per layer for the plaquette variant of the three-dimensional toric code using the extraction scheme consisting of layers. We obtain a finite value for the topological entropy in the topologically ordered phase $\beta > \beta_c$. A broadening peak emerges slightly below the inverse transition temperature for larger system sizes.

11. Results for stabilizer codes

layer of $\gamma/L = \ln 2$ at inverse temperatures $\beta > \beta_c$. Upon increasing the system size, there seems to emerge a broad peak slightly below the phase transition whose right leg approaches β_c . It is worthwhile to note that *no* interim behavior appears in this simulation. Its absence can be understood from the fact that the collection of layers — as opposed to a true bulk — does not allow for bulk order effects in subsystem A . The latter would separate the critical behavior of the subsystems A and B due to the *effective* inverse temperature of 2β in subsystem A .

11.2.3. Membrane tension

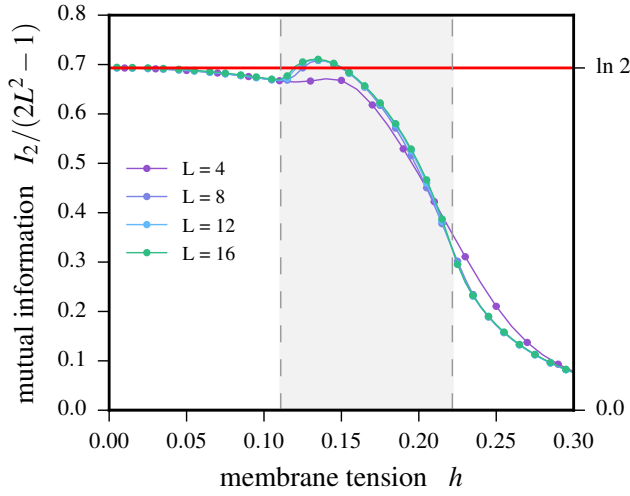


Figure 11.16.: Mutual information per boundary element of the three-dimensional toric code model placed in an external membrane tension. The bipartition employed for this computation cuts the cube into two halves. We observe a finite value of $\ln 2$ in the topologically ordered low- h phase which vanishes for large h . In an intermediate region between $h_c/2 < h < h_c$, a light overshooting of the mutual information appears. At the critical membrane tension $h_c \approx 0.221656$ the mutual information strongly breaks down.

vertex-cluster flip updates for the simulation of this system. However, both types must be extended by global updates of single winding membranes in order to seize the entire degenerate ensemble. This system can be mapped to the three-dimensional Ising model at varying temperature by transforming membranes to domain walls of the Ising spins. We thus know that there is a phase transition at $h_c = \beta_c^{(\text{Is})} \approx 0.221656$ in the three-dimensional toric code from the topologically ordered low-tension phase to the paramagnet for $h > h_c$.

We first consider the mutual information $I_2(A : B)$ for regions A and B which are each exactly one half of the cube (in periodic boundary conditions). Since contributions from the boundary between A and B are not cancelled in the definition of the mutual information, we divide the data by $(2L^2 - 1)$ which corresponds to

We place the plaquette variant of the three-dimensional toric code in a finite magnetic field h — denoted as membrane tension — and consider the corresponding Hamiltonian (9.20) at its groundstate where only closed membranes are allowed. As in the two-dimensional case, we implicitly assume a finite temperature which satisfies $h \ll T \ll J_p$ such that the external field does not suppress any configurations which have spins pointing down. The resulting ensemble is invariant under flips of all six spins of a vertex. It is hence natural to employ single-vertex flip or

the boundary size lowered by one. The explanation for the reduction is similar to the two-dimensional toric code, the crucial difference being that we do not consider piercings of loop segments through the boundary of A — yielding points — but rather the intersecting object of a closed membrane with a plane — a closed loop. Closed loops on a square lattice always have an even number of edges, i.e. spins. Therefore, we can reuse the same combinatorial argument that the number of spins pointing down on the plane boundaries must be even which leads to the entropy reduction of one bit of information. Our results for the mutual information are plotted in Fig. 11.16. We observe, that the topologically ordered phase in the limit $h \rightarrow 0$ is reflected by a finite contribution of $\ln 2$ per free boundary element to the mutual information. The mutual information vanishes in the other limit where the configuration of the system is polarized and the Rényi entropies of A and B are zero. We note that only the curve for the very small system size $L = 4$ can be distinguished from the otherwise collapsing curves. This is explained by the strong suppression of h -dependent constant contributions to the mutual information from the division by $(2L^2 - 1)$. The downside of this collapse is that crossing points can hardly be determined. Hence, not much can be gained about the behavior at the expected phase transition h_c apart from a rough proximity to the inflection point of the decreasing curves. At the second Rényi artifactual transition at $h_c/2$, however we note a common local minimum in the data. Finally, also an interim behavior between $h_c/2$ and h_c where the curves undergo a transient increase can be spotted in the mutual information.

For the generation and extraction of a topological entropy in the membrane tension variant we use the scheme 10.2c. In principle, the setup is the three-dimensional variant of the previously discussed connectivity contribution in two dimensions, see Fig. 11.4. In simulations of three dimensional systems we are obviously more restricted in computationally accessible linear system sizes L . We obtain the topological entropy γ for systems up to $L = 20$ which are shown in Fig. 11.17. The data confirm the presence of a topologically ordered phase by exhibiting a finite $\gamma = \ln 2$ in the low mem-

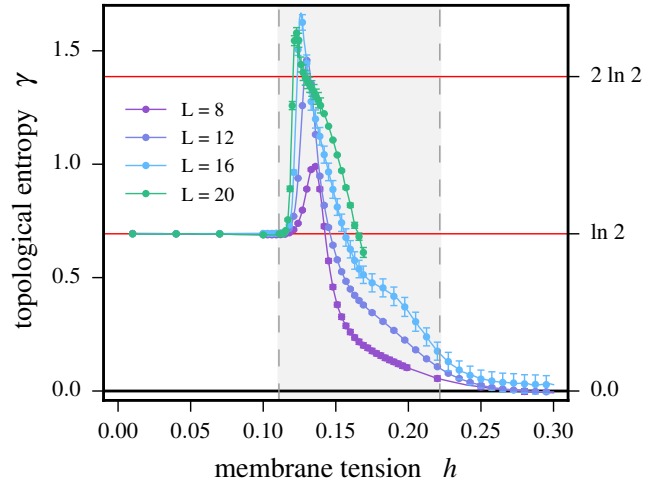


Figure 11.17.: Topological entropy of the plaquette variant of the three-dimensional toric code placed in an external membrane tension h . The topological term is extracted using the scheme in Fig. 10.2c. As expected, we have a finite topological term of $\gamma = \ln 2$ at low h . In the intermediate regime $h_c/2 < h < h_c$, we see first signatures of a connectivity contribution upon increasing the system size. The topological entropy vanishes for $h > h_c$.

11. Results for stabilizer codes

brane tension limit. This topological entropy vanishes for $h \gtrsim 0.25$, i.e. close to the known phase transition at $h_c \approx 0.221656$. A sharp increase of γ is revealed slightly above $h_c/2$, but this feature does not seem to be divergent upon increasing the system size as the peak of $L = 20$ is below the one of $L = 16$. It appears rather plausible that a plateau at $\gamma = 2 \ln 2$ is developed in the intermediate region $h_c/2 < h < h_c$ which corresponds to the connectivity contribution. The curve of $L = 20$ possibly moves towards such a saturation at $h \approx 0.13$. Similar to the mutual information, no clear footprint of the physical phase transition can be worked out in the topological entropy near h_c in the present data. Regarding this issue, it remains to be investigated how the shoulder of the curves at $h \approx 0.2$ behaves upon further increasing the system size.

11.2.4. Quantum to classical mapping

We finally consider the anisotropic plaquette variant of the three-dimensional toric code and tune the membrane tensions in the x - y -plane as to effectively represent the two-dimensional quantum toric code in a transverse field. Here, we primarily assess the numerical feasibility of a simulation of the topological entropy. As pointed out in Sec. 9.3, we fix the lattice spacing in imaginary time dimension (z) to $\Delta = 0.76141$ such that the critical point of the three-dimensional classical model is precisely the isotropic setup $h_z^{(\text{Is})} = h_{x/y}^{(\text{Is})} \approx 0.221656$. The membrane tension in the z -direction is consequently fixed to $h_z = 0.58224$ and we vary h_{xy} in order to observe the phase transition in the topological entropy γ .

We perform simulations employing global Wolff updates of clusters of vertices and measure the magnetizations of both the z -spins and of the spins in the x - y -plane. In order to extract the topological entropy we use the Lewin-Wen addition scheme in Fig. 10.2c since it has no boundaries between consecutive imaginary-time slices and hence does not capture effects coming from the imaginary-time expansion. Although we want to vary h_{xy} but not h_z we nevertheless expect that the collective behavior of the spins in the x - y -plane also impinges on the z spins. This effect necessitates the *double* thermodynamic integration as discussed in Sec. 10.1.2.2, and thereby requires a large number of individual simulations of a dense two-dimensional grid of tuples $(h_{xy}, h_z) \in [0, h_c] \times [0, h_c]$. We present our data for the smallest reasonable linear system size of $L = 8$. For the inevitable discretization of the h_z membrane tension, we have selected eight equidistant points, while a very fine resolution is simulated for the h_{xy} parameter. The top panel of Fig. 11.18 shows the *first* integration in Eq. (10.3) of the measured quantity $\langle m_{xy} m_z \rangle - \langle m_{xy} \rangle \langle m_z \rangle$, namely the one over h_{xy} . These ‘raw’ data reveal the difficulty in obtaining accurate results for the topological entropy using the double integration: The moving extrema for varying h_z should cancel in the second integration — which is only possible if we have a very fine resolution of h_z data points in the grid. Upon increasing h_z the peaks vanish in proximity of the artifactual transition, i.e. the membrane tension at which half of the Ising critical temperature is effectively tuned. In the bottom panel of Fig. 11.18 we carry out the second part of the thermodynamic integration by simply accumulating the curves of the first integration and multiplying them by $\Delta h_z = h_c/8$. Obviously, the oscillating right half of the result is

strongly inaccurate due to the mentioned effect of the peaks and demands a finer resolution. Nevertheless, we have reason to believe that the method is in principle capable of yielding the topological entropy of the quantum-to-classical mapped system. To support

this hypothesis, we compare the double integration with a (conceptually inaccurate) application of the simple thermodynamic integration, Eq. (10.2). In this computation, we have measured m_{xy} for varying h_{xy} at fixed h_z . This simplification is only correct if we can ignore the issue that m_z depends implicitly on h_{xy} . The corresponding curve shows a similar behavior as the isotropic case (Fig. 11.17) and begins developing a peak at the artifactual transition. However, it does *not* saturate at $\gamma = 0$ in the large- h_{xy} limit — demonstrating the inaccuracy of the simplified integration. The point we want to make is, that for $h_{xy} \lesssim 0.3$ the two curves compare rather well even though the double integration has been done on a too coarse discretization. We emphasize that the first peak at $h_{xy} \approx 0.25$ is not simply the leftmost peak of the top panel of Fig. 11.18, but a result of at least the curves of $h_z/h_c = 0.875$ and 1.0. Hence, we conclude that — even though numerically tedious — the double thermodynamic integration is the proper way to

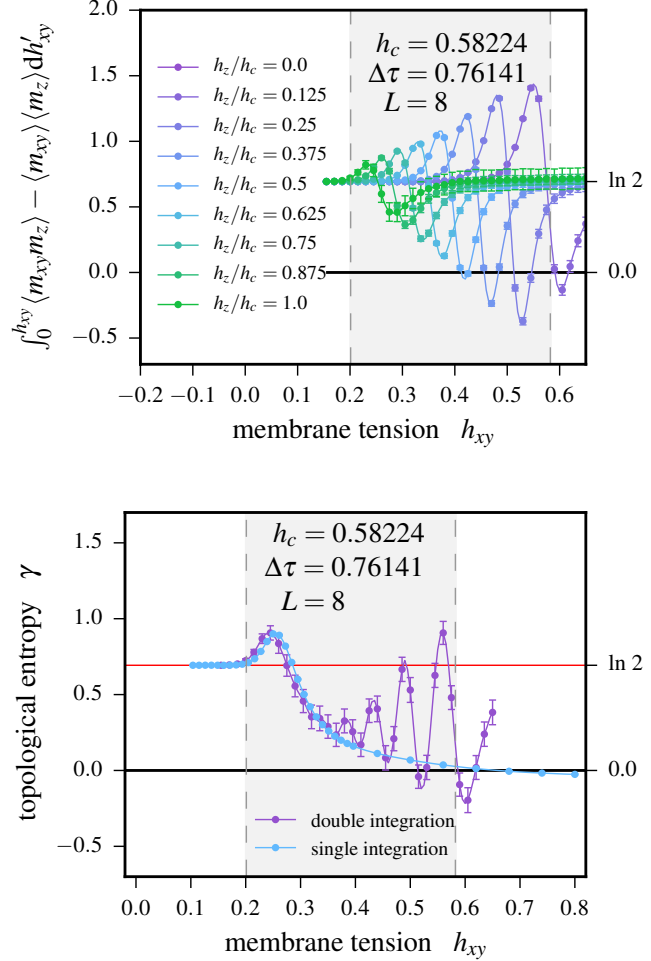


Figure 11.18.: Top panel: Results of the first integration for the computation of the topological entropy of an anisotropic three-dimensional toric code model in an external loop tension. The integration over h_{xy} is carried out for different fixed values of h_z . Bottom panel: Comparison of the computations of the topological entropy using the double integration of $\langle m_{xy} m_z \rangle - \langle m_{xy} \rangle \langle m_z \rangle$ versus a single integration following the concept of all previous thermodynamic integrations. The data basis for the double integration is clearly insufficient which causes the oscillating behavior. The single integration reveals its inaccuracy as it does not saturate at $\gamma = 0$ for large h_{xy} . Slightly above the artifactual critical membrane tension which corresponds to $h^{(ds)} = 0.221656/2$, both curves show a similar behavior.

11. Results for stabilizer codes

compute the topological entropy of the classical three-dimensional toric code with anisotropic membrane tension and thereby the two-dimensional quantum toric code with transverse loop tension.

12. Summary

In this Part of the thesis we have presented the use of entanglement entropies and their classical counterparts for the realm of topological order. Specifically, we have focussed on many-body systems in which topological order constitutes the exploited feature that makes them candidates for quantum memories.

The groundstate phenomenon of topological order is manifested in the entanglement entropies by a negative constant correction to the leading boundary law. In order to establish this connection, we have discussed the nature of this form of order by regarding it as a result of long-ranged entanglement. Further, we have worked out how its underlying structures can be seized by the bipartite entanglement measures used in this thesis. For this endeavor, it turned out that the perspective of loopgases is sufficient for our considered models. The emergent entanglement reduction depends on the specific choice of the bipartition for the entropy computation — a fact which is exploited when employing addition schemes in order to calculate this reduction, the so-called topological entropy.

Understanding the combinatorial mechanism that leads to a finite topological entropy suggested that such a feature should be revealed in classical settings as well. To this end, we defined analogues of entanglement entropies for classical statistical-mechanics ensembles which have been designed to replace the quantum superposition of the groundstate condensates. These classical bipartite entropies indeed turned out to indicate classical topological order — alternatively denoted as topological ergodicity breaking.

Our objects of study in this Part of the thesis have been Hamiltonians which represent quantum error-correcting codes. To provide an understanding of the important properties of such Hamiltonians we have introduced the context and strategy of quantum error correction. These quantum Hamiltonians are designed in order that their groundstates represent the code space of the underlying stabilizer code. Thermal excitations or other perturbations map to errors in the code and can be detected and corrected by appropriate protocols. We have focussed on the Hamiltonian perspective and chosen to work mainly on prototypical examples for topologically protected quantum memories — namely toric code models and variants thereof. The two-dimensional toric code has been discussed in great detail in the light of its (exactly known) groundstate properties, excitations and perturbations by an external longitudinal field. Most importantly, we have derived a classical variant of this model which enabled us to carry out the investigation of classical topological order from an entanglement entropy perspective. These considerations could be straightforwardly transferred to similarly defined quantum Hamiltonians in three dimensions. A major motivation for the interest in three-dimensional models is the thermal instability of topological order in two-dimensional systems for any finite temperature. If, on the other hand, a system turns out to reveal a robustness of

12. Summary

topological order up to a finite temperature, we expect a phase transition to happen at this temperature which is indicated by the vanishing of the topological entropy. We have introduced the three-dimensional toric code and the X-cube code, which are likewise defined on a lattice with degrees of freedom on the edges, as well as Haah's cubic code. Those models which are not self-dual (the toric code in three dimensions and the X-cube code) allow for two different classical variants with significantly different finite-temperature behavior.

Since we have mapped the problem of finding stable quantum memories to a condensed-matter context of phases of matter, we need a numerical tool for the computation of macroscopic observables in a statistical-mechanics ensemble. To this end, we have chosen the approach of Monte Carlo simulations. We have amply explained how we implement its two basic steps, namely the walk through the configuration space and the measurement of appropriate observables in each visited configuration. For the computation of the topological Rényi entropy, the quantity to be measured is simply the energy (or magnetization) just like for the specific heat. However, a modified system has to be designed in order to access the necessary partial trace over one of the subsystem of the bipartitioning. Moreover, a post-processing of the energy measurement is required for the Rényi entropy. The usage of addition schemes finalizes the measurement routine.

The Markov chain engendering the walk through the configuration space is created by well-designed updates of the respective current configuration. Local updates are the simplest way of creating new configurations. But we have demonstrated that in some circumstances these updates are not sufficient for the simulation of the full ensemble. Therefore we have extended our set of updates by global modifications to the configurations. Such updates also increase the efficiency of the simulation if the system is close to a critical points.

The application of the introduced framework and methods led to a number of insights on the basis of our numerical results. For the two-dimensional toric code we were able to verify the expected transient finite-temperature behavior of the topological entropy, including the corresponding finite-size scaling. We further investigated the effect of a finite loop tension to the groundstate ensemble. In principle, a signature of a transition is expected from a known mapping of this setting to the two-dimensional Ising model. We have found the mutual information and topological entropy to indicate the topologically ordered phase and to vanish in the trivial phase. However, already the probe of the perturbation via the mutual information revealed the existence of an intermediate regime between the critical loop tension and half its value — showing singular behavior for the second Rényi entropy. Even more strikingly, the topological entropy itself saturates in the intermediate regime at twice its ordinary value of $\gamma = \ln 2$ for the indication of topological order in the classical toric code. We were able to explain the origin of this behavior by considering the separated parameter regimes in which the subsystem A and B order in the modified system. Our first conclusion is therefore that the usage of Rényi entropies instead of the von Neumann entropy involves artifactual behavior of the quantities of interest. Beyond this qualitative finding we also established a quantitative explanation for the interim overshooting of the topological entropy. To this end, we considered the effect of the seemingly pointless application of the addition scheme

to the two-dimensional Ising model which is free of topological order. It turned out that a similar saturation of the topological entropy at a non-zero value is found in the intermediate regime. Hence, this feature constitutes an additional reduction of the Rényi entropy which is due to the disconnectedness of one or more bipartitions in the addition scheme. We therefore decided to name it *connectivity contribution*.

For the three-dimensional models considered we expected a finite-temperature transition for at least one of their classical variants. We have succeeded in finding this transition from computing the specific heat for a range of inverse temperatures and observing whether divergent peaks show up. From an extrapolation of the peak location and its height, we were able to obtain values for the critical exponents of the correlation length ν and of the specific heat α . In the case of the three-dimensional toric code they agree remarkably well with those of the three-dimensional Ising model and the extrapolated value of the peak position yields the known phase transition of the Ising three-dimensional lattice gauge theory. Also for the X-cube model we could verify our expectations about the presence/absence of a finite-temperature transition for each of the two classical variants. Furthermore, we turned to the topological entropy in the three-dimensional toric code. For the finite-temperature behavior we have found it to indicate the breakdown of topological order for the variant in which string operator induce excitations. More attention needs to be paid to the choice of the addition scheme if we want to detect topological order in the other classical variant which is characterized by membrane structures. For the detection of a finite topological entropy in the topologically ordered phase, it turned out useful to design the addition scheme based on (two-dimensional) layers instead of three-dimensional subsystems A . We have found the vanishing of γ to take place in proximity of the known phase transition in this case. Finally, we placed the three-dimensional toric code in an external field — a membrane tension. For an isotropic field, the resulting Hamiltonian can be mapped to the three-dimensional Ising model such that we could find the corresponding phase transition and its Rényi artifact in the topological entropy. Moreover, it does not imply substantially more complexity to make the field anisotropic by allowing the edges in the z -direction to take a different value of the magnetization. This modification allowed us to directly simulate a two-dimensional quantum toric code in an external field via the $2 + 1$ dimensional quantum-to-classical correspondence.

13. Conclusion

In this thesis we have gained a thorough insight of various aspects of the powerful concept of entanglement entropy in many-body systems. It has been elucidated why and how this quantity measures quantum correlations in groundstates and thereby enables an identification of different phases of quantum systems at zero temperature. The methodological necessity to introduce a bipartition in the many-body system provides a toolbox for the extraction of information associated with particular physical phenomena of interest. The key to using the bipartition as a resource is the prevalent boundary law which extracts universal quantities from a scaling of the entanglement entropies with the size of the boundary between the subsystems. Specifically, these quantities are the coefficients of the subleading contributions. Depending on the selected size and geometry of the subsystem, we were able to induce different coefficients.

The boundary coefficient is non-universal but reflects the increase of the correlation length at phase transitions accompanied by symmetry breaking. In the models we have considered in Part one, this coefficient showed a local maximum at the transition upon tuning the relevant parameter. While a decrease towards the disordered side is not surprising as the correlation length vanishes, such a decay is not a priori expected on the ordered side. The reason for this decay is, that there exist amplitude modes which are gapless at the transition but gapped further away from it. The more gapless excitations are present in the spectrum the larger is the boundary coefficient, hence the local maximum at the transition. A further study of how the boundary coefficient behaves for a model devoid of amplitude modes, e.g. suppressed by a magnetic field, would help to further examine the significance of entanglement entropies for probing the interplay between phase transitions and amplitude modes.

A universal quantity for phase transitions is the coefficient of the logarithmic contribution to the boundary law. We have confirmed this statement for interacting theories, where the critical point is of Wilson-Fisher type. Furthermore, we have applied the entanglement entropy analysis to the two-dimensional free boson and free Dirac fermion lattice field theories. To this end, we have selected a subsystem with corners in our bipartitions and thereby induced the logarithmic contribution. We were able to draw conclusions about this quantity, in particular, how it depends on the opening angle of the corner and on the Rényi order. The logarithmic contribution is related to the degrees of freedom of low-lying excitations of the conformal field theories describing the free boson and the free Dirac fermion. Its calculation would hence be a useful numerical approach for the investigation of quantum phase transition in which the low-energy behavior is unknown. As little is known about three-dimensional free theories, an obvious and straightforward generalization would be to apply this numerical analysis to these cases. Also other quantum

13. Conclusion

critical systems — for example a fermion model with quadratic band touching — represent interesting case studies for low-energy physics which is tractable by our method.

The most important application of the entanglement entropy analysis refers to the domain of topological order. Often, the only accessible approach to identify this phenomenon in many-body systems is to check for a finite constant (‘topological’) contribution to the boundary law of entanglement entropy. We have pointed out that the effect of long-ranged correlations leading to a finite topological contribution can be partly reproduced in pure classical systems. This perspective enabled us to numerically investigate classical many-body systems exhibiting topological order by Monte Carlo simulations. To this end, we picked the toric code model in two and three dimensions as our object of study. We could assess the role of the topological contribution in tracking transition between topologically ordered and trivial phases driven by a varying temperature or an external loop tension. In particular, the finite-temperature transitions are of crucial significance for models designed to be self-correcting quantum memories. In order that a model can be such a memory, both types of interactions in the quantum Hamiltonian, that is, the σ^x and the σ^z interactions, have to exhibit a phase transition when mapped to corresponding classical models. We have not seen such a behavior in any of the toric code models considered in this thesis up to three dimensions.

A finite-temperature phase transition can alternatively be detected by determining the specific heat at varying temperatures for different lattice sizes. We have followed this approach for the toric code models but also for the X-cube and the cubic code in three dimensions. We were able to confirm our expected behavior for the toric and the X-cube code. By improving the numerical setup, e.g., including parallel tempering in the simulations, we might further pinpoint our found transition temperature and exponents.

For Haah’s cubic code, the specific heat measurement were not successful due to the immense and varying groundstate degeneracy and the fractal structure of the excited states. Again, parallel tempering could help lower the statistical uncertainties. The same goal could be achieved by the development of Monte Carlo updates more specialized to the cubic code than the simple single-spin flips. Also, an entanglement entropy analysis of the X-cube and the cubic code would be a follow-up investigation to our work. These efforts could help answering the question whether the cubic code is a suitable self-correcting quantum memory.

Regarding the toric code models, further aspects such as the inclusion of Ising-like perturbations of neighboring spins [155] could be included in subsequent studies. It would also be desirable to perform a complementary *Quantum* Monte Carlo simulation of the original quantum toric code Hamiltonian using a stochastic series expansion. This finite-temperature method could provide a numerical verification of the expected size-dependent breakdown of groundstate topological order when cranking up temperature. However, the four-body interactions hamper this approach if combined with the loop updates strategy [156]. We would hence have to combine an insertion of mutually annihilating pairs of σ^x interactions with our classical update techniques performed on equal-time slices of the imaginary time expansion. Having such a simulational setup, a very interesting endeavor would be the investi-

gation of a so-called *conformal quantum critical point* [53] in the two-dimensional toric code model — obtained if the groundstate wavefunction itself (instead of the Hamiltonian) is made critical. We could observe how the transitions with different dynamic critical exponents $z = 1$ ($z = 2$) from a Hamiltonian (wavefunction) deformation, respectively, are reflected in the topological entanglement entropy.

We finally remark that the toric code model is of practical relevance as there are proposals how to physically implement it as so-called surface codes using superconducting circuits [157] and thereby actually build quantum computers. As for the concept of entanglement entropies in general we close our considerations in this thesis by emphasizing two future challenges: First, the limitations of Rényi entropies compared with the von Neumann entropy have to be fully unveiled in order to avoid unphysical conclusions from artifactual critical points — one such artifact has been understood in this thesis. Second, the availability of an experimental setup for the measurement of Rényi entropies in optical lattices may lead to further establishing entanglement entropies as a common tool for analyzing critical behavior and identifying topological order in theoretical and experimental many-body physics.

Acknowledgements

First of all, I thank my supervisor Simon Trebst for his guidance in research and the opportunity to work in his group at the University of Cologne. I enjoyed a great time during the preparation of this thesis in a lively environment. Simon also enabled and encouraged me to spend three month at the Perimeter Institute in Waterloo, Ontario, Canada in Fall 2015. I thank him one more time for this great experience.

Further, I am very grateful to Stefan Wessel and Roger Melko as part of this thesis was developed under their supervision.

I also learned a lot from my collaborators in the diverse projects — Jean-Marie Stéphan, Lauren Hayward Sierens, Anushya Chandran and William Witczak-Kremppa. We had many fruitful discussions and I benefited very much from their assistance for which I thank them.

All of the aforementioned people have helped me extraordinarily by proofreading parts of this thesis, as well as Kevin O’Brien, Peter Bröcker, Josselin Bernardoff, Matthijs Hogervorst, Maria Hermanns and Max H. Gerlach. I am grateful for this assistance.

Further, I thank Achim Rosch as I profited a lot from his input on my research.

The numerical simulations in this thesis have been performed on the Cologne High Efficiency Operating Platform for Science (CHEOPS). I thank the CHEOPS team for their laborious work.

I enjoyed the support from the Bonn-Cologne Graduate School of Physics and Astronomy (BCGS) to a very large extent for which I am indebted to this institution, especially to Petra Neubauer-Guenther for her warm and constant helpfulness.

My stay at the Perimeter Institute was funded by the research program Quantum Matter and Materials (QM2). On this occasion, I thank Andreas Sindermann for the administrative support.

Neben den vielen helfenden Händen und Köpfen aus der Physik möchte ich auch den Menschen danken, die mir während meiner Promotionszeit persönlich stets zur Seite gestanden haben. Ganz besonders danke ich hier meinen Eltern, sowie D.D., J.H., M.K. und I.V.

Der größte Dank gilt meiner Frau dafür, dass sie mir in der letzten Zeit so sehr den Rücken freigehalten hat, und meiner Tochter, dass sie es uns dabei so leicht gemacht hat, wie man es sich von einer Einjährigen nicht besser wünschen kann.

A. Quantum Monte Carlo updates for bilayer models

In order to design a quantum Monte Carlo algorithm in a stochastic series expansion (SSE) [106] of the partition function

$$Z = \text{Tr} e^{-\beta H} = \sum_{\alpha} \sum_{n=0}^{\infty} \left\langle \alpha \left| \frac{(-\beta H)^n}{n!} \right| \alpha \right\rangle, \quad (\text{A.1})$$

we perform so-called *diagonal* and *off-diagonal* updates on a world-line representation of this series. To this endeavor, it is helpful to rewrite the Hamiltonian of the respective bilayer as a sum over bonds, i.e.

$$H = - \sum_{b=1}^{N_b} (H_{b,d} - H_{b,o}) - C, \quad (\text{A.2})$$

with a constant C and diagonal (d) and off-diagonal (o) bond matrix elements

$$H_{b,d} = J \left(\frac{1}{4} \underbrace{-\mathbf{S}_i^z \mathbf{S}_j^z}_{\text{only Heisenberg}} \right), \quad \& \quad H_{b,o} = \frac{1}{2} J (\mathbf{S}_i^+ \mathbf{S}_j^- + \mathbf{S}_i^- \mathbf{S}_j^+). \quad (\text{A.3})$$

Diagonal update The insertion or removal of diagonal bond operators $H_{b,d}$ at a randomly chosen bond b is performed with probability

$$P_{\text{accept}}(n \rightarrow n+1) = \min \left(\frac{N_b \beta \langle \alpha | H_{b,d} | \alpha \rangle}{M - n}, 1 \right), \quad (\text{A.4})$$

for a series of order M with $n < M$ occupied imaginary time slices.

For the bilayer Heisenberg model, the only non-vanishing diagonal elements α after adjusting the constant C to remove negative elements are $\langle \uparrow\downarrow | H_{b,d} | \uparrow\downarrow \rangle = J/2$ and $\langle \downarrow\uparrow | H_{b,d} | \downarrow\uparrow \rangle = J/2$. No diagonal bond elements vanish for the bilayer and necklace XY model, such that we have additionally have $\langle \uparrow\uparrow | H_{b,d} | \uparrow\uparrow \rangle = \langle \downarrow\downarrow | H_{b,d} | \downarrow\downarrow \rangle = J/2$.

Off-diagonal update

In order to include also the off-diagonal element $\langle \uparrow\downarrow | H_{b,o} | \downarrow\uparrow \rangle = \langle \downarrow\uparrow | H_{b,o} | \uparrow\downarrow \rangle = J/2$ in the sampling, we perform loop updates in the world-line representation of the series [156]. For the Heisenberg bilayer, this update can be done deterministically since the loop entering a bond operator has to

A. Quantum Monte Carlo updates for bilayer models

leave it via the bond neighbor on the same side. This is different for the XY models, as also the neighbor on the other side of the operator can be taken as the exit for the loop. Hence, for these models, the loop algorithm is not deterministic since a random decision has to be made at every operator while constructing the loop. For details of this procedure, we refer to Ref. [64].

B. Formulae for the entanglement entropy from groundstate correlations

In this Appendix we establish the connection between a diagonal form of the reduced density matrix $\rho_A = \exp(-H_A)/\text{Tr} \exp(-H_A)$ and the explicit formulae for the entanglement entropies, Eqs. (5.11),(5.12),(5.26),(5.27) for both the free boson (see Sec. B.1) and the Dirac fermion (see Sec. B.2).

B.1. Free boson

First we briefly consider the case of the von Neumann entropy formula, Eq. (5.12). The eigenenergies of the entanglement Hamiltonian $H_A = \sum_q \varepsilon_q b_q^\dagger b_q$ are known via the eigenvalues ν_q of the correlation matrix due to Eq. (5.10) which we rewrite as

$$\nu_q = \frac{1}{2} \frac{e^{\varepsilon_q} + 1}{e^{\varepsilon_q} - 1} = \frac{1}{2} + \frac{1}{e^{\varepsilon_q} - 1}. \quad (\text{B.1})$$

The elements of ρ_A can be interpreted as Boltzmann weights for $\beta = 1$ so that we can use the expression of the entropy for bosons in statistical physics [99]

$$S = - \sum_q \ln(1 - e^{-\varepsilon_q}) + \sum_q \frac{\varepsilon_q}{e^{\varepsilon_q} - 1} \quad (\text{B.2})$$

and simply insert Eq. (B.1). This directly yields (5.12) by inserting the matrix instead of the eigenvalues and performing the trace.

For the Rényi entropies, we first compute the normalization constant $\text{Tr} \exp(-H_A)$ using boson number operators $\hat{n}_q = b_q^\dagger b_q$

$$\begin{aligned} \text{Tr} e^{-H_A} &= \left(\sum_{n_1=0}^{\infty} e^{-\varepsilon_1 n_1} \right) \left(\sum_{n_2=0}^{\infty} e^{-\varepsilon_2 n_2} \right) \cdots \left(\sum_{n_M=0}^{\infty} e^{-\varepsilon_M n_M} \right) \\ &= \prod_q \left(\frac{1}{1 - e^{-\varepsilon_q}} \right), \end{aligned} \quad (\text{B.3})$$

where the sums were identified as geometric series. Since $[\hat{n}_p, \hat{n}_q] = 0$ we can factorize

$$\rho_A^\alpha = \prod_q e^{-\alpha \varepsilon_q \hat{n}_q} (1 - e^{-\varepsilon_q})^\alpha \quad (\text{B.4})$$

We insert this in the definition of the Rényi entropies, Eq. 2.7, where we have to perform the trace over all basis states of the Fock space $|n_1, n_2, \dots, n_M\rangle$. For our

B. Formulae for the entanglement entropy from groundstate correlations

factorization this total trace is also obtained by multiplying the one-particle traces, such that we have

$$\begin{aligned}
S_\alpha &= \frac{1}{1-\alpha} \ln [\text{Tr} \rho_A^\alpha] \\
&= \frac{1}{1-\alpha} \ln \prod_q \sum_{n=0}^{\infty} \langle n | e^{-\alpha \varepsilon_q \hat{n}} (1 - e^{\varepsilon_q})^\alpha | n \rangle \\
&= \frac{1}{1-\alpha} \ln \prod_q \frac{(1 - e^{\varepsilon_q})^\alpha}{1 - e^{\alpha \varepsilon_q}} \\
&= \frac{1}{\alpha - 1} \sum_q \ln \left[\frac{e^{\alpha \varepsilon_q}}{(e^{\varepsilon_q} - 1)^\alpha} - \frac{1}{(e^{\varepsilon_q} - 1)^\alpha} \right]. \tag{B.5}
\end{aligned}$$

From Eq. (B.1) we deduce $\nu_q + \frac{1}{2} = 1/(1 - e^{-\varepsilon_q})$ and $\nu_q - \frac{1}{2} = 1/(e^{\varepsilon_q} - 1)$ so that we arrive at the formula for the Rényi entropy in terms of the ν_q

$$S_\alpha = \frac{1}{\alpha - 1} \sum_q \ln \left[\left(\nu_q + \frac{1}{2} \right)^\alpha - \left(\nu_q - \frac{1}{2} \right)^\alpha \right], \tag{B.6}$$

where we only have to replace the eigenvalues by the matrix C_A and the sum by the trace to get Eq. 5.11.

B.2. Free Dirac fermion

Very similar to the boson, we can derive the formula for the von Neumann entropy of a Dirac fermion by using the corresponding statistical physics entropy of many independent fermions,

$$S = \sum_q \ln(1 + e^{-\varepsilon_q}) + \sum_q \frac{\varepsilon_q}{e^{\varepsilon_q} + 1}. \tag{B.7}$$

Inserting the relation $\zeta_q = 1/(e^{\varepsilon_q} + 1)$ we obtain Eq. (5.27). We note, that ζ_q is just the probability that there is one fermion at momentum q . Hence, $1 - \zeta_q$ is the probability of the opposite event. The formula for the von Neumann entropy can therefore be regarded as the Shannon entropy of the random event of possible occupations of momenta q with Boltzmann distributed probabilities ζ_q .

The derivation for the Rényi entropies is also similar to the boson case. We start by noting that a factorization of ρ_A into the single-particle contributions in $H_A = \sum_q \varepsilon_q f_q^\dagger f_q = \sum_q \varepsilon_q \hat{n}_q$ is possible, since also for fermionic number operators we have $[\hat{n}_q, \hat{n}_p] = 0$. Therefore, we can compute $\text{Tr} \exp(-H_A)$ similar as in Eq. B.3

$$\begin{aligned}
\text{Tr} e^{-H_A} &= \left(\sum_{n_1=0}^1 e^{-\varepsilon_1 n_1} \right) \left(\sum_{n_2=0}^1 e^{-\varepsilon_2 n_2} \right) \cdots \left(\sum_{n_M=0}^1 e^{-\varepsilon_M n_M} \right) \\
&= \prod_q (1 + e^{-\varepsilon_q}), \tag{B.8}
\end{aligned}$$

the main difference being the absence of the geometric series as fermions can have at most a single occupancy. For the factorization of ρ_A we can distribute the factors of the normalization constant accordingly so that we get

$$\rho_A^\alpha = \prod_q \left(\frac{e^{-\varepsilon_q \hat{n}_q}}{1 + e^{-\varepsilon_q}} \right)^\alpha. \quad (\text{B.9})$$

Tracing over all basis states for the Rényi entropies can be carried out on the single-particle factors and by multiplying the sums

$$\begin{aligned} S_\alpha &= \frac{1}{1-\alpha} \ln [\text{Tr} \rho_A^\alpha] \\ &= \frac{1}{1-\alpha} \ln \prod_q \sum_{n=0}^1 \left\langle n \left| \left(\frac{e^{-\varepsilon_q \hat{n}_q}}{1 + e^{-\varepsilon_q}} \right)^\alpha \right| n \right\rangle \\ &= \frac{1}{1-\alpha} \ln \prod_q \left(\frac{1}{1 + e^{-\varepsilon_q}} \right)^\alpha + \left(\frac{e^{-\varepsilon_q}}{1 + e^{-\varepsilon_q}} \right)^\alpha \\ &= \frac{1}{1-\alpha} \sum_q \ln [\zeta_q^\alpha + (1 - \zeta_q)^\alpha]. \end{aligned} \quad (\text{B.10})$$

The last expression is already Eq. (5.26).

References

- [1] L. D. Landau, *Zur Theorie der Phasenumwandlungen II*, Phys. Z. Sowjetunion **11**, 26 (1937).
- [2] K. G. Wilson, *Renormalization Group and Critical Phenomena. I. Renormalization Group and the Kadanoff Scaling Picture*, Physical Review B **4**, 3174 (1971).
- [3] L. Amico, R. Fazio, A. Osterloh, and V. Vedral, *Entanglement in many-body systems*, Reviews of Modern Physics **80**, 517 (2008).
- [4] M. B. Plenio and S. Virmani, *An introduction to entanglement measures*, Quantum Information & Computation **7**, 1 (2007).
- [5] J. Eisert, M. Cramer, and M. B. Plenio, *Colloquium: Area laws for the entanglement entropy*, Reviews of Modern Physics **82**, 277 (2010).
- [6] I. Frérot and T. Roscilde, *Entanglement Entropy across the Superfluid-Insulator Transition: A Signature of Bosonic Criticality*, Physical Review Letters **116**, 190401 (2016).
- [7] H. Casini and M. Huerta, *Universal terms for the entanglement entropy in dimensions*, Nuclear Physics B **764**, 183 (2007).
- [8] X. G. Wen, *Vacuum degeneracy of chiral spin states in compactified space*, Physical Review B **40**, 7387 (1989).
- [9] D. C. Tsui, H. L. Stormer, and A. C. Gossard, *Two-Dimensional Magneto-transport in the Extreme Quantum Limit*, Physical Review Letters **48**, 1559 (1982).
- [10] A. Y. Kitaev, *Fault-tolerant quantum computation by anyons*, Annals of Physics **303**, 2 (2003).
- [11] C. Castelnovo and C. Chamon, *Entanglement and topological entropy of the toric code at finite temperature*, Physical Review B **76**, 184442 (2007).
- [12] A. Einstein, B. Podolsky, and N. Rosen, *Can Quantum-Mechanical Description of Physical Reality Be Considered Complete?*, Physical Review **47**, 777 (1935).
- [13] J. S. Bell, *On the Einstein Podolsky Rosen paradox*, Physics **1**, 195 (1964).
- [14] A. Aspect, J. Dalibard, and G. Roger, *Experimental Test of Bell's Inequalities Using Time-Varying Analyzers*, Physical Review Letters **49**, 1804 (1982).
- [15] G. Weihs, T. Jennewein, C. Simon, H. Weinfurter, and A. Zeilinger, *Violation of Bell's Inequality under Strict Einstein Locality Conditions*, Physical Review Letters **81**, 5039 (1998).

References

- [16] J.-W. Pan, D. Bouwmeester, M. Daniell, H. Weinfurter, and A. Zeilinger, *Experimental test of quantum nonlocality in three-photon Greenberger-Horne-Zeilinger entanglement*, Nature **403**, 515 (2000).
- [17] C. H. Bennett, H. J. Bernstein, S. Popescu, and B. Schumacher, *Concentrating partial entanglement by local operations*, Physical Review A **53**, 2046 (1996).
- [18] J. von Neumann, *Thermodynamik quantenmechanischer Gesamtheiten*, Nachrichten von der Gesellschaft der Wissenschaften zu Göttingen, 273 (1927).
- [19] C. E. Shannon, *A mathematical theory of communication*, Bell System Technical Journal **27**, 379 (1948).
- [20] A. Rényi, *On Measures of Entropy and Information*, in Proc. of the 4th Berkeley Symp. Math. Statist. and Prob. Vol. 1 (1961), pp. 547–561.
- [21] H. Li and F. D. M. Haldane, *Entanglement Spectrum as a Generalization of Entanglement Entropy: Identification of Topological Order in Non-Abelian Fractional Quantum Hall Effect States*, Physical Review Letters **101**, 010504 (2008).
- [22] A. Wehrl, *General properties of entropy*, Reviews of Modern Physics **50**, 221 (1978).
- [23] A. Chandran, V. Khemani, and S. L. Sondhi, *How Universal Is the Entanglement Spectrum?*, Physical Review Letters **113**, 060501 (2014).
- [24] P. Calabrese and J. Cardy, *Entanglement entropy and quantum field theory*, Journal of Statistical Mechanics: Theory and Experiment **2004**, P06002 (2004).
- [25] P. V. Buividovich and M. I. Polikarpov, *Numerical study of entanglement entropy in lattice gauge theory*, Nuclear Physics B **802**, 458 (2008).
- [26] M. A. Metlitski, C. A. Fuertes, and S. Sachdev, *Entanglement entropy in the $O(N)$ model*, Physical Review B **80**, 115122 (2009).
- [27] R. G. Melko, A. B. Kallin, and M. B. Hastings, *Finite-size scaling of mutual information in Monte Carlo simulations: Application to the spin- $\frac{1}{2}$ XXZ model*, Physical Review B **82**, 100409 (2010).
- [28] R. Islam, R. Ma, P. M. Preiss, M. Eric Tai, A. Lukin, M. Rispoli, and M. Greiner, *Measuring entanglement entropy in a quantum many-body system*, Nature **528**, 77 (2015).
- [29] I. Bloch, *Ultracold quantum gases in optical lattices*, Nature Physics **1**, 23 (2005).
- [30] O. Mandel, M. Greiner, A. Widera, T. Rom, T. W. Hänsch, and I. Bloch, *Controlled collisions for multi-particle entanglement of optically trapped atoms*, Nature **425**, 937 (2003).
- [31] C. Moura Alves and D. Jaksch, *Multipartite Entanglement Detection in Bosons*, Physical Review Letters **93**, 110501 (2004).

- [32] A. J. Daley, H. Pichler, J. Schachenmayer, and P. Zoller, *Measuring Entanglement Growth in Quench Dynamics of Bosons in an Optical Lattice*, Physical Review Letters **109**, 020505 (2012).
- [33] L. Bombelli, R. K. Koul, J. Lee, and R. D. Sorkin, *Quantum source of entropy for black holes*, Physical Review D **34**, 373 (1986).
- [34] J. D. Bekenstein, *Black Holes and Entropy*, Physical Review D **7**, 2333 (1973).
- [35] S. W. Hawking, *Black hole explosions?*, Nature **248**, 30 (1974).
- [36] M. Srednicki, *Entropy and area*, Physical Review Letters **71**, 666 (1993).
- [37] A. Riera and J. I. Latorre, *Area law and vacuum reordering in harmonic networks*, Physical Review A **74**, 052326 (2006).
- [38] S. R. White, *Density matrix formulation for quantum renormalization groups*, Physical Review Letters **69**, 2863 (1992).
- [39] U. Schollwöck, *The density-matrix renormalization group*, Reviews of Modern Physics **77**, 259 (2005).
- [40] V. Murg, F. Verstraete, and J. I. Cirac, *Variational study of hard-core bosons in a two-dimensional optical lattice using projected entangled pair states*, Physical Review A **75**, 033605 (2007).
- [41] P. Corboz, R. Orús, B. Bauer, and G. Vidal, *Simulation of strongly correlated fermions in two spatial dimensions with fermionic projected entangled-pair states*, Physical Review B **81**, 165104 (2010).
- [42] G. Vidal, *Entanglement Renormalization*, Physical Review Letters **99**, 220405 (2007).
- [43] K. Audenaert, J. Eisert, M. B. Plenio, and R. F. Werner, *Entanglement properties of the harmonic chain*, Physical Review A **66**, 042327 (2002).
- [44] A. R. Its, B.-Q. Jin, and V. E. Korepin, *Entanglement in the XY spin chain*, Journal of Physics A: Mathematical and General **38**, 2975 (2005).
- [45] M. B. Hastings, *An area law for one-dimensional quantum systems*, Journal of Statistical Mechanics: Theory and Experiment **2007**, P08024 (2007).
- [46] C. Callan and F. Wilczek, *On geometric entropy*, Physics Letters B **333**, 55 (1994).
- [47] C. Holzhey, F. Larsen, and F. Wilczek, *Geometric and renormalized entropy in conformal field theory*, Nuclear Physics B **424**, 443 (1994).
- [48] G. Vidal, J. I. Latorre, E. Rico, and A. Kitaev, *Entanglement in Quantum Critical Phenomena*, Physical Review Letters **90**, 227902 (2003).
- [49] M. B. Plenio, J. Eisert, J. Dreißig, and M. Cramer, *Entropy, Entanglement, and Area: Analytical Results for Harmonic Lattice Systems*, Physical Review Letters **94**, 060503 (2005).
- [50] D. Gioev and I. Klich, *Entanglement Entropy of Fermions in Any Dimension and the Widom Conjecture*, Physical Review Letters **96**, 100503 (2006).

References

- [51] M. M. Wolf, *Violation of the Entropic Area Law for Fermions*, Physical Review Letters **96**, 010404 (2006).
- [52] E. Fradkin and J. E. Moore, *Entanglement Entropy of 2D Conformal Quantum Critical Points: Hearing the Shape of a Quantum Drum*, Physical Review Letters **97**, 050404 (2006).
- [53] E. Ardonne, P. Fendley, and E. Fradkin, *Topological order and conformal quantum critical points*, Annals of Physics **310**, 493 (2004).
- [54] E. Fradkin, *Field Theories of Condensed Matter Physics*, 2nd edition (Cambridge University Press, Cambridge, 2013), 856 pp.
- [55] J. L. Cardy and I. Peschel, *Finite-size dependence of the free energy in two-dimensional critical systems*, Nuclear Physics B **300**, 377 (1988).
- [56] M. A. Metlitski and T. Grover, *Entanglement Entropy of Systems with Spontaneously Broken Continuous Symmetry*, arXiv:1112.5166 (2011).
- [57] X.-G. Wen, *Topological orders and edge excitations in fractional quantum Hall states*, Advances in Physics **44**, 405 (1995).
- [58] A. Kitaev and J. Preskill, *Topological Entanglement Entropy*, Physical Review Letters **96**, 110404 (2006).
- [59] M. Levin and X.-G. Wen, *Detecting Topological Order in a Ground State Wave Function*, Physical Review Letters **96**, 110405 (2006).
- [60] M. A. Nielsen and I. L. Chuang, *Quantum Computation and Quantum Information (Cambridge Series on Information and the Natural Sciences)*, 1st edition (Cambridge University Press, 2000).
- [61] G. Vidal, *Entanglement monotones*, Journal of Modern Optics **47**, 355 (2000).
- [62] M. B. Hastings, *Private Communication*.
- [63] Govind, Ajay, and R. S. Tripathi, *Superconducting properties of bilayer cuprates: role of CuO chains*, Physica C: Superconductivity **334**, 215 (2000).
- [64] O. F. Syljuåsen and A. W. Sandvik, *Quantum Monte Carlo with directed loops*, Physical Review E **66**, 046701 (2002).
- [65] L. Wang, K. S. D. Beach, and A. W. Sandvik, *High-precision finite-size scaling analysis of the quantum-critical point of $S = 1/2$ Heisenberg antiferromagnetic bilayers*, Physical Review B **73**, 014431 (2006).
- [66] J. Helmes and S. Wessel, *Correlations and entanglement in quantum critical bilayer and necklace XY models*, Physical Review B **92**, 125120 (2015).
- [67] S. Ryu and T. Takayanagi, *Holographic Derivation of Entanglement Entropy from the anti – de Sitter Space/Conformal Field Theory Correspondence*, Physical Review Letters **96**, 181602 (2006).
- [68] J.-M. Stéphan, H. Ju, P. Fendley, and R. G. Melko, *Entanglement in gapless resonating-valence-bond states*, New Journal of Physics **15**, 015004 (2013).
- [69] D. Pekker and C. M. Varma, *Amplitude/Higgs Modes in Condensed Matter Physics*, Annual Review of Condensed Matter Physics **6**, 269 (2015).

- [70] J. Goldstone, A. Salam, and S. Weinberg, *Broken Symmetries*, Physical Review **127**, 965 (1962).
- [71] P. W. Anderson, *Plasmons, Gauge Invariance, and Mass*, Physical Review **130**, 439 (1963).
- [72] P. W. Higgs, *Broken Symmetries and the Masses of Gauge Bosons*, Physical Review Letters **13**, 508 (1964).
- [73] S. Weinberg, *A Model of Leptons*, Physical Review Letters **19**, 1264 (1967).
- [74] T. Stöferle, H. Moritz, C. Schori, M. Köhl, and T. Esslinger, *Transition from a Strongly Interacting 1D Superfluid to a Mott Insulator*, Physical Review Letters **92**, 130403 (2004).
- [75] M. Endres, T. Fukuhara, D. Pekker, M. Cheneau, P. Schauß, C. Gross, E. Demler, S. Kuhr, and I. Bloch, *The ‘Higgs’ amplitude mode at the two-dimensional superfluid/Mott insulator transition*, Nature **487**, 454 (2012).
- [76] R. Sooryakumar and M. V. Klein, *Raman Scattering by Superconducting-Gap Excitations and Their Coupling to Charge-Density Waves*, Physical Review Letters **45**, 660 (1980).
- [77] C. Rüegg, B. Normand, M. Matsumoto, A. Furrer, D. F. McMorrow, K. W. Krämer, H. -U. Güdel, S. N. Gvasaliya, H. Mutka, and M. Boehm, *Quantum Magnets under Pressure: Controlling Elementary Excitations in TlCuCl_3* , Physical Review Letters **100**, 205701 (2008).
- [78] S. Humeniuk and T. Roscilde, *Quantum Monte Carlo calculation of entanglement Rényi entropies for generic quantum systems*, Physical Review B **86**, 235116 (2012).
- [79] M. Hasenbusch, *Eliminating leading corrections to scaling in the three-dimensional $O(N)$ -symmetric ϕ^4 model: $N = 3$ and 4*, Journal of Physics A: Mathematical and General **34**, 8221 (2001).
- [80] A. B. Kallin, M. B. Hastings, R. G. Melko, and R. R. P. Singh, *Anomalies in the entanglement properties of the square-lattice Heisenberg model*, Physical Review B **84**, 165134 (2011).
- [81] J. Helmes and S. Wessel, *Entanglement entropy scaling in the bilayer Heisenberg spin system*, Physical Review B **89**, 245120 (2014).
- [82] B. Kulchytskyy, C. M. Herdman, S. Inglis, and R. G. Melko, *Detecting Goldstone modes with entanglement entropy*, Physical Review B **92**, 115146 (2015).
- [83] V. Coffman, J. Kundu, and W. K. Wootters, *Distributed entanglement*, Physical Review A **61**, 052306 (2000).
- [84] H. Casini, M. Huerta, and L. Leita, *Entanglement entropy for a Dirac fermion in three dimensions: Vertex contribution*, Nuclear Physics B **814**, 594 (2009).

References

- [85] E. M. Stoudenmire, P. Gustainis, R. Johal, S. Wessel, and R. G. Melko, *Corner contribution to the entanglement entropy of strongly interacting $O(2)$ quantum critical systems in $2+1$ dimensions*, Physical Review B **90**, 235106 (2014).
- [86] A. B. Kallin, E. M. Stoudenmire, P. Fendley, R. R. P. Singh, and R. G. Melko, *Corner contribution to the entanglement entropy of an $O(3)$ quantum critical point in $2+1$ dimensions*, Journal of Statistical Mechanics: Theory and Experiment **2014**, P06009 (2014).
- [87] T. Hirata and T. Takayanagi, *AdS/CFT and strong subadditivity of entanglement entropy*, Journal of High Energy Physics **2007**, 042 (2007).
- [88] P. Bueno, R. C. Myers, and W. Witczak-Krempa, *Universality of Corner Entanglement in Conformal Field Theories*, Physical Review Letters **115**, 021602 (2015).
- [89] T. Faulkner, R. G. Leigh, and O. Parrikar, *Shape dependence of entanglement entropy in conformal field theories*, Journal of High Energy Physics **2016**, 1 (2016).
- [90] P. Bueno, R. C. Myers, and W. Witczak-Krempa, *Universal corner entanglement from twist operators*, Journal of High Energy Physics **2015**, 1 (2015).
- [91] H. Casini and M. Huerta, *Entanglement entropy in free quantum field theory*, Journal of Physics A: Mathematical and Theoretical **42**, 504007 (2009).
- [92] J. Helmes, L. E. Hayward Sierens, A. Chandran, W. Witczak-Krempa, and R. G. Melko, *Universal corner entanglement of Dirac fermions and gapless bosons from the continuum to the lattice*, Physical Review B **94**, 125142 (2016).
- [93] A. B. Zamolodchikov, *Irreversibility of the Flux of the Renormalization Group in a 2D Field Theory*, JETP Lett. **43**, 730 (1986).
- [94] A. Cappelli, D. Friedan, and J. Latorre, *c-theorem and spectral representation*, Nuclear Physics B **352**, 616 (1991).
- [95] R. C. Myers and A. Sinha, *Holographic c-theorems in arbitrary dimensions*, Journal of High Energy Physics **2011**, 1 (2011).
- [96] I. R. Klebanov, S. S. Pufu, and B. R. Safdi, *F-theorem without supersymmetry*, Journal of High Energy Physics **2011**, 1 (2011).
- [97] Z. Komargodski and A. Schwimmer, *On renormalization group flows in four dimensions*, Journal of High Energy Physics **2011**, 1 (2011).
- [98] H. Osborn and A. Petkou, *Implications of Conformal Invariance in Field Theories for General Dimensions*, Annals of Physics **231**, 311 (1994).
- [99] I. Peschel and V. Eisler, *Reduced density matrices and entanglement entropy in free lattice models*, Journal of Physics A: Mathematical and Theoretical **42**, 504003 (2009).

- [100] S. Sahoo, E. M. Stoudenmire, J.-M. Stéphan, T. Devakul, R. R. P. Singh, and R. G. Melko, *Unusual corrections to scaling and convergence of universal Renyi properties at quantum critical points*, Physical Review B **93**, 085120 (2016).
- [101] I. Peschel, *Calculation of reduced density matrices from correlation functions*, Journal of Physics A: Mathematical and General **36**, L205 (2003).
- [102] M. Cramer, J. Eisert, M. B. Plenio, and J. Dreißig, *Entanglement-area law for general bosonic harmonic lattice systems*, Physical Review A **73**, 012309 (2006).
- [103] A. Chandran, *Private Communication*.
- [104] N. Laflorencie, D. J. Luitz, and F. Alet, *Spin-wave approach for entanglement entropies of the $J_1 - J_2$ Heisenberg antiferromagnet on the square lattice*, Physical Review B **92**, 115126 (2015).
- [105] A. B. Kallin, K. Hyatt, R. R. P. Singh, and R. G. Melko, *Entanglement at a Two-Dimensional Quantum Critical Point: A Numerical Linked-Cluster Expansion Study*, Physical Review Letters **110**, 135702 (2013).
- [106] A. W. Sandvik and J. Kurkijärvi, *Quantum Monte Carlo simulation method for spin systems*, Physical Review B **43**, 5950 (1991).
- [107] M. B. Hastings, I. González, A. B. Kallin, and R. G. Melko, *Measuring Renyi Entanglement Entropy in Quantum Monte Carlo Simulations*, Physical Review Letters **104**, 157201 (2010).
- [108] S. Inglis and R. G. Melko, *Entanglement at a two-dimensional quantum critical point: a $T = 0$ projector quantum Monte Carlo study*, New Journal of Physics **15**, 073048 (2013).
- [109] F. Kos, D. Poland, and D. Simmons-Duffin, *Bootstrapping the $O(N)$ vector models*, Journal of High Energy Physics **2014**, 1 (2014).
- [110] C. D. Nobili, A. Coser, and E. Tonni, *Entanglement negativity in a two dimensional harmonic lattice: area law and corner contributions*, Journal of Statistical Mechanics: Theory and Experiment **2016**, 083102 (2016).
- [111] R. B. Laughlin, *Anomalous Quantum Hall Effect: An Incompressible Quantum Fluid with Fractionally Charged Excitations*, Physical Review Letters **50**, 1395 (1983).
- [112] X. G. Wen, *Topological orders in rigid states*, International Journal of Modern Physics B **04**, 239 (1990).
- [113] X. G. Wen and Q. Niu, *Ground-state degeneracy of the fractional quantum Hall states in the presence of a random potential and on high-genus Riemann surfaces*, Physical Review B **41**, 9377 (1990).
- [114] X.-G. Wen, *Topological Order: From Long-Range Entangled Quantum Matter to a Unified Origin of Light and Electrons*, International Scholarly Research Notices **2013**, 1 (2013).
- [115] T. Einarsson, *Fractional statistics on a torus*, Physical Review Letters **64**, 1995 (1990).

References

- [116] E. Witten, *Topological quantum field theory*, Communications in Mathematical Physics **117**, 353 (1988).
- [117] X. Chen, Z.-C. Gu, and X.-G. Wen, *Local unitary transformation, long-range quantum entanglement, wave function renormalization, and topological order*, Physical Review B **82**, 155138 (2010).
- [118] A. Hamma, R. Ionicioiu, and P. Zanardi, *Bipartite entanglement and entropic boundary law in lattice spin systems*, Physical Review A **71**, 022315 (2005).
- [119] M. Hermanns and S. Trebst, *Renyi entropies for classical string-net models*, Physical Review B **89**, 205107 (2014).
- [120] M. A. Levin and X.-G. Wen, *String-net condensation: A physical mechanism for topological phases*, Physical Review B **71**, 045110 (2005).
- [121] M. Hermanns, *Private Communication*.
- [122] C. Castelnovo and C. Chamon, *Topological order and topological entropy in classical systems*, Physical Review B **76**, 174416 (2007).
- [123] J. Iaconis, S. Inglis, A. B. Kallin, and R. G. Melko, *Detecting classical phase transitions with Renyi mutual information*, Physical Review B **87**, 195134 (2013).
- [124] E. Dennis, A. Kitaev, A. Landahl, and J. Preskill, *Topological quantum memory*, Journal of Mathematical Physics **43**, 4452 (2002).
- [125] K. Siva and B. Yoshida, *Topological order and memory time in marginally-self-correcting quantum memory*, Physical Review A **95**, 032324 (2017).
- [126] B. M. Terhal, *Quantum error correction for quantum memories*, Reviews of Modern Physics **87**, 307 (2015).
- [127] P. W. Shor, *Scheme for reducing decoherence in quantum computer memory*, Physical Review A **52**, R2493 (1995).
- [128] D. Gottesman, *Stabilizer Codes and Quantum Error Correction*, PhD thesis (California Institute of Technology, Pasadena, CA, 1997).
- [129] B. J. Brown, D. Loss, J. K. Pachos, C. N. Self, and J. R. Wootton, *Quantum memories at finite temperature*, Reviews of Modern Physics **88**, 045005 (2016).
- [130] P. W. Shor, *Fault-tolerant quantum computation*, in 37th Annual Symposium on Foundations of Computer Science (1996), pp. 56–65.
- [131] J. v. Neumann, *Probabilistic logics and synthesis of reliable organisms from unreliable components*, in Automata Studies, edited by C. Shannon and J. McCarthy (1956), pp. 43–98.
- [132] E. Knill, R. Laflamme, and W. H. Zurek, *Resilient quantum computation: error models and thresholds*, Proceedings of the Royal Society of London A: Mathematical, Physical and Engineering Sciences **454**, 365 (1998).
- [133] D. Bacon, *Operator quantum error-correcting subsystems for self-correcting quantum memories*, Physical Review A **73**, 012340 (2006).

- [134] S. Bravyi and J. Haah, *Quantum Self-Correction in the 3D Cubic Code Model*, Physical Review Letters **111**, 200501 (2013).
- [135] H. A. Kramers and G. H. Wannier, *Statistics of the Two-Dimensional Ferromagnet. Part I*, Physical Review **60**, 252 (1941).
- [136] J. B. Kogut, *An introduction to lattice gauge theory and spin systems*, Reviews of Modern Physics **51**, 659 (1979).
- [137] R. Savit, *Duality in field theory and statistical systems*, Reviews of Modern Physics **52**, 453 (1980).
- [138] G. K. Brennen and J. K. Pachos, *Why should anyone care about computing with anyons?*, Proceedings of the Royal Society of London A: Mathematical, Physical and Engineering Sciences **464**, 1 (2008).
- [139] C. Castelnovo and C. Chamon, *Topological order in a three-dimensional toric code at finite temperature*, Physical Review B **78**, 155120 (2008).
- [140] S. Trebst, P. Werner, M. Troyer, K. Shtengel, and C. Nayak, *Breakdown of a Topological Phase: Quantum Phase Transition in a Loop Gas Model with Tension*, Physical Review Letters **98**, 070602 (2007).
- [141] H. W. J. Blöte and Y. Deng, *Cluster Monte Carlo simulation of the transverse Ising model*, Physical Review E **66**, 066110 (2002).
- [142] S. Suzuki, J. Inoue, and B. K. Chakrabarti, *Quantum Ising Phases and Transitions in Transverse Ising Models*, Vol. 862, Lecture Notes in Physics (Springer, Berlin, Heidelberg, 2013).
- [143] J. Vidal, S. Dusuel, and K. P. Schmidt, *Low-energy effective theory of the toric code model in a parallel magnetic field*, Physical Review B **79**, 033109 (2009).
- [144] J. Vidal, R. Thomale, K. P. Schmidt, and S. Dusuel, *Self-duality and bound states of the toric code model in a transverse field*, Physical Review B **80**, 081104 (2009).
- [145] M. Caselle, M. Hasenbusch, and M. Panero, *String effects in the 3d gauge Ising model*, Journal of High Energy Physics **2003**, 057 (2003).
- [146] A. M. Ferrenberg and D. P. Landau, *Critical behavior of the three-dimensional Ising model: A high-resolution Monte Carlo study*, Physical Review B **44**, 5081 (1991).
- [147] S. Vijay, J. Haah, and L. Fu, *Fracton topological order, generalized lattice gauge theory, and duality*, Physical Review B **94**, 235157 (2016).
- [148] S. Bravyi and B. Terhal, *A no-go theorem for a two-dimensional self-correcting quantum memory based on stabilizer codes*, New Journal of Physics **11**, 043029 (2009).
- [149] J. Haah, *Local stabilizer codes in three dimensions without string logical operators*, Physical Review A **83**, 042330 (2011).
- [150] B. Efron, *Bootstrap Methods: Another Look at the Jackknife*, The Annals of Statistics **7**, 1 (1979).

References

- [151] N. Metropolis, A. W. Rosenbluth, M. N. Rosenbluth, A. H. Teller, and E. Teller, *Equation of State Calculations by Fast Computing Machines*, Journal of Chemical Physics **21**, 1087 (1953).
- [152] U. Wolff, *Collective Monte Carlo Updating for Spin Systems*, Physical Review Letters **62**, 361 (1989).
- [153] J. Helmes, J.-M. Stéphan, and S. Trebst, *Rényi entropy perspective on topological order in classical toric code models*, Physical Review B **92**, 125144 (2015).
- [154] M. Caselle and M. Hasenbusch, *Deconfinement transition and dimensional cross-over in the 3D gauge Ising model*, Nuclear Physics B **470**, 435 (1996).
- [155] Y. Kamiya, Y. Kato, J. Nasu, and Y. Motome, *Magnetic three states of matter: A quantum Monte Carlo study of spin liquids*, Physical Review B **92**, 100403 (2015).
- [156] H. G. Evertz, *The loop algorithm*, Advances in Physics **52**, 1 (2003).
- [157] A. G. Fowler, M. Mariantoni, J. M. Martinis, and A. N. Cleland, *Surface codes: Towards practical large-scale quantum computation*, Physical Review A **86**, 032324 (2012).

Erklärung zur Dissertation

Ich versichere, dass ich die von mir vorgelegte Dissertation selbständig angefertigt, die benutzten Quellen und Hilfsmittel vollständig angegeben und die Stellen der Arbeit — einschließlich Tabellen, Karten und Abbildungen —, die anderen Werken im Wortlaut oder dem Sinn nach entnommen sind, in jedem Einzelfall als Entlehnung kenntlich gemacht habe; dass diese Dissertation noch keiner anderen Fakultät oder Universität zur Prüfung vorgelegen hat; dass sie — abgesehen von unten angegebenen Teilpublikationen — noch nicht veröffentlicht worden ist sowie, dass ich eine solche Veröffentlichung vor Abschluss des Promotionsverfahrens nicht vornehmen werde. Die Bestimmungen der Promotionsordnung sind mir bekannt. Die von mir vorgelegte Dissertation ist von Prof. Dr. Simon Trebst betreut worden.

Publikationen

J. Helmes and S. Wessel, *Entanglement entropy scaling in the bilayer Heisenberg spin system*, Physical Review B **89**, 245120 (2014).

J. Helmes and S. Wessel, *Correlations and entanglement in quantum critical bilayer and necklace XY models*, Physical Review B **92**, 125120 (2015).

J. Helmes, J.-M. Stéphan, and S. Trebst, *Rényi entropy perspective on topological order in classical toric code models*, Physical Review B **92**, 125144 (2015).

J. Helmes, L. Hayward Sierens, A. Chandran, W. Witczak-Krempa, and R. Melko, *Universal corner entanglement of Dirac fermions and gapless bosons from the continuum to the lattice*, Physical Review B **94**, 125142 (2016).